

AD-A131 738

MICROWAVE LANDING SYSTEM PHASE II TRACKER ERROR STUDY

1/3

(U) FEDERAL AVIATION ADMINISTRATION WASHINGTON DC

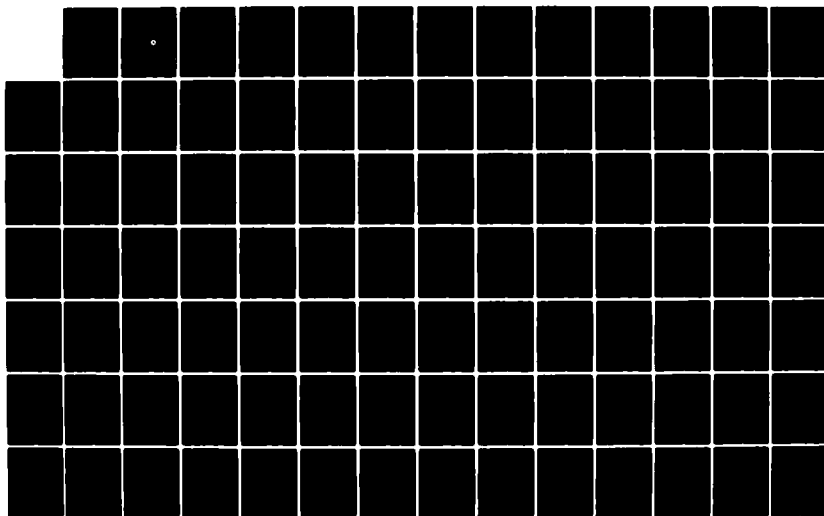
SYSTEMS RESEARCH AND DEVELOPMENT SERVICE DEC 74

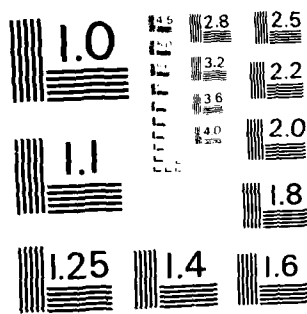
UNCLASSIFIED

FAA/RD-74-207

F/G 17/7

NL





MICROCOPY RESOLUTION TEST CHART  
NATIONAL BUREAU OF STANDARDS - 1963 - A

Report No. FAA-RD-74-207

AD A131738

# MICROWAVE LANDING SYSTEM PHASE II TRACKER ERROR STUDY



December 1974

Document is available to the public through the  
National Technical Information Service,  
Springfield, Virginia 22151

Prepared for

**U.S. DEPARTMENT OF TRANSPORTATION**  
**FEDERAL AVIATION ADMINISTRATION**  
Systems Research & Development Service  
Washington, D.C. 20590

DTIC FILE COPY

DTIC  
CTE  
1983

83 08 24 00 8

1. Report No. FAA-RD-74-207	2. Government Accession No. AD A131738	3. Recipient's Catalog No.	
4. Title and Subtitle Microwave Landing System Phase II Tracker Error Study		5. Report Date December 1974	
		6. Performing Organization Code	
7. Author(s)		8. Performing Organization Report No.	
9. Performing Organization Name and Address U. S. Department of Transportation Federal Aviation Administration Systems Research & Development Service Washington, D.C. 20591		10. Work Unit No. (TRAIS)	
		11. Contract or Grant No.	
12. Sponsoring Agency Name and Address U. S. Department of Transportation Federal Aviation Administration Systems Research & Development Service Washington, D.C. 20591		13. Type of Report and Period Covered Final Study Report	
14. Sponsoring Agency Code			
15. Supplementary Notes This document is disseminated under the sponsorship of the Department of Transportation in the interest of information exchange. The United States Government assumes no liability for its contents or use thereof.			
16. Abstract  This report documents a study of the types and amounts of errors inherent in the various instrumentation systems used for close-in and far-field dynamic flight tests for the Microwave Landing System (MLS) Development Program Phase II, at the two test sites and the four runways utilized, one for each contractor MLS. Analysis of Phase II flight test data depended on comparison of MLS azimuth, elevation and range functions with the same functions generated by ground tracker data, the difference being the error of the MLS functions if the error in the tracker functions is smaller by at least an order of magnitude. This study not only summarizes the results of hardware calibrations, data processing techniques and tracker error studies made during Phase II to define and reduce tracker errors, but projects the impact of remaining tracker error on MLS Phase II test results.			
17. Key Words  Microwave Landing System Approach and Landing Systems Instrumentation Error		18. Distribution Statement  Copies are available to the public through The National Technical Information Service, Springfield, Virginia 22151	
19. Security Classif. (of this report)  Unclassified	20. Security Classif. (of this page)  Unclassified	21. No. of Pages  198	22. Price

## TABLE OF CONTENTS

	<u>Page</u>
I. INTRODUCTION .....	I-1
A. Objectives .....	I-1
B. Description of Tracking Systems .....	I-2
1. NAFEC .....	I-2
2. Wallops Station .....	I-10
C. Error Categories .....	I-19
II. TRACKER STUDIES .....	II-1
A. Wallops Station .....	II-1
1. Aircraft Tracking Capabilities with the AN/FPS-16 and GSN-5 Radars at Wallops Station ....	II-1
2. Technical Characteristics AN/FPS-16 .....	II-9
3. Photogrammetric Error Analysis .....	II-13
B. NAFEC .....	II-41
1. Evaluation of NAFEC Tracking System in an MLS Test Program Environment .....	II-41
2. Phototheodolite Error Analysis .....	II-45
3. Technical Characteristics .....	II-58
III. OPERATIONAL CALIBRATIONS/TESTS .....	III-1
A. Wallops Station .....	III-1
1. AN/FPS-16 Radar .....	III-1
2. Photogrammetric System .....	III-9

# Table of Contents (Cont.)

	<u>Page</u>
B. NAPEC .....	III-11
1. Phototheodolites .....	III-11
IV. DATA PROCESSING TECHNIQUES .....	IV-1
A. Outlier Screening .....	IV-1
1. FPS-16 Radar .....	IV-1
2. Photogrammetric System .....	IV-1
3. EAIR and Phototheodolites .....	IV-2
B. Filtering .....	IV-4
1. FPS-16 Radar, EAIR and Phototheodolites (Real Time Data Only) .....	IV-4
2. Phototheodolite (Film Corrected) and Photogrammetry.	IV-15
3. Filter Cutoff Frequency .....	IV-18
C. Data Merge Process .....	IV-24
V. TRACKER MLS PHASE II DATA STUDIES.....	V-1
A. EAIR Versus Phototheodolites .....	V-1
1. Range Evaluation .....	V-1
2. Angle Evaluation .....	V-6
B. Phototheodolite Real-Time Versus Phototheodolite Film-Corrected Data .....	V-7
C. FPS-16 Radar Lower Limits of Coverage - Runway 22.....	V-12

# Table of Contents (Cont.)

	<u>Page</u>
VI. IMPACT ON MLS TEST RESULTS .....	VI-1
A. General .....	VI-1
B. Wallops Station .....	VI-2
1. FPS-16 Radar .....	VI-2
2. Photogrammetric System (PMS) .....	VI-4
C. NAFEC .....	VI-13
1. Phototheodolite System .....	VI-13
2. EAIR .....	VI-13

Accession For

NTIS	<input checked="" type="checkbox"/>
DTIC	<input type="checkbox"/>
AD	<input type="checkbox"/>
AS	<input type="checkbox"/>
NSA	<input type="checkbox"/>
NSA/CSS	<input type="checkbox"/>
NSA/CSS/ISS	<input type="checkbox"/>
NSA/CSS/INT	<input type="checkbox"/>
NSA/CSS/OPR	<input type="checkbox"/>
NSA/CSS/PLN	<input type="checkbox"/>
NSA/CSS/SEC	<input type="checkbox"/>
NSA/CSS/STN	<input type="checkbox"/>
NSA/CSS/TECH	<input type="checkbox"/>
NSA/CSS/TRA	<input type="checkbox"/>
NSA/CSS/VAL	<input type="checkbox"/>
NSA/CSS/WHI	<input type="checkbox"/>
NSA/CSS/WHI/INT	<input type="checkbox"/>
NSA/CSS/WHI/PLN	<input type="checkbox"/>
NSA/CSS/WHI/SEC	<input type="checkbox"/>
NSA/CSS/WHI/STN	<input type="checkbox"/>
NSA/CSS/WHI/TECH	<input type="checkbox"/>
NSA/CSS/WHI/TRA	<input type="checkbox"/>
NSA/CSS/WHI/VAL	<input type="checkbox"/>
NSA/CSS/WHI/WHI	<input type="checkbox"/>

A



## I. INTRODUCTION

### A. Objectives

The basic approach to the analysis of Phase II flight test data is to compare the MLS functions to the same functions generated from ground tracker data. The Phase II Test Requirements and Coordination Plan defines error in the following manner:

$$\text{Error} = \text{MLS Function} - \text{Tracker Function}$$

This definition is valid if, and only if, the error in the tracker function is small compared to the error in the MLS function, i.e., approximately one tenth or less of the MLS error. If the tracker error equals the MLS error, then the difference between the two functions would be the summation of the two error contributors and the band of uncertainty about the measured error value would be equal to the MLS function error. If the tracker error were to exceed MLS error, the differences between the two functions would be due primarily to the tracker, and the band of uncertainty about the measured difference would become increasingly large.

During the Phase II program a number of tracker error studies were completed and hardware calibrations and data processing techniques were adopted in order to define and reduce the tracker errors. This report



summarizes the results of the various activities in this area and assesses the impact of tracker error on the MLS Phase II test results.

## B. Description of Tracking Systems

### 1. NAFEC

Two ground tracking systems were used at NAFEC for the Phase II Test Program. They were the Extended Area Instrumentation Radar (EAIR) and the Phototheodolite Facility. Normally, the EAIR was used for tracking beyond 24,000 feet from the MLS azimuth site and the phototheodolites for the region from 24,000 feet through touchdown and rollout.

Descriptions of the two tracker facilities are contained in the following sections:

#### a. Extended Area Instrumentation Radar (EAIR) Facility

The precision tracking radar of the EAIR Facility measures displays and records the slant range, azimuth and elevation angles of an aircraft. Maximum tracking distance of the EAIR Facility is 100 nautical miles when operated in its primary (skin tracking) mode, or 190 miles when in secondary (beacon tracking) mode. Maximum tracking rate is 5,000 miles per hour. Minimum tracking distance is one nautical mile. Digital output data consisting of slant range, azimuth angle, elevation angle, and real time are recorded on magnetic tape in IBM 7090-compatible format. Analog data in Z-Y, X-H coordinates are recorded in real-time on 30-inch plot paper.

The EAIR Facility consists of a radar building and an adjacent 18-foot tower that supports the radar antenna. Figure I-1 shows the geographical location of the EAIR Facility. The building provides separate climate-controlled rooms for radar equipment, computer equipment and ancillary equipment. A Radar Room contains the precision instrumentation radar, and a Computer Room contains the polar-to-cartesian coordinate conversion computer, dual-pen X-Y, X-H plotter, digital data converter, and magnetic tape recorder. The antenna pedestal and a 14-foot parabolic reflector are mounted atop the steel-enclosed concrete tower. The center of the radar beam is 102.97 feet above mean sea level. A 26.5-foot rigid foamed-plastic radome protects the antenna and pedestal from wind and weather.

The tracking radar is a Model 661 precision C-band instrumentation radar system, which measures the slant range, azimuth angle, and elevation angle of the aircraft being tracked. Either skin track or beacon track can be selected. For beacon track, a transponder must be installed in the aircraft. The transponder is triggered by the transmitted radar pulse and sends back a signal that is received by the radar antenna system in the same manner as the reflected pulse is received during skin tracking. Other performance features of the radar system include automatic tracking, aided range tracking, and raster scanning. Automatic tracking, once the aircraft is acquired, enables the radar antenna and



range system to automatically follow aircraft movements. The aided range tracking feature enables a range gate to be set at target (aircraft) velocity to facilitate angle lock-on or tracking during poor signal conditions. Raster scanning is used to assist in target acquisition. The radar system has the capability of providing or receiving synchronizing and slaving information to or from other radars, optical trackers, and programmers, both in angle and in range. Radar data is supplied in both analog and digital forms for slant range, azimuth angle, and elevation angle.

An X-Y, X-H ink-trace plot of aircraft trajectory and precise timing marks are available on a 30-inch x 30-inch plotting board. Timing marks are available at selectable rates of 1 per second or 1 per 10 seconds. The Plotting Board range is continuously adjustable from 6,000 yards to 1,200,000 yards. A software program converted the digitally accorded slant range, azimuth angle and elevation angle into X, Y, and Z coordinates referenced to the center of radiation of the MLS azimuth antenna.

The EAIR radar errors are in polar coordinates of azimuth, elevation and range. This radar is less accurate than the FPS-16 at Wallops Station, having theoretical angular errors of 0.15 mils rms and range errors of 20 yards rms. For both incoming flight paths the radar line of sight becomes normal to the runway centerlines.

This condition occurs near runway 13 threshold and on final approach just before runway 4 threshold. The range error is the most significant error on final approach, touchdown and rollout, and transforms into an azimuth angle error throughout this region. Farther out on approach, the cross-coupling of errors decreases and the range errors primarily affect DME values.

b. Phototheodolite Facility

The Phototheodolite Facility is a four-station optical instrumentation complex that is used to accurately determine position-time data concerning a target. The final data obtained from the Phototheodolite Facility are the following: a real-time plot of the X-Y and X-Z or Y-Z coordinates and digital recordings of the X, Y, and Z coordinates.

Each of the four stations of the Phototheodolite Facility is a specially constructed tower that provides a stable mounting for a phototheodolite instrument. The phototheodolite towers are in the NAFEC Airport area and are located to permit visual surveillance of the runways and environs. The geographical locations of the four phototheodolite towers are indicated on Figure I-1.

A Contraves Model C phototheodolite instrument is mounted in the top of each of the four towers. Two operators are required to operate each instrument; one controls the azimuth drive and the other

controls the elevation drive. The dome which protects the phototheodolite instrument is slaved to the azimuth drive system of the instrument so that the dome rotates when the instrument is rotated:

Although each theodolite has hemispherical coverage, space position data is most accurate in regions where the lines of sight from two or more theodolites are normal to each other. The target is photographed on 35-mm film at timed and synchronized intervals, and the theodolite optical axis measured by digital encoders. The film data is edited and read, and the information is placed on punched cards for eventual position solution by the IBM-7090 Computer. The encoder data is recorded on magnetic tape and is used for real time plotting and for position computations using the IBM-7090 computer.

The phototheodolites measure angles to a target in spherical coordinates, and aircraft position must be obtained from the intersection of two or more lines of sight (LOS). The positional error in the phototheodolite system varies along a family of hyperbolas, with the highest positional accuracy obtained when the LOS intersect at right angles along a line halfway between the two stations and perpendicular to it. Coming closer in or going farther out will increase the error. The linear error components are not equal, and form ellipses or ellipsoids of error, greatest (in the horizontal plane) when the LOS are parallel to each other. The greatest positional errors occur on the line between two theodolite stations, and far out where LOS

nearly become parallel. When more than two theodolites are used, additional accuracy may be obtained, especially at the apex of the triad for the three available stations. This region is in the vicinity of the stop end of runway 4-22 (slightly to the southeast) and at an altitude of about 5,000 feet.

Phototheodolite towers P-29, P-36, and P-8 (see Figure I-1) were used during Phase II testing, tower P-13 being inactive. Towers P-29 and P-36 provide good two-station coverage for the approach region of runway 13-31. However, the base leg is relatively short (6,468 feet) and the accuracy tends to degrade rather quickly beyond 1 nmi from threshold. In addition, a three-station solution using tower P-8 has little merit since it is significantly farther away from the approach region and has an unfavorable geometry for a position solution with respect to the other two phototheodolite towers. In the flare, touchdown and rollout regions for runways 13-31 and 4-22, the three towers provide excellent coverage, and no significant geometry problems are present.

In the approach region for runway 4-22, towers P-36 and P-8 are located about 4 nm from the start of the approach region, and the position computations tend to be degraded by the angular measurement accuracy of the phototheodolites. However, this factor is offset by the relatively long baselines (over 10,000 feet) for tower pairs P-8 to P-29 and P-8 to P-36. The geometry of the phototheodolites for runway 4-22 indicate that a three-station solution improves the positional accuracy in the approach region to the runway.

c. Aircraft Tracking Points

The two primary test aircraft at NAFEC were a C-118 (Bendix) and a DC-6 (ITT/Gilfillan). To facilitate consistent tracking, both aircraft were equipped with beacons for radar tracking and the nose of the aircraft was used for phototheodolite tracking. Since the radar beacons, the phototheodolite reference point and the MLS antennas do not have the same physical locations on the aircraft, certain errors will be introduced into merged data from this source. To determine the magnitude of the problem it is necessary to know the distances between these reference points. For purposes of this study a cartesian coordinate system (x, y & z) with the following conventions are defined to establish these distances:

- 1) The center of the aircraft nose is defined as the 0, 0, 0 reference point.
- 2) The (+) x direction is toward the tail of the aircraft.
- 3) The (+) z direction is above the center of the aircraft nose.
- 4) The (+) y direction is to the left of the aircraft nose as faced (starboard of the aircraft).

The locations of the reference points for the two aircraft are listed in Table I-1.



TABLE I-1: NAFEC AIRCRAFT REFERENCE POINTS.

Aircraft/Contractor	Reference Point	Displacement in Feet		
		x	y	z
C-118 (Bendix)	Center of Acft Nose	0.00	0.00	0.00
	Radar Beacon	+16.31	0.00	-4.50
	C-Band Antenna	+2.48	+0.25	+1.50
	Ku-Band Antenna	+2.48	-0.25	+1.50
DC-6 (ITT/Gilfillan)	Center of Acft Nose	0.00	0.00	0.00
	Phototheodolite Cross	+1.58	0.00	+1.16
	Radar Beacon	+16.81	0.00	-4.50
	C-Band Antenna #1	+2.48	-0.54	0.00
	" " #2	+2.48	+0.25	+1.50
	" " #3	+2.48	-0.25	+1.50
	Omni Antenna #1	+10.73	0.00	-5.75
	" " #2	+13.64	0.00	-5.75

## 2. Wallops Station

Two ground tracking systems were employed during the Phase III testing at Wallops Station. They are an AN/FPS-16 tracking radar and a four camera photogrammetric system. The FPS-16 was used for tracking beyond 12,000 feet from the MLS azimuth site and the photogrammetric system was used for the low angle region from 12,000 feet through touchdown.

Descriptions of the two tracking systems are contained in the following sections:

a. Tracking Radar AN/FPS-16

The AN/FPS-16 is a C-band, high-precision, monopulse tracking radar. The theoretical accuracy of the AN/FPS-16 is 0.1 mil rms in azimuth and elevation and 5 yards rms in range with a signal-to-noise ratio of 20 dB or greater. The AN/FPS-16 provides outputs in the following forms:

- (1) Synchro voltages representing slant range and azimuth and elevation angles.
- (2) Potentiometer voltages representing slant range and azimuth cosine functions of azimuth and elevations angles.
- (3) Precision digital data representing slant range and azimuth and elevation angles.

The AN/FPS-16 radar also provides real-time, present-position analog data for range safety use.

Maximum instrumented tracking range is 1,000,000 yards with system track range of 272,000 yards on a 1-square-meter target. Beacon operation is used primarily to increase angular tracking accuracy. Tracking performance is expected to be maintained down to elevation angles of approximately  $0.5^{\circ}$ . Minimum tracking range is 500 yards.

The AN/FPS-16 Tracking Radar Facility at Wallops Station consists of a radar building and an adjacent tower which supports the

radar antenna. The AN/FPS-16 is located just north of runway 10-28 and parallel to a vehicular roadway, 2100 feet from runway 28 threshold. See Figure I-2. The building provides climatic controlled rooms for radar equipment and ancillary equipment such as plotting boards. The antenna pedestal and a 12-foot parabolic reflector is mounted atop the radar tower.

The tracking radar is a former Apollo-program ship-borne precision C-band instrumentation radar system. It measures the slant range, azimuth angle, and elevation angle of the aircraft being tracked. Either skin track or beacon track can be selected. For beacon track, a transponder is installed in the aircraft. Other performance features of the radar system include automatic tracking and aided range tracking. Automatic tracking, once the aircraft is acquired, enables the radar antenna and range system to automatically follow aircraft movements. The aided range tracking feature enables a range gate to be set at target (aircraft) velocity to facilitate angle lock-on or tracking during poor signal conditions. Radar data is supplied in both analog and digital forms for slant range, azimuth angle, and elevation angle.

An X-Y, X-H ink-trace plot of aircraft trajectory and precise timing marks are available on a 30-inch x 30-inch plotting board. Timing marks are available at selectable rates of 1 per second or 1 per

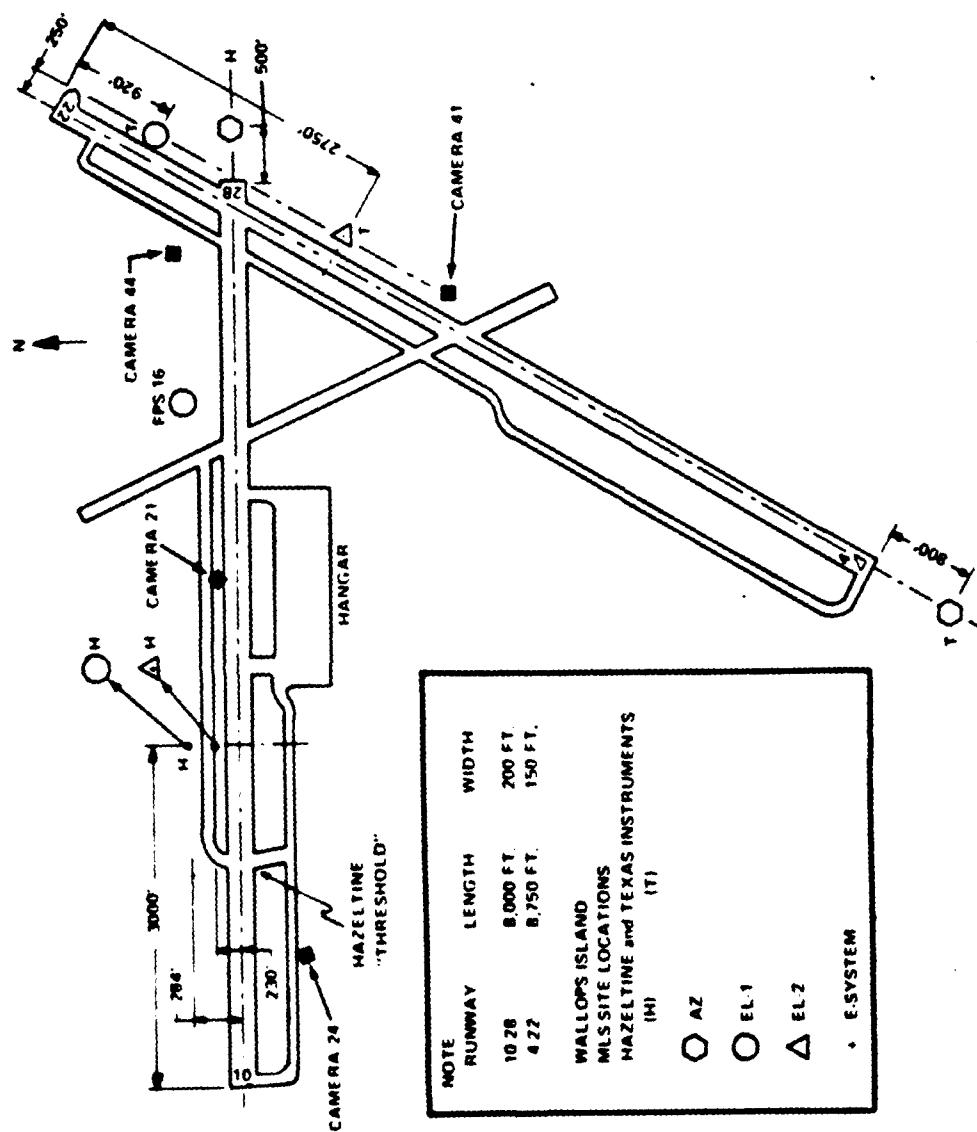


Figure I-2: Wallops Station MLS Phase II Test Site Locations.

10 seconds. The plotting board range is continuously adjustable from 6,000 yards to 1,200,000 yards.

A software program converted the digitally recorded function (slant range, azimuth angle and elevation angle) into the MLS coordinate system.

The AN/FPS-16 radar operates in polar coordinates of azimuth, elevation and range. Since the MLS transmitters are not located at the radar station, the errors in measurement of aircraft position must be transformed to MLS coordinate system. The angle errors in linear distance originally are  $R \times \Delta\theta$  and  $R \times \Delta\phi$ , while range is simply  $\Delta R$ . The theoretical accuracy of the FPS-16 is 0.1 mil rms for angle measurements and 5 yards rms for range measurements. Close in, i.e., 5,000 yards or less, the range error predominates; thus its effect must be considered in the region of final approach, touchdown and rollout, particularly for runway 22. The predominant error, caused by range error, is in the MLS azimuth values on runway 22 touchdown location. There the range error is coupled directly to azimuth values. The angle errors at this short range will be minimal, although low angle radar values below half beam width (about  $1/2^\circ$ ) may cause erratic tracking, especially at touchdown and beyond. The vehicular road and runway 10-28 surface cause ground reflection, and at times the radar even tracks the A/C image. The angle error values are reflected in

azimuth and elevation far out on initial straight in approach, while range error is reflected into DME. For intermediate distances on final approach, the errors are cross coupled and are related to angle between radar line of sight and flight path. For incoming flights on runway 10, the radar line of sight is almost along the flight path itself, with angle errors related directly to MLS azimuth and elevation, and range errors to DME.

b. Photogrammetric Facility

The Camera Photogrammetric Facility determines aircraft position coordinates during final approach by use of at least two fixed cameras whose LOS coverage intersect in the region of interest. This system was implemented when the error studies at Wallops Station showed a low angle tracking problem for the AN/FPS-16 in the vicinity of runway threshold and touchdown.

A total of four fixed Hulcher cameras covers approximately 6,000 feet of the final approach, touchdown and rollout. The cameras take pictures of aircraft and reference ground targets during test runs. The frames are subsequently read and the data used to calculate aircraft spatial position.

Four Hulcher 70 Model 103 cameras are used, three sideline cameras and one end camera as shown in Figure I-3. The sideline cameras, using a 47mm lens, have 66° of coverage, while the end camera,



using a 152-mm lens, has a 21° coverage. The camera film has range timing markings for synchronization in computing of position data.

The developed 70-mm film is read using Mann Type 422F Comparator to obtain aircraft angular coordinate position relative to surveyed target boards. The aircraft film frame fiducial coordinates are transformed to horizontal reference coordinates, from which azimuth and elevation angles or planes are computed (only azimuth from end camera is used). The aircraft position is computed from intersection of the three planes, and a coordinate translation performed to the MLS azimuth site.

c. Aircraft Tracking Points

The two primary test aircraft at Wallops Station were a C-131 (Texas Instruments) and a C-54 (Hazeltine). To facilitate consistent tracking both aircraft were equipped with beacons for radar tracking and large crosses on the nose for photogrammetric tracking. The crosses were 3-inch white strips on a black background. Since the radar beacons, the photogrammetric crosses and the MLS antennas do not have the same physical locations on the aircraft, certain errors will be introduced into merged data from this source. To determine the magnitude of the



problem it is necessary to know the distances between these reference points. For purposes of this study a cartesian coordinate system (x, y & z) with the following conventions are defined to establish these distances:

- 1) The center of the photogrammetric cross is defined as the 0, 0, 0 reference point.
- 2) The (+) x direction will be toward the tail of the aircraft.
- 3) The (+) z direction will be above the horizontal bar of the photogrammetric cross.
- 4) The (+) y direction will be to the left of the vertical bar of the photogrammetric cross as you face the nose of the aircraft.

The locations of the reference points for the two aircraft are listed in Table I-2.

TABLE I-2: WALLOPS STATION AIRCRAFT REFERENCE POINT.

Aircraft/Contractor	Reference Point	Displacement in Feet		
		x	y	z
C-131 (T.I.)	Photogrammetry Cross	0.00	0.00	0.00
	Radar Beacon	+2.25	0.00	+1.92
	C-Band Angle Antenna	+0.58	+0.23	0.00
	Ku-Band Angle Antenna	+0.58	0.00	0.00
	C-Band DME Antenna	+0.58	-0.23	0.00
	DME Omni Antenna	+14.33	0.00	-0.41
	Angle Omni	+62.50	0.00	-2.87
C-54 (Hazeltine)	Photogrammetry Cross	0.00	0.00	0.00
	Radar Beacon	+15.30	0.00	+6.83
	Ku-Band Antenna	+4.50	0.00	+2.50
	C-Band Antenna	+5.25	0.00	+2.75

### C. Error Categories

The MLS Phase II Test Requirements and Coordination Plan established standard data partitions and error calculations for the dynamic test data. The data partitions were 3 nmi in length at longer ranges and 2,000 feet in length in the flare, touchdown and rollout regions. The basic error calculations required for each partition were as follows:

- (1) Least-squares straight-line curve fit
- (2) 97.5 and 2.5 percentiles about straight-line fit
- (3) Standard deviation about straight line
- (4) Peak bias of straight line
- (5) Mean value

In order to correlate the tracker errors with standard error calculations, the tracker errors are defined in Table I-3.

TABLE I-3: TRACKER ERROR DEFINITIONS

Tracker Error Category	Definition	Affects Std. Calculations
(1) Data Outlier	Data point which grossly differs adjacent data points	All standard Calculations
(2) High Frequency (>0.5 Hz)	>0.5 Hz	Standard Deviation and Percentiles
(3) Low Frequency	<0.5 Hz but <1/60 Hz	All Standard Calculations
(4) Bias	>1/60 Hz	Primarily the Mean Value

## II. TRACKER STUDIES

### A. Wallops Station

#### 1. Aircraft Tracking Capabilities with the AN/FPS-16 and GSN-5 Radars at Wallops Station

Wolfe Associates carried out an analytical study of test data in order to determine the tracking accuracy of the FPS-16 (ASIR) at Wallops Station. The study utilized static calibrations, concurrent tracking of the GEOS-11 satellite by ASIR and 2 C-band radars at Wallops Station and concurrent tracking of the MLS test aircraft approaching runways 10 and 22.

The general conclusions concerning the Wallops Station FPS-16 installation (ASIR) were:

- Given appropriate calibration information to remove measurement biases, the ASIR system performs at least as well as the other C-Band radars at high elevations.
- At low elevations, ASIR angle measurements are subject to considerable environmental disturbance, and such disturbances are of sufficiently high magnitude and low frequency as to drastically reduce confidence in point estimator trajectory generation schemes.

- ASIR range measurements appear to be affected by these disturbances to a far lesser degree.

In addition, the report presented a position uncertainty analysis for the approaches to runways 10 and 22. The analysis employed a computer program (ERAN) to model the Wallops Station data reduction procedures and to propagate position uncertainties along the flight paths. The tracking errors propagated in the analysis were as listed in Table II-1.

TABLE II-1: WALLOPS STATION ASIR TRACKING ERRORS

Function	Bias	Noise
- Range	2.0 Meters	2.0 Meters
- AZ	0.05 MIL	0.1 MIL
- EL	0.05 MIL	0.1 MIL

(Adjustments were made in environmental disturbance and multipath areas)

The x, y and z uncertainties for runway 22 are presented in Figures II-1, II-2 and II-3, and for runway 10 in Figures II-4, II-5 & II-6.

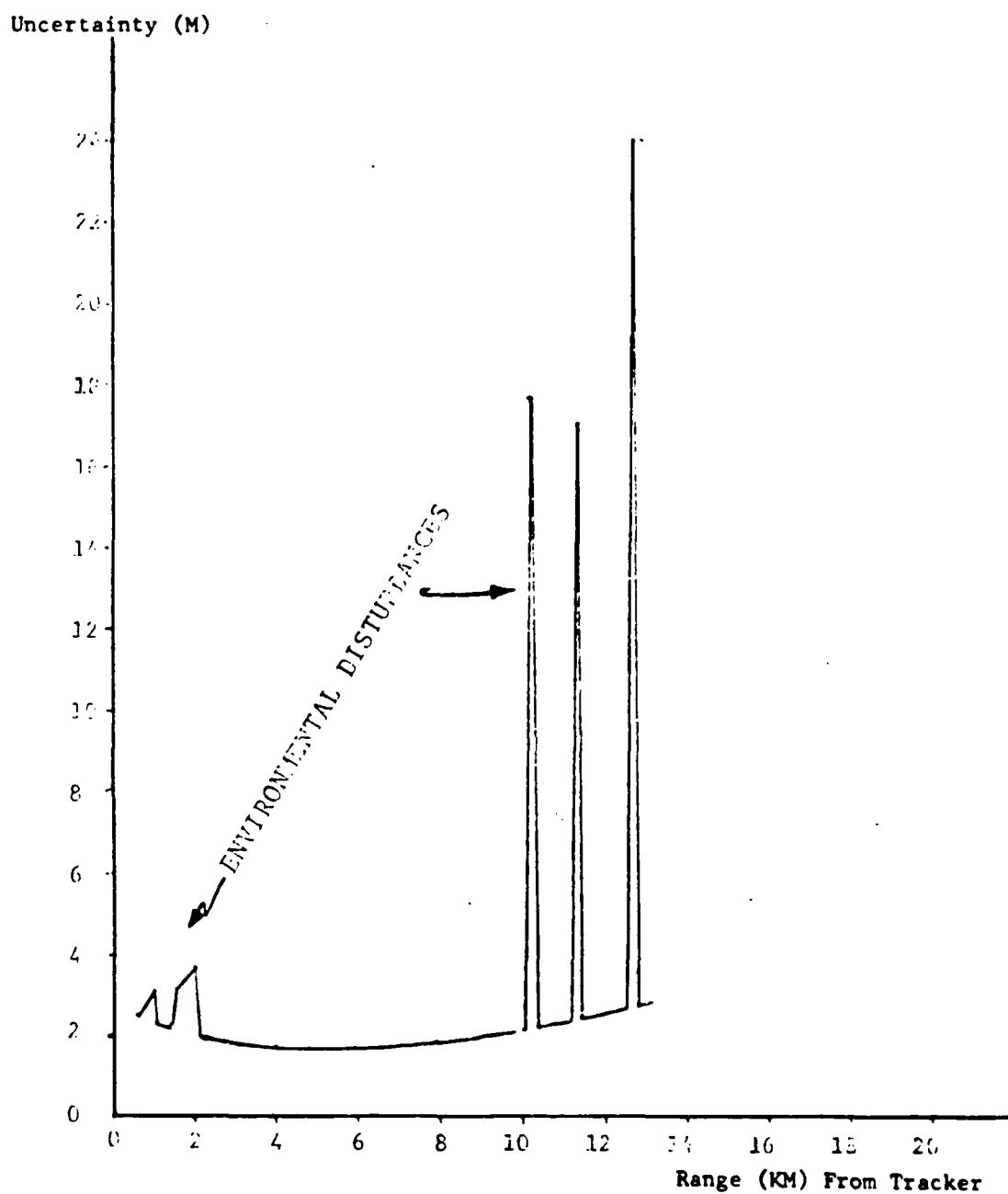


Figure II-1. X (East) Uncertainty, ASIR Only, Runway 22, Low Pass

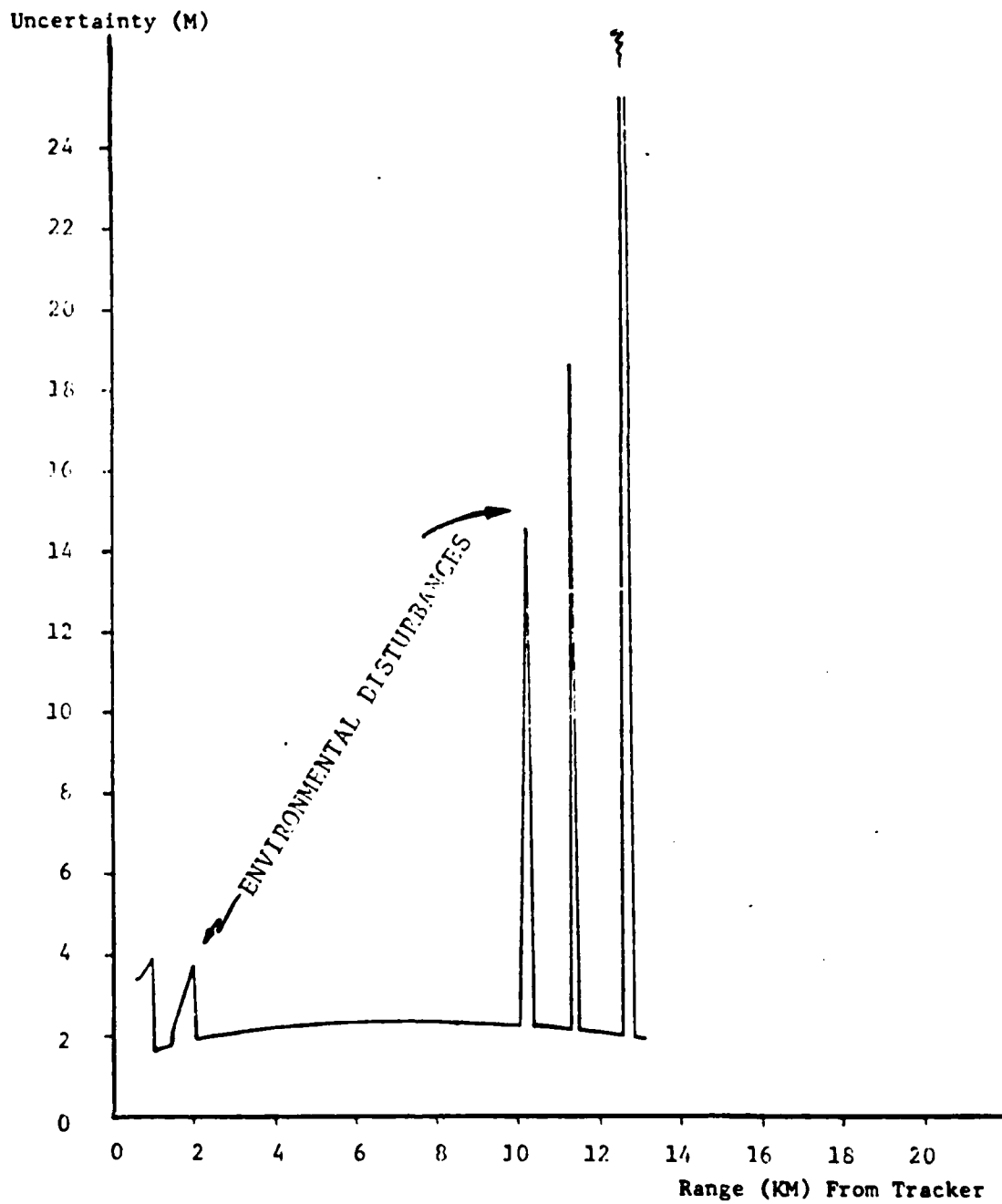


Figure II-2. Y (North) Uncertainty, ASIR Only, Runway 22, Low Pass

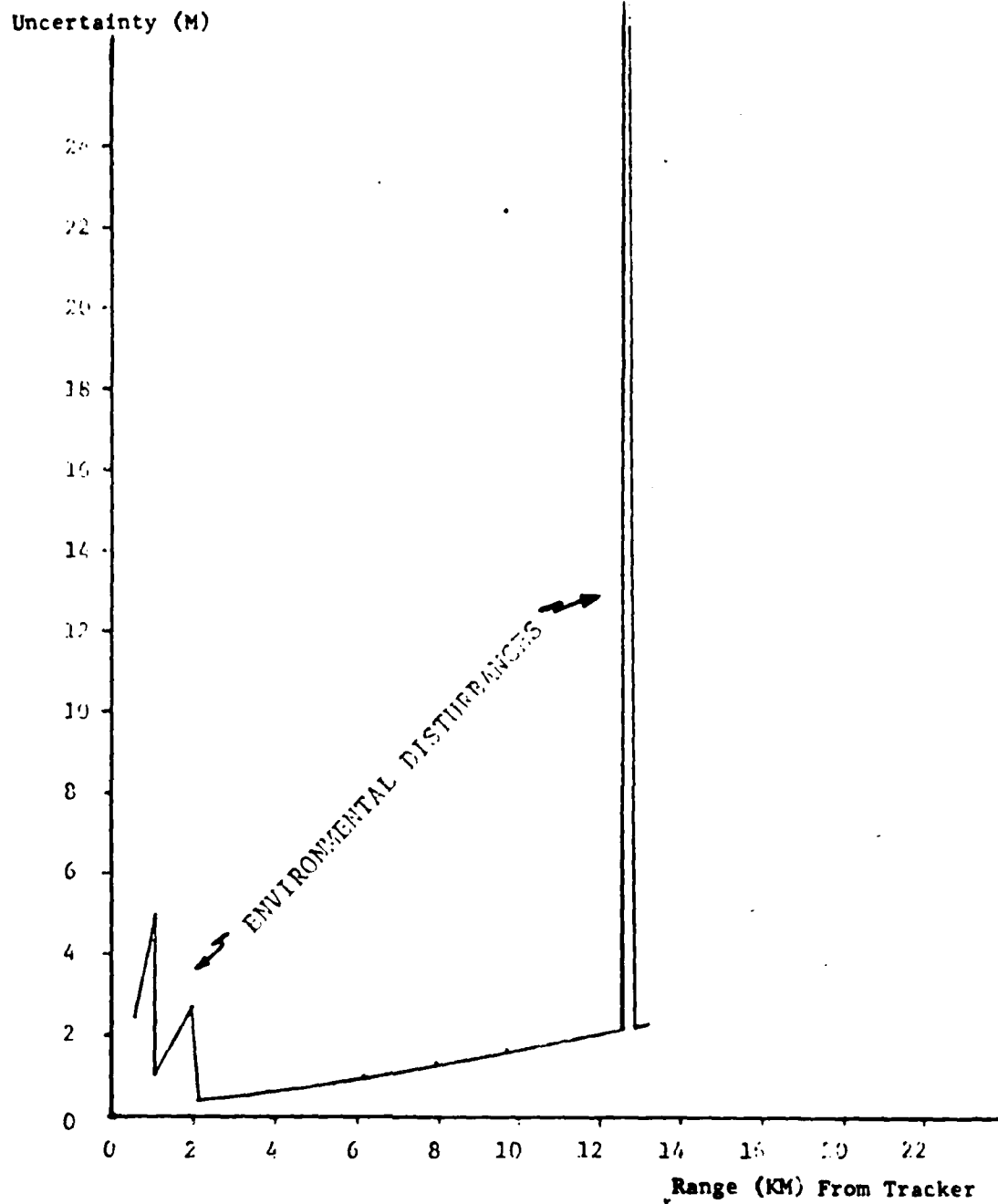


Figure II-3. Vertical Uncertainty, ASIR Only, Runway 22, Low Pass



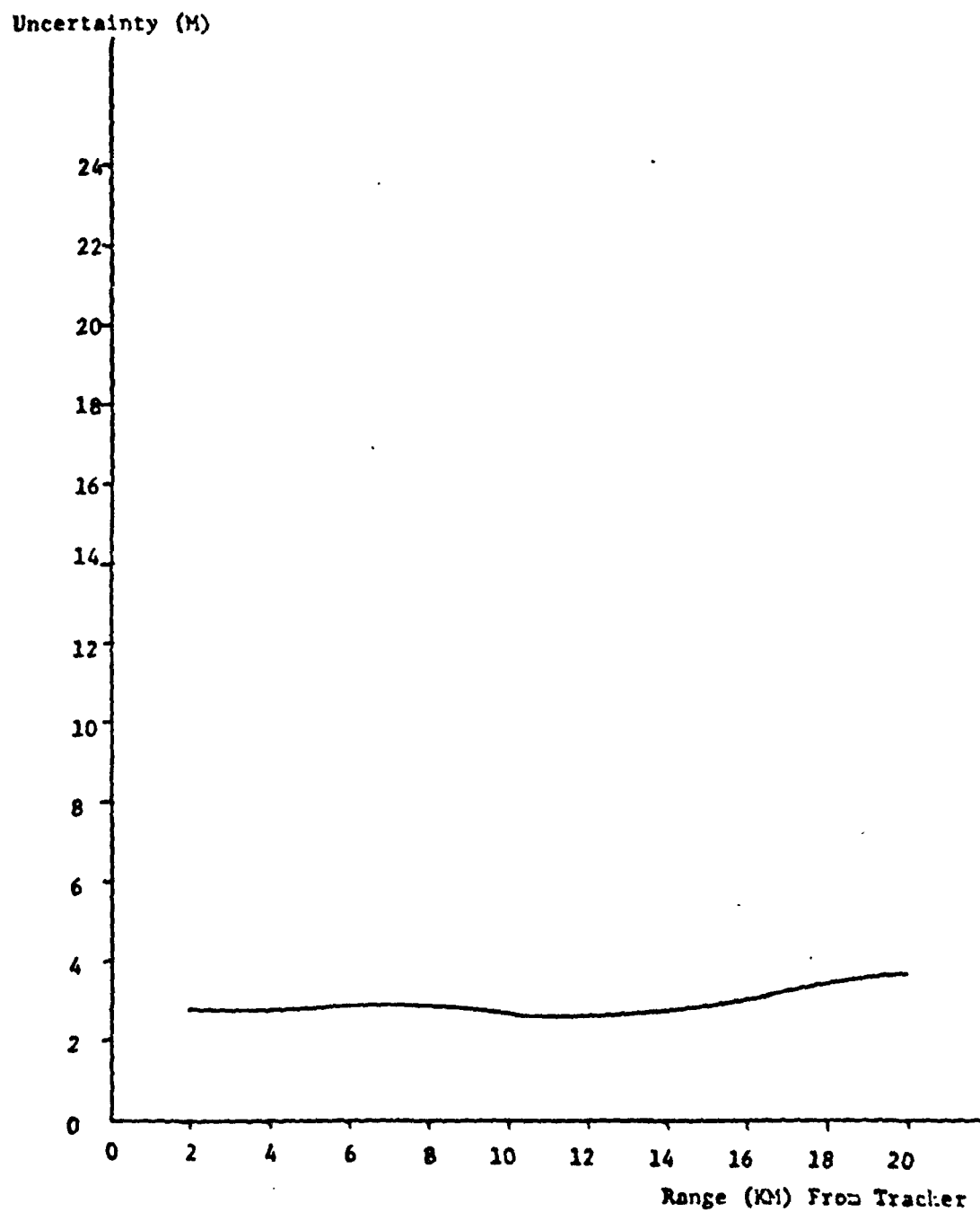


Figure II-4. X (East) Uncertainty, ASIR Only, Runway 10

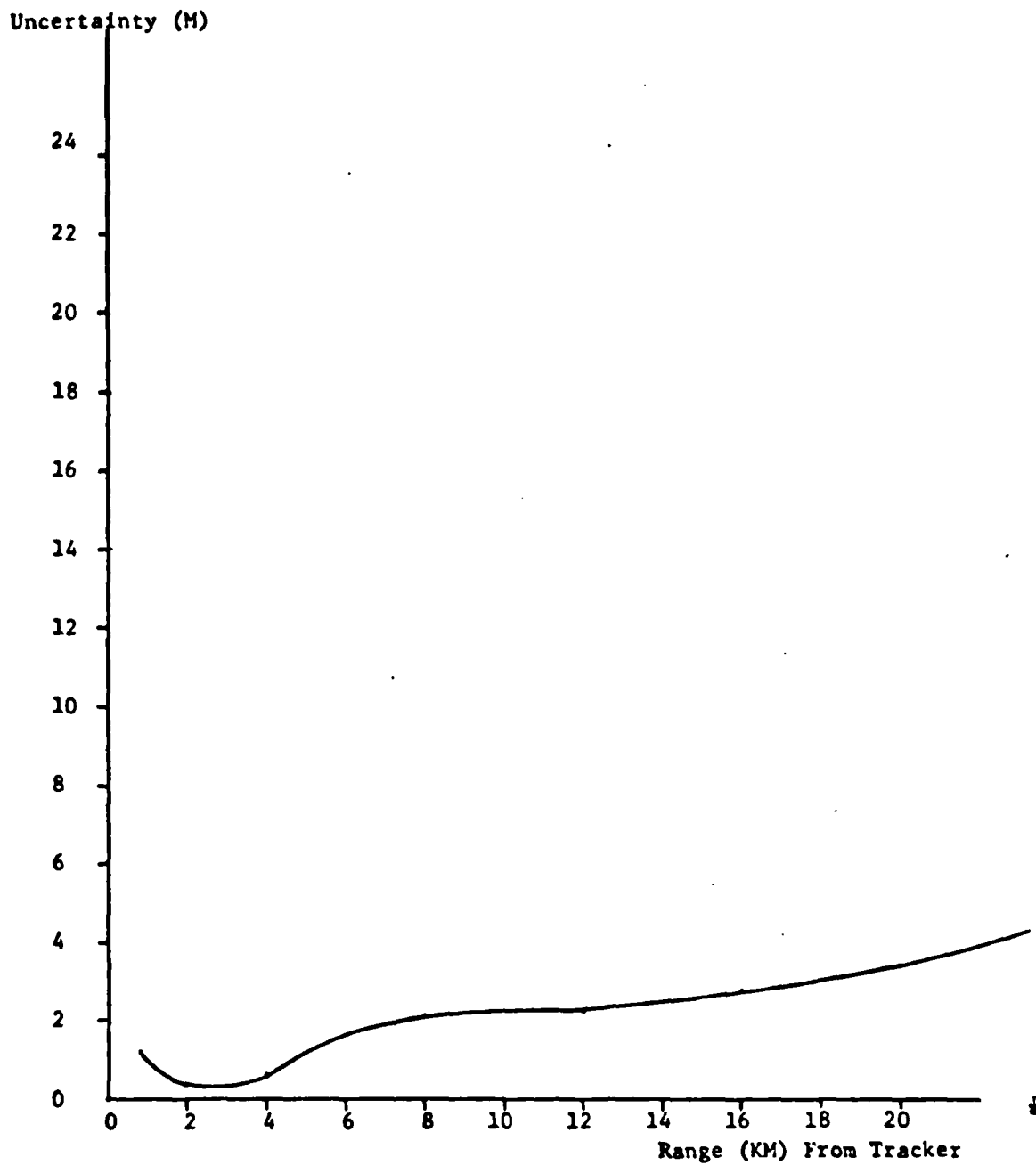


Figure II-5. Y (North) Uncertainty, ASIR Only, Runway 10

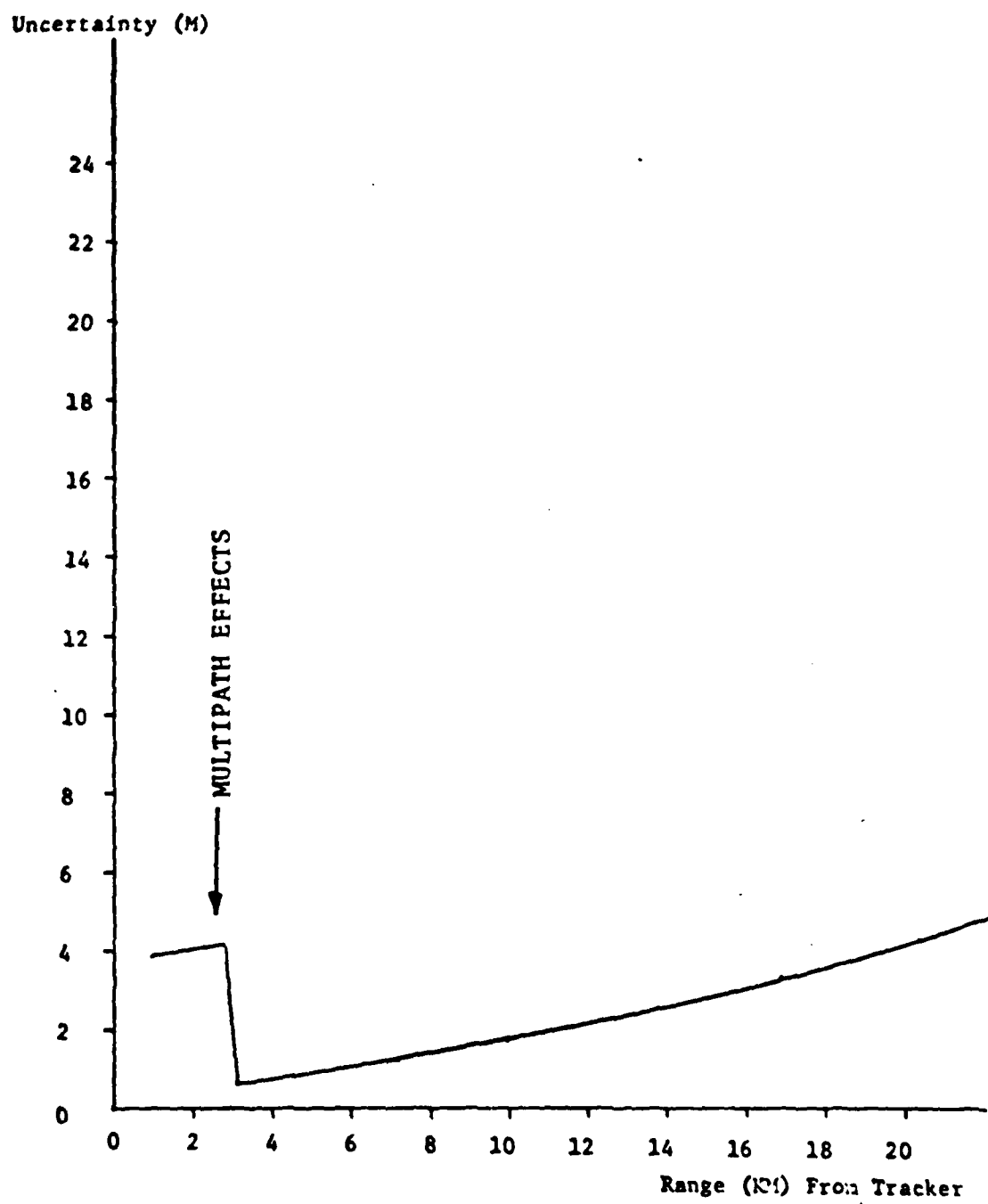


Figure II-6. Vertical Uncertainty, ASIR Only, Runway 10

## 2. Technical Characteristics AN/FPS-16

The technical characteristics of the AN/FPS-16 radar installed at Wallops Station are presented in Table II-2.

TABLE II-2: RADAR SET AN/FPS-16 TECHNICAL CHARACTERISTICS.

LEADING PARTICULAR	CHARACTERISTIC
Transmitting System	
Frequency range	5450 to 5825 MHz
Peak power	1 megw (fixed)
Average power	1.7 kw
Output power tube	Magnetron
Pulse widths	0.25, 0.5, and 1 second
	160, 640, 1024 pps
Frequency accuracy	$\pm 1.5$ mc
Pulse shape	Square
Modulator	High-vacuum type
Power programmer	0 to 30 db
Receiving System	
Type	Superheterodyne
Frequency	5400 to 5900 MHz
I-f frequency	30 mc
Sensitivity	-110 dbm without parametric amp.
Noise figure	11 db
Bandwidth	1.8 and 8 mc (narrow-wide)
Dynamic range	-93 db with stc
Power Programmer	0 to 30 db
Ranging System	
Maximum range	32,000 nautical miles
Minimum range	500 yards
Maximum tracking rate	20,000 yards/second
Maximum slew rate	40,000 yards/second
Bandwidth (maximum)	10 cps
Acceleration	4000 yards/second <sup>2</sup>
Master oscillator frequency	82 kc
Oscillator stability	1 in 10 <sup>6</sup>
Range accuracy	$\pm 5$ yards
Tracking gates	0.5, 1, 1.5 $\mu$ sec
Target designation	Manual or automatic modes
Range tracking	Manual, rate aided, or automatic
Tracking noise	Angle std deviation, 0.1 mil
Dispersion	Range std deviation, 1.5 yards

Table II-2: Radar Set AN/FPS-16 Technical Characteristics (Cont.).

LEADING PARTICULAR	CHARACTERISTIC
Antenna system	
Type	16-foot parabolic reflector
Feed	4-horn monopulse multi-mode
F/D ratio	0.3
Beam crossover	0 db
Gain	46 db
Beam width	0.8°
Polarization	Vertical, horizontal, circular
Tracking point	Center of main lobe (no crossover point)
Drive	Hydraulic
Antenna temperature	40° K above 50° elevation (dark sky)
Side lobe location	1.72° (1st)
Type of scan	Monopulse
R-f transmission line	Rectangular waveguide
Line loss receiving	1.3 db
Line loss transmitting	2.3 db
System Facts	
Azimuth coverage	360°
Elevation coverage	-10° to 190° (tracking -10° to 85°)
Range accuracy	±5 yards
Readout rate	10, 20, 40 pps
Granularity, range	1.953125 yards
Tracking rates	Azimuth: 42°/second Elevation: 22/5°/second
Slewing rates	Range: 10,000 yards/second Azimuth: 45°/second Elevation: 22.5°/second
Accelerations	Azimuth: 45°/second Elevation: 24°/second Range: 40,000 yards/second
Bearing accuracy	Azimuth: 0.1 mil Elevation: 0.1 mil
Range on 1 square meter	272,000 yards
Random noise errors in output data	Slant range: $\sigma_R$ 1.5 yards Azimuth & elevation: $\sigma_A$ , $\sigma_E$ 0.1 mil
Systematic errors	Zero setting errors: ±0.7 to 2.0 yds Drift errors due to external beacon delay variations estimated to be less than 100 feet Total mechanical errors: 0.04 mil rms

Table II-2: Radar Set AN/FPS-16 Technical Characteristics

LEADING PARTICULAR	CHARACTERISTIC
System Data Readout	
Data box	35-mm Mitchell camera for the following: azimuth and elevation synchro dials, timing lights, sync pulses, and signal tone
Range scope	35-mm Mitchell camera photographs 2000-yard segment of range and 72,000 yards synchro
Nixie readout	35-mm pulse-operated flight research camera: azimuth, elevation, and range; timing; model number; and radar mode of operation
Pedestal cursor dial	Azimuth: 35-mm flight research camera Elevation: 35-mm flight research camera
Ungated video	Boresight: 80-inch EFL lens with 35-mm research camera Tektronix scope, 2000-yard segment of range, 35-mm flight research camera
Consolidated recorder	Agc, WWV, range timing, radar timing, radar camera shutter pulse, CHU
Sanborn recorder	Four channels; can record any four of the following: agc, 2000-yard range synchro output, timing, sync pulse, WWV, CHU, azimuth and elevation error, and range error signals
Magnetic tape system	Records binary output of range, azimuth, timing, azimuth error, and elevation error
System Power Load	3 phase, 120/208 volt, 100 kva

### 3. Photogrammetric Error Analysis

#### a. Introduction

This analysis presents the measurement errors associated with the Photogrammetry Measurement System (PMS) that was designed, fabricated, installed and operated by Vitro Laboratories at Wallops Station, Va., to support the Microwave Landing System (MLS) Phase II Feasibility Demonstration test program. The basic error data was obtained from competent sources such as camera and film manufacturers and government survey teams, and/or from a statistical examination of considerable quantities of test data.

The general approach to this analysis was to determine the value of each error source in the image plane; statistically sum these errors; translate these errors to the MLS coordinate system; and project these translated errors to points along the runway centerline and its extension beyond approach threshold.

#### b. Camera Characteristics

The PMS cameras used during these MLS tests were Hulcher 70 Model 103s. The relevant characteristics of the 152mm focal length end cameras, and the 47mm focal length side cameras, are shown by Table II-3.



TABLE II-3: HULCHER 70 MODEL 103 CAMERA  
- General Specifications -

<p>70-mm FILM</p> <p>TYPE II PERFORATIONS</p> <p>DUAL LIGHT EMITTING DIODE (LED) TIMING LIGHTS TOP AND BOTTOM</p> <p>5 OR 10 FRAMES PER SECOND</p> <p>1/25 - 1/2000 SHUTTER SPEEDS</p> <p>NEAR FOCAL PLAN DISC TYPE SHUTTER</p> <p>12V DC MOTOR DRIVEN</p>	
47-mm LENS	152-mm LENS
<p>60° COVERAGE</p> <p>2.4" X 2.4" FORMAT</p> <p>f8-32</p>	<p>21° COVERAGE</p> <p>2.25" X 2.25" FORMAT</p> <p>f4.5-32</p>

c. Error Sources

The PMS error sources considered in this report are:

Image Reading	Shutter Motion
Lens Distortion	Frame Timing
Focal Length	Sprocket Count
Film Distortion-Temperature	Comparator Mechanism
Film Distortion-Humidity	Installation Orientation
Film Distortion-Mechanical	Plate Flatness
Site Survey	Film Resolution
Atmospheric Refraction	Computation
Image Motion	

The evaluation of each of these error sources is presented in the following sections.

c.1 Image Reading

The image reading error is related to the skills of the image readers. These individuals underwent a training program, conducted by highly skilled operators of the National Ocean Survey Office, Rockville, Md. A competent reader can measure a star plate image to 1.5 microns with the comparator. The image points on the MLS test frames were somewhat more difficult to read than the star plates, but reading accuracies of 6 microns reasonably were anticipated. However, a comprehensive statistical examination of many readings revealed a 1-sigma reading noise value of 21.8 microns in measuring the distance between two points in the image plane, and this value is used in the error budget.

### c.2 Lens Distortion

The lenses of the PMS cameras were calibrated by the laboratories of the U.S. National Geological Survey, Reston, Va. The calibrations were quantized, and included in the aircraft trajectory computer program. However, there is a residual error of 7 microns associated with this calibration, and this value is used in the error budget.

### c.3 Focal Length

Focal length for all PMS camera lenses is provided as an integral feature of the lens calibration, and the error in this value as substantiated by focal length computation from test frames was negligible except for camera 4. Aircraft trajectory bias measurement errors associated with camera 4 accordingly were corrected by computing the focal length from known positions of targets. The image position error caused by the error in determining focal length is a function of the distance between image point and fiducial center. Referring to Figure II-7 the focal length error  $\epsilon_{fo}$  attributable to a reading error  $\epsilon_{ro}$  at a distance  $d$  from focal center is:

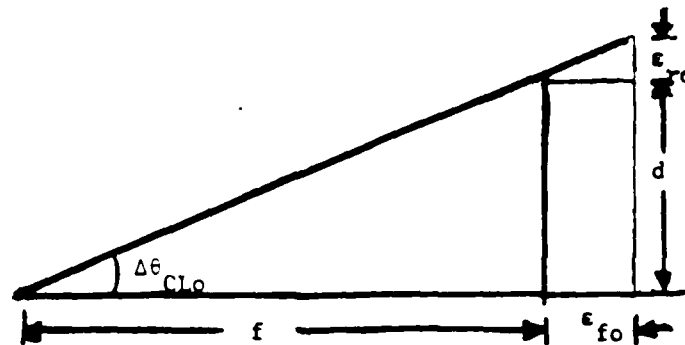
$$\epsilon_{fo} = \epsilon_{ro} / \tan \Delta\theta_{Cl0}$$

and the measurement error  $\epsilon_f$  in reading target position at any angle

$\Delta\theta_{Cl}$  is:

$$\epsilon_f = \epsilon_{fo} \tan \Delta\theta_{Cl} \quad \text{Equation 1}$$

where  $\Delta\theta_{Cl}$  is the angle between camera centerline, and line connecting camera and aircraft.



$d$  = distance focal center to target  
 $\epsilon_{ro}$  = measurement error in reading target position  
 $f$  = nominal focal length  
 $\epsilon_{fo}$  = focal length error caused by reading error

Figure II-7: Focal Length Error Geometry

#### c.4 Film Distortion - Temperature

The estar base film used in the PMS cameras expands and contracts uniformly with temperature, according to the Figure II-8 data furnished by Kodak. This temperature effect was accommodated by providing the computer program with the appropriate expansion/contraction constant, and the temperature difference on each run between field test and reading room environments. There is no significant residual error for this parameter after these values are introduced into the computer program.

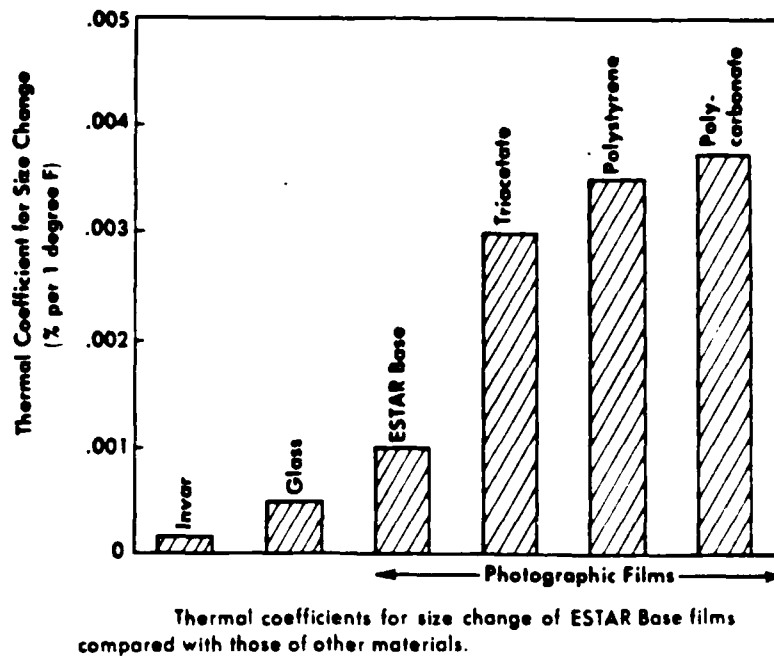
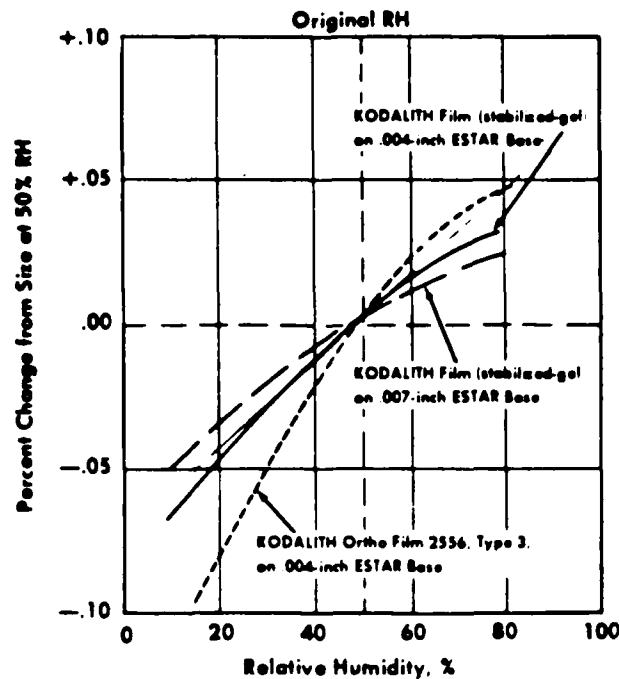


Figure II-8: Film Temperature Correction.

#### c.5 Film Distortion - Humidity

The ester base film used in the PMS cameras expands and contracts uniformly with humidity, according to the Figure II-9 data furnished by Kodak. This humidity effect was accommodated by providing the computer program with the appropriate expansion/contraction constant, and the humidity differences on each run between field test and reading room environments. There is no significant residual error for this parameter after these values are introduced into the computer program.



In this graph, the size at 50% RH is taken as the zero point; the curves show the percent size-change of unprocessed stabilized-gel KODALITH Film on two thicknesses of ESTAR Base and regular KODALITH Ortho Film 2556, Type 3 (ESTAR Base), after the films have been conditioned to air at a different RH.

Figure II-9: Film Humidity Correction.

#### c.6 Film Distortion - Mechanical

The estar base film used in the PMS cameras expands less than 2 microns when subjected to normal loads associated with taking and developing films. This value is considered too small to be included in the error budget, particularly when it is statistically added to much larger PMS noise errors.

#### c.7 Site Survey

The PMS camera and target locations were surveyed to an accuracy of 1/4 inch. This value is considered too small to be included in the error budget, particularly when it is statistically added to much larger PMS noise errors.

#### c.8 Atmospheric Refraction

This error is not unique to photogrammetry. It occurs with equal magnitude with the laser measurement system, and even affects to some degree the MLS systems accuracies. The identified constants apply to average values of the visual spectrum refraction in air. The magnitude of the refraction is related to the relative refractive indices of the mediums penetrated by the radiation, and the angle of penetration, i.e.:

$$\frac{\sin i}{\sin r} = \frac{n_s}{n} \quad \text{Equation (2)}$$

where:  $i$  is the incident, or initial, angle

$r$  is the refracted, or final, angle

$n_s$  is the refractive index of the initial medium

(=1.00027 for standard sea level air)

$$(n - 1) = (n_s - 1) \rho / \rho_o \quad \text{Equation (3)}$$

where:  $\rho_o$  is the sea level standard air density

$\rho$  is the density at altitude

The density at altitude, with standard density at sea level is:

$$\frac{P}{P_0} = \left(\frac{P}{P_0}\right) \left(\frac{T_0}{T}\right) \quad \text{Equation (4)}$$

where:  $P_0$  is the sea level standard air pressure (1013.2 millibars)

$P$  is the pressure at altitude

$T_0$  is the sea level standard air temperature (288° K)

$T$  is the temperature at altitude

All pressures are in millibars, and all temperatures are in degrees centigrade absolute. The temperatures at altitude are determined by the assumed lapse rates, and the pressures are determined by:

$$P = P_0 \left(1 - \frac{\beta H}{T_0}\right)^{\frac{g}{R \beta}} \quad \text{Equation (5)}$$

where:  $\beta$  is the lapse rate in degrees per meter

$H$  is the altitude

$g/R\beta$  is a sea level standard air constant (5.2568)

Only the standard lapse rates, and those where temperature increases with altitude, i.e., temperature inversions, are considered. When the temperature decreases rapidly with altitude, the refractive indices are less than those for a standard atmosphere. In fact, when the temperature decreases with height at a rate of 1°C. per 29.27 meters, the air is of uniform density and no refraction occurs. When the lapse rate exceeds that value, auto-convection occurs and the resulting mixing action tends to reduce the lapse rate.



It is recognized that the change in temperature with altitude normally is not abrupt, and that the ray path thus is curved. However, this situation can be approximated closely by considering an atmospheric sample between camera and object consisting of two layers, each of constant but different density, interfacing at an altitude between camera and object altitude.

Referring to Figure II-10, since the atmospheric density discontinuity is assumed to be at approximately half the object altitude, the error caused by refraction is:

$$\epsilon = \epsilon_1 = \epsilon_2$$

The angle package at the camera location is:

$$90^\circ = \theta + \epsilon + r$$

and at the object location:

$$90^\circ = (90^\circ - \theta) + \epsilon + (90 - i)$$

solving for  $\epsilon$ :

$$\epsilon = \frac{r-i}{2} \quad \text{Equation (6)}$$

which states that the refraction error is half the difference between the refraction and incident angles.

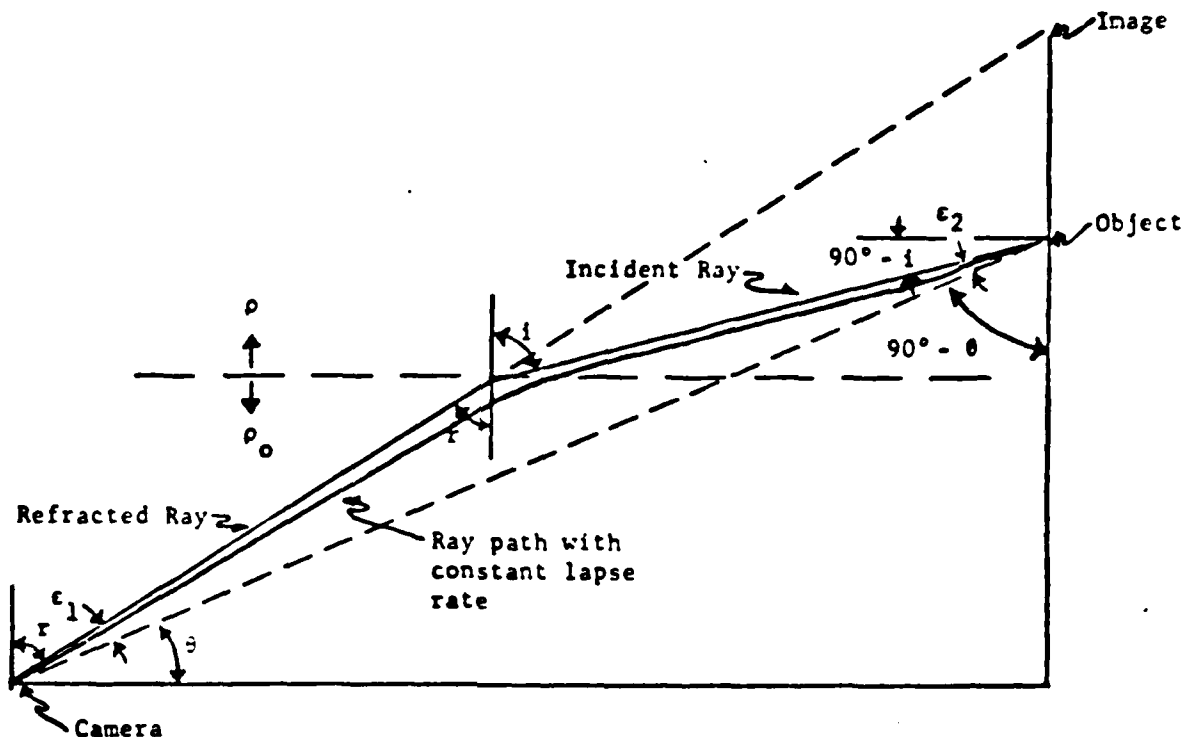


Figure II-10: Ray Path with Linearized Geometry

Three refraction situations now are examined, i.e.: (1) standard atmosphere; (2) strong inversion; and (3) camera and/or objects in mirage region.

Case 1: Standard Atmosphere, H=100 meters

$$\frac{\rho}{\rho_0} = 0.99044 \text{ (U.S. Standard Atmosphere)}$$

$$n_s = 1.00027 \text{ (any textbook)}$$

Thus, from equation (3), the refractive index at the density discontinuity level, when applying the equation (6) approximation, is:

$$\begin{aligned}(n - 1) &= (n_s - 1) \frac{\rho}{\rho_0} \\ &= (1.00027 - 1) 0.99044 \\ n &= 0.0002674\end{aligned}$$

and, with an elevation angle of  $3^\circ$ , which approximates problem conditions, the incident angle  $i = 90^\circ - 3 = 87^\circ$ , thus from equation (2):

$$\begin{aligned}r &= \sin^{-1} \left[ \frac{1.0002674}{1.00027} \sin 87^\circ \right] \\ &= 86.997^\circ\end{aligned}$$

thus, from equation (6) the error angle is:

$$e = \frac{r - i}{2} = \frac{86.997 - 87}{2} = -0.0015^\circ$$

which is considered negligible.

Case 2: Strong Inversion ( $10^\circ/100$  meters),  $H = 100$  meters

The pressure at 100 meters must be determined by equation (5), before  $\frac{\rho}{\rho_0}$  is established. The only variable in the term  $g/R\beta$  is the lapse rate  $\beta$ , being  $0.0065^\circ/\text{meter}$  in the standard atmosphere and  $-0.01^\circ/\text{meter}$  with the specified inversion. Thus the "constant" for the inversion condition reduces to:

$$g/R\beta = 5.2568 \left( \frac{0.0065}{-0.1} \right) = -0.342$$

and, inserting this value in equation (5):

$$\begin{aligned}P &= P_0 \left[ 1 - \frac{-0.1 (100)}{288} \right]^{-0.342} \\ P/P_0 &= 0.98840\end{aligned}$$

from equation (4):

$$\begin{aligned}\frac{\rho}{\rho_0} &= (P/P_0) (T_0/T) \\ &= 0.99840 \left( \frac{288}{298} \right) \\ &= 0.95523\end{aligned}$$

thus, the refractive index is:

$$\begin{aligned}(n - 1) &= (1.00027 - 1) 0.95523 \\ n &= 1.0002579\end{aligned}$$

and from equation (1):

$$\begin{aligned}r &= \sin^{-1} \left[ \frac{1.0002579}{1.00027} \sin 87^\circ \right] \\ &= 86.987^\circ\end{aligned}$$

thus, from equation (6), the error angle is:

$$e = \frac{r - i}{2} = \frac{86.987 - 87}{2} \approx -0.007^\circ$$

### Case 3: Mirage Region

Consider an extreme situation, but one which could occur in early morning with a stagnant warm air mass over cool ground, with camera at  $H = 1$  meter and the object (either marker or aircraft reference point) at  $H = 2$  meters, and with a  $20^\circ$  temperature difference between these points. Application of equation (5) shows that  $P = P_0$ , to well within computation accuracy for this problem. Thus, from equation (4):

$$\rho/\rho_0 = T_0/T = 288/308 = 0.93506$$

thus the refractive index is:

$$\begin{aligned} n - 1 &= (1.00027 - 1) (0.93506) \\ n &= 0.0002525 \end{aligned}$$

The incident angle for this case is:

$$90^\circ - \tan(1/300) = 90^\circ - 0.191^\circ = 89.809^\circ$$

thus the refraction angle, from equation (1), is:

$$\begin{aligned} r &= \sin^{-1} \frac{1.0002525}{1.00027} \sin 89.809^\circ \\ &= 89.611 \end{aligned}$$

and, from equation (5), the error angle is:

$$e = \frac{r - i}{2} = \frac{89.611 - 89.809}{2} = -0.1^\circ$$

which is significant and probably intolerable, but can be avoided by proper selection of minimum camera and object elevations. Accordingly, cameras and markers should be located at least 4 feet above ground level, and the tracking point on the aircraft should be as high as practical. For example, the nose wheel should not be used as the tracking point.

Horizontal temperature gradients, caused for example by temperature discontinuities between the air above hot runways and cool grass, were not considered because time did not permit acquiring and analyzing statistical data on that phenomena.

It is reasonable to assume that the usual vertical gradients at Wallops Station did not approach the severe case 2 strong inversion conditions. The mirage region was avoided by vertical siting of cameras and

targets, and by using a target point on the aircraft several feet above the ground. Accordingly, the atmospheric refraction error value, in the absence of unusual gradients, is too small to be included in the error budget.

c.9 Image Motion

Consider a worst case image motion smear, with an approach speed of 140 mph, and a camera shutter speed of 1/500 second to accommodate poor lighting conditions with film having an ASA rating of 400 and a lens aperture of F4.5. Flights normally were made in weather conditions that equal or exceed these light conditions, in order to maintain image motion smear within these stated worst case values. Horizontal and vertical smear are separately examined, since there is substantially less smear associated with the more critical vertical motion.

The horizontal smear is:

$$(140 \text{ mph}) (88/60) (1/500) = 0.41 \text{ ft.} = 4.9''$$

However, on a clear day when a 1/1000 shutter speed is available, this horizontal smear reduces to:

$$4.9 (500/1000) = 2.5''$$

This error is considerably less than the smear, because of the manner in which the image is read. The smear broadens the width of the vertical arm of the target cross on the aircraft from 6" to  $(6 + 4.9) = 10.9''$ , and the comparator operator centers the vertical cross-hair at the center

of this vertical arm. The reading could be corrected by an assumed aircraft speed/shutter speed constant for each set of runs. This would reduce the smear error to a value corresponding to the incremental difficulty of centering a cross-hair in a larger vertical arm. However, this condition was not made because of the small contribution from this error source, and it is not included in the error budget.

The vertical smear error is less than the horizontal smear error proportional to the tangent of the glide slope angle, i.e.:

$$4.9'' \tan 3^\circ = 0.25''$$

which is too small even to require a centering correction.

#### c.10 Shutter Motion

The shutter sweeps across the frame, and thus an image recorded near the start of the sweep will be recorded earlier than an image recorded near the end of the sweep. Considering the actual problem conditions, with the Hulcher 70 Model 103 constants, and a frame rate of 10 frames/sec., the distance from shutter center of rotation to frame center being 2.75", and the frame width being 2.25". The angle subtended from the center of shutter rotation to the frame edges is:

$$\theta = 2 \tan^{-1} \left( \frac{1.175}{2.75} \right) = 46.3^\circ$$

The shutter angular velocity is:

$$\dot{\theta} = (360) (10) = 3600^\circ/\text{sec.}$$

Thus, the time required for the shutter to traverse the frame is:

$$t = (\theta/\dot{\theta}) = (46.3/3600) = 0.0129 \text{ sec.}$$

The error associated with this traverse time is not tolerable in a system that requires time measurement accuracies on the order of a couple of milliseconds. Accordingly, a time correction is applied to the computer program that is a function of image position relative to frame center. The resulting corrected shutter motion error is negligible, and accordingly is not included in the error budget.

#### c.11 Frame Timing

The primary timing marks on the frames are 0.01 second apart. Timing marks on some regions of the time track are spaced 0.001 second, and when a time end point occurs in the 0.001-second region accuracies near this value can be obtained. However, in this instance a worst case again is considered, and in the 0.01-second region the timing marks can be interpolated reasonably to about 0.003 seconds.

Another frame timing error of about the same value is introduced by establishing on each roll of film the distance between frame center during exposure, and the location in the film transport hardware at which the timing marks are burned into the film. This is accomplished by centering the shutter on the first frame and burning into the film a reference mark on that frame. The distance between these two marks can be read to an accuracy that converts to about 0.003 seconds in the time domain.



The total frame timing error is the statistical sum of these two 0.003 second errors, i.e., 4.2 ms. This error is manifested by a position error that is a function of velocity. For example, at an aircraft velocity of 200 ft./sec., the error in the direction of aircraft motion would be:

$$(200 \text{ ft/sec}) \times (.0042 \text{ sec}) = .84 \text{ ft.}$$

c.12 Comparator Mechanism

The mechanical linkages that center the comparator cross-hairs on the target introduce a small error into this measurement. The comparator is calibrated, and the readings are corrected to calibrated values. A residual error of 1 micron still remains, but this is too small to be included in the error budget.

c.13 Installation Orientation

Any inadvertent horizontal misalignment of the camera relative to the line of targets, which in essence is a horizontal tilt, can be computed from the known target/camera geometry. Vertical tilt can be computed from target/fiducial mark geometry. Accordingly, these items need not be considered in the error budget.

c.14 Plate Flatness

During the brief film exposure time, any physical distortion of the film caused by either plate flatness perturbations or the ability of the camera mechanism to hold the film flat against the plate could cause

image errors. However, errors from these sources are negligible in the selected camera, and need not be considered in the error budget.

c.15 Resolution

The resolution of the lens/film combination, as determined during the lens calibration, was in some instances as low as 20 lines/mm. This means that image points must be at least 50 microns apart to distinguish each point. However, resolution is not viewed as an error source in the present problem. The only resolution requirement is the ability to distinguish the target crosses, both those on the ground and on the aircraft, from the background. This posed no problems during the tests.

c.16 Computation

The computer is programmed to round out calculations beyond the least significant number associated with the PMS errors. Accordingly, the computation error need not be considered in the error budget.

c.17 Geometry Dependent Errors

The geometry dependent errors are those that vary with the crossing angles between cameras lines-of-sight. The significant errors in this category, included in subsequent calculations, are:

Image Reading      21.8 $\mu$

Residual Lens Distortion      7 $\mu$

c.18 Geometry Independent Errors

The geometry independent errors are those that do not vary with the crossing angles between cameras lines-of-sight. The only significant error in this category, is:

Frame Timing: 0.84 ft (along flight path, at Acft velocity of 200 ft/sec)

This error is velocity dependent, and is not included in the error curves.

d. Simplifying Assumptions

The simplifying geometric assumptions of the geometry dependent errors, made to facilitate error computations, are separately considered in the elevation, azimuth, and range dimensions.

d.1 Elevation

The geometry dependent elevation error is caused entirely by the sideline cameras. It is determined by projecting the vertical error in the sideline cameras image planes, to selected points on the runway centerline.

d.2 Azimuth

The geometry dependent azimuth error is caused by both sideline and end cameras. It is determined by computing the statistical sum of:

- a. The horizontal component of the sideline camera image plane error, projected on a line perpendicular to the runway centerline, and

- b. The horizontal component of the end camera image plane error, projected on a line perpendicular to the runway centerline.

d.3 Range Error

The geometry dependent range error is caused entirely by the sideline cameras. It is determined by projecting the sideline camera image plane error to selected segments on and along the runway centerline.

e. Photogrammetric Measurement System (PMS) Error Equations

Step 1: Determine filtered value of noise error in image plane associated with the reading of each aircraft/target point pair.

The error associated with each reading is  $21.8\mu$ .

However, the aircraft trajectory data is filtered by the computer before plotting. It has been experimentally determined by using large data samples that this filtering reduces the noise by a factor of 3.7. Accordingly, this reading error is reduced to:

$$e_r = 21.8/3.7 = 5.9\mu$$

Step 2: Determine total value of error in image plane associated with the reading of each aircraft/target point pair. This error is the statistical sum of the filtered noise error of  $5.9\mu$ , and the residual lens distortion error of  $7\mu$ , i.e.:

$$\left[ 5.9^2 + 7^2 \right]^{1/2} = 9.2\mu$$

Step 3: Determine bias error in image plane associated with the locating of the master target board relative to the fiducial center.

This measurement is made on the first 5 frames for each run, and thus the applicable image plane error contributed by the reading error of  $21.8\mu$  and the residual lens distortion error of  $7\mu$  of  $(21.8^2 + 7^2)^{1/2} = 22.9\mu$  is reduced by a factor of  $\sqrt{5}$ . Thus, the bias error is:

$$\epsilon_b = 22.9 / \sqrt{5} = 10.2\mu$$

Step 4: Determine focal length error in image plane.

This error is established in section 4.3 of this report as  $\epsilon_f = \epsilon_{fo} \tan \Delta\theta_{ClO}$  where  $\epsilon_{fo} = \epsilon_{ro} / \tan \Delta\theta_{ClO}$ . The value of  $\epsilon_{fo}$  was determined from image reading error and camera/target geometry for Camera 44 on the TI runway as  $14\mu$ , and for Camera 24 on the Hazeltine runway as  $28\mu$ . Thus, the focal length error in the image plane for the TI runway is:

$$\epsilon_{fTI} = 14 \tan \Delta\theta_{Cl}$$

and for the Hazeltine runway:

$$\epsilon_{fH} = 28 \tan \Delta\theta_{Cl}$$

Step 5: Determine total image plane error.

The total image plane error is the statistical sum of the

reading, bias and focal length errors. The bias error can be summed in this manner, since it is an apriori unknown value. The error in the image plane for the TI runway is:

$$\epsilon_{TI} = \left[ 9.2^2 + 10.2^2 + (14 \tan \Delta\theta_{Cl})^2 \right]^{1/2}$$

$$\epsilon_H = \left[ 9.2^2 + 10.2^2 + (28 \tan \Delta\theta_{Cl})^2 \right]^{1/2}$$

Step 6: Determine EL error

The EL error is determined by projecting the image plane error in that dimension out to the runway centerline. The vertical angle between camera centerline and line joining camera and aircraft is sufficiently small to assume  $\tan \Delta\theta_{Cl} \approx 0$ , and thus the image plane error is the same for both the TI and Hazeltine runways, i.e.:

$$\epsilon_{TI} = \epsilon_H = (9.2^2 + 10.2^2)^{1/2} = 13.7\mu$$

and this error, when projected to the runway centerline is:

$$E_{EL} = \frac{13.7 D}{47 \times 10^3}$$

where D is distance from camera to selected point on runway centerline, and  $47 \times 10^3$  is focal length of sideline camera in microns.

Step 7: Determine AZ error in image plane contributed by sideline camera.

This AZ error is determined by rotating the image plane

error of the sideline camera perpendicular to the runway centerline. It is evident from the Figure II-11 geometry that this error contribution is:

$$\epsilon_{AZs} = \epsilon_1 \cos \Delta\theta_{C1} \sin(\theta_{C1} + \Delta\theta_{C1})$$

where  $\epsilon_1$  is the image plane error for the particular runway.

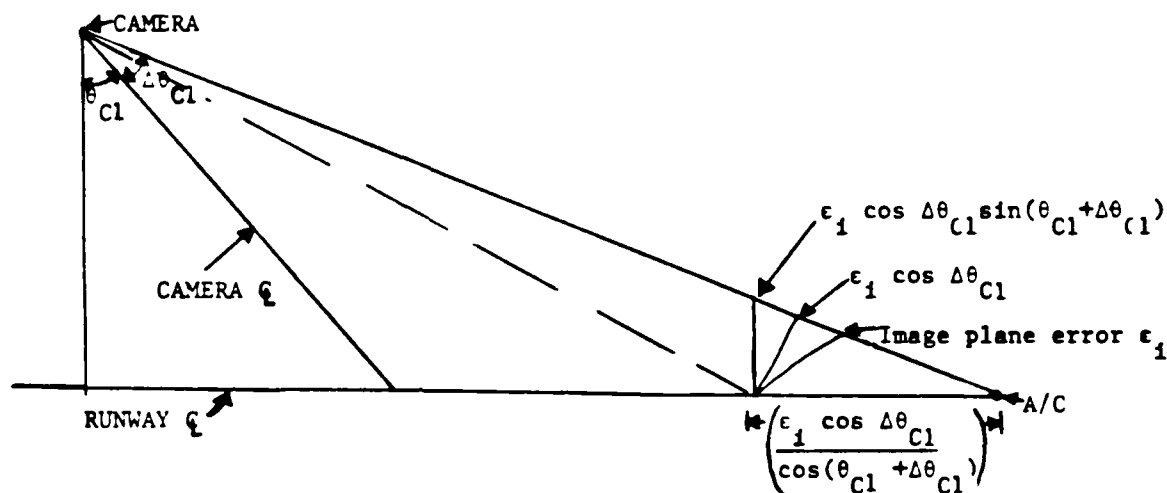


Figure II-11: Projection Error Geometry

Step 8: Determine AZ error in image plane contributed by end camera.

This AZ error is closely approximated by the statistical sum of the filtered reading noise of  $5.9\mu$  and the bias error in determining the location of the master target board of  $10.2\mu$ . This value is  $13.7\mu$ . No significant errors in calibrated focal length were observed with these cameras.

Step 9: Project sideline camera image plane AZ error to runway centerline.

This AZ error component is projected by:

$$E_{AZs} = \frac{\epsilon_{AZs} D_s}{47 \times 10^3}$$

where  $D_s$  is distance from sideline camera to selected point on runway centerline, and  $47 \times 10^3$  is focal length of this camera in microns. The computed focal length is sufficiently close to this value to permit its use for this computation.

Step 10: Project end camera image plane AZ error to runway centerline.

This AZ error is projected by:

$$E_{AZe} = \frac{\epsilon_{AZe} D_e}{152 \times 10^3}$$

where  $D_e$  is distance from end camera to selected point on runway centerline, and  $152 \times 10^3$  is focal length of this camera in microns.

Step 11: Determine AZ error

The AZ error is the statistical sum of the contributions of the AZ errors from the sideline and end cameras, i.e.:

$$E_{AZ} = (E_{AZs}^2 + E_{AZe}^2)^{1/2}$$



Step 12: Determine Range Error in Image Plane.

This range error is determined by rotating the image plane error of the sideline camera parallel to the runway centerline. It is evident from the Figure II-11 geometry that this error is:

$$\epsilon_r = \epsilon_1 \cos \Delta\theta_{Cl} / \cos (\theta_{Cl} + \Delta\theta_{Cl})$$

Step 13: Determine Range Error

This R error is determined by projecting its value in the image plane out to the runway centerline, i.e.:

$$E_r = \frac{\epsilon_r D_s}{47 \times 10^3}$$

where  $D_s$  is distance from sideline camera to selected points on runway centerline, and  $47 \times 10^3$  is focal length of this camera in microns.

f. Runway Centerline Errors

The FMS errors along the runway centerlines are shown for the TI runway in Figure II-12, and for the Hazeltine runway in Figure II-13. These are 2-sigma curves, obtained by doubling the 1-sigma values obtained by the foregoing analysis. The errors are projected throughout the entire region along the centerline and its extension for which merged tapes were provided, i.e., to 5200 feet from the TI EL-2 site.

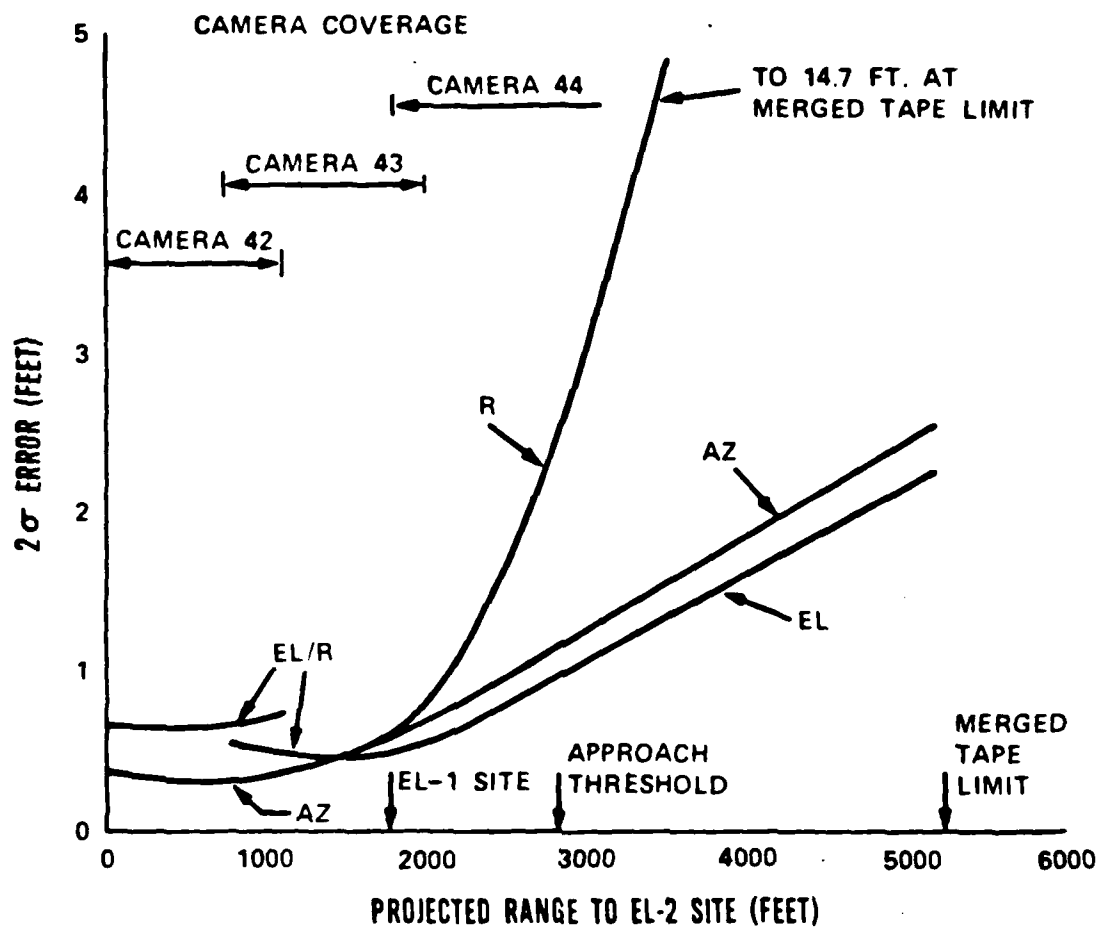


Figure II-12: PMS Errors on T.I. Runway Centerline

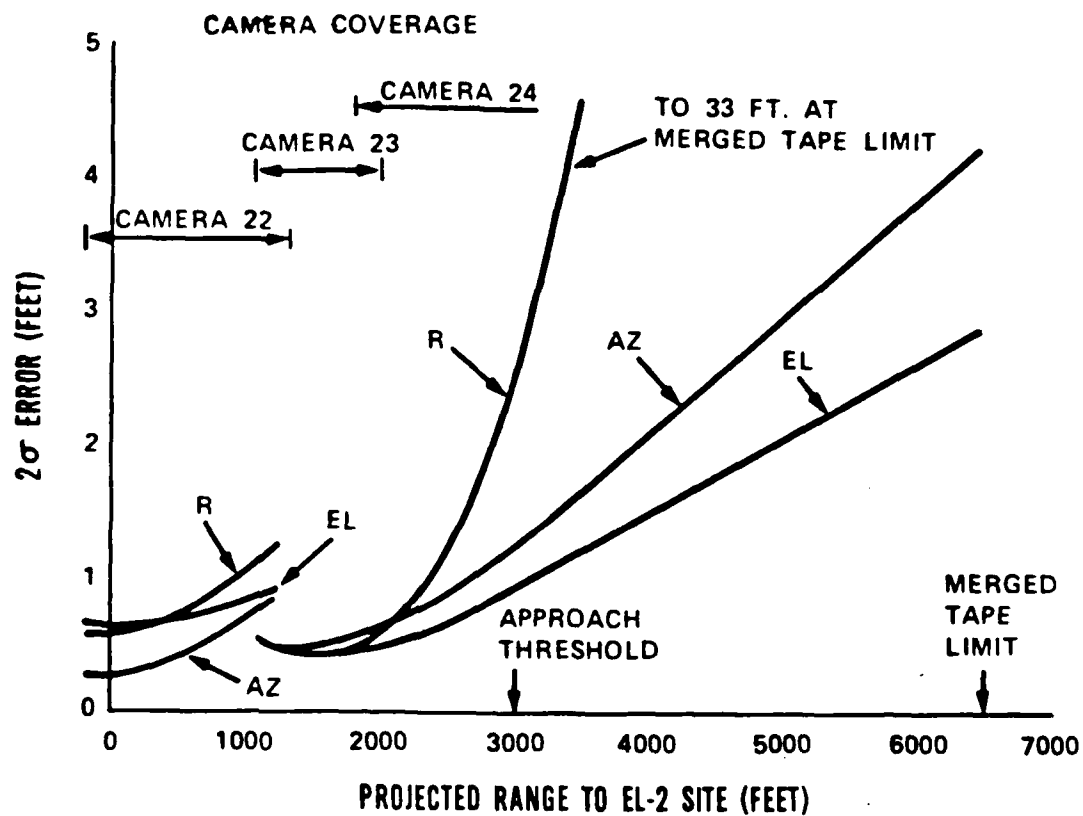


Figure II-13: PMS Errors on Hazeltine Runway Centerline

## B. NAFEC

### 1. Evaluation of NAFEC Tracking Systems in an MLS Test

#### Program Environment

Princeton University carried out an analytical study of test data in order to determine the tracking accuracy of the phototheodolite system and the Extended Area Instrumentation Radar (EAIR) at NAFEC. The study utilized the data from four flights -- 2 approaches to runway 4 and 2 approaches to runway 13. The flight paths utilized were the curved/segmented flight paths described in Section E.4 of the Phase II Test Requirements and Coordination Plan. One right and one left-hand approach were made to each runway. The Princeton study utilized tracker data which was not subjected to current NAFEC outlier removal procedures and was unfiltered. The study employed a variance-covariance analysis using 2nd difference data between the EAIR and phototheodolites. The study in effect concentrated on the high frequency noise characteristics of the two tracking systems. However, since filtering and outlier removal techniques were subsequently employed on the Phase II test data, the results of the study do not define the high frequency errors in the actual test data. The basic output of the study was a series of confidence ellipsoids along each flight path. Figure II-14 defines the data segments used to compute the confidence ellipsoids and Figure II-15 presents the confidence ellipsoids computed for one flight path.

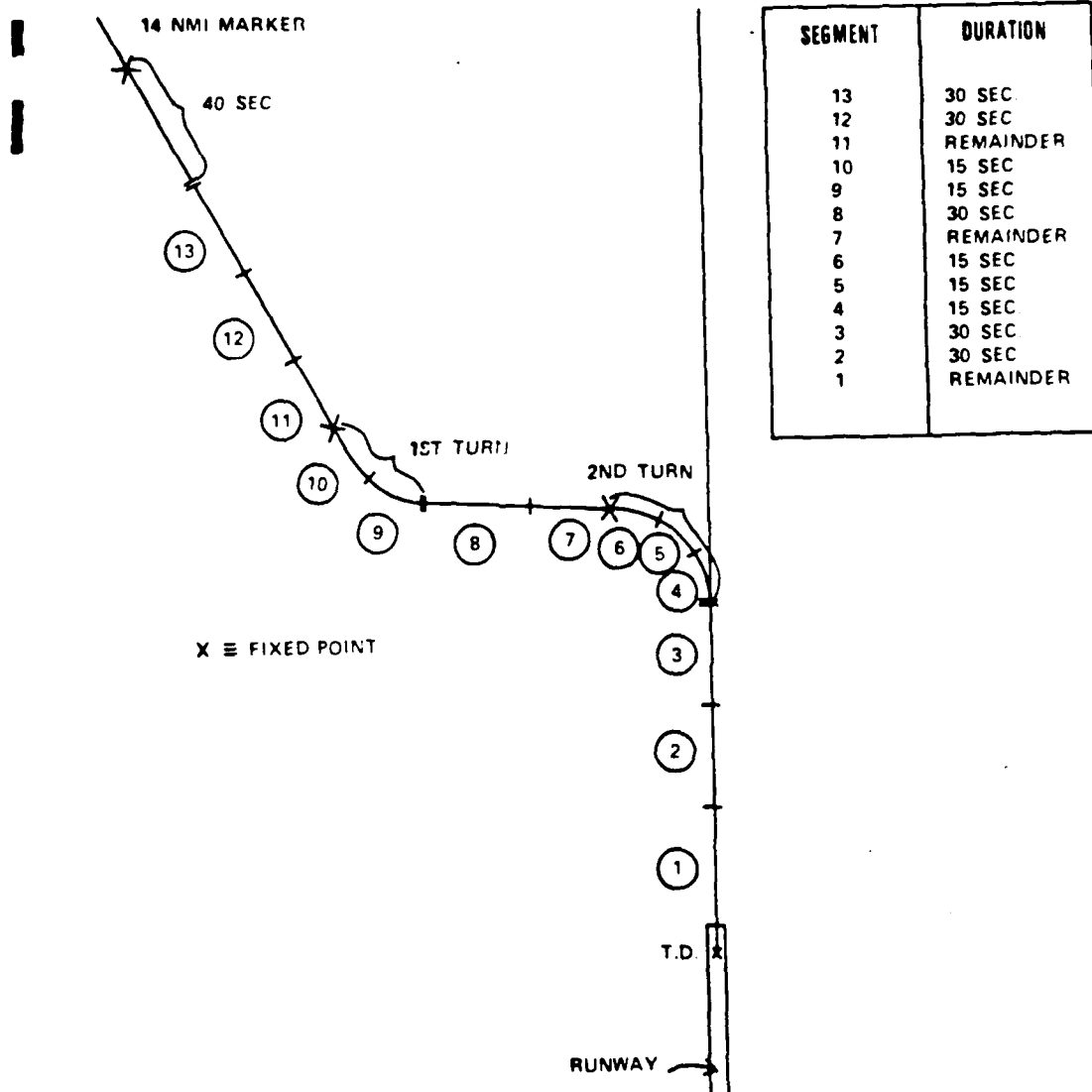


Figure II-14: Flight Path with Segments

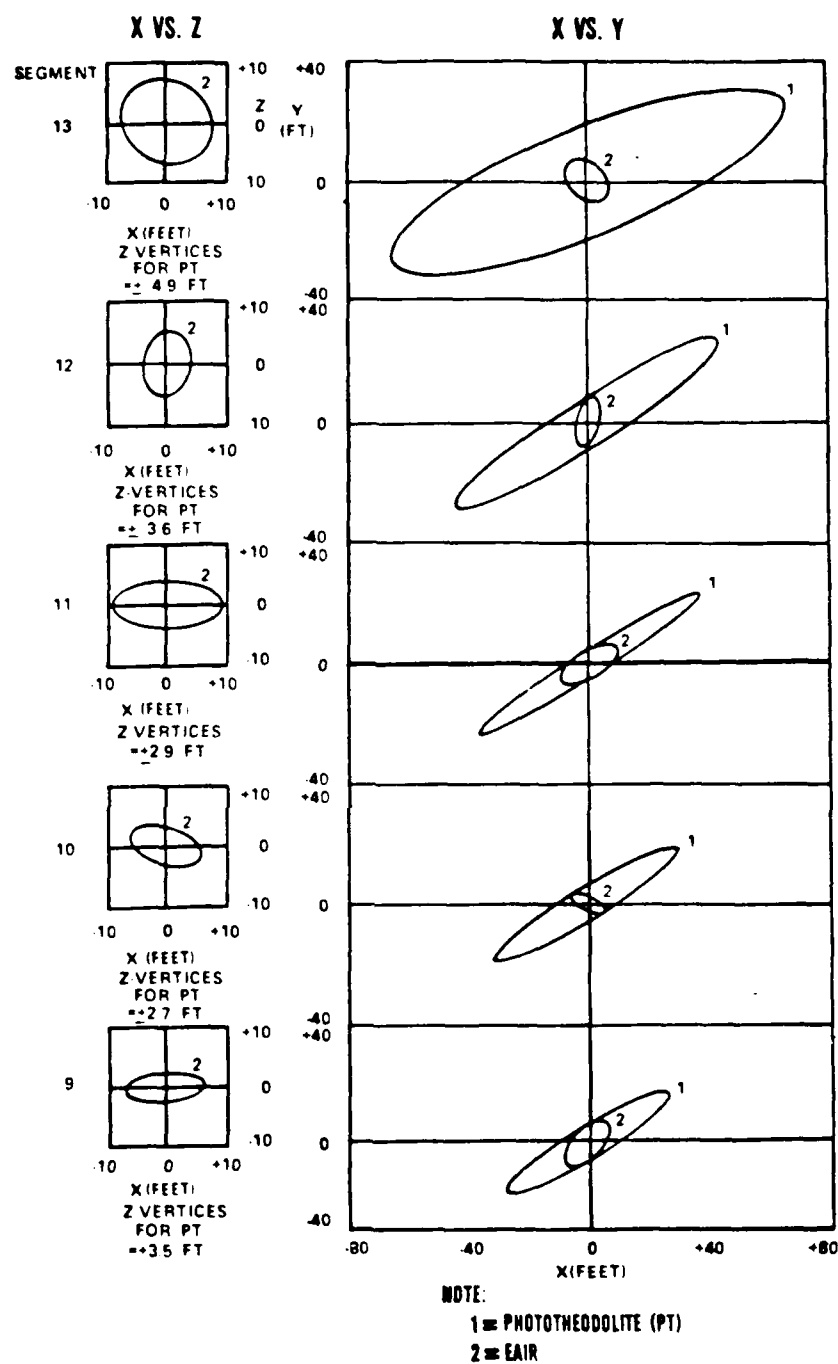


Figure II-15: Confidence (95%) Ellipses Pattern for 4 R,

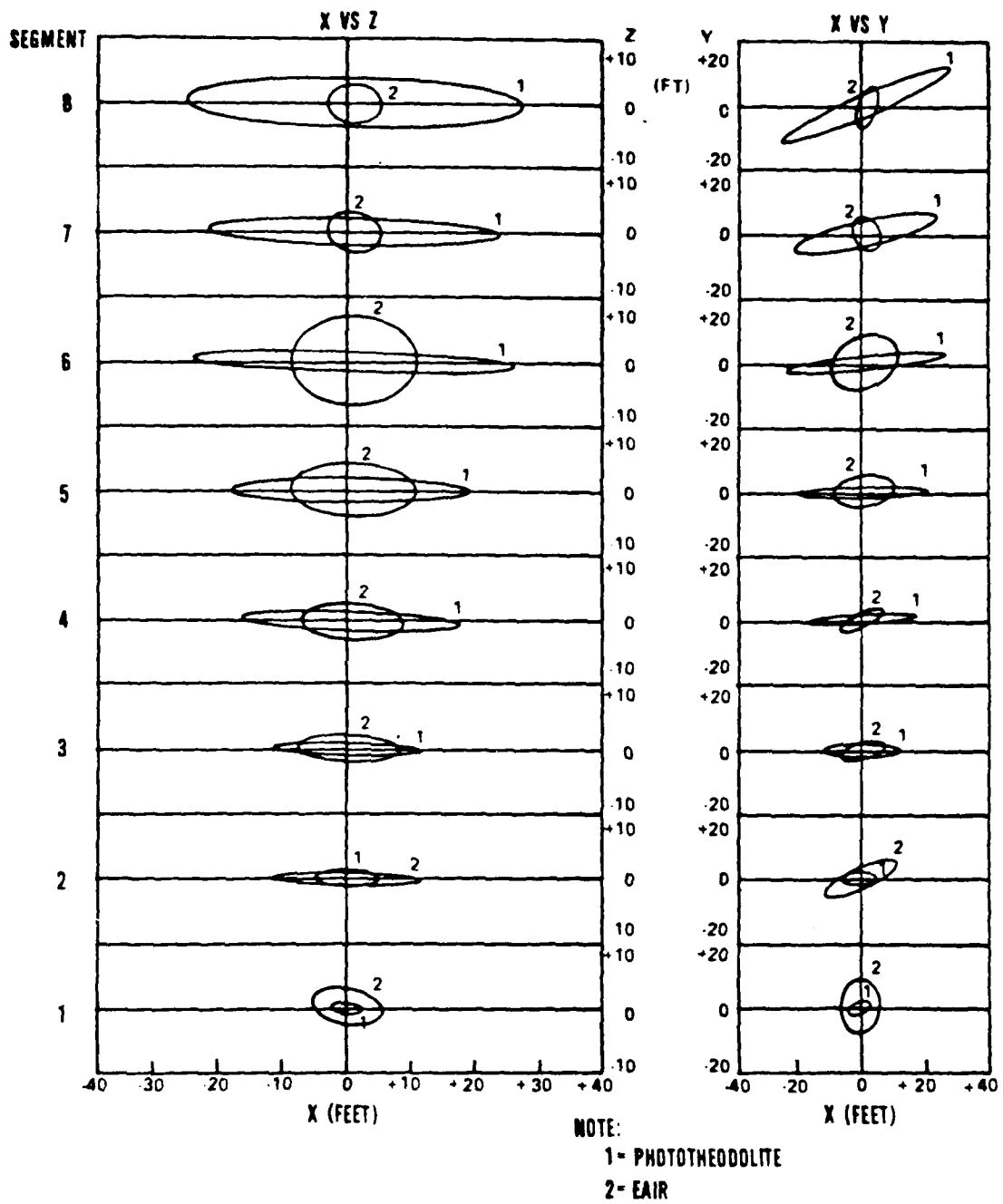


Figure II-15: Confidence (95%) Ellipses Pattern for 4 R (Cont.).

## 2. Phototheodolite Error Analysis

### a. Accuracy

The accuracy of the space-position-time of a target as defined by the coordinates determined by the Phototheodolite Facility depends on the location of the target with respect to the base line of the phototheodolites. Figures II-16 and II-17 present error curves that are used to compute the approximate range error of a space-position determined by the Phototheodolite Facility. The error is computed by use of the following equation:

$$E = B \cdot e \cdot d$$

where: E = maximum range error in feet

B = base-line distance in feet between the two phototheodolites.

Table II-4 lists the base line distance of the phototheodolites.

d = factor obtained from the range error curves in Figures II-16 and II-17.

e = maximum angular error of the line of sight in radians as indicated in the following:

$e = 4.83 \cdot 10^{-5}$  for coordinates computed from photographic film data when high quality control and repetition are used in data processing.

$e = 9.66 \cdot 10^{-5}$  for coordinates computed from photographic film data when regular production handling is used in data processing.

$e = 43.49 \cdot 10^{-5}$  for coordinates obtained from the tabular or from coordinates computed from the IBM format tape data.



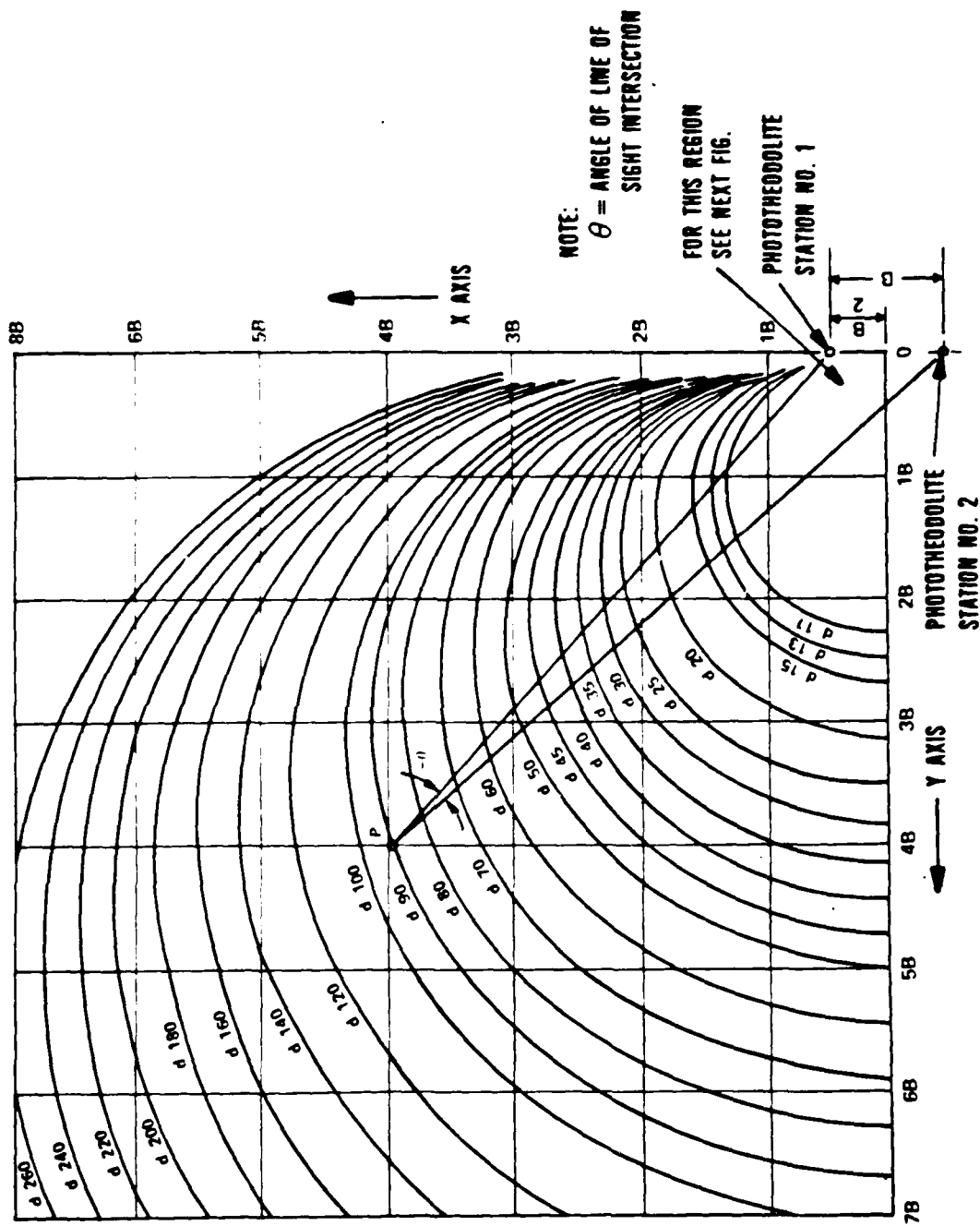


Figure II-16: Phototheodolite Range Error Curve.

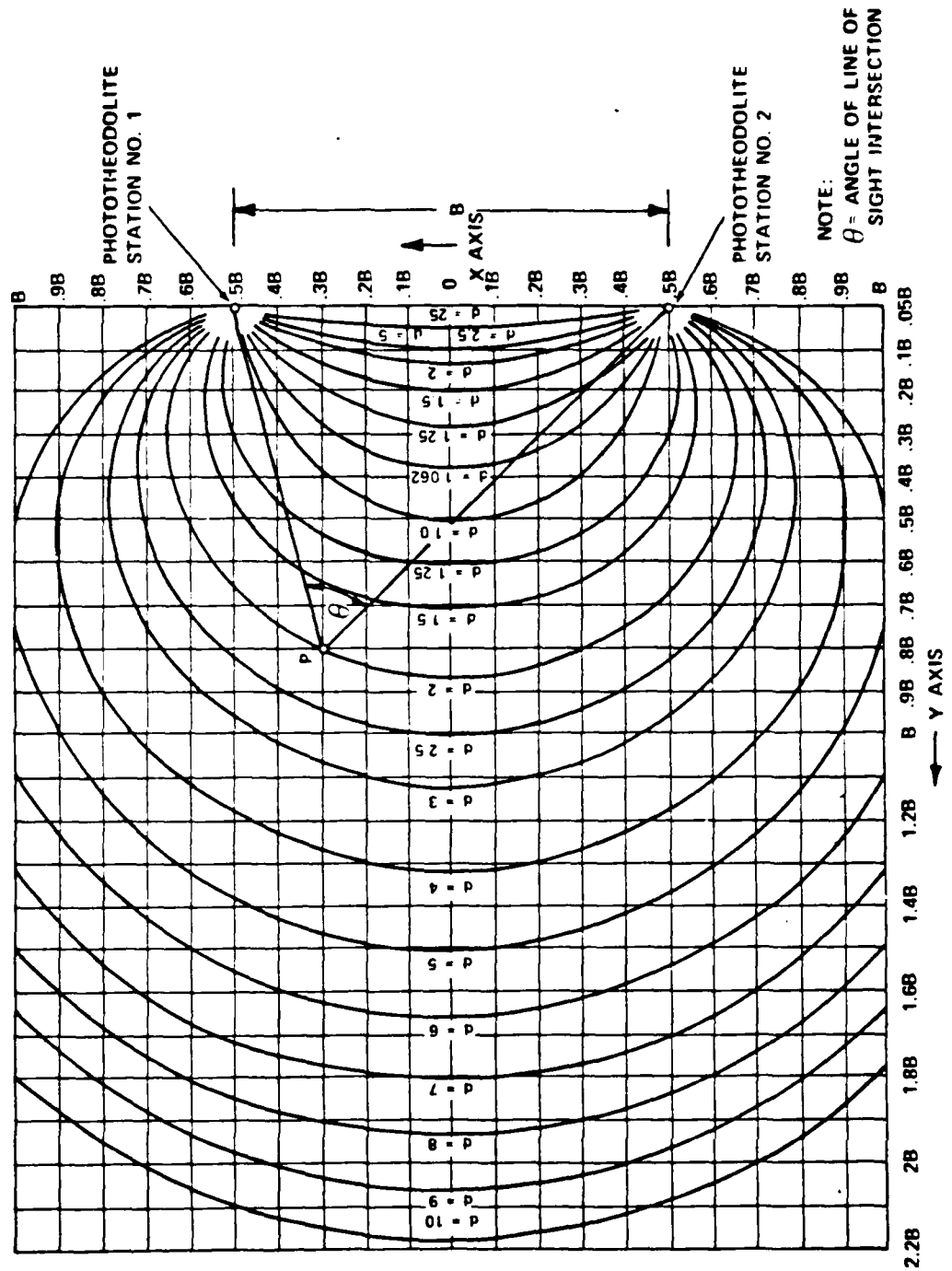


Figure II-17: Photodolite Range Error Curve For Targets At Close Range.

TABLE II-4: PHOTOTHEODOLITE BASE-LINE DISTANCE.

Base-Line Number	Phototheodolite (or Pair)	Base-Line Distance in feet
1	P-29	8,663
2	P-36	10,847
3	P-8	6,383
4	P-29 and P-36	6,468
5	P-8 and P-29	11,816
6	P-8 and P-36	10,084

The range error of the space-position-time data for point P (Figure II-16) when phototheodolites P-13 and P-29 are used is calculated as follows:

$$\begin{aligned}
 E &= B \cdot e \cdot d \\
 &= 8663 \cdot 9.66 \cdot 10^{-5} \cdot 90 \\
 &= 75.4 \text{ feet}
 \end{aligned}$$

The factor "d" can be computed for any point that is not covered by the curves. The factor "d" is equal to  $d_1$  or  $d_2$ , whichever is the larger value.

The following equations are used for "d":

$$d_1 = \sqrt{\frac{[(1+x)^2 + y^2][(1-x)^2 + y^2]}{2y}}$$

$$d_2 = d_1 \sqrt{x^2 + y^2}$$

$$x = \frac{2X}{B}$$

$$y = \frac{2Y}{B}$$

where:

X and Y are the coordinates of the point in feet, and:

B = base-line distance in feet between two phototheodolites.

The equation and the error curves provide an approximate indication of the order of accuracy that can be expected when a target is tracked by two phototheodolite stations. The actual accuracy of data obtained when two phototheodolite stations are used, and the accuracy obtained when three or four phototheodolite stations are used, must be considered on an individual basis.

b. Tracking

The phototheodolites have a tracking velocity of 33 degrees per second. This tracking velocity provides the capability of tracking a target moving at approximately 770 knots when the target is at a phototheodolite instrument's minimum range of 2,000 feet. The phototheodolites are therefore capable of tracking any of the aircraft normally used in the NAFEC area.

A phototheodolite instrument has a tracking range of 2,000 feet to 15 nautical miles in range, 360 degrees in azimuth, and from -5 degrees to +90 degrees in elevation. A target that passes over the phototheodolite can be tracked by rotating the phototheodolite and the dome 180 degrees. Although each phototheodolite instrument has a minimum range of 2,000 feet, the Phototheodolite Facility is considered to have a minimum range of 0 feet because a target which is too close to one phototheodolite can be tracked by any combination of the other three phototheodolites.

c. Three-Station Solution

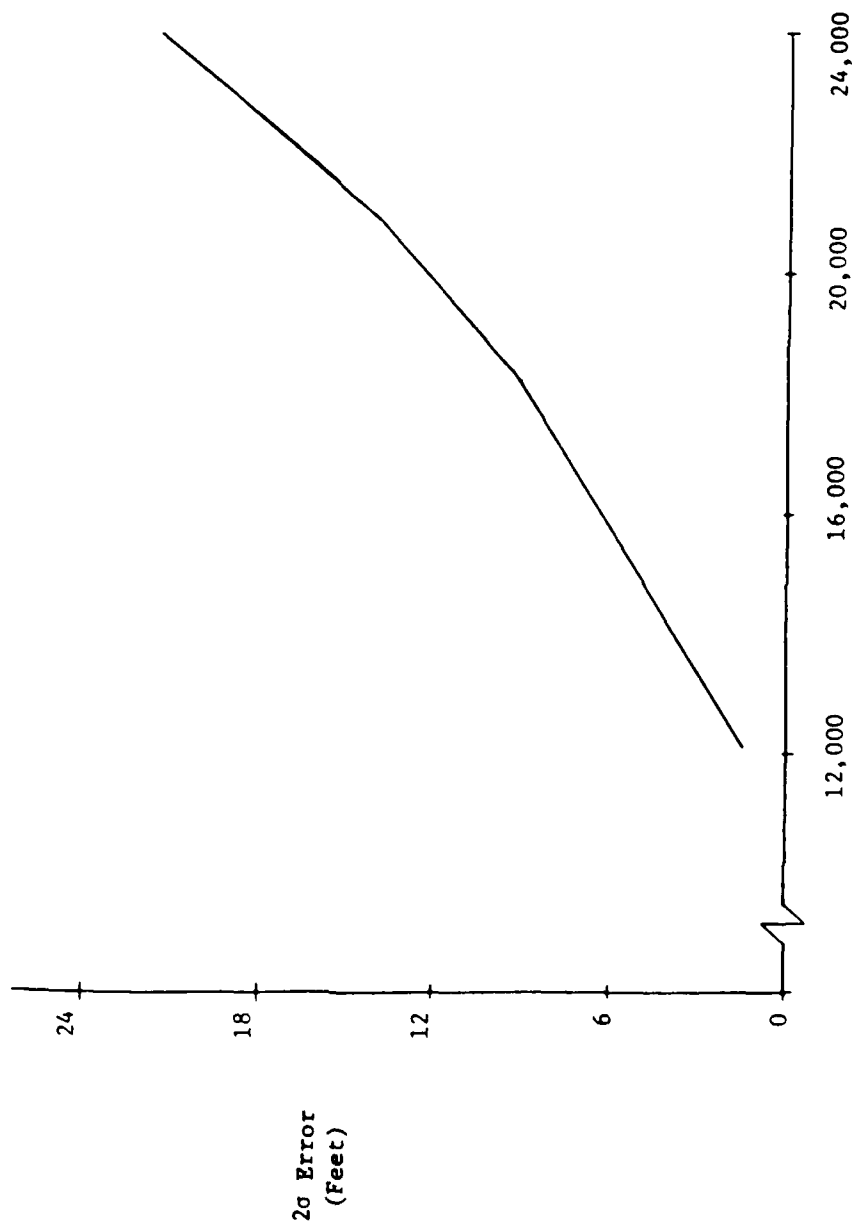
The three-station phototheodolite solution used at NAFEC was based on a report by Mr. R. C. Davis, U.S. Naval Test Station, China Lake, California, titled "Techniques For the Statistical Analysis of Cinetheodolite Data" (NAVORD Report 1299) dated 22 March 1951. This document describes a least squares technique for estimating the spatial position of a missile tracked by a system of "n" phototheodolites (where "n"  $\geq$  2).

The basic data obtained from a theodolite consists of azimuth and elevation angles. Because of the presence of unknown errors in the instruments, the rays from a system of instruments will intersect with a probability approaching zero. The basic problem therefore is estimating the position of the tracked object at a given time from observations yielding a set of nonintersecting lines in space. The method described consists of estimating the position of a missile at that point in space which minimizes the sum of the squares of certain residuals (either angles or distances).

The actual implementation of the least-squares solution at NAFEC is not documented in sufficient detail to permit an exact estimate of the improvement in precision of a 3-station solution versus a 2-station solution. However, an inspection of the geometrical relationships of the three stations and an evaluation of the static test data indicates that the overall improvement in precision is insignificant. The most important contribution of the third station is to maintain a good 2-station cross angle throughout the test regions of importance.

d. Theoretical 2-Sigma Errors

The 2 $\sigma$  errors in the phototheodolite measurements were calculated for the ITT/G and Bendix runways using the equations defined in section "a", above. The factor "e" =  $9.66 \cdot 10^{-5}$  (standard film processing) was used in all calculations. The calculations covered the region from 12,000 to 24,000 feet from the azimuth site. The 24,000-foot point is the phototheodolite-to-EAIR switchover point, and below 12,000 feet static measurements are available. Figures II-18, II-19 and II-20 present the 2 $\sigma$  X, Y and Z error curves for the ITT/G runway and Figures II-21, II-22 and II-23 present the 2 $\sigma$  X, Y and Z error curves for the Bendix runway.



Range (Feet) Referenced to MLS AZ Site  
 Figure II-18: Phototheodolite Error, "X" Axis, Runway 13 (ITT/G).

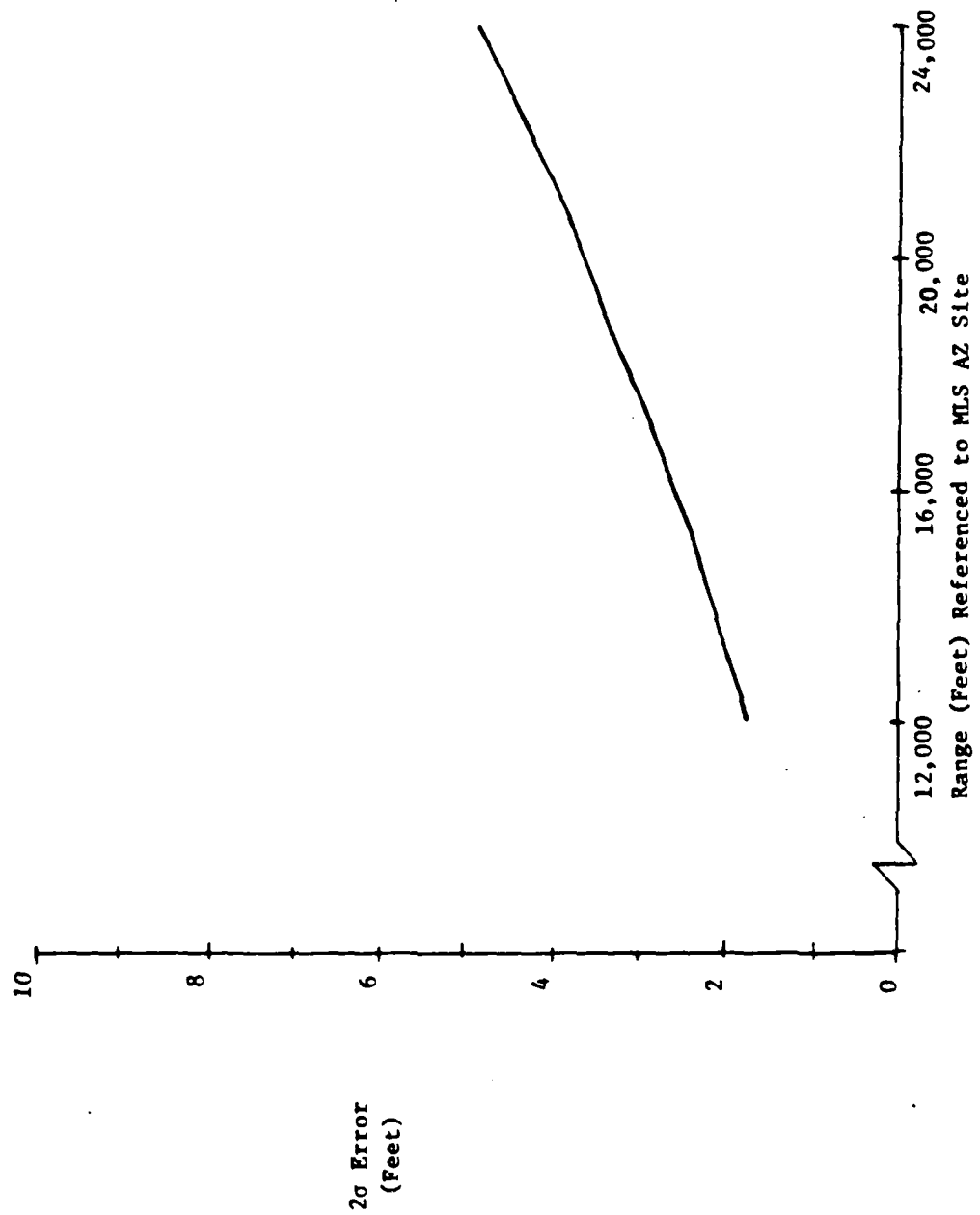


Figure II-19: Phototheodolite Error, "Y" Axis, Runway 13 (ITT/G).



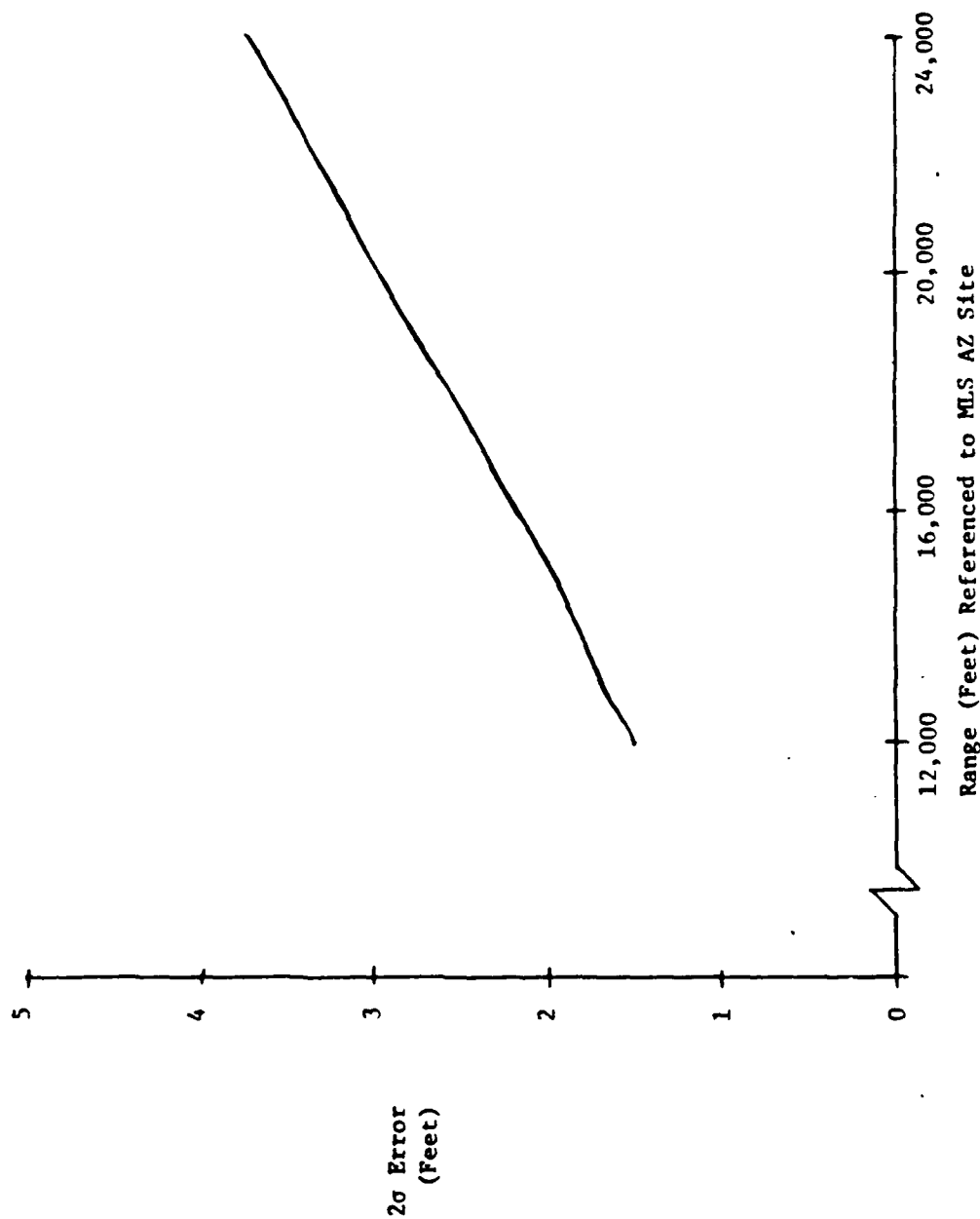


Figure II-20: Phototheodolite Error, "Z" Axis, Runway 13 (ITT/G).

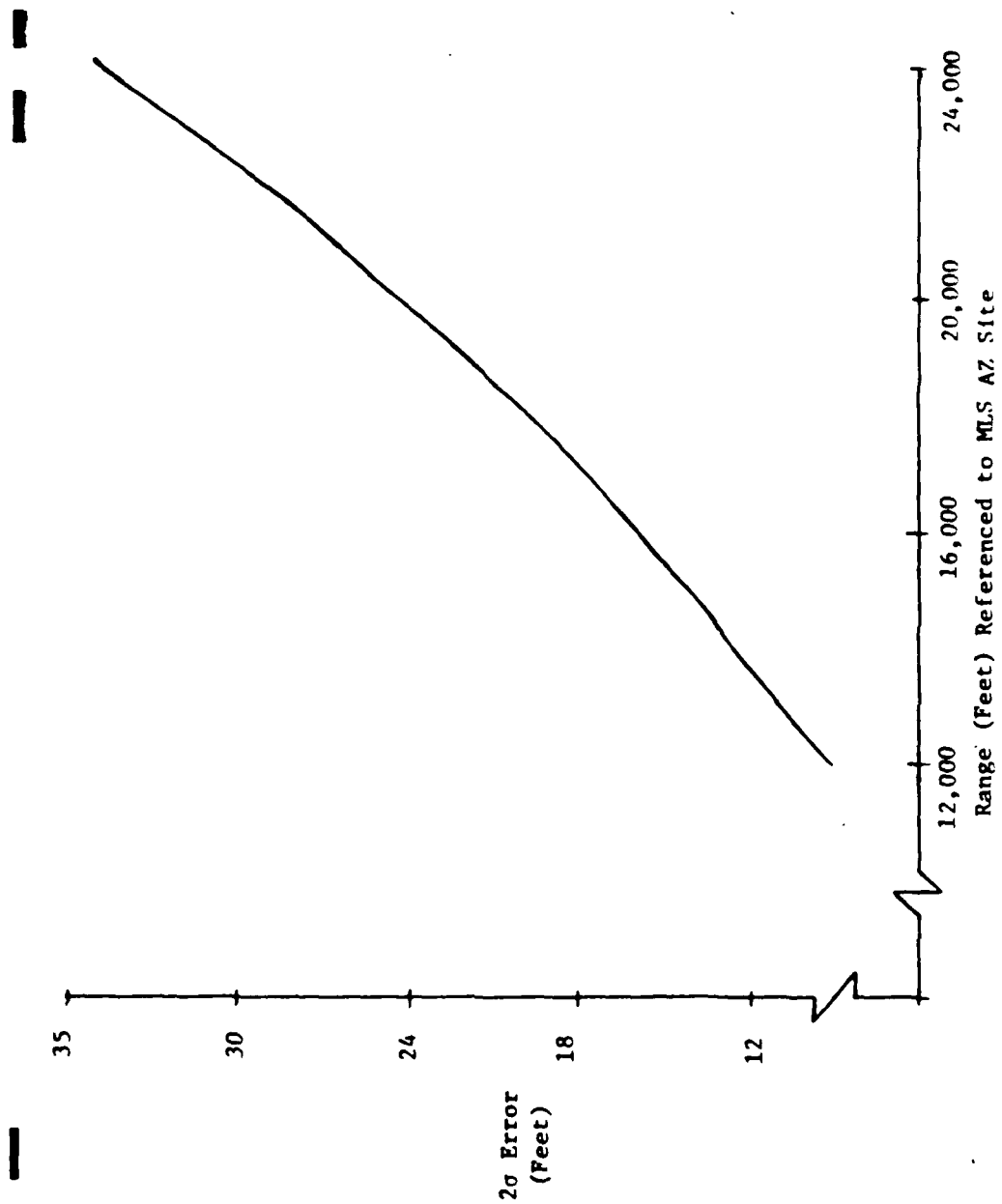


Figure II-21: Phototheodolite Error, "X" Axis, Runway 22 (Bendix).

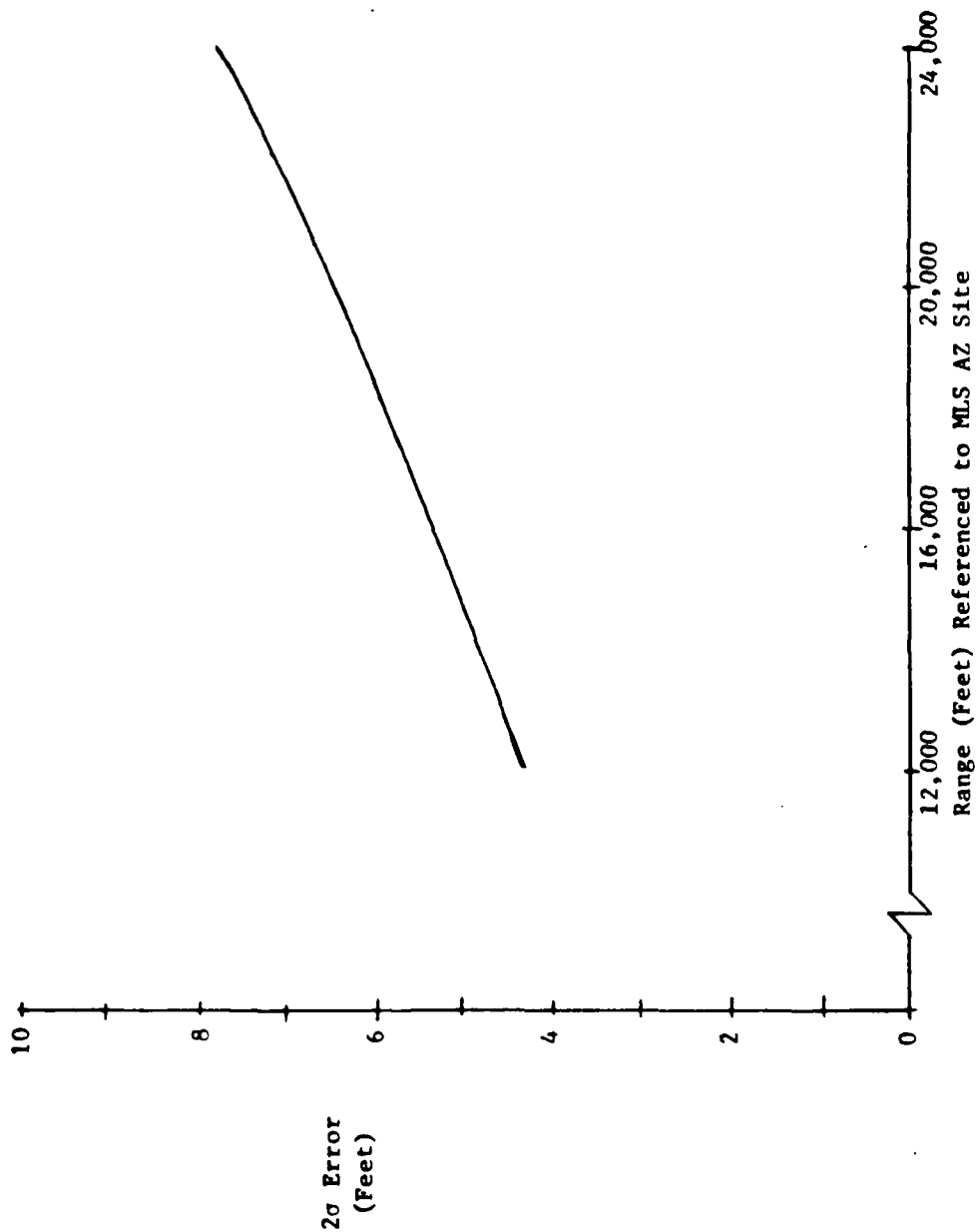


Figure II-22: Phototheodolite Error, "Y" Axis, Runway 22 (Bendix).

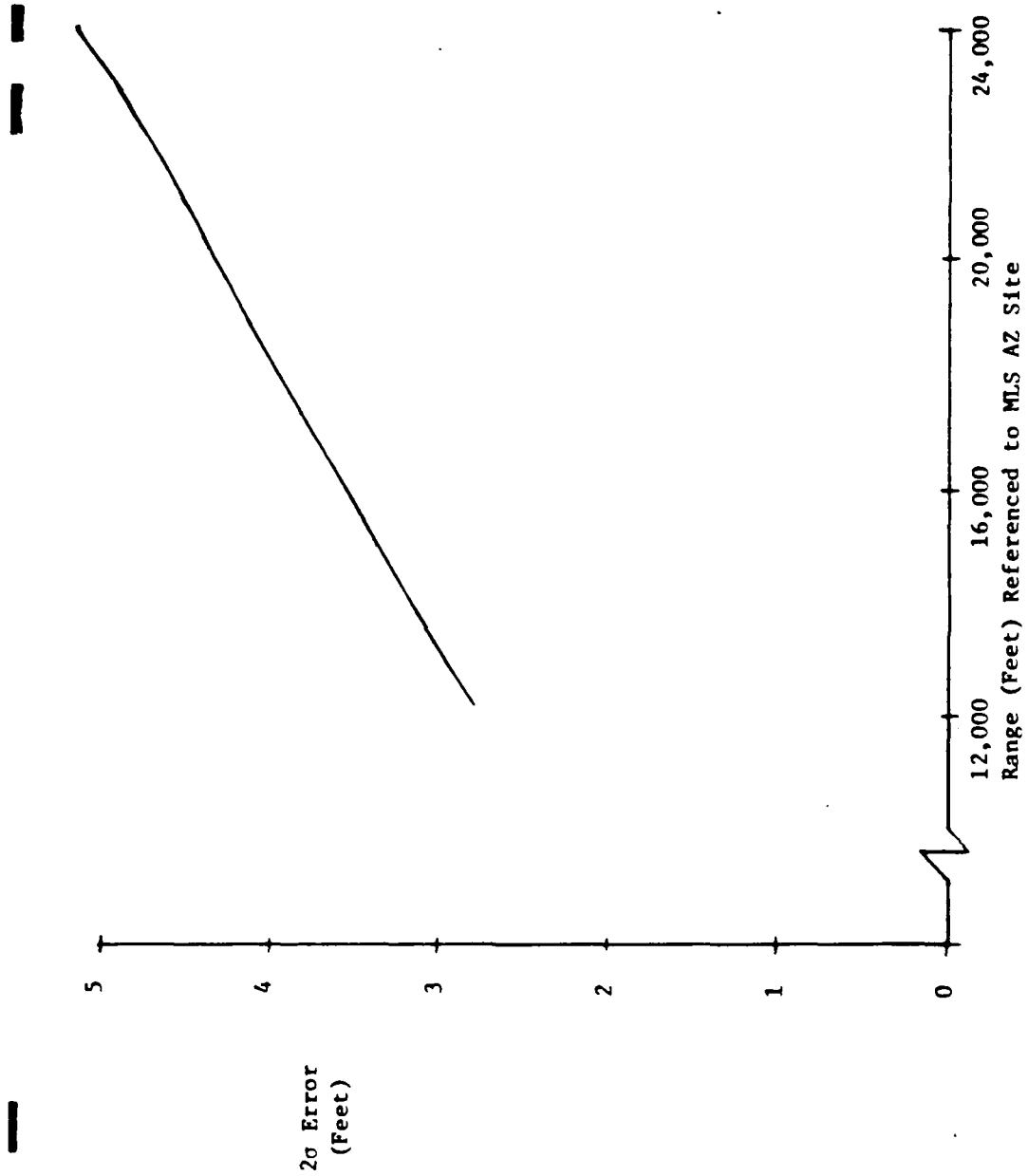


Figure II-23: Phototheodolite Error, "7" Axis, Runway 22 (Bendix).

### 3. Technical Characteristics

The technical characteristics of the EAIR radar installation are presented in Table II-5 and the technical characteristics of the phototheodolite system are presented in Table II-6.

TABLE II-5: EAIR FACILITY TECHNICAL CHARACTERISTICS.

LEADING PARTICULAR	CHARACTERISTIC
Radar	
Transmitter	
Frequency	C-Band, 5450 to 5825 megacycles
Magnetron	Tunable, Type 7156
Peak Power Output	$\frac{1}{2}$ megawatt (Double or triple pulse capability)
Pulse Repetition Frequency	410 Pulses per Second
Pulse Duration	0.8 Microsecond
Antenna	
Reflector	14-foot parabolic
Scanner Polarization	Linear Vertical
(Remote Selectable)	Linear Horizontal
	Right-hand Circular
	Left-hand Circular
Gain	45 db
Side Lobe Level	At least -22 db referred to peak of main lobe
Static Beam Width	0.9
Crossover	80%
Dynamic Beam Width	1.39 at 80% crossover
Nutation Rate	1800 rpm
Antenna Positioning	
Elevation	-1 $\frac{1}{2}$ and -181 $\frac{1}{2}$
Azimuth	Continuous 360
Limit Settings (Elevation)	-3 and 183 (beginning of energy absorption - absolute limits -8 and 188)
Electrical	-1 $\frac{1}{2}$ and -181 $\frac{1}{2}$ . With excess speed, auxiliary limits at 7 and 173
Modes - Manual incl. raster	Manually positioned synchros and follow-ups
Remote	Controlled by one speed synchro information from remote source

Table II-5: EAIR Facility Technical Characteristics (Cont.).

LEADING PARTICULAR	CHARACTERISTIC
Automatic	Controlled by radar error signal generated by 30-cycle conical scan. Double integration of error signal to provide tracking with negligible velocity error and acceleration constant depending on smoothing setting. Separate selection of modes for azimuth and elevation possible for test or operations. 0.2 milliradian (0.011 degrees)
AZ and EL accuracy	
Receiver System	
Amplifier	Tunnel Diode
Minimum discernible signal	Below -104 DBM
Noise Figure	Less than 5.0 db
AGC dynamic range	Minimum of 65 db with 25 db inserted manually for total of 90 db
Beacon delay	Continuously variable 0-600 yards delay of tracking gate
General	Dual local oscillators permit simultaneous radar and beacon tracking, radar AFC circuit referenced to transmitted frequency, beacon AFC circuit referenced to received signal
Range System	
Master Timing	81.946 kc crystal-controlled oscillator (one in use, one standby). Temperature stability of crystals is better than 0.1 part/million/degree centigrade. Crystals are mounted in ovens having temperature stability of 1.2 yards
Range Calibration Accuracy	10,000 yards/sec. min.
Automatic Range Tracking Rate	40,000 yards/sec.
Manual Range Tracking Slew Rate	With 12 db signal-to-noise ration, RMS error will not exceed 20 yards, exclusive of beacon or propagation errors, at 3000 yard/second range rate. Will track at range rates up to 10,000 yard/second with less than 50 yards range error.
Tracking Accuracy Range	

Table II-5: EAIR Facility Technical Characteristics (Cont.).

LEADING PARTICULAR	CHARACTERISTIC
Angle	Acceleration lags are defined by the acceleration constants. RMS tracking at signal-to-noise ratio of 18 db will be about 0.15-mil RMS for low acceleration conditions. The radar will perform automatic tracking at rates up to 50 per second.
Maximum Range Skin Track	100 nautical miles
Beacon Track	190 nautical miles
Maximum Tracking Rate	5,000 miles per hour
Plotting Board Size	30 x 30 inches
Time Mark Intervals from Range Control Central Map Scales	1 PPS and 1 PP10S Continuously adjustable from 200 yards/inch to 40,000 yards/inch
Polar-to-Cartesian Coordinate Converter	
Maximum Range	400,000 yards
Parallax Adjustments	
X and Y	0-50,000 yards
H	0-10,000 yards
Earth Curvature Correction Outputs (X,Y and H)	Provided for both range and height
Digital Data Converter Magnetic Tape Data	DC voltage to plotting boards
Range Word	18-bit natural binary represents 400,000 yards of range to a resolution of 2 yards
Azimuth and Elevation Word	17-bit natural binary represents 360 of angle to a resolution of better than 10 seconds of arc
Time Word	28-bit binary coded decimal represents 46 hours, 26 minutes, 26.5 seconds to a resolution of 0.1 second
Auxiliary Word	27-bit front panel switch selectable
IBM Format Recorder Type	Ampex Model TM-4 Tape Transp. W/model DE-20 read/write electronics



Table II-5: EAIR Facility Technical Characteristics (Cont.).

LEADING PARTICULAR	CHARACTERISTIC
Magnetic Tape Running Time (Full Reel)	Approximately 6 hours
Tape width	$\frac{1}{2}$ inch
Recording Rate	75 inches per second
Number of tracks	7
Sampling Rate	10 samples per second (1 word consists of 20 samples)

TABLE II-6: PHOTOTHEODOLITE FACILITY TECHNICAL CHARACTERISTICS.

LEADING PARTICULAR	CHARACTERISTIC
Phototheodolite Instrument	Contraves Model C
Maximum Range	15 miles (nominal)
Photographic Film Size	35 millimeter
Azimuth or Elevation Tracking Velocity	33 degrees per second
Azimuth or Elevation Tracking Acceleration	60 degrees per second
Azimuth Range	360 degrees
Elevation Range	5 degrees to 90 degrees
Data Sampling Rates	
Photographic film data	5 or 20 frames per second
Plotting board	5 samples per second
IBM format tape	20 samples per second
Tabulator	5 sets of coordinates per second
Real-time tabulator	5 sets of coordinates per second
Raw Data Recorder	
Type	Ampex Model FR 1100
Tape size	$\frac{1}{2}$ inch
Number of channels	7
Recording speed	7.5 inches per second
Recording time for a 2400-foot roll of tape	1 hour
IBM Format Recorder	
Type	Ampex Model FR 1100
Tape size	$\frac{1}{2}$ inch
Channels	7
Recording speed	20.8 inches per second
Recording time for a 2400-foot	20 minutes
Coordinate Conversion Computer	
Full-Scale Output	
X or Y	100,000 feet
Z	25,000 feet
Plotting Board	
Size	30 inches by 30 inches
Area mode scales (maximum range)	
X - Y	100,000 feet
	50,000 feet
	25,000 feet
	10,000 feet

Table II-6: Phototheodolite Facility Technical Characteristics (Cont.).

LEADING PARTICULAR	CHARACTERISTIC
2	0 to 20,000 feet 0 to 10,000 feet 0 to 5,000 feet
Approach mode scales (maximum range)	
1	X = 50,000 to 20,000 feet Y = 6,250 feet Z = 0 to 4,000 feet
2	X = 20,000 to 5,000 feet Y = 2,500 feet Z = 0 to 4,000 feet
3	X = 5,000 to 1,000 feet Y = 1,000 feet Z = 0 to 1,600 feet
D2 master scale	Scale set with gain and parallax controls
D3 master scale	Straight-through input to plotting board
Output Data Recorder	
Type	Ampex Model 932322
Tape size	$\frac{1}{2}$ inch
Number of channels	3
Recording speed	3.75 inches per second
Playback speed	3.75 or 1.25 inches per second
Recording time for a 2400-foot roll of tape	2 hours
Binary-Decimal Translator and Punch	
Punch type	Teletype Corporation Model BRPE-2
Input	Binary data
Output	Binary-coded decimal data
Levels per character	6
Speed	60 characters per second
Tabulator	
Type	Friden Model FPC-8 "Flexowriter" Tabulator
Outputs	
X coordinate in feet	5-digit decimal number
Y coordinate in feet	5-digit decimal number
Z coordinate in tenths of feet	6-digit decimal number

Table II-6: Phototheodolite Facility Technical Characteristics (Cont.).

LEADING PARTICULAR	CHARACTERISTIC
Real-Time Tabulator	Franklin Series 1000 Digital Printer
Type	
Outputs	
X coordinate in feet	5-digit number preceded by its sign
Y coordinate in feet	5-digit number preceded by its sign
Z coordinate in feet	5-digit number
Real time	3-digit number
Data Reduction Rates	
Film-reading machine	50 frames per hour
Tabulator	15 times real time
Real-time Tabulator	5 lines per second (this corresponds to the maximum data rate of the real-time system)
	1 line per second
	1 line per five seconds

### III. OPERATIONAL CALIBRATIONS/TESTS

#### A. Wallops Station

##### 1. AN/FPS-16 Radar

The FPS-16 is calibrated in angle and range before and after each flight. The calibration procedure consists essentially of directing the radar at fixed targets and recording the angle and range data outputs.

For angle calibration, the radar is boresighted, using a tower located approximately 500 yards from the radar site. The angle data from the boresight is recorded on the digital magnetic tracking tape. For range calibration, a range target at a distance of 5.5 nautical miles is acquired in SKIN GATE and BEACON GATE and the indicated range is recorded on the digital magnetic tracking tape. The recording LSB weight is 0.0027 degrees for the angle functions and 6 feet for range.

The pre- and post-calibrations (AZ, EL and range) from the tracking tape were evaluated for the period covering January through June 1974. A total of 31 samples (pre- and post-calibrations) were used for each function. A histogram of the differences between the pre- and post-azimuth calibrations for each sample flight are presented in Figure III-1. The distribution of the differences is basically normal with a mean of 0.0003 degree and a standard deviation of 0.0064 degree. A time history of the absolute values of the azimuth pre-calibrations are presented in Figure III-2. There are no significant trends with time.

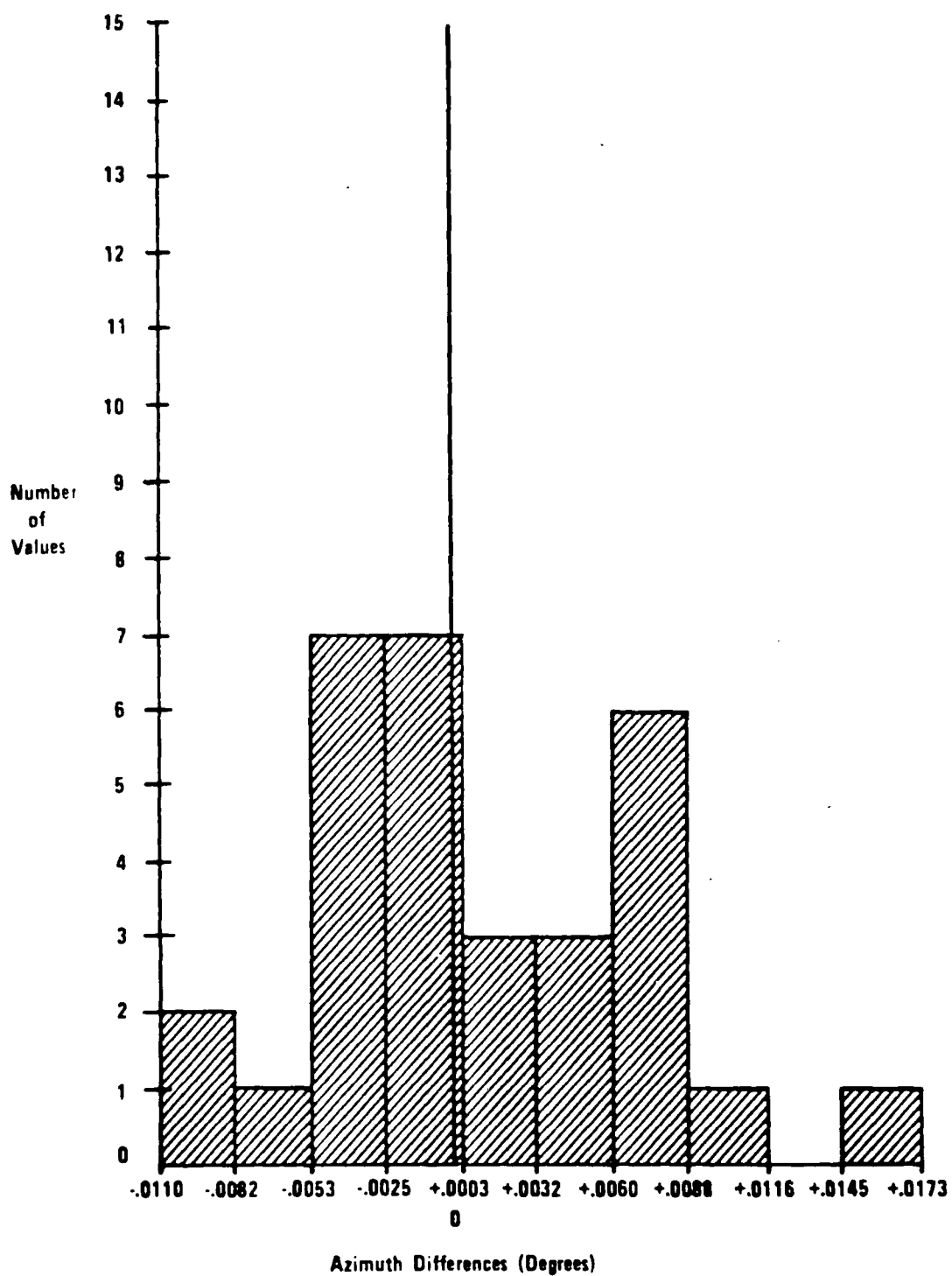


Figure III-1: Distribution of Azimuth Differences  
(Pre- Minus Post-Calibrations).

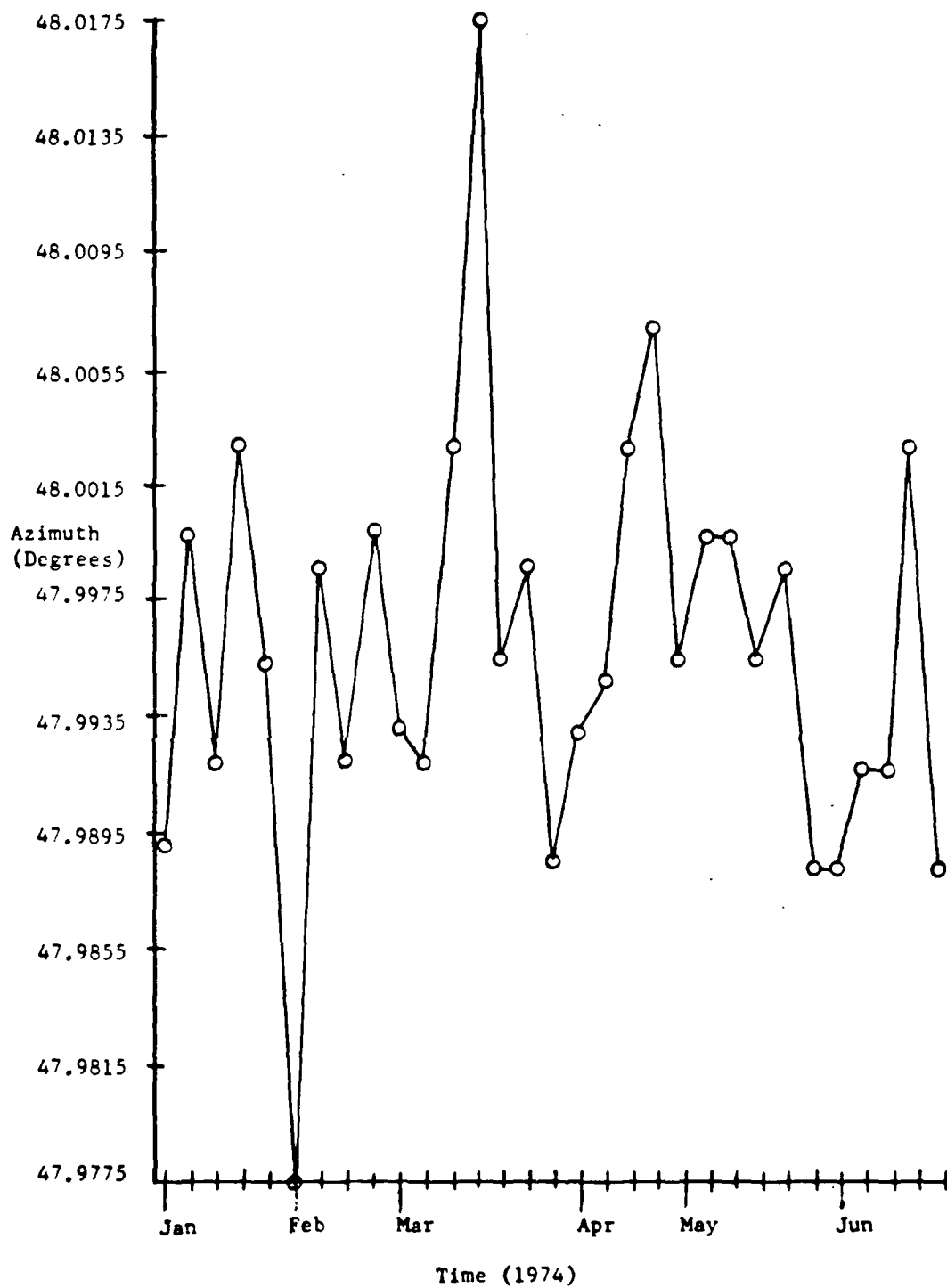


Figure III-2: Azimuth Pre-Calibration Values Versus Time.

The mean of the absolute values is 47.9911 degrees and the standard deviation is 0.0054 degrees. Figure III-3 is a histogram of the differences between the pre- and post-elevation calibration for each flight. The distribution of the differences is basically normal with a mean of -0.0001 degrees and a standard deviation of 0.0063 degrees. A time history of the absolute values of the elevation pre-calibrations are presented in Figure III-4. The mean of the absolute values is 3.3043 degrees and the standard deviation is 0.0069 degrees. There are no significant trends with time. Figure III-5 is a histogram of the differences between the pre- and post-range calibrations. This distribution is basically normal with a mean of -0.4 feet and a standard deviation of 8.6 feet. A time history of the absolute values of the range pre-calibrations are presented in Figure III-6. These pre-calibrations are from the beacon gate mode and thus are grouped into two range regions, because of different beacon delay values for Hazeltine and T.I. This difference in delay values results in a range difference of 100 feet since no actual beacon was employed in the calibrations. Fifteen of the sample calibrations used the T.I. delay; the mean of the absolute pre-calibration value was 30,933 feet and the standard deviation 1.6 feet. Sixteen of the sample calibrations used the Hazeltine delay; the mean of the absolute pre-calibration values was 31,033 feet and the standard deviation was 3 feet.

Other radar tests check power, pulsewidth, PRF, L.O. frequency, etc. These tests are not normally performed unless there is indication of trouble.



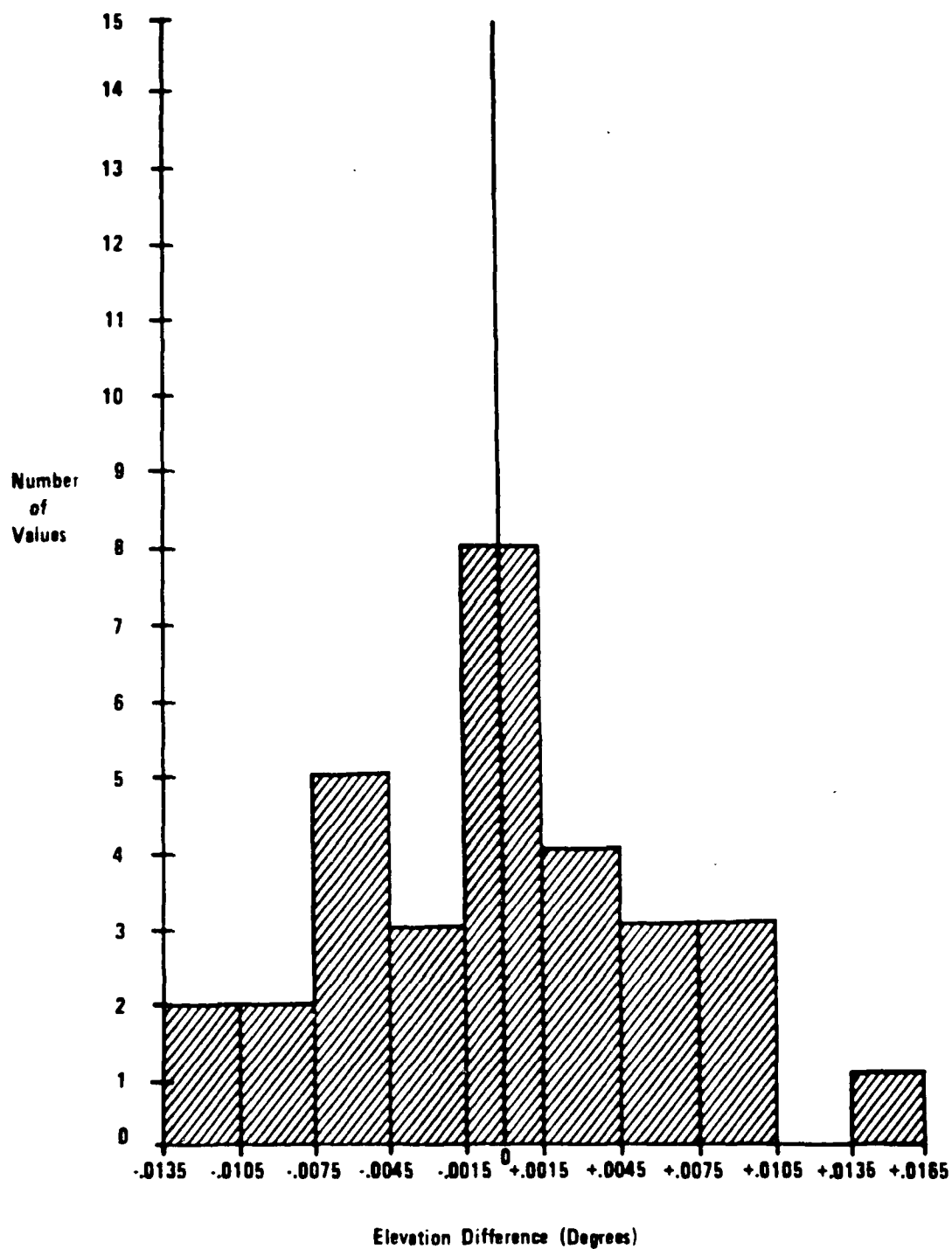


Figure III-3: Distribution of Elevation Differences  
(Pre- Minus Post-Calibrations).

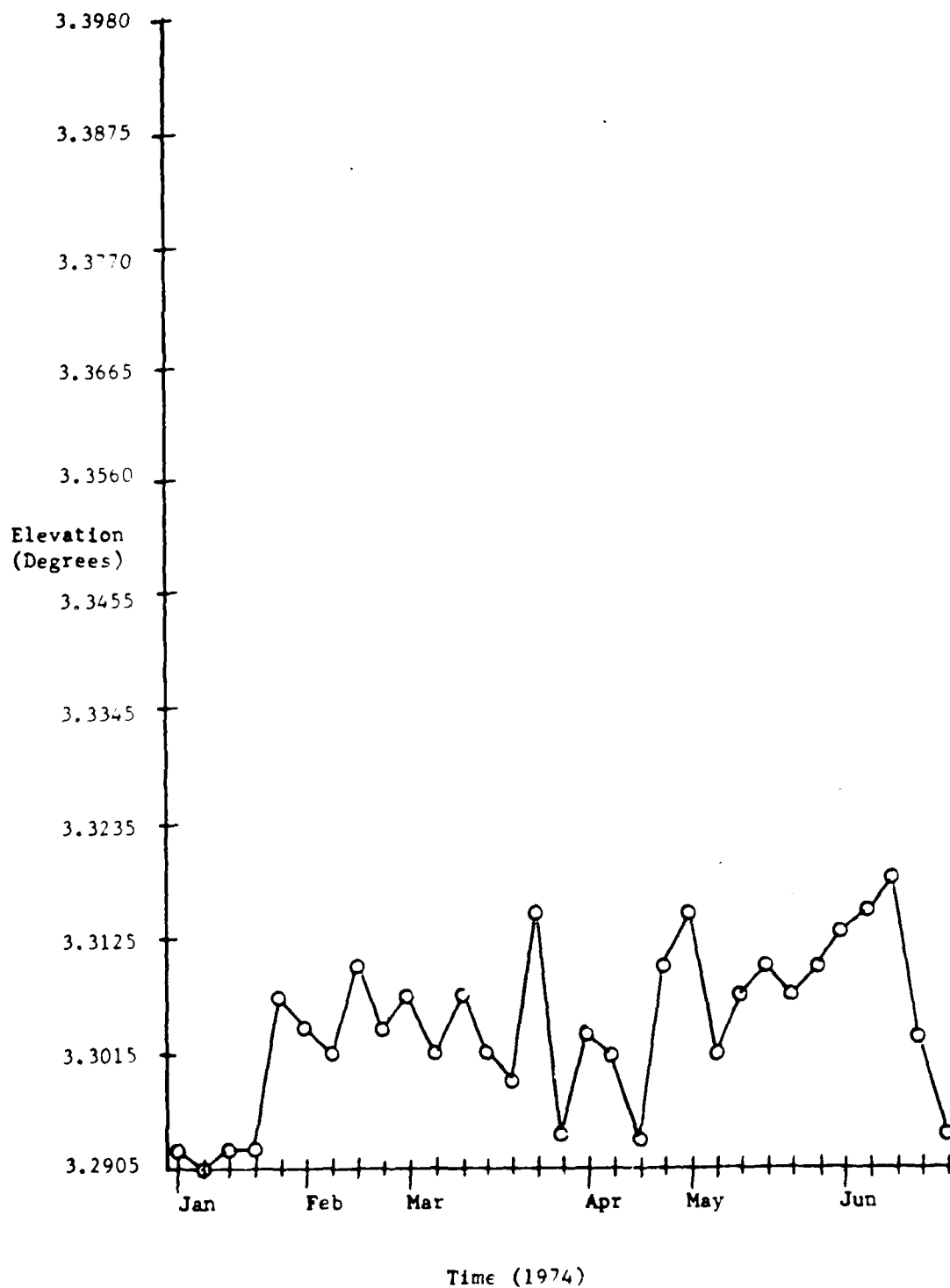


Figure III-4: Elevation Pre-Calibration Values Versus Time.

AD-A131 738

MICROWAVE LANDING SYSTEM PHASE II TRACKER ERROR STUDY  
(U) FEDERAL AVIATION ADMINISTRATION WASHINGTON DC  
SYSTEMS RESEARCH AND DEVELOPMENT SERVICE DEC 74

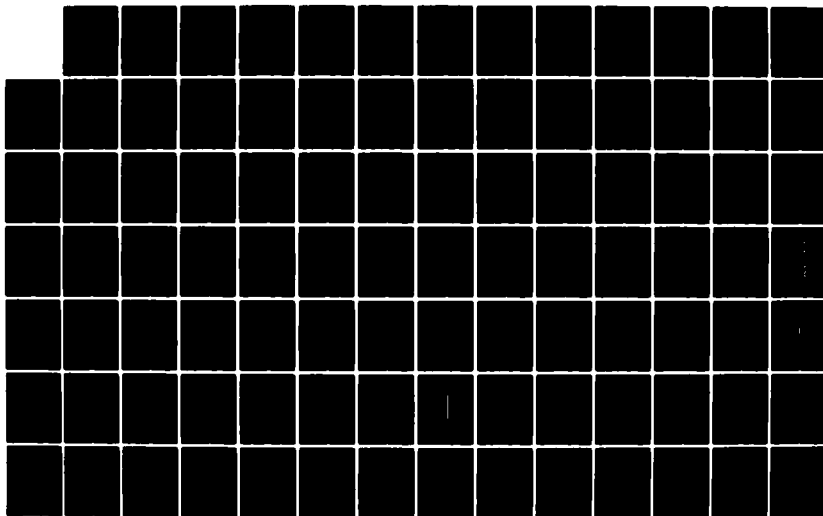
23

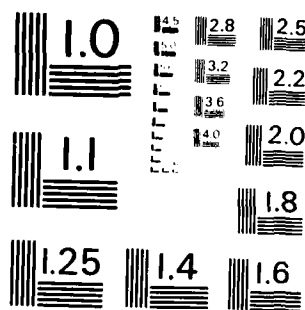
UNCLASSIFIED

FAA/RD-74-207

F/G 17/7

NL





MICROCOPY RESOLUTION TEST CHART  
 NATIONAL BUREAU OF STANDARDS-1963-A

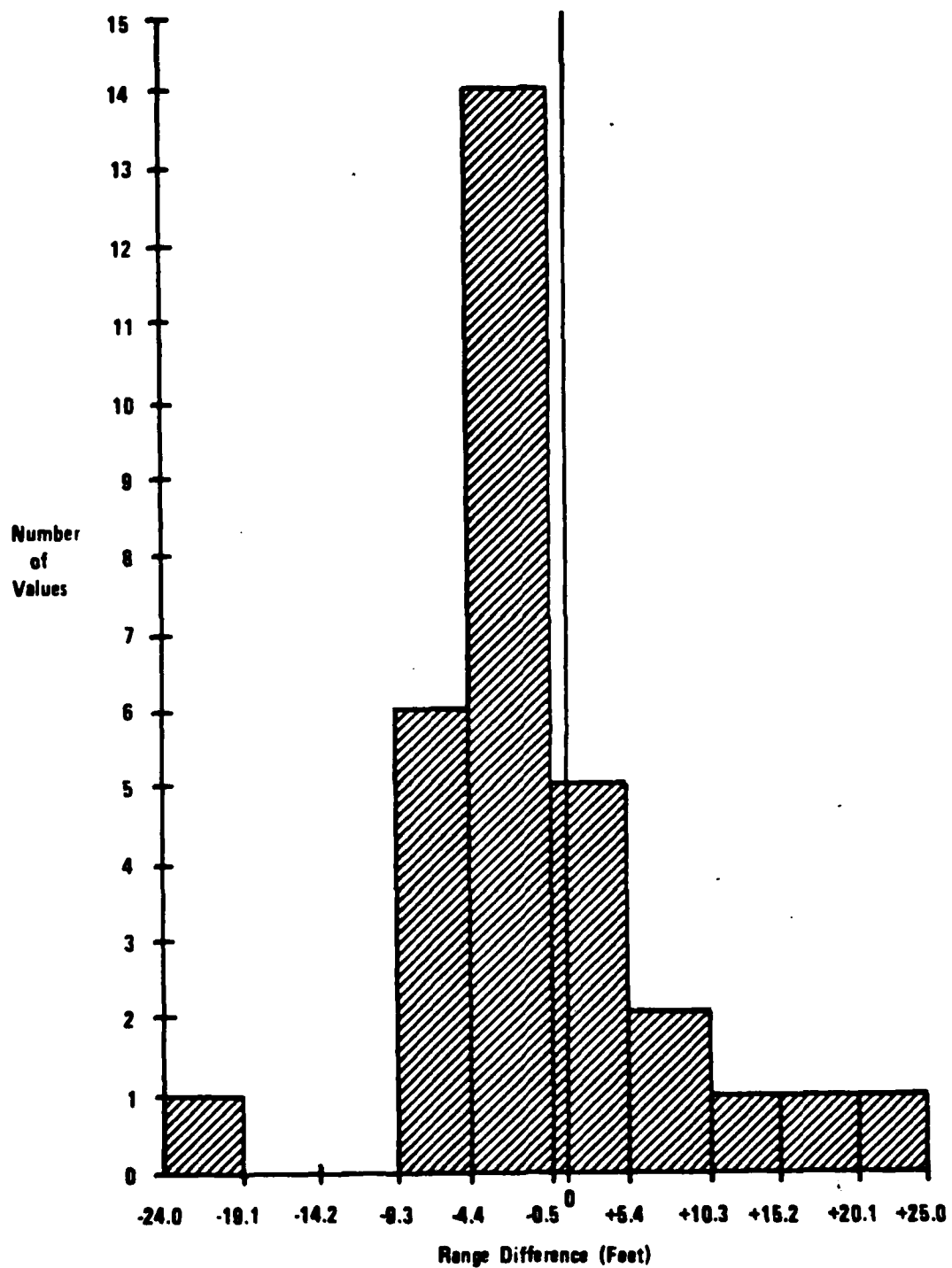


Figure III-5: Distribution of Range Differences  
(Pre- Minus Post-Calibrations).

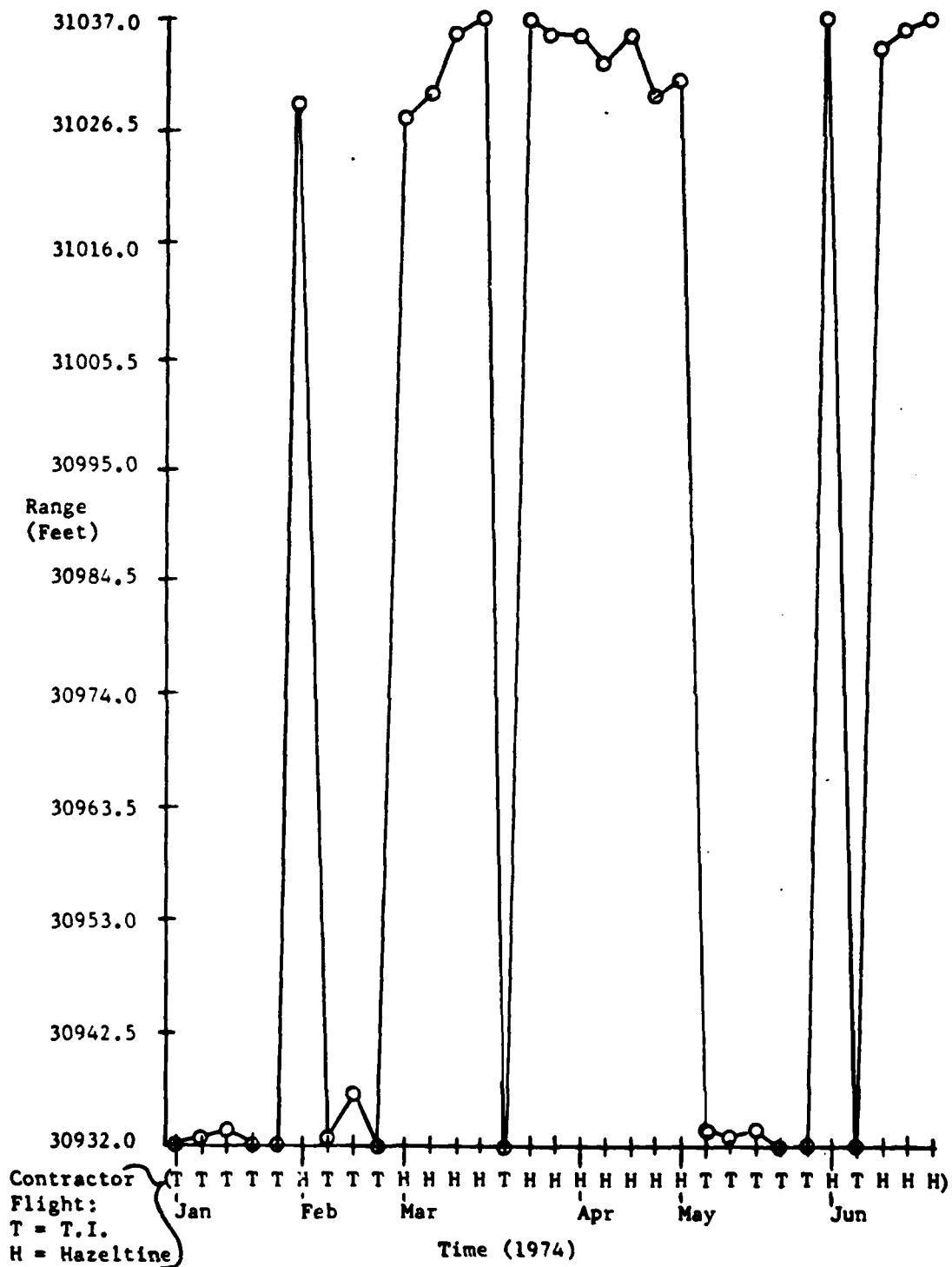


Figure III-6: Range Pre-calibration Values Versus Time.

## 2. Photogrammetric System

After the initial installation and survey of the photogrammetric system, a series of static calibration tests are performed. These tests consist of locating the MLS test van at survey points along the runway centerline and photographing a target on the tower of the test van. The spatial position of the test target is then computed using photogrammetric data. The results of the photogrammetric computations are then compared to the actual spatial position of the test target. Table III-1 presents the results of the static tests for runway 22 (T.I.) and Table III-2 presents the results of the static tests for runway 10 (Hazeltine).

After initial installation and checkout of the photogrammetric system, the position of the target board centers are rechecked before each day's testing to ascertain that the centers are still over the survey markers. Since the camera orientation is not especially critical, the operator sights the camera at the center target board at the beginning of the first run of the day; further checks on orientation may be made by examining the developed film. Focal length or film stretch problems are monitored by measuring the target-board separation and comparing the results with the known value.

At the beginning of each run, time-code signals at each camera site are displayed on an oscilloscope to ascertain that the proper signals are present and free of interference.

TABLE III-1. RUNWAY 22 STATIC TEST RESULTS (FEET)

Run Number	Data Pts.	Test Point	Cameras	$X'_s$	$\bar{X}'_p$	$\Delta X' \left( \frac{X-X}{p-s} \right)$	Sigma	$Y'_s$	$Y'_p$	$\Delta Y' \left( \frac{Y-Y}{p-s} \right)$	Sigma	$Z'_s$	$Z'_p$	$\Delta Z' \left( \frac{Z-Z}{p-s} \right)$	Sigma
4X007	19	49	1 & 2	7200.289	7200.924	0.135	0.094	0.140	0.088	-0.051	0.082	38.67	38.291	-0.397	0.015
4X013	19	56	1 & 3	7800.184	7801.844	1.660	0.177	0.174	0.1387	-0.035	0.029	38.63	38.368	-0.261	0.158
4X018	36	74	1 & 4	9400.392	9468.180	2.783	0.266	-0.192	0.2697	0.461	0.013	34.925	35.220	0.295	0.074

TABLE III-2. RUNWAY 10 STATIC TEST RESULTS (FEET)

Run Number	Data Pts.	Test Point	Cameras	$X'_s$	$\bar{X}'_p$	$\Delta X' \left( \frac{X-X}{p-s} \right)$	Sigma	$Y'_e$	$Y'_p$	$\Delta Y' \left( \frac{Y-Y}{p-s} \right)$	Sigma	$Z'_s$	$Z'_p$	$\Delta Z' \left( \frac{Z-Z}{p-s} \right)$	Sigma
2X213	17	148	1 & 3	6900.860	6901.770	0.9097	0.15	0.0434	0.191	0.1476	0.203	11.87	11.914	0.044	0.902
2X214	13	163	1 & 4	8301.880	8302.069	0.189	0.255	0.0616	0.1561	0.2177	0.014	-9.03	-9.754	-0.674	0.40
		129	1 & 2	5500.00		CAMERA ?	FAILURE								



The image and the time codes are recorded sequentially.

Since the length of the loop of film between the two recording points will vary from one roll to the next, it is necessary to establish the time lag at the beginning of each roll. This is done by exposing a

frame with the film transport mechanism off and time signals on.

#### B. NAFEC

##### 1. Phototheodolites

Pre- and post-flight optical checks and digital checks are performed on the phototheodolite system. The optical checks test alignment and level. Each phototheodolite is sighted on a target board in both NORMAL and DUMPED positions, and the azimuth and elevation angles recorded on film. Distance to the target boards is about 2,000 feet. The digital checks consist of comparing encoder outputs with known inputs.

The pre- and post-flight optical checks were evaluated for a number of flights during the period from March through July of 1974. The data for the evaluation was obtained from the film-corrected phototheodolite runs. The results of the evaluation for each theodolite are indicated in Table III-3:

TABLE III-3: PHOTOTHEODOLITE EVALUATION

Photo-theod.	Site	Single Size	Pre Calibration	Sample Size	Post Calibration	Sample Size	$\Delta$ 's (Pre-Post)
P-8	<u>AZ:</u>	9	$\bar{\mu} = 201.4901$	6	$\bar{\mu} = 201.4897$	6	$\bar{\mu} = 0.0002$
		"	$\sigma = 0.009$	"	$\sigma = 0.0020$	"	$\sigma = 0.0019$
	<u>EL:</u>	"	$\bar{\mu} = 358.2425$	"	$\bar{\mu} = 358.2410$	"	$\bar{\mu} = -0.0001$
		"	$\sigma = 0.0027$	"	$\sigma = 0.0021$	"	$\sigma = 0.0009$
P-29	<u>AZ:</u>	12	$\bar{\mu} = 46.0990$	7	$\bar{\mu} = 46.0775$	7	$\bar{\mu} = 0.0015$
		"	$\sigma = 0.0012$	"	$\sigma = 0.0026$	"	$\sigma = 0.0028$
	<u>EL:</u>	13	$\bar{\mu} = 358.4567$	"	$\bar{\mu} = 358.4563$	"	$\bar{\mu} = -0.0011$
		"	$\sigma = 0.0027$	"	$\sigma = 0.0029$	"	$\sigma = 0.0048$
P-36	<u>AZ:</u>	9	$\bar{\mu} = 145.5037^\circ$	"	$\bar{\mu} = 145.5046^\circ$	6	$\bar{\mu} = 0.0011$
		"	$\sigma = 0.0027^\circ$	"	$\sigma = 0.0016$	"	$\sigma = 0.0031$
	<u>EL:</u>	7	$\bar{\mu} = 358.8867^\circ$	"	$\bar{\mu} = 358.8880$	"	$\bar{\mu} = -0.0012$
		"	$\sigma = 0.0015^\circ$	"	$\sigma = 0.0018$	"	$\sigma = 0.0019$

The phototheodolite system was cross-calibrated with the MLS static survey points in accordance with Appendix G (Section G.1) of the MLS Phase II Test Requirements and Coordination Plan. A total of 10 seconds of tracker data (100 samples) was recorded at each test point. In addition,

the 10 seconds of test data was divided into 3 distinctive theodolite sightings, i.e., after each 3.3-second interval the theodolites were slewed away from the target and then the target was reacquired. The test data was reduced at NAPEC and the mean and standard deviation of the differences (phototheodolite minus survey point) was computed for each test point. The data sets from specific locations along the runway centerline were tested to determine if they came from different distributions. These tests showed no significant differences for 23 out of 24 data sets. These tests also showed that the residual noise level of the system was the primary contributor to the difference values, rather than different phototheodolite geometries. As a result, the mean values from all test points were pooled on a per-function basis and plotted in histograms. Figures III-7, III-8 and III-9 present the  $\bar{x}$ ,  $\bar{y}$  and  $\bar{z}$  histograms for the Bendix runway and Figures III-10, III-11 and III-12 for the ITT/G runway. The mean differences are basically normally distributed with the indicated characteristics in Table III-4:

TABLE III-4: RUNWAY MEAN SURVEY DIFFERENCE FUNCTION DATA.

Runway	Function	Distribution	Standard Deviation * (Feet)
Bendix	$\bar{x}$	Approx. Normal	0.7
	$\bar{y}$	" "	1.0
	$\bar{z}$	" "	0.9
ITT/G	$\bar{x}$	" "	0.8
	$\bar{y}$	" "	1.1
	$\bar{z}$	" "	1.1

\* About zero

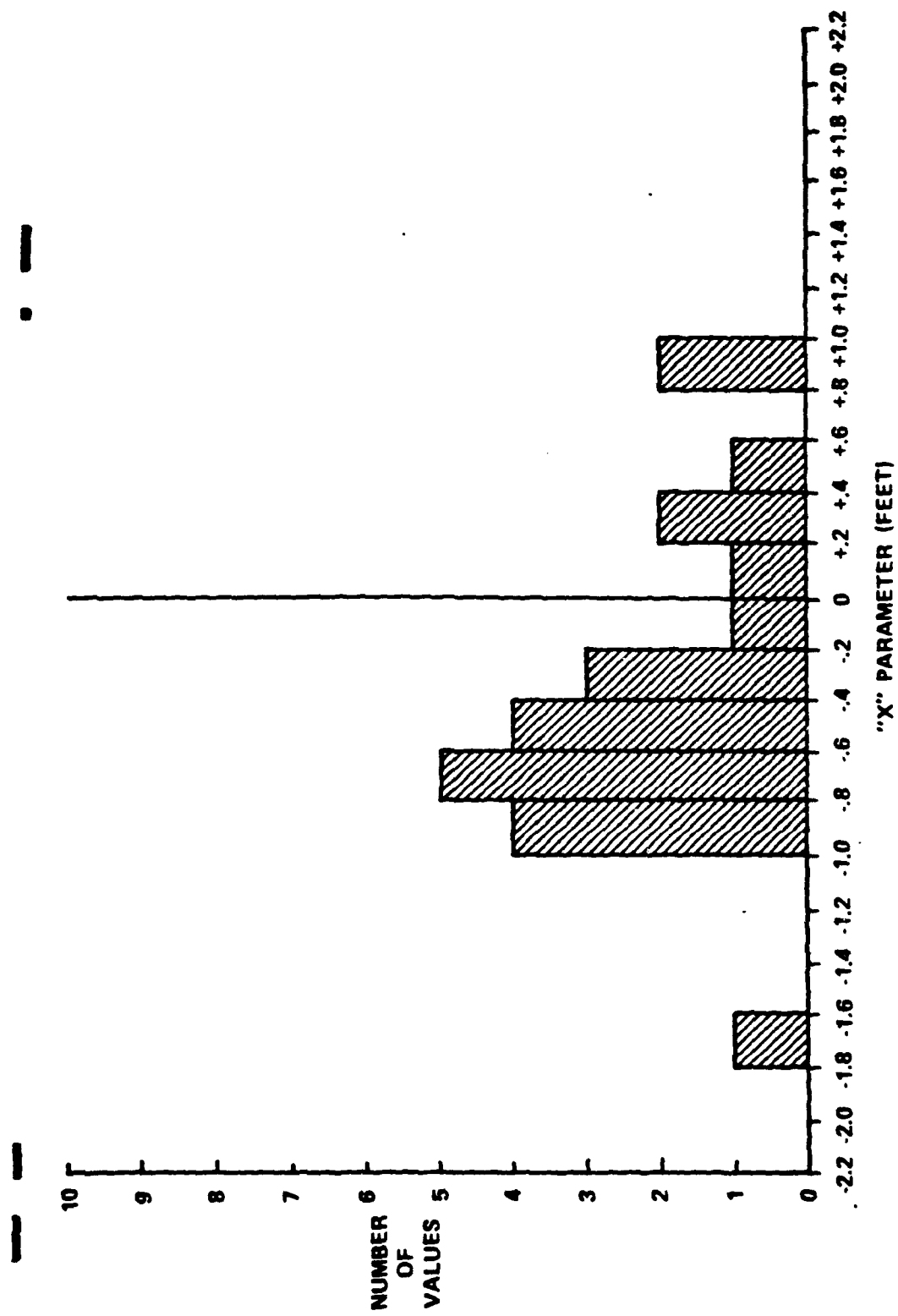


Figure III-7: Phototheodolite Static Test Data Distribution of  $\bar{X}$  Values, Bendix Runway.

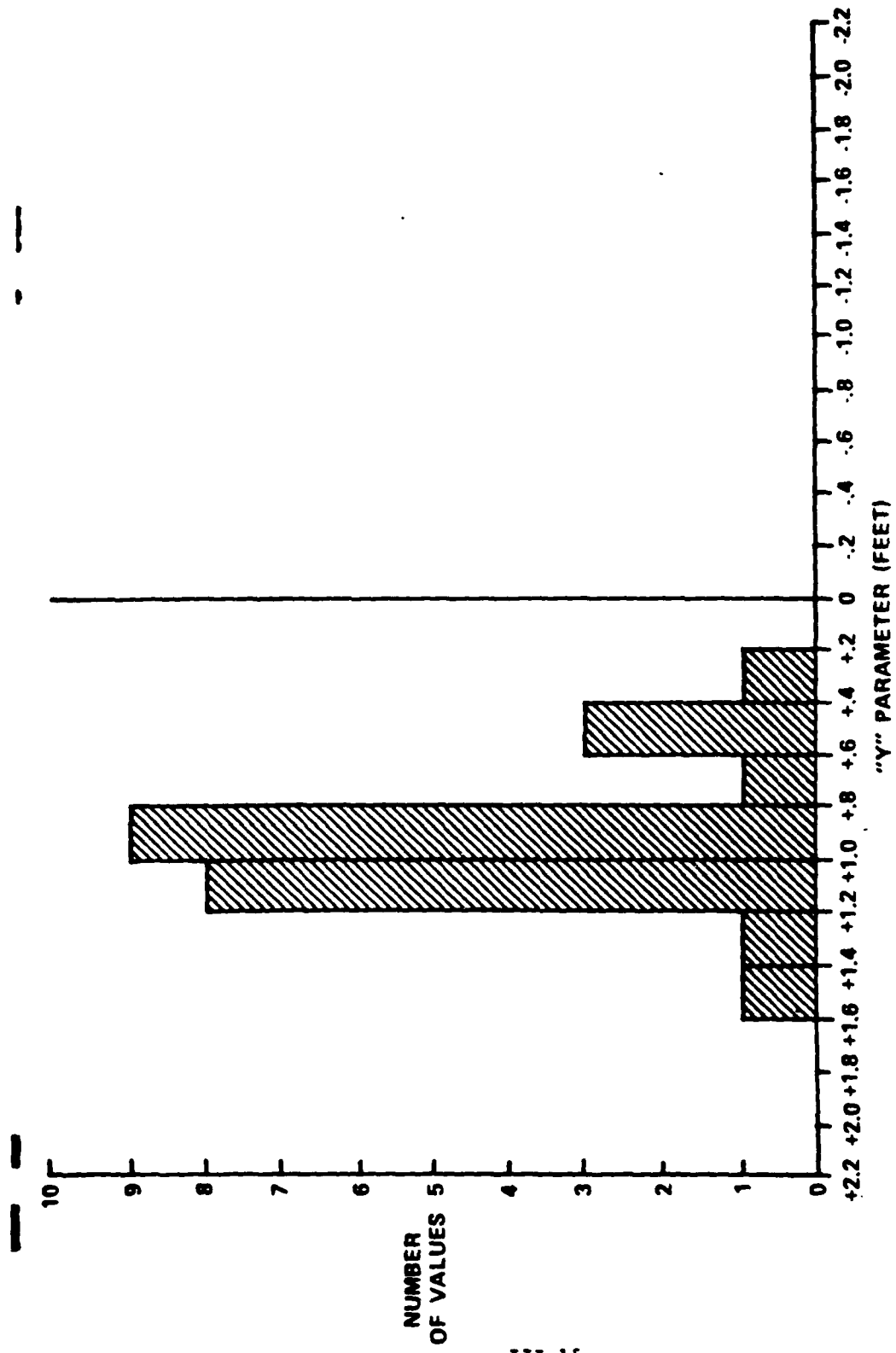


Figure III-8: Phototheodolite Static Test Data Distribution of  $\bar{X}$  Values, Bendix Runway.

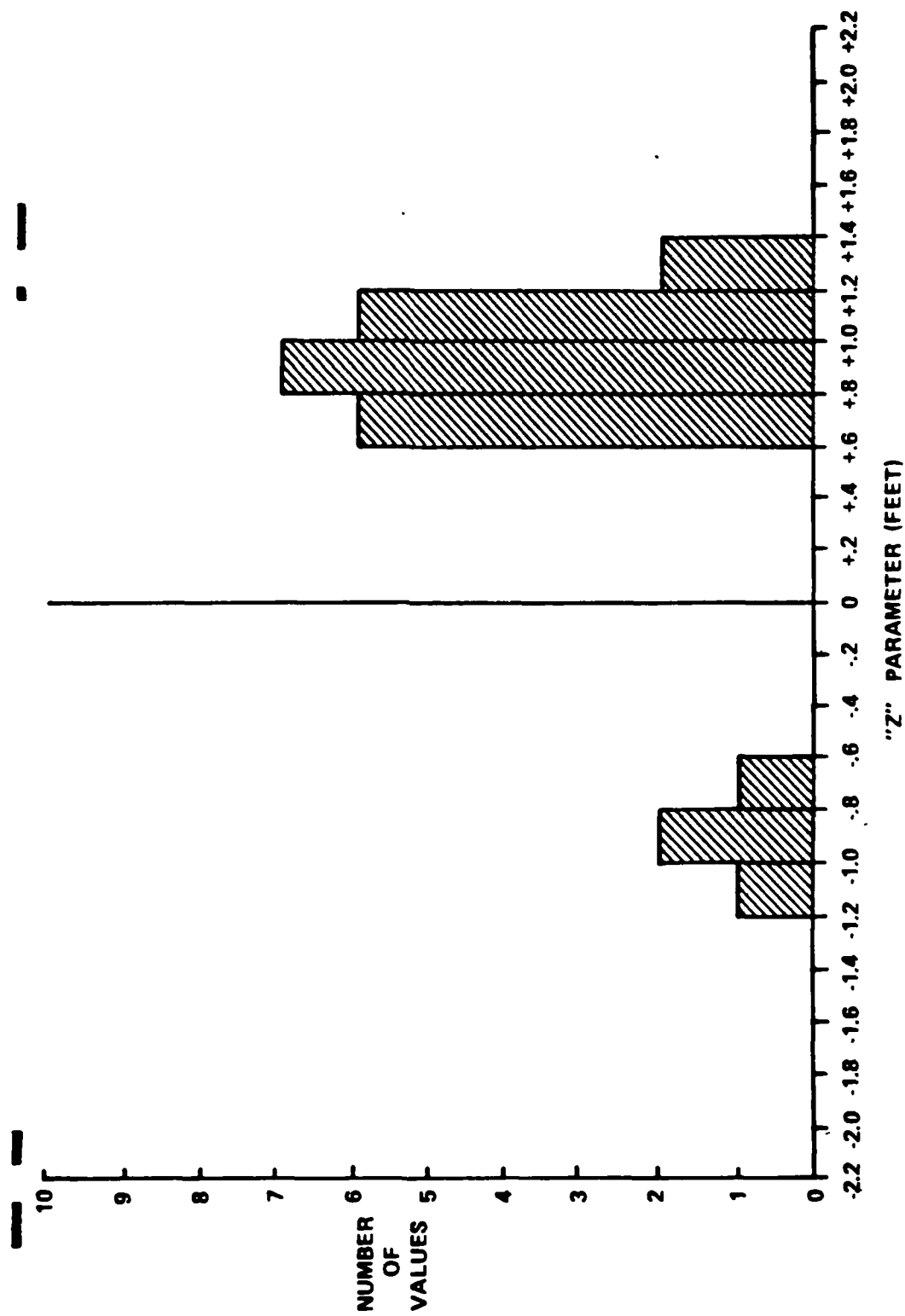


Figure III-9: Phototheodolite Static Test Data Distribution of X Values, Bendix Runway.

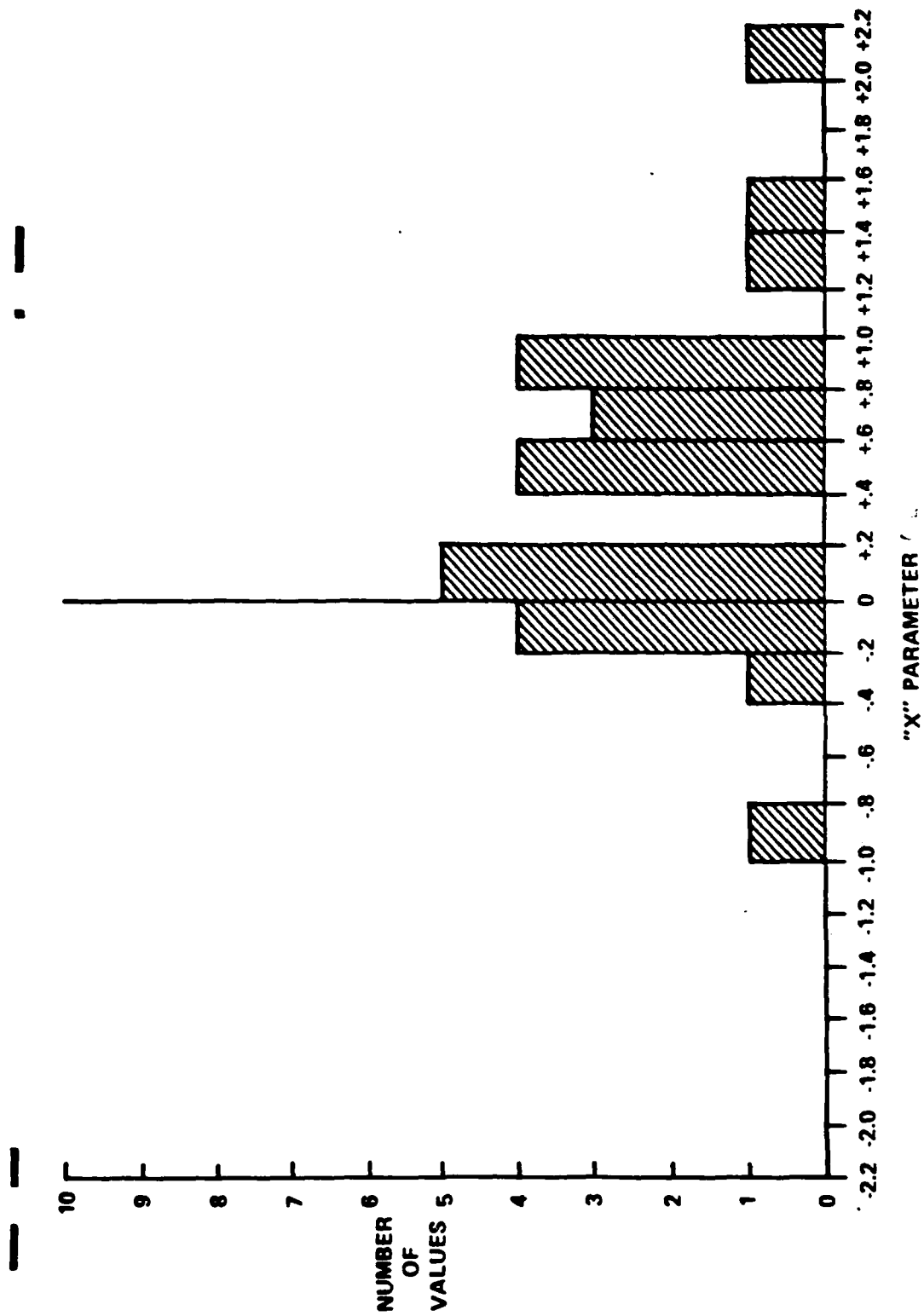


Figure III-10: Phototheodolite Static Test Data Distribution of  $\bar{X}$  Values, ITT/G Runway.

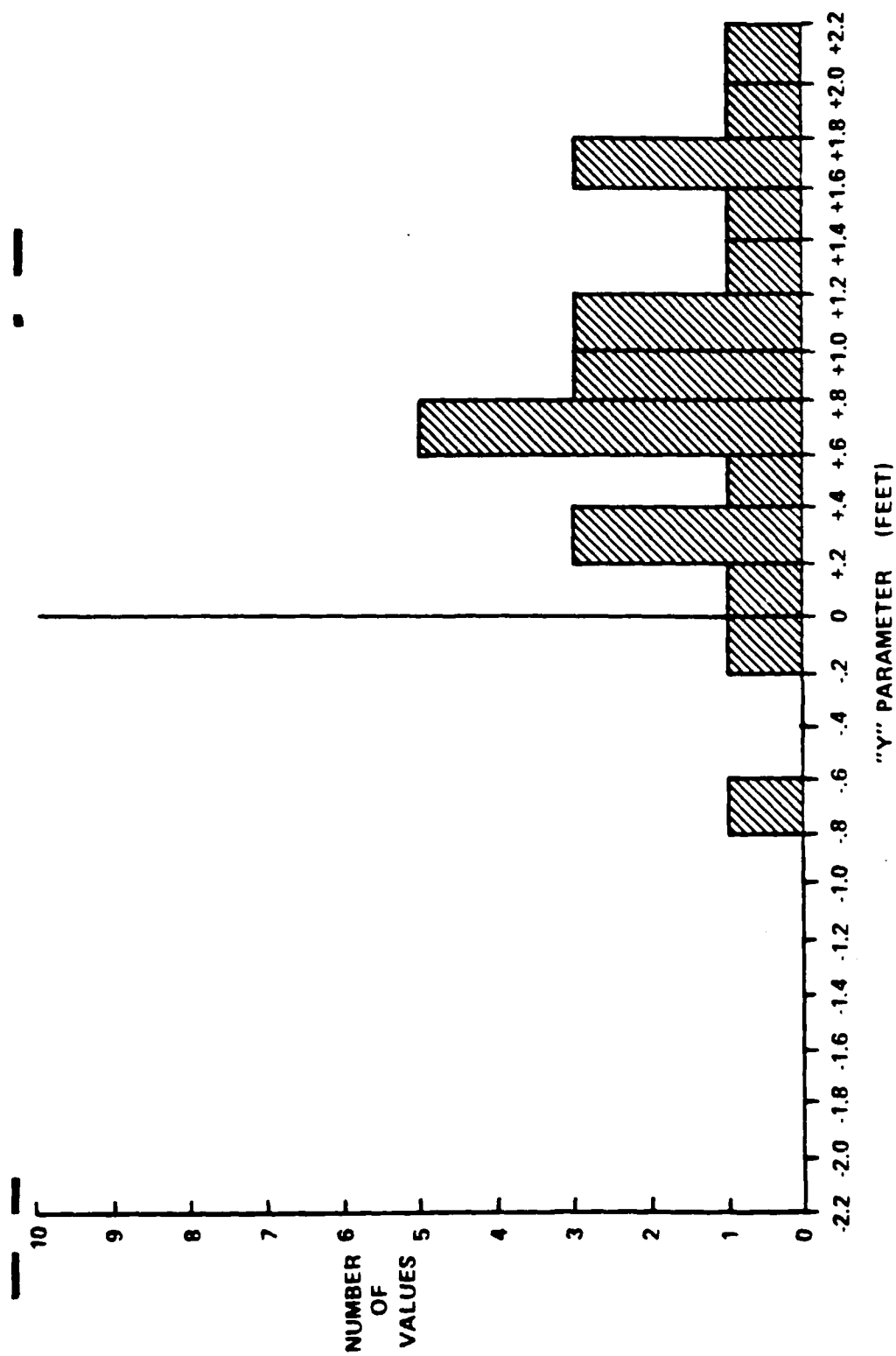


Figure III-11: Phototheodolite Static Test Data Distribution of  $\bar{X}$  Values, ITT/G Runway



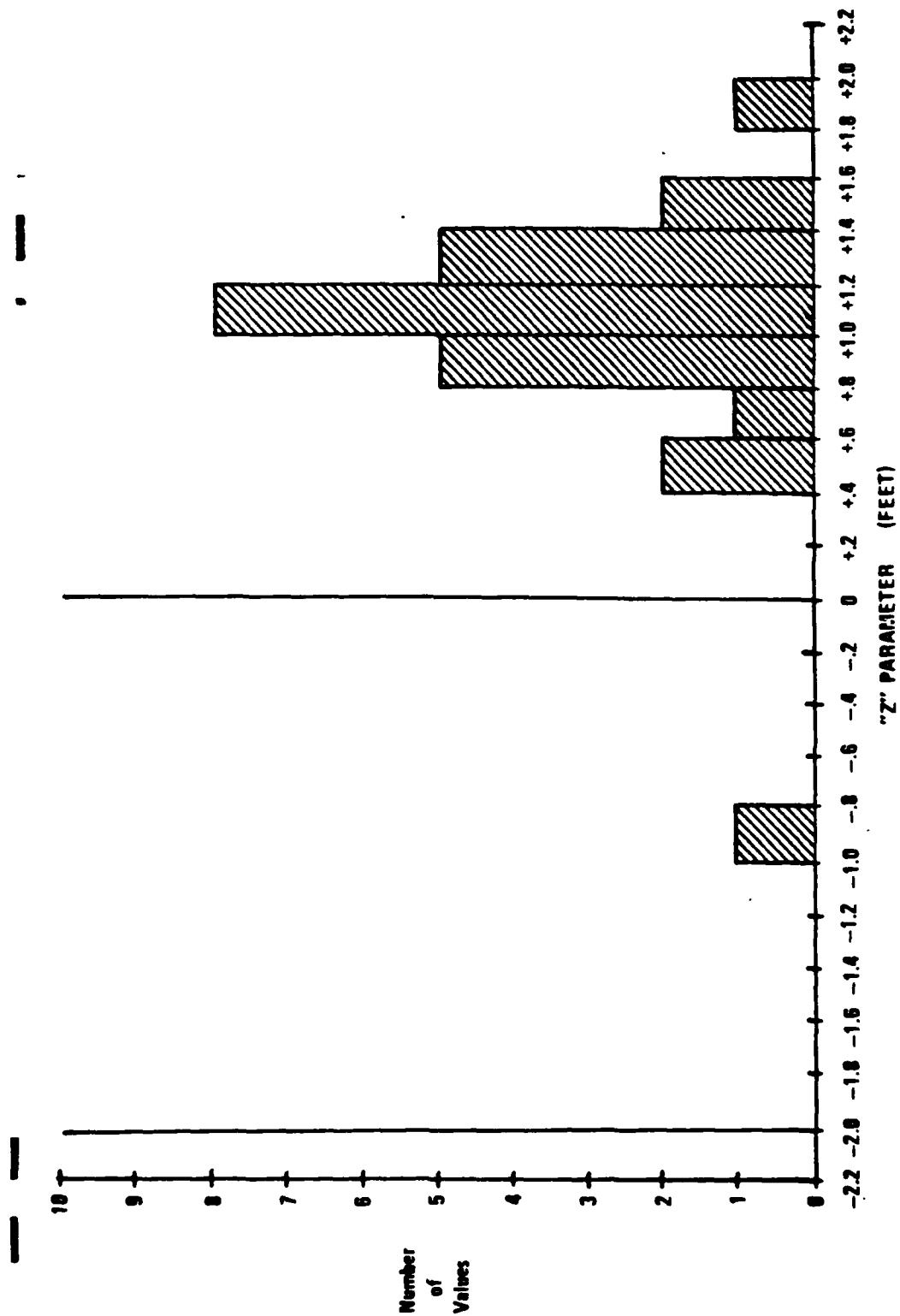


Figure III-12: Phototheodolite Static Test Data Distribution of  $\bar{X}$  Values, ITT/G Runway.

#### IV. DATA PROCESSING TECHNIQUES

##### A. Outlier Screening

###### 1. FPS-16 Radar

The Wallops Station Data Processing Facility performs the outlier screening and removal operation for the FPS-16. This procedure is a manual operation with experienced radar data processors scanning all raw data from a day's flight. When a data point is observed that is inconsistent with the general data level for that portion of a flight, the data point is removed from the raw radar type. The data point is subsequently replaced using a straight line interpolation between two adjacent good points.

###### 2. Photogrammetric System

The photogrammetric film reading process generates a deck of IBM cards for each run. These IBM cards contain raw measurements from the film (in microns) and time. Prior to processing of the data, the IBM cards are run through a Quality Control program to eliminate outliers introduced by the manual film reading process. This program performs the following checks:

- a. Proper sequencing of frame I.D.'s
- b. Proper sequencing of time
- c. Proper number of readings per frame
- d. The left and right target board readings are in the proper relationship.
- e. The difference between a pair of readings (each reading is performed twice) is less than 30 microns.

Data points eliminated by the Quality Control program are reinserted prior to filtering out the data. Lagrangian interpolation is used to compute values for all missing points for which:

- a. The missing point is not contained in a gap of more than three missing points;
- b. At least three out of both the five values preceding and the five values following the missing value are present.

If these criteria are not met, the filter is reinitialized at the end of the gap containing the missing value. Reinitialization uses the smoothed value just preceding the missing data points. If more than 10% of the data is not present, the run will not be processed.

### 3. EAIR and Phototheodolites

The outlier screening and removal process at NAFEC is performed using the General Automation minicomputers. The tracker tapes are automatically scanned on a record by record basis. The general procedure is outlined below where "i" is the dimension x,y,z for phototheodolites or AZ, EL, range for EAIR, and "j" is the frame pointer from 1 to 30.

- a. Calculate first differences:  $\dot{x}_{1,j} = x_{1,j} - x_{1,j-1}$

- b. Calculate mean and deviation:

$$\mu_{xi} = \frac{\sum \dot{x}_{1,j}}{N} ; \quad \sigma_{xi} = \sqrt{\frac{\sum \dot{x}_{1,j}^2}{N} - (\mu_{xi})^2}$$

- c. Compute test condition for outliers:

$$r_1 = K_{1min} < 3\sigma_{xi} < K_{1max}$$

where  $K_{1min}$  is the smallest accepted value and  $K_{1max}$  is the largest accepted value, per Table IV-1.

TABLE IV-1: OUTLIER TEST CONDITIONS.

System	Dimensions	Ki min	Ki max
Phototheodolite	x	50 feet	100 feet
	y	5 feet	10 feet
	z	5 feet	10 feet
EAIR	AZ	.5°	.1°
	EL	.5°	.15°
	Range	50 feet	100 feet

d. Test each velocity term with test criteria

$$|\dot{x}_{1,j} - \mu_{x1}| > \tau_1$$

if any values fail this test, the entire buffer is displayed on the CRT for operator intervention.

When a record is displayed, the operator has the following

choices to modify the data:

- Average the preceding and following data points and replace the outlier with this value.
- Insert a new value for the outliers.
- Modify the outlier by the preceding but add an entered velocity.
- Do nothing to the point - this is normally used when there is very noisy data that cannot be corrected.

During this outlier processing, occasional timing errors are detected, commonly a zero time or some type of bit error. The software system checks that time is incrementing by 0.1 seconds between samples and permits the operator to modify a single time in the record. When there are actually

missing time samples, the entire record is either deleted or written in its erroneous form as there is no mechanism for creating new records on the tape. Any gaps in time are later interpolated.

#### B. Filtering

1. FPS-16 Radar, EAIR and Phototheodolites (Real-Time Data only)

The filter used for smoothing the radar data and the real time phototheodolite data was provided by the Wallops Station Data Processing Facility. The Wallops filter is a nonrecursive digital filter having a nonrealizable form, i.e., it uses future input values to compute the present output. The filter is normally called a Martin-Graham filter and was first described in 1957. The filter is defined by three parameters

- (1) the cutoff frequency ( $r_c$ )
- (2) the transition bandwidth ( $2h$ ) and
- (3) the number of terms ( $2N+1$ ).

Figure IV-1 illustrates the parameters in relation to the desired frequency response of the filter. Interpreting this, the frequency response should be flat up to the cutoff frequency. In the transition band, a sine wave roll-off characteristic is desired and in the stop band, the response should be zero. This filter minimizes the mean square error between the spec and its frequency response.

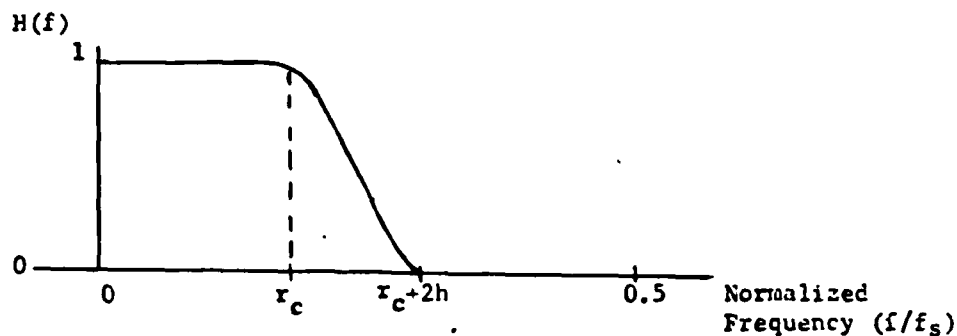


Figure IV-1: Wallops Filter Specification.

Table IV-2 summarizes the characteristics of the two specific filters used based on a 10 Hz sampling frequency. The 41-point filter was used to smooth all radar parameters and the "y" and "x" parameters of the phototheodolites. The 9-point filter was used to smooth the "z" parameter of the phototheodolite in order to reduce potential filter error during the touchdown phase of a test. It was anticipated that higher "z" rates would be experienced at this time.

TABLE IV-2: CHARACTERISTICS OF FILTERS.

Filter	Design Parameters			Cutoff* Freq. (Hz)	Rise Time (Sec) **	Variance Reduction	Error at Touchdown***
	$r_c$	h	N				
9-point	0.0	.09	4	0.652	0.55	.1355	0.08h
41-point	0.0	.02	20	0.135	2.43	.0301	0.38h

\*Half-power

\*\*10-90%

\*\*\*based on no-flare  
(ramp response)

The interpretation of the variance reduction ratio is: if the input noise to the filter has a standard deviation of 10 feet, the output noise will have a standard deviation of 3.7 feet (9-point) or 1.7 feet (41-point). The interpretation of the error at touchdown is: if the sink rate (h) is 10 ft/sec, the error at touchdown in the filter output is 3.8 feet.

Following are the details of the analysis including definitions and derivations of the performance measures and all results.

a. Transfer Function

The transfer function of  $2N+1$  tap, nonrecursive filter is:

$$H(z) = \sum_{i=-N}^N b_i z^i$$

where  $z = \exp(j2\pi f/f_s)$  is the z-transform delay variable,  $f$  is frequency and  $f_s$  is the sampling frequency. Since the Wallops filter has symmetric coefficients ( $b_i = b_{-i}$ ), the transfer function can be written as:

$$H(z) = b_0 + 2 \sum_{i=1}^N b_i \cos 2\pi i f/f_s$$

where:

$$b_i = h_i + \frac{\Delta}{2N+1}$$

$$\Delta = 1 - \sum_{i=-N}^N h_i$$

$$h_i = \left( \frac{\cos 2\pi i h}{1 - 16i^2 h^2} \right) \left( \frac{\sin 2\pi i (r_c + h)}{\pi i} \right)$$

and  $h$  is one-half the normalized transition bandwidth and  $r_c$  is the normalized cutoff frequency. Substituting and simplifying gives:

$$H(z) = h_0 + 2 \sum_{i=1}^N h_i \cos 2\pi i f/f_s + \left( \frac{\Delta}{2N+1} \right) \left( \frac{\sin(2N+1)\pi f/f_s}{\sin \pi f/f_s} \right)$$

Figure IV-2 shows the magnitude squared as a function of normalized frequency ( $f/f_s$ ) for a filter with the parameters:

$$r_c = 0.0$$

$$h = 0.09$$

$$N = 4$$

This is the 9-point filter used at NAFEC. Figure IV-3 is for a filter with the parameters:

$$r_c = 0.0$$

$$h = 0.02$$

$$N = 20$$

This is the 41-point filter.

#### b. Variance Reduction Ratio

If the noise input to the filter is flat over the Nyquist interval  $(0, f_s)$  having a value  $N_0$ , a variance reduction ratio for the filter can be defined as :

$$V = \frac{1}{f_s} \int_0^{f_s} |H(z)|^2 df$$

where  $H(z)$  is the transfer function of the filter. Then the variance of the input is :

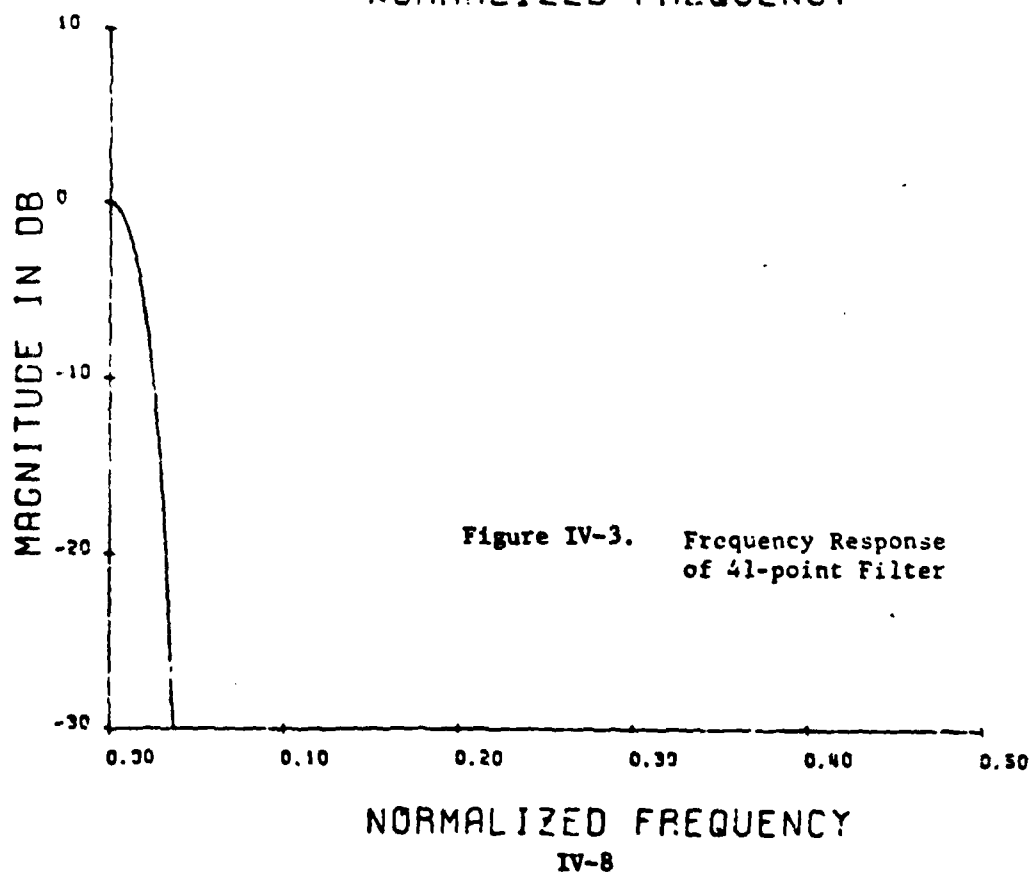
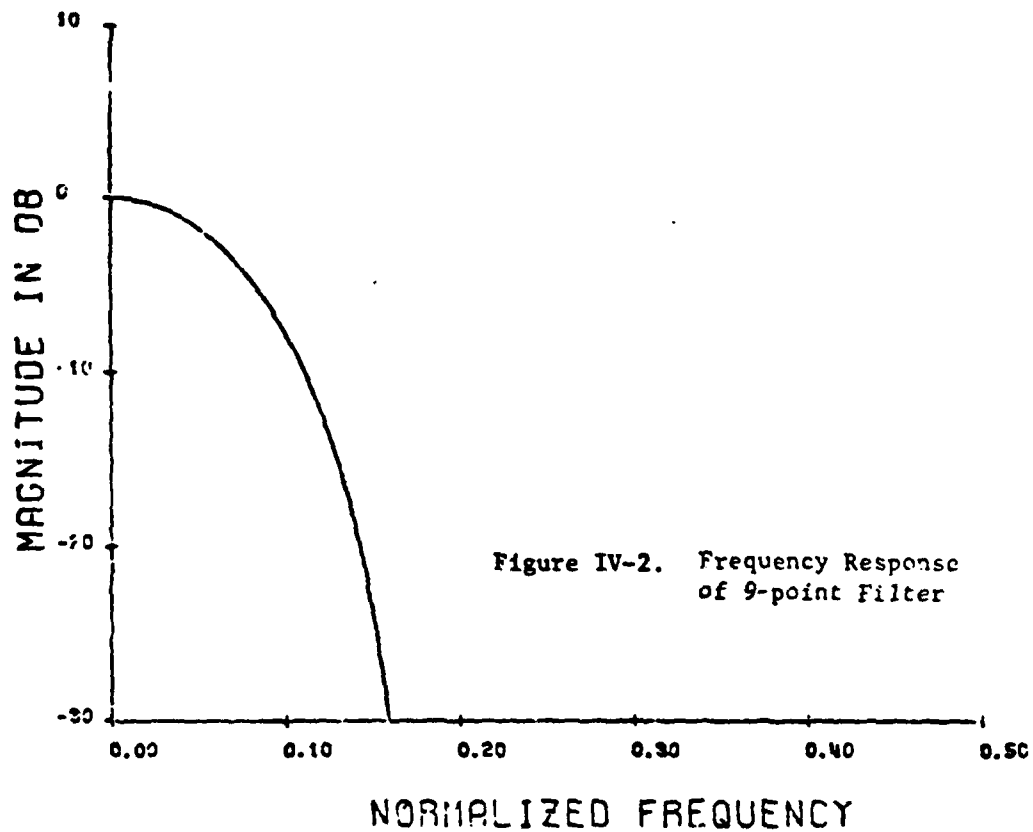
$$\sigma_x^2 = N_0 f_s$$

and the variance of the output is:

$$\sigma_y^2 = V \sigma_x^2$$

For a nonrecursive filter, it is easy to show that the variance reduction ratio is:





$$V = \sum_{i=-N}^N b_i^2$$

For the filters of interest this computes to values indicated in Table IV-3.

TABLE IV-3: FILTER VARIANCE REDUCTION RATIO.

Filter	V	V(dB)	$\sqrt{V}$
9-point	.1355	-8.68	.3681
41-point	.0301	-15.22	.1735

### c. Step Response

The difference equation for the Wallops filter is:

$$y(k) = \sum_{i=-N}^N b_i x(k+i)$$

where  $y(k)$  is the output at time step  $k$  and  $x(k)$  is the input.

The initialization scheme for the filter consists of an expanding symmetric window with adjustment for unity gain. The difference equation during initialization is:

$$y(k) = \frac{\sum_{i=-k}^k b_i x(k+i)}{\sum_{i=-k}^k b_i}, k \leq N$$

Notice that two types of transient response can be defined. The first is when the step occurs and the filter is not initialized and the second when the filter is already initialized when the step occurs.

For a step at time zero,  $x(k) = 1$ , the filter output is always one, i.e.,

$$y(k) = x(k) = 1$$

Essentially, this means there is little smoothing during the initialization.

Figure IV-4 shows the response of the 41-point Wallops filter to a step after initialization. Since the filter uses future values for smoothing, the precursor (anticipation) of the step occurs. Figure IV-5 shows the same response for the 9-point Wallops filter.

#### d. Ramp Response

The same equations apply from the previous section. For the case when the ramp occurs and the filter is not initialized, the output is:

$$y(k) = \frac{\sum_{i=-k}^k b_i (k+1)}{\sum_{i=-k}^k b_i}$$

and since  $b_i = b_{-i}$ ,

$$y(k) = k.$$

During initialization, the Wallops filter responds exactly to a ramp.

Figure IV-6 shows the response of the 41-point Wallops filter to a ramp input after initialization. There is no steady-state lag error. Also shown in Figure IV-6 is the response of the filter when the ramp is limited. This corresponds to something like touchdown. Figure IV-7 shows the same response for the 9-point Wallops filter.

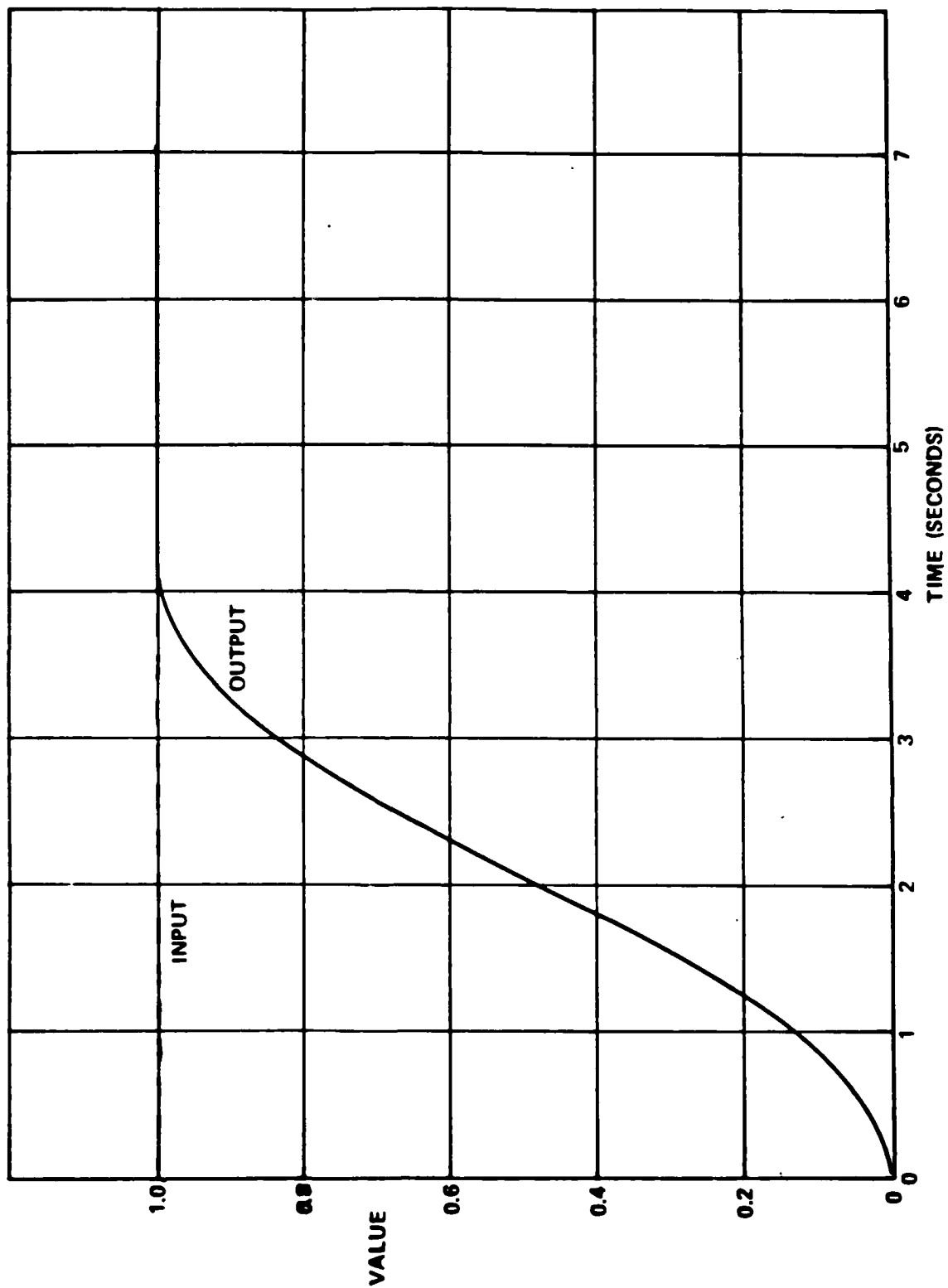


Figure IV-4: Step Response For 41-Point Wallops Filter ( $r_c = 0.0$ ,  $h = 0.02$ ,  $N = 20$ ).

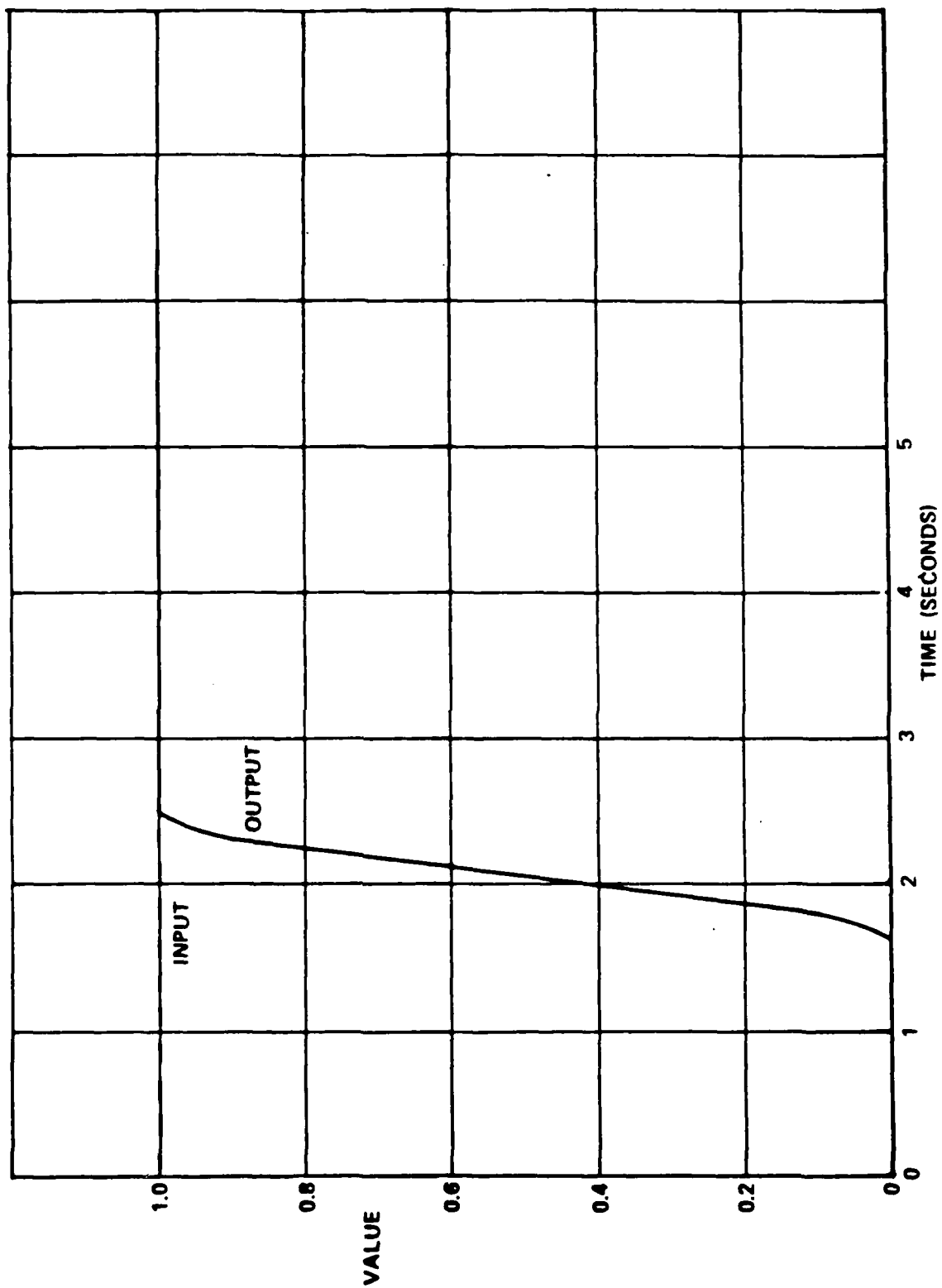


Figure IV-5: Step Response For 9-Point Wallops Filter ( $r_c = 0.0$ ,  $h = 0.09$ ,  $N = 4$ ).

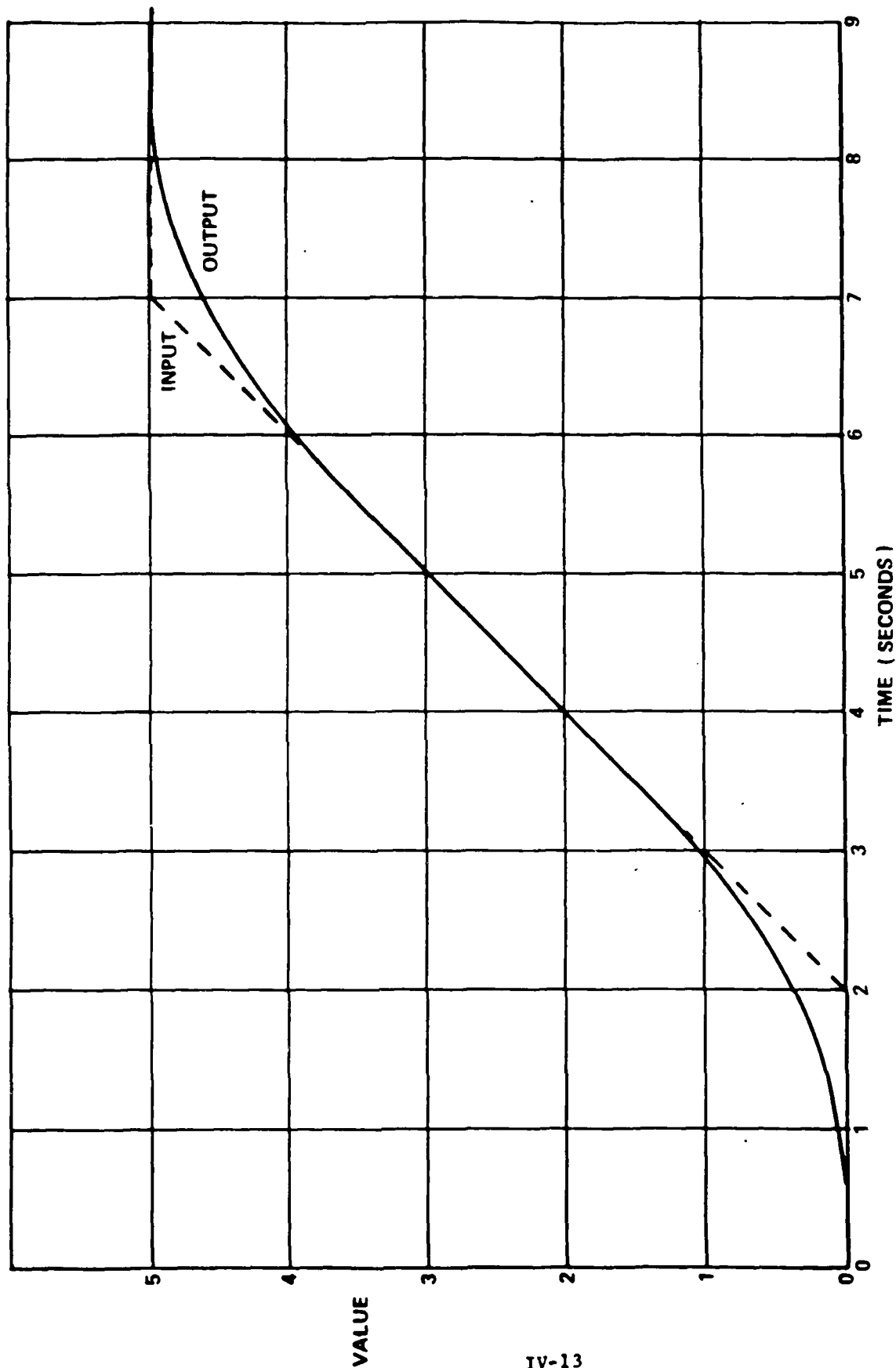


Figure IV-6: Ramp Response For 41-Point Wallops Filter ( $r_c = 0.0$ ,  $h = 0.02$ ,  $N = 20$ ).

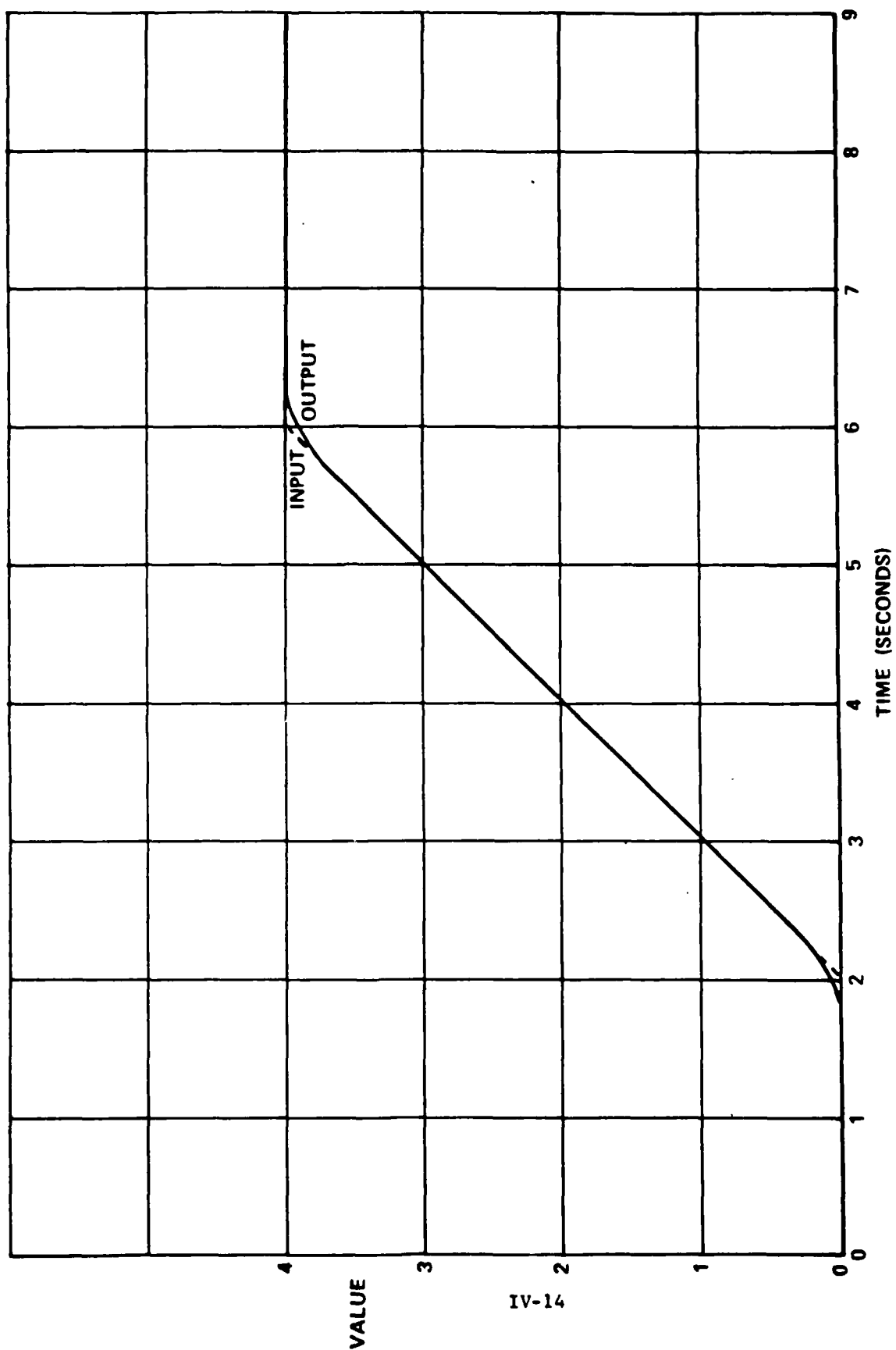


Figure IV-7: Ramp Response For 9-Point Wallops Filter ( $r_c = 0.0$ ,  $h = 0.09$ ,  $N = 4$ ).

## 2. Phototheodolite (Film Corrected) and Photogrammetry

A second-order Butterworth filter was selected to smooth the phototheodolite (film corrected) and photogrammetric data. This film was selected because of its gain linearity in the bandpass region, its high noise rejection capability and its ease of implementation. The cutoff frequency (-3db point) is set at 0.5 Hz. A plot of gain versus frequency is shown in Figure IV-8. The time delay correction for the filter is 0.45 seconds. Figure IV-9 is a plot of filtered versus unfiltered "z" values. The "z" axis is changing rapidly and is therefore sensitive to timing errors.

This transfer function for the digitized Butterworth filter

is:

$$y(z) = \frac{b_0 [z^{-2} + 2z^{-1} + 1]}{a_2 z^{-2} + a_1 z^{-1} + a_0}$$

where:

$$b_0 = \pi^2 f_c^2$$

$$a_0 = \pi^2 f_c^2 + \pi\sqrt{2} f_c + 1, \pi = 3.1416$$

$$a_1 = 2\pi^2 f_c^2 - 2$$

$$a_2 = \pi^2 f_c^2 - \pi\sqrt{2} f_c + 1$$

and

$$f_c = \text{prewarped normalized cutoff frequency.}$$

$$= \frac{1}{\pi} \tan\left(\frac{\pi f_c}{f_s}\right)$$

where:

$$f_c = \text{cutoff frequency}$$

$$f_s = \text{sampling frequency-}$$



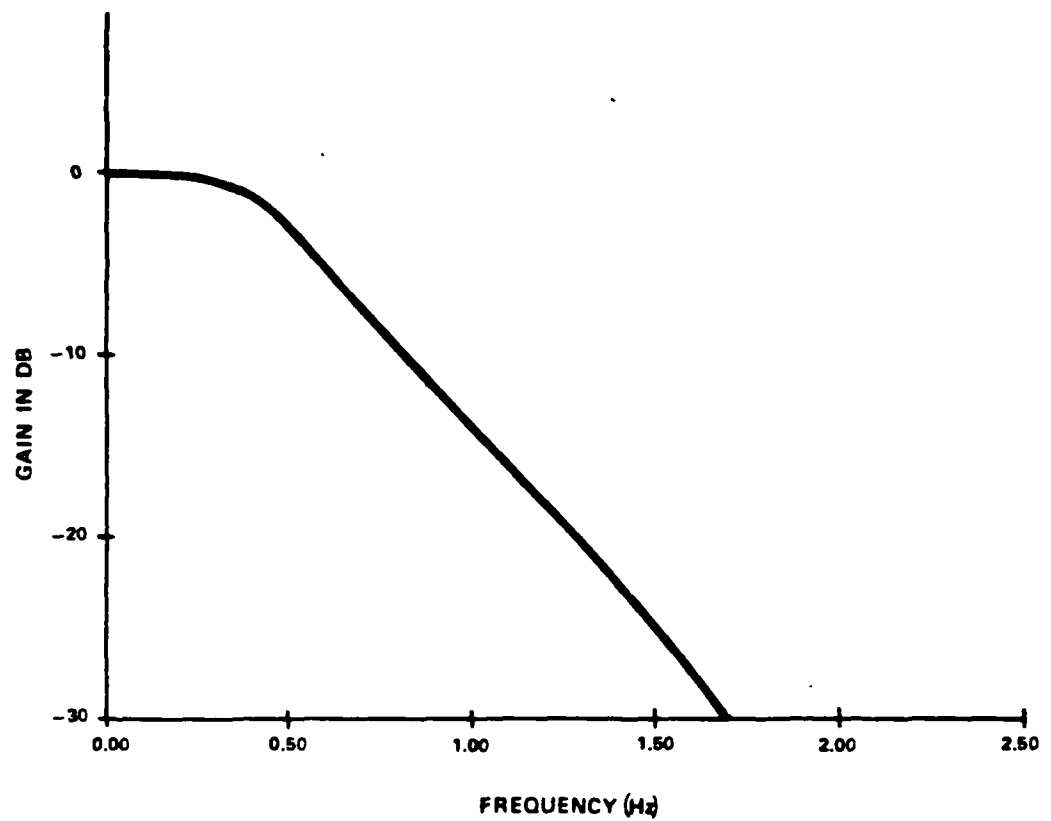


Figure IV-8: Butterworth Filter Gain vs. Frequency.

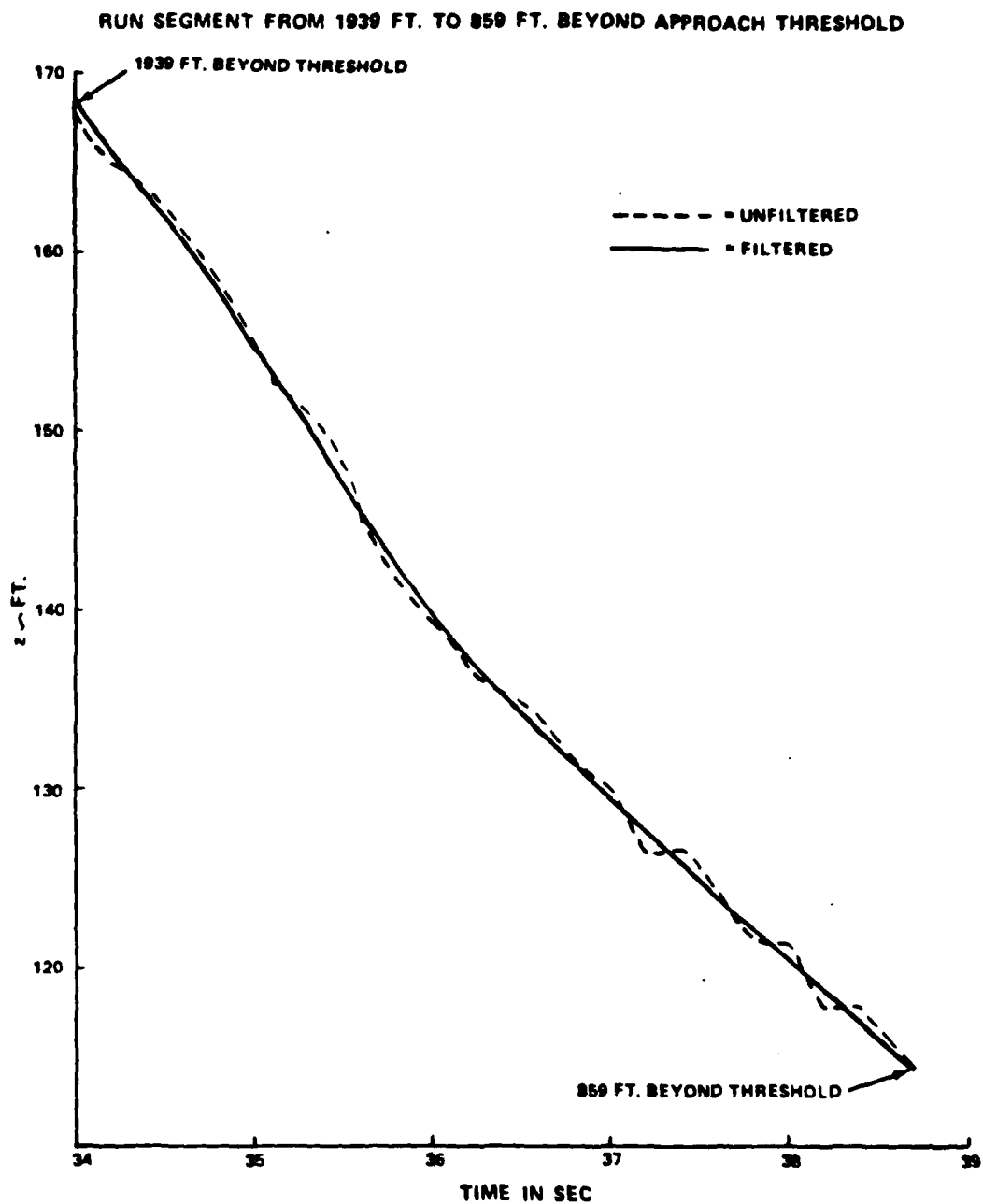


Figure IV-9: Comparison of Unfiltered and Butterworth-Filtered "Z" Values.

The filter is implemented in the following manner:

Let  $\{\alpha_i, i=1, \dots, k\}$  be a set of time dependent data such that  $\alpha_j$  is the value associated with the  $j$ th time; then a set  $\{\beta_i, i=1, \dots, k\}$  of smoothed values is generated by:

$$\beta_n = \frac{b_0}{a_0} [\alpha_{n-2} + 2\alpha_{n-1} + \alpha_n] - \frac{a_1}{a_0} \beta_{n-1} - \frac{a_2}{a_1} \beta_{n-2}$$

where:

$$\alpha_0, \alpha_{-1}, \beta_0, \beta_{-1} = \alpha_1$$

and reinitialization at  $\alpha_n$  uses the value  $\alpha_{n-1}$  for  $\beta_{n-2}, \beta_{n-1}, \alpha_{n-2}$ , and  $\alpha_{n-1}$ .

The noise rejection capability of the implemented filter was verified in the following manner. A random number generator was used to produce input noise with a specified standard deviation and at the system rate of 5 samples per second. The noise was processed through the filter and the output standard deviation calculated. The output noise standard deviation was 0.27 times the input standard deviation.

### 3. Filter Cutoff Frequency

The cutoff frequencies for the tracking filters should be above the region of aircraft motion. This is necessary since the MLS functions are unfiltered and aircraft motion removed from the tracking functions would appear to be MLS error. Evaluation of the aircraft control systems by the MLS contractors showed that no control system motion would be present above 1 radian/sec (or 0.15 Hz). However, motion of the aircraft due to turbulent air during the testing program was not defined. As a result a special study was undertaken to determine if the tracking filters could have removed any significant amount of aircraft motion.

The approach selected was as follows:

- (1) Identify test day or days with the most turbulent air conditions.
- (2) Process unfiltered MLS functions (AZ and EL) through PSD program.
- (3) Determine the highest significant frequencies present in the signals.

March 21, 1974 was identified as the roughest flight day at Wallops. The Hazeltine "E" system was performing accuracy runs on this day.

The MLS azimuth and elevation signals were processed through an FFT spectral analysis program at Vitro. The initial runs were conducted on the EL signal with the mean level removed and all frequencies up to the Nyquist frequency (5 Hz) computed. Approximately 200 seconds of data was used, (from 10 nmi to run termination). Figure IV-10 shows the results of this run. A second run was conducted on the same data set but with the data detrended and filtered (-3 db at 3 Hz) to ensure that no foldover was occurring from frequencies above 5 Hz. The results are presented in Figure IV-11. The azimuth and elevation data sets were then reprocessed with the upperbound set at 1 Hz and the mean level removed, data detrended, and filtered at 3 Hz. The results are presented in Figures IV-12 and IV-13. As can be observed from these two figures no significant frequencies are present above 0.1 Hz. The basic conclusion from this study is that the tracker filters have not removed any aircraft motion of significance.

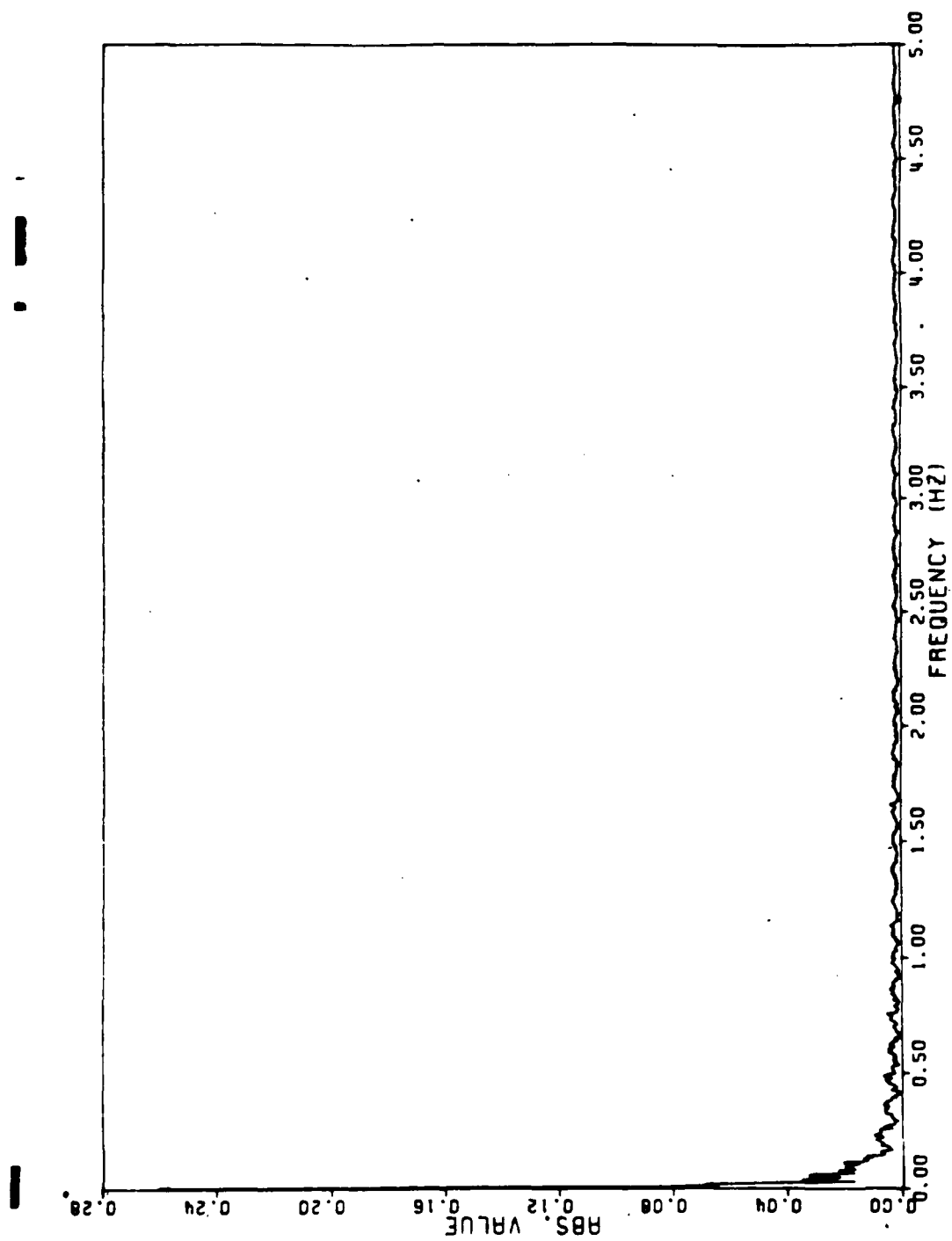
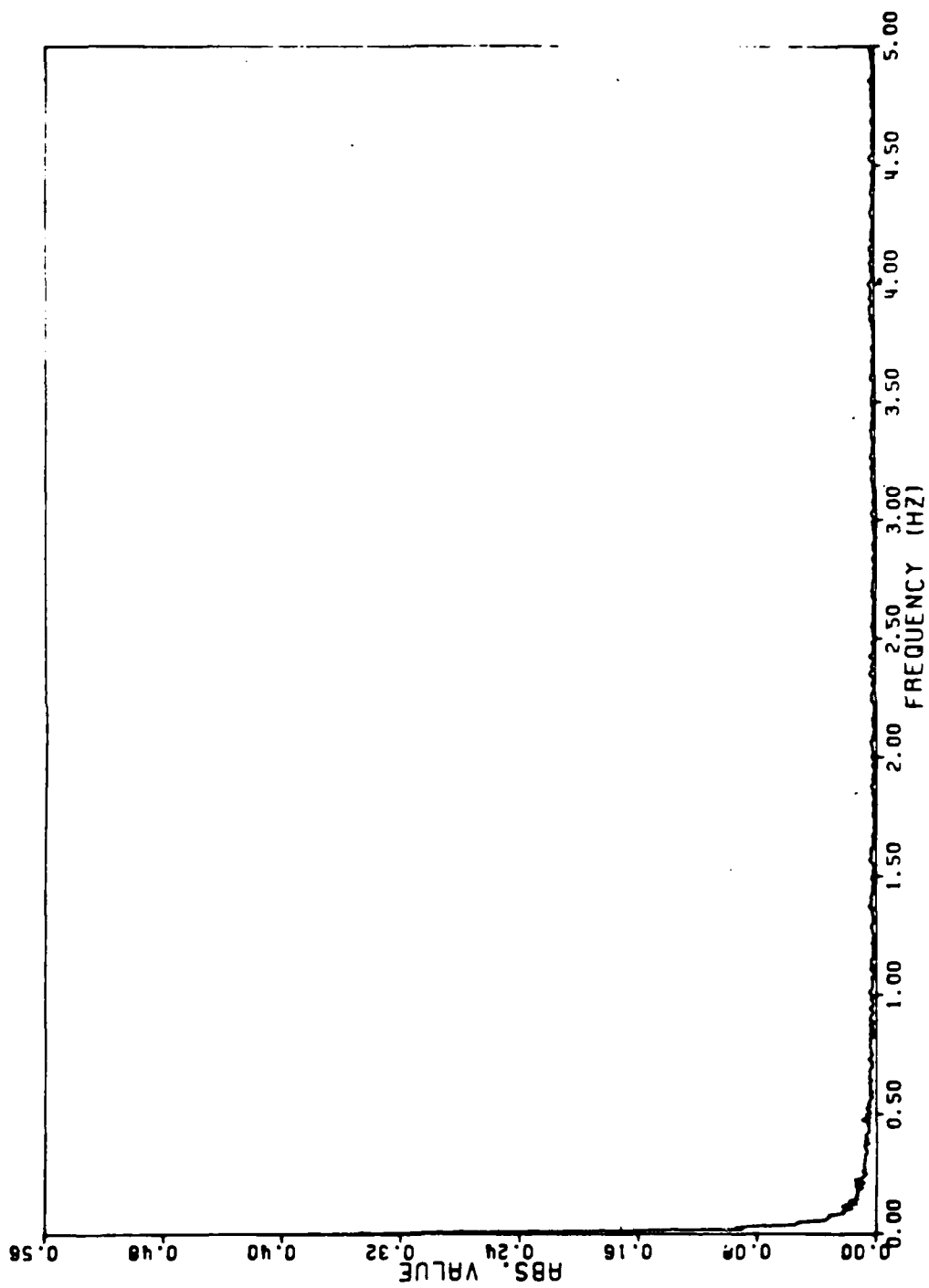


Figure IV-10: EL - Mean Removed, Detrended and Filtered.



IV-21

Figure IV-11: EL (Mean Removed but no Filter).

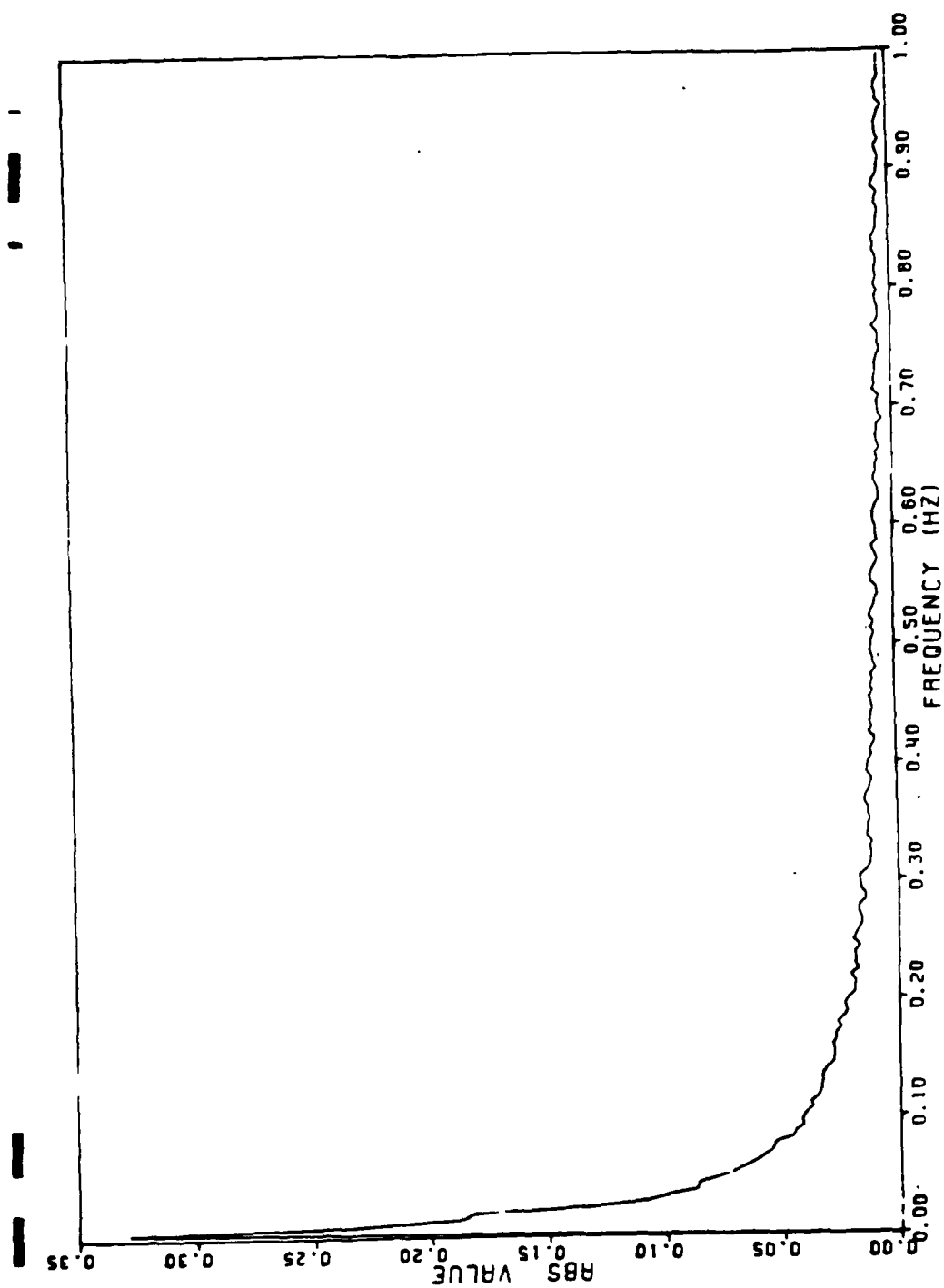


Figure IV-12: AZ - Detrended, Filtered.

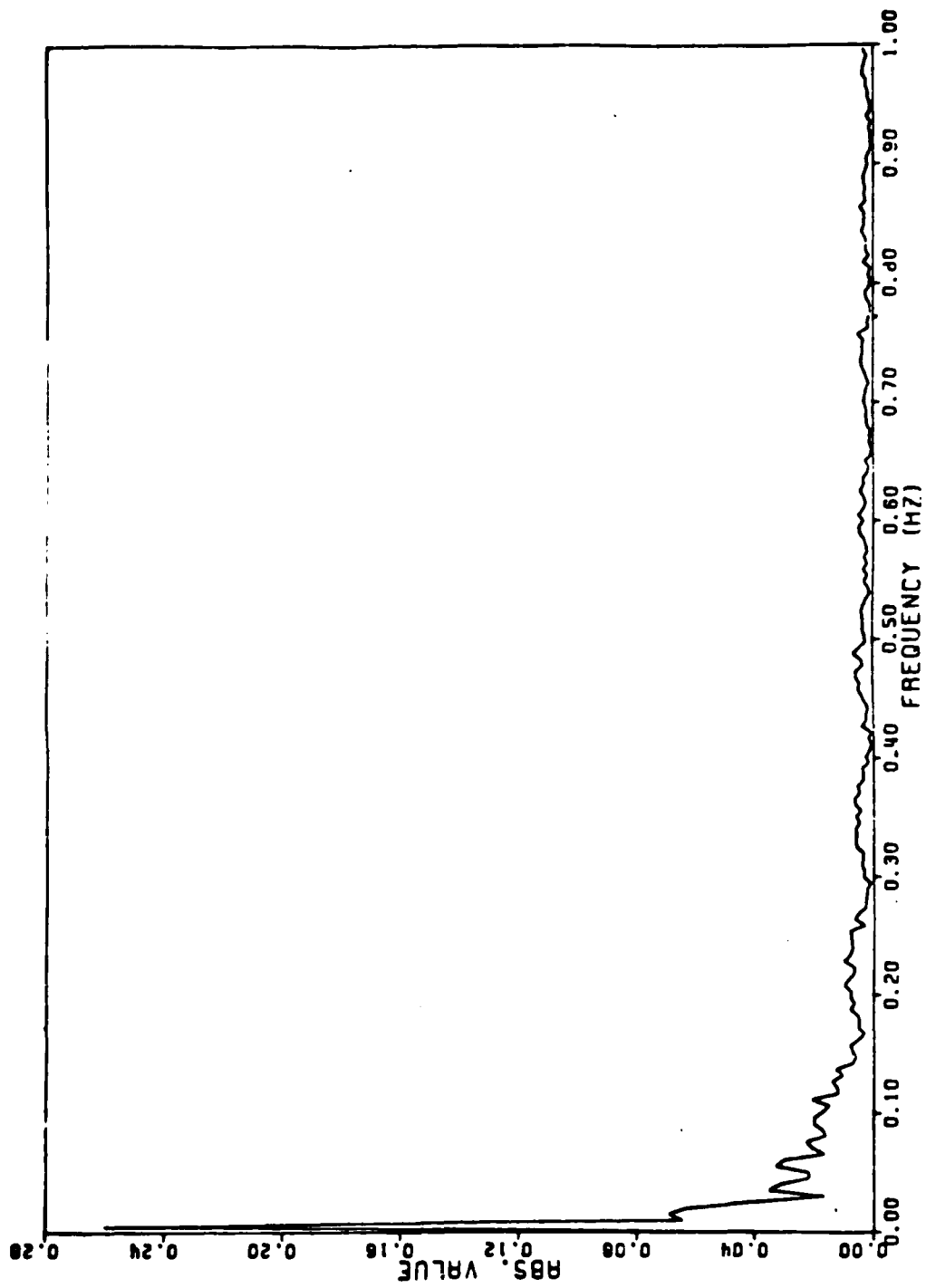


Figure IV-13: EL, - Detrended, Filtered and  
Mean Removed.



### C. Data Merge Process

After the tracker data has had all outliers removed and has been filtered, the data is merged with the MLS airborne tape and the differences calculated. The functional steps in the merged process are shown in Figure IV-14. The computational requirements for the merge process which affect accuracy are listed in Table IV-4.

TABLE IV-4: DATA MERGE FUNCTIONS AND RESOLUTIONS

Function	Resolution
x, y and z	0.1 foot
Computed AZ and EL	0.005 degree
Computed Slant Range	1.0 foot
Slant Range	1.0 foot (second)
Computation Time	$\pm$ 0.001 Second

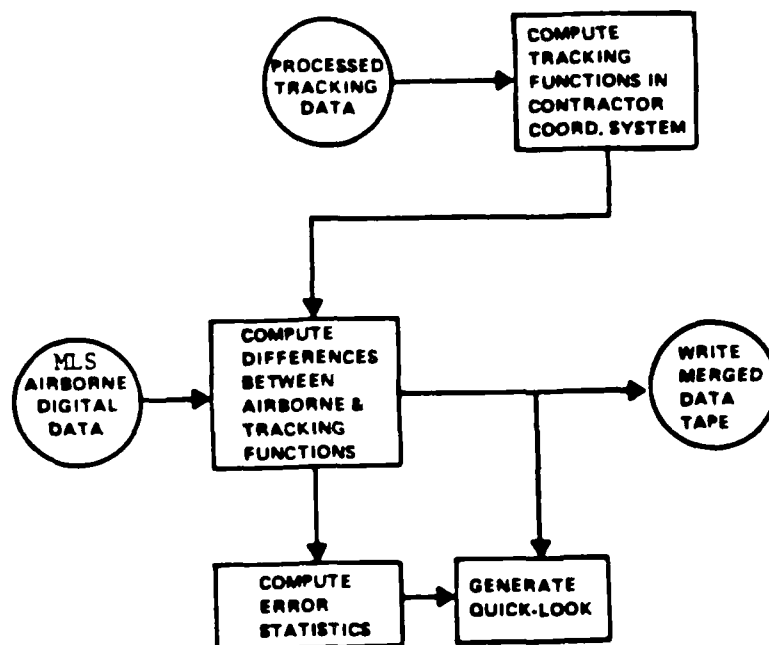


Figure IV-14: Data Merge Process.

## V. TRACKER MLS PHASE II DATA STUDIES

### A. EAIR Versus Phototheodolites

#### 1. Range Evaluation

When the initial MLS test data was evaluated, it quickly became apparent that there existed very large bias and low frequency differences between EAIR and Phototheodolite position data. Any bias or low frequency differences between systems would not show up in the variance-covariance matrix solution employed during the Princeton Study (see Section II.B.1). At this point, a set of statistics was computed for the raw differences between EAIR and phototheodolite. A sample of this type of data is shown in Table V-1. It can be noted that not only is the range bias much larger than the standard deviation, but that there is a variation of range error with distance from the EAIR location. The distance partitions are measured with respect to the ITT/Gilfillan azimuth site with range, AZ, and EL referenced to the EAIR location. Distance partitions were set at 3000 feet each, with each sample containing 150 data points. There is some overlapping of this data, i.e., the same piece of data may be included in two distance partitions, but it is felt that this technique only affects the overall computation for the run, and the constant sample size permits a more realistic look at the variation of the standard deviation. Data

TABLE V-1: EAIR AND PHOTOTHEODOLITE RAW DIFFERENCES.

Run No. (all on 9/27/73)	Distance Partition- SMLS (Feet)		Range Difference (Feet)		Azimuth Difference (Milliradians)		Elevation Differences (Milliradians)	
	Start	Stop	Mean	1 $\sigma$	Mean	1 $\sigma$	Mean	1 $\sigma$
3	24990.	21994.	102.45	23.02	0.24	0.42	-0.51	0.18
	21994.	19117.	136.97	24.41	0.43	0.77	-0.58	0.24
	18987.	15857.	128.18	21.27	0.90	1.03	-0.68	0.42
	15989.	12816.	87.20	10.11	1.77	1.20	-0.77	0.70
	12995.	9887.	124.55	21.18	3.03	1.97	1.79	4.39
4	33994.	30584.	135.15	20.33	0.02	0.48	-0.44	0.26
	30999.	27561.	101.12	24.61	0.18	0.34	-0.37	0.14
	27988.	24680.	144.65	19.89	0.23	0.41	-0.37	0.21
	24988.	21380.	114.37	16.28	0.18	0.51	-0.47	0.24
	21983.	18102.	147.76	21.28	0.45	0.61	-0.60	0.20
	19018.	15879.	130.14	33.79	1.56	7.96	-0.62	0.42
	15986.	12364.	91.22	9.19	2.35	1.73	-0.95	0.54
	12981.	9684.	121.91	19.28	3.48	3.38	2.49	4.59
5	36983.	33609.	88.77	21.00	0.03	0.45	-0.39	0.20
	33981.	30716.	123.91	28.48	-0.07	0.35	-0.38	0.13
	30985.	27812.	94.80	22.06	0.16	0.38	-0.45	0.16
	27995.	24948.	138.69	16.39	0.32	0.40	-0.41	0.15
	24993.	21914.	115.77	14.83	0.30	0.56	-0.41	0.25
	21989.	18932.	146.27	21.39	0.50	0.82	-0.64	0.23
	18990.	15859.	127.61	23.37	0.86	0.82	-0.56	0.19
	16000.	12894.	86.22	6.33	2.16	0.94	-0.69	0.43
	12999.	9798.	118.42	19.40	2.53	3.00	1.76	4.06

collected for the Princeton Study and later for the ITT/Gilfillan and Bendix flight tests showed basically the same pattern. A series of runs were then plotted to qualitatively and quantitatively determine the extent of the errors on the possibility of removing these errors by mathematical techniques. Figure V-1 is a sample plot of 10 runs from the Princeton Study. Figure V-2 shows 9 Bendix runs from March 23, 1974. It should be noted that although there is a different bias between the two dates shown, both the period of oscillation and the amplitude are very similar. These facts along with similar findings by ITT/Gilfillan in slant range error showed the oscillation to be both repeatable and predictable enough to remove with post-processing techniques.

A study of the EAIR system isolated this problem to the ranging servo system in which the phase shifter is driven to a null. Since there is no adjustment for this mechanism, it was decided to post-process all EAIR data to remove this error. As this phase shifter is on the 6000-feet-per-resolution shaft, it was assumed that the error equation had the form:

$$E = K_0 + K_1 \sin(X - X_0) 6000$$

where: E is the slant range error

$K_0$  is the constant bias error

$K_1$  is the amplitude of the cyclic error

$X_0$  is the phase of the cyclic error

X is the indicated distance to EAIR

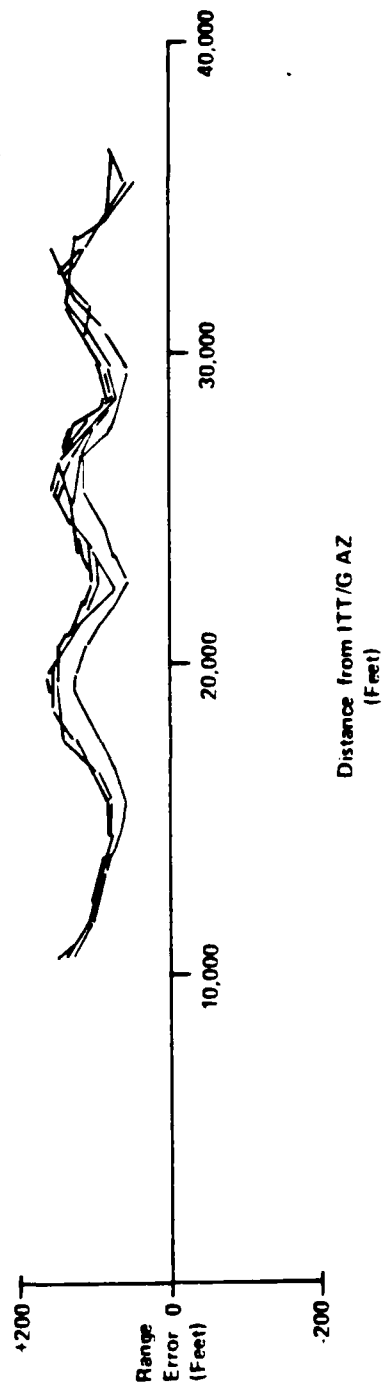


Figure V-1: EAIR Range Error Versus Range, Princeton Flight of 9/27 - 10 Runs.

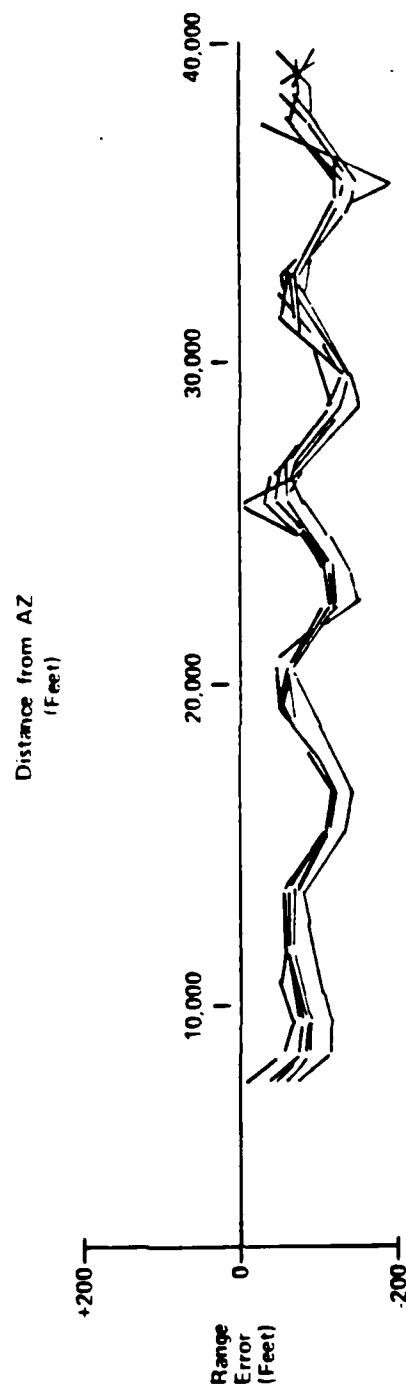


Figure V-2: FAIR Range Error Versus Range, Bendix Flight of 3/25 - 9 Runs.

The values  $K_1$  and  $X_0$  were determined by a "cut and try" procedure which minimized the errors over the region where there was overlapping EIR and phototheodolite coverage. It should be noted that small inaccuracies in these values will not drastically change the data, as would inaccuracies in the period of 6000 feet. The value  $K_0$  must be determined for each day's flight, as this value is readjusted daily in calibrating the ranging system. The day-long variation in the bias was normally less than 30 feet while the day-to-day variation was on the order of 200 to 300 feet. The constants used in this equation are only valid for aircraft approaching the EIR facility. There is considerable backlash in the range servo mechanism, which results in a different phase constant for aircraft moving away from EIR. This change was not mechanized, as there are very few cases when this occurs and these cases are confined to coverage flights where accuracy is not as critical.

## 2. Angle Evaluation

The reference MLS angle values computed from the EIR and the phototheodolites were compared during periods of simultaneous tracking. A total of 10 runs from 9/27/73 and 4 runs from 2/24/74 were used in the evaluation. NAFEC partitioned the data and computed the mean and standard deviation of the difference for each partition. Two partitions, one from 25,000 feet down to 22,000 feet and one from 22,000 feet down to 14,000, were included in the evaluation. This resulted in 2 sample values from each run for a total of 28 samples.



For azimuth the mean of the 28 mean values and the  $2\sigma$  variation of the mean values were calculated. The mean of the data was approximately zero and the  $2\sigma$  variation was  $0.0573^\circ$ . This value represents both the EAIR and the phototheodolite errors. To remove the phototheodolite error, it was assumed that the composite error was represented by an RSS of the two system errors, i.e.,

$$0.0573^\circ = \sqrt{(\text{EAIR error})^2 + (\text{phototheodolite error})^2}$$

thus:

$$0.0573^\circ = \sqrt{(\text{EAIR error})^2 + (0.015^\circ)^2}$$

and

$$\text{EAIR azimuth error } (2\sigma) = 0.055 \text{ degrees}$$

For elevation the mean of the data set was a  $(-)$   $0.0435$  degrees and the  $2\sigma$  variation was  $0.0366$  degrees.

Thus:

$$0.0366^\circ = \sqrt{(\text{EAIR error})^2 + (0.014^\circ)^2}$$

and:

$$\text{EAIR elevation error } (2\sigma) = 0.034 \text{ degrees}$$

about a mean level of  $(-)$   $0.0435$  degrees.

#### B. Phototheodolite Real-Time Versus Phototheodolite Film-Corrected Data

On 9 June 1974, fourteen touch-and-go approaches were made to NAFEC runway 13. During these approaches the aircraft was tracked with three

---

\*Phototheodolite error is calculated in Section II.B.2.

theodolites (P-8, P-29 and P-36). The aircraft spatial position as a function of time was computed in the MLS coordinate system with both the real-time phototheodolite data and the film-corrected phototheodolite data. Both sets of data were processed through the standard (MLS) outlier removal process and both data sets used the three-station phototheodolite solution. No filtering was employed on either data set.

A point-by-point comparison was made at the x, y, and z values computed from the real-time and film-corrected phototheodolite computations. Table V-2 presents the statistical summary of the differences for 11 of the runs. Three of the runs were removed from the statistical summary because of timing errors in the film-corrected data. The manual nature of the film reading process makes it susceptible to this type of error. The combined mean and standard deviation of differences for all runs is also shown at the bottom of Table V-2.

Figure V-3 is a composite of the differences (for all eleven runs) plotted as a function of ground range to the MLS azimuth site. The "x" axis shows a consistent lag of approximately 3.4 feet in real time. The "y" and "z" axes show smaller lags, with a tendency for errors on both sides of zero, particularly in the flare region of the approach.

Figure V-4 shows the differences for run #5 between the real-time phototheodolite data and the film-corrected phototheodolite data as a function of ground range to azimuth. The "y" axis differences demonstrate

TABLE V-2: REAL TIME MINUS FILM READ DIFFERENCES (FEET).

Run *	x	$\sigma_x$	y	$\sigma_y$	z	$\sigma_z$
290	3.38	1.53	.63	1.75	1.28	.97
269	2.93	1.46	1.27	1.45	1.06	.87
217	2.16	1.58	1.60	1.95	.68	.82
242	3.16	2.04	1.70	1.57	1.07	.94
201	3.59	2.20	2.35	2.44	.96	1.10
254	3.14	1.82	1.08	1.68	1.32	.83
245	3.35	1.73	.96	1.31	.89	1.07
224	3.92	2.43	1.47	1.67	1.08	.94
229	3.11	1.66	1.45	1.49	1.28	1.38
221	4.54	2.91	3.81	2.77	1.35	.91
220	4.54	3.92	1.19	3.18	1.27	1.17
2612	3.42	2.29	1.54	2.14	1.12	1.03

\* Average region of runs was from 15,020 feet to 6,902 feet, referenced to A2.

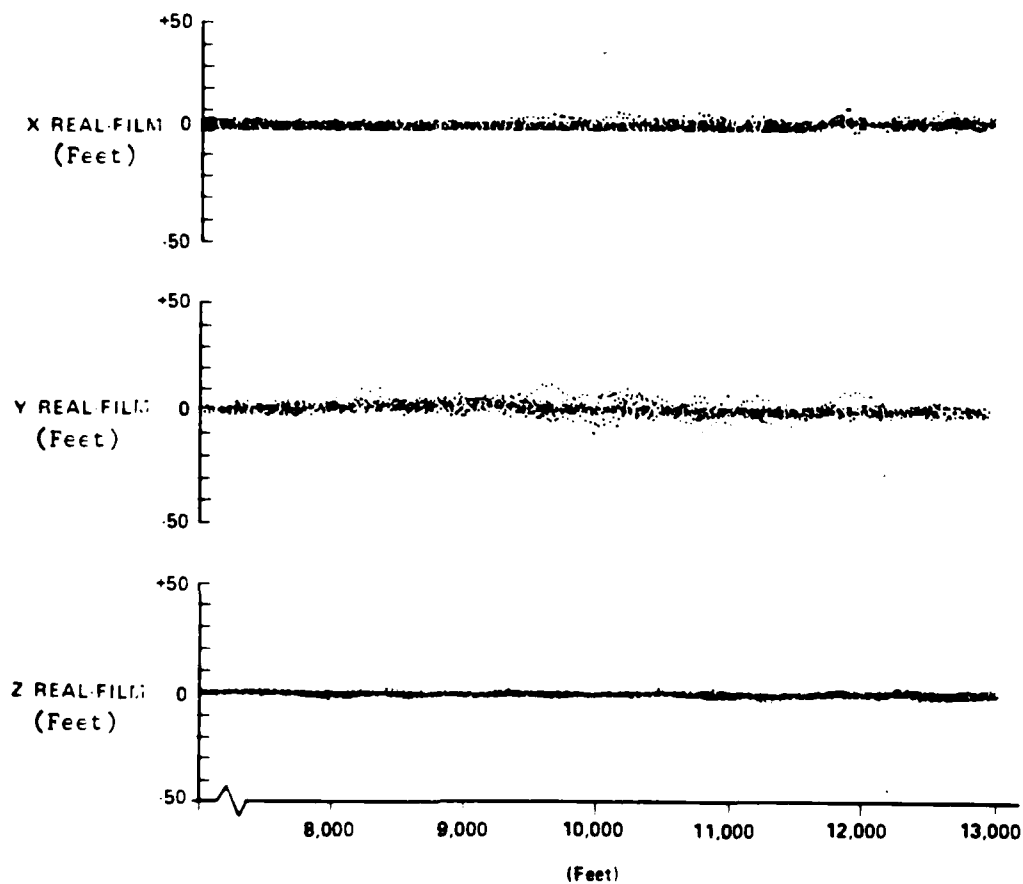


Figure V-3: Composite of Differences (all runs) as a Function of Ground Range.

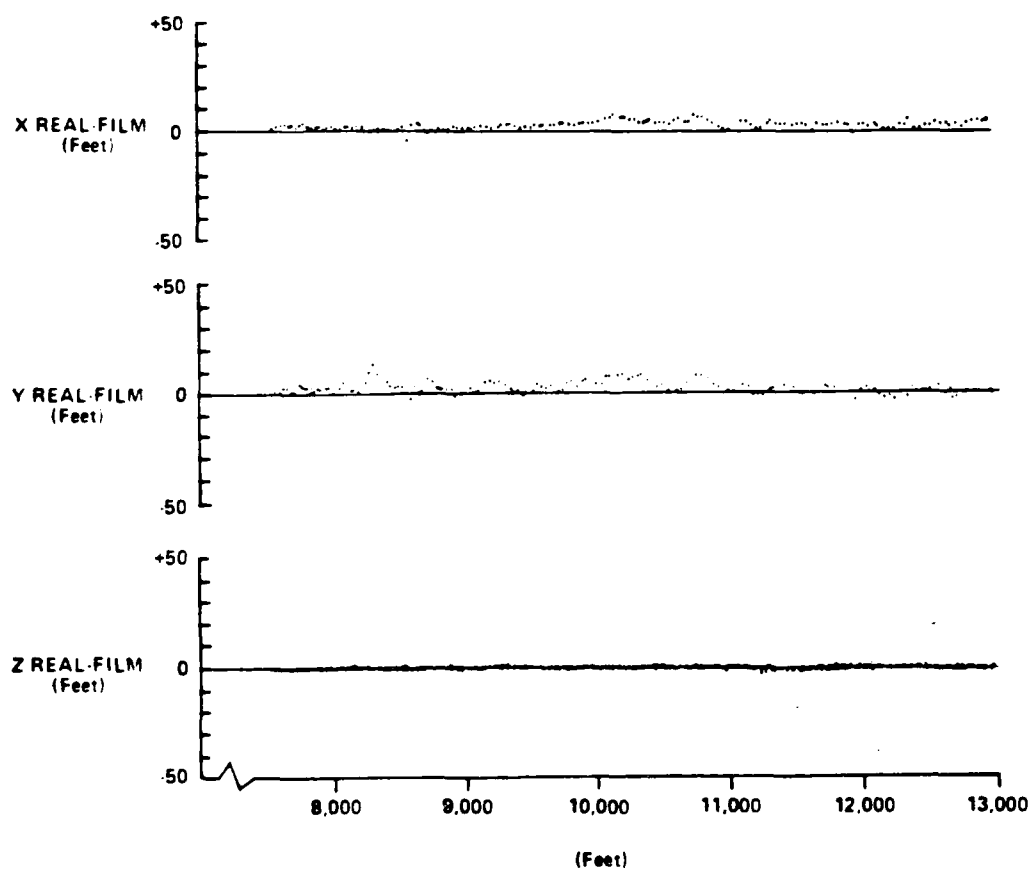


Figure V-4. Differences For Run No. 5 (Real Time Minus Film Corrected) as a Function of Ground Range.

the unpredictable nature of these differences and also the need for film correction for tests that have regions of critical importance, i.e., multipath tests and the flare region of the accuracy tests.

C. FPS-16 Radar Lower Limits of coverage - Runway 22

To the northeast of the FPS-16 Instrumentation Radar there is a considerable number of manmade structures that block the line of sight from the radar to the Texas Instruments glide slope to runway 22, shadowing the incoming aircraft.

In clockwise order there is a 60-foot tracker, an old beacon tower, the radar boresight tower, the 60-foot and 85-foot trackers, and the 30-foot tracker. As the aircraft flies on a normal glide slope it passes through the regions of shadowing, and some angular tracking deviations occur. The most serious one occurs just prior to runway 22 threshold, where the most sizeable blockage of the line of sight occurs. In addition, a ground reflection problem occurs near the intersection of runways 4-22 and 10-28, which results in the radar tracking a reflected image. Figure V-5 shows the areas of blockage on the approach to runway 22.

The jitter in angle is minor for the cases of FPS-16 tracking through the 60-foot tracker, beacon tower, boresight tower and 30-foot tracker but is considerable when tracking through the 60-foot and 85-foot trackers, even losing the target track on occasions. The lost track occurs when the big dish axis is pointing towards the FPS-16, and with continuous but jittery track when the big dish is viewed edgewise from the FPS-16.

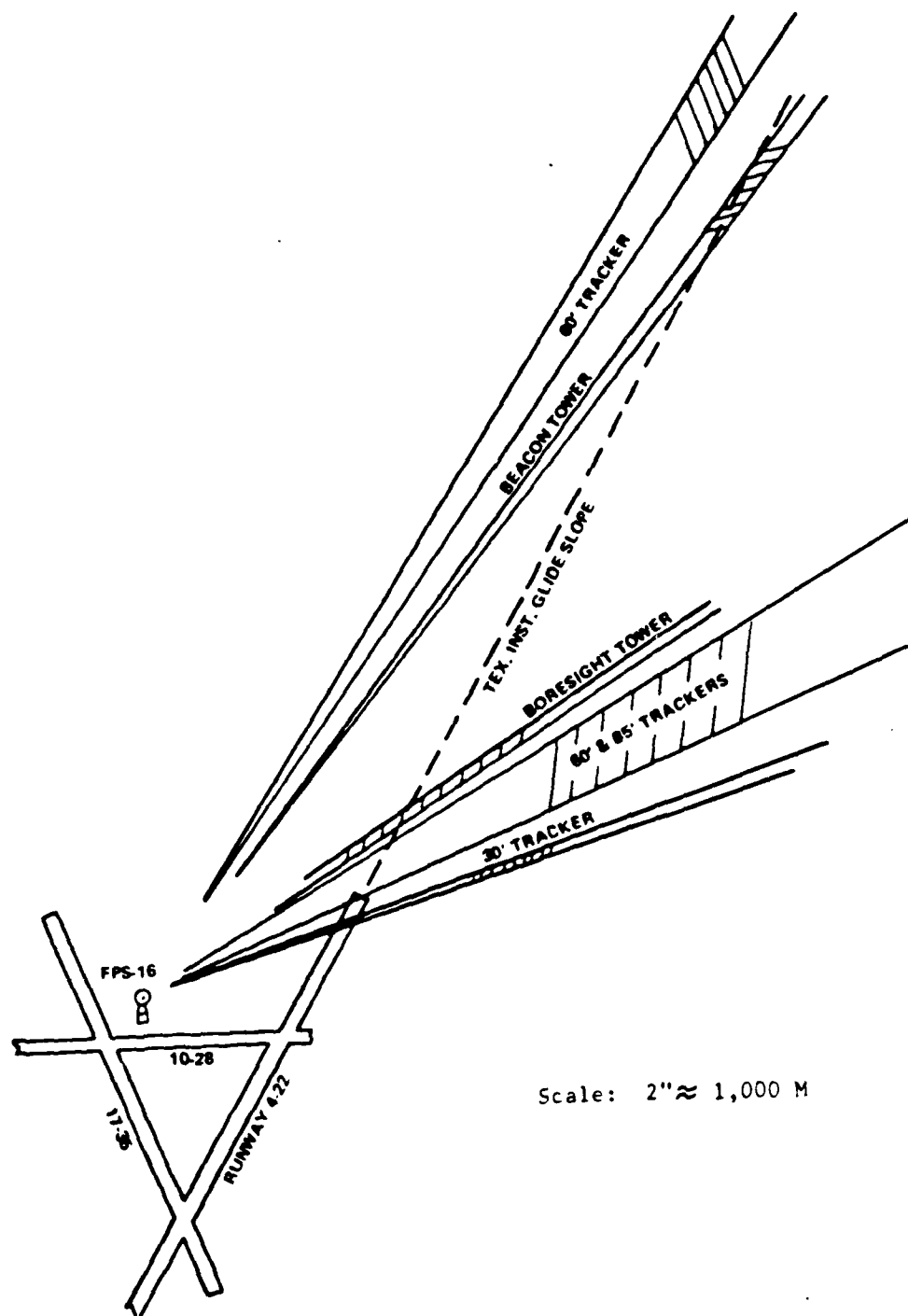


Figure V-5: FPS-16 Blockage on Wallops Station Runway 22 Approach.

The same effect of shadowing occurs off the normal glide slope, when the aircraft turns in toward the runway centerline. There is very little possibility when the approach is from the west, but considerable when approaching from the east (i.e., from seaward or from Chincoteague). In those cases, the effect lasts for longer periods of time, as the blockage is an angular problem, increasing with distance.

These structures are the source of environmental disturbances noted in the Wolfe Study (Section IV.3.1). An evaluation of MLS flight data was conducted in order to define the practical tower limits of coverage for the FRP-16 on runway 22. T.I. "K" system accuracy flights conducted on 1/8/74 were selected for the study. The flights were on a 30° glideslope and a total of six flights were evaluated. The results of the evaluation were as follows:

Azimuth: 1) Erratic and inconsistent results below approximately 12,000 ft. from MLS AZ site. Figure V-6 is a sample error plot.

2) Oscillation in FPS-16 azimuth signal in the region from 19,000 ft. to 24,000 ft. from touchdown. Figure V-7 is a sample error plot.

Elevation: 1) Inconsistent results below approximately 12,000 ft. from MLS AZ site.

2) Major disturbances between 7,000 ft. and 10,000 ft. from AZ. Figure V-8 is sample error plot.

Range (Ref. to DME Site): 1) No major degradations noted.



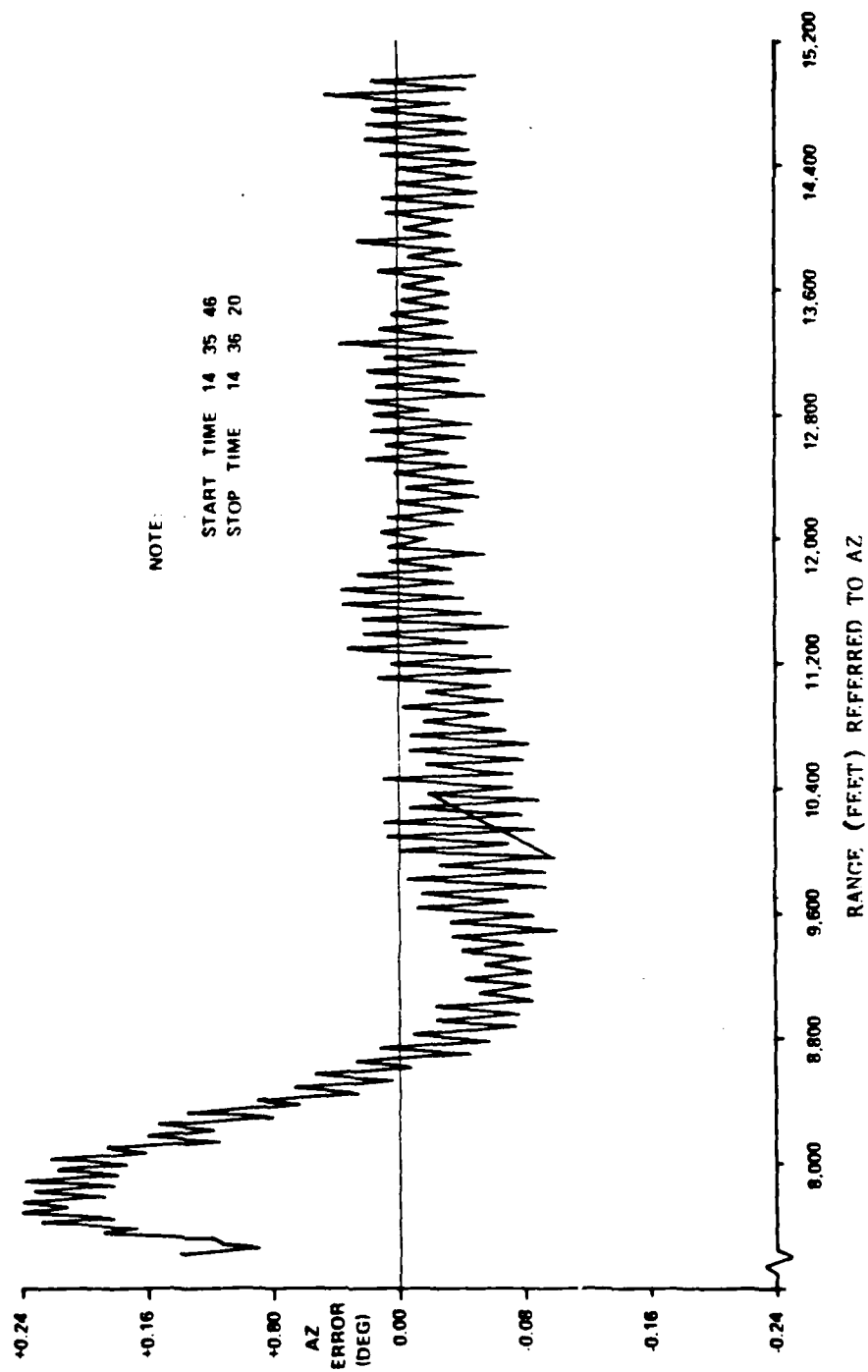


Figure V-6: Azimuth Shadowing.

NOTE:

START TIME 14 17 54  
STOP TIME 14 19 6

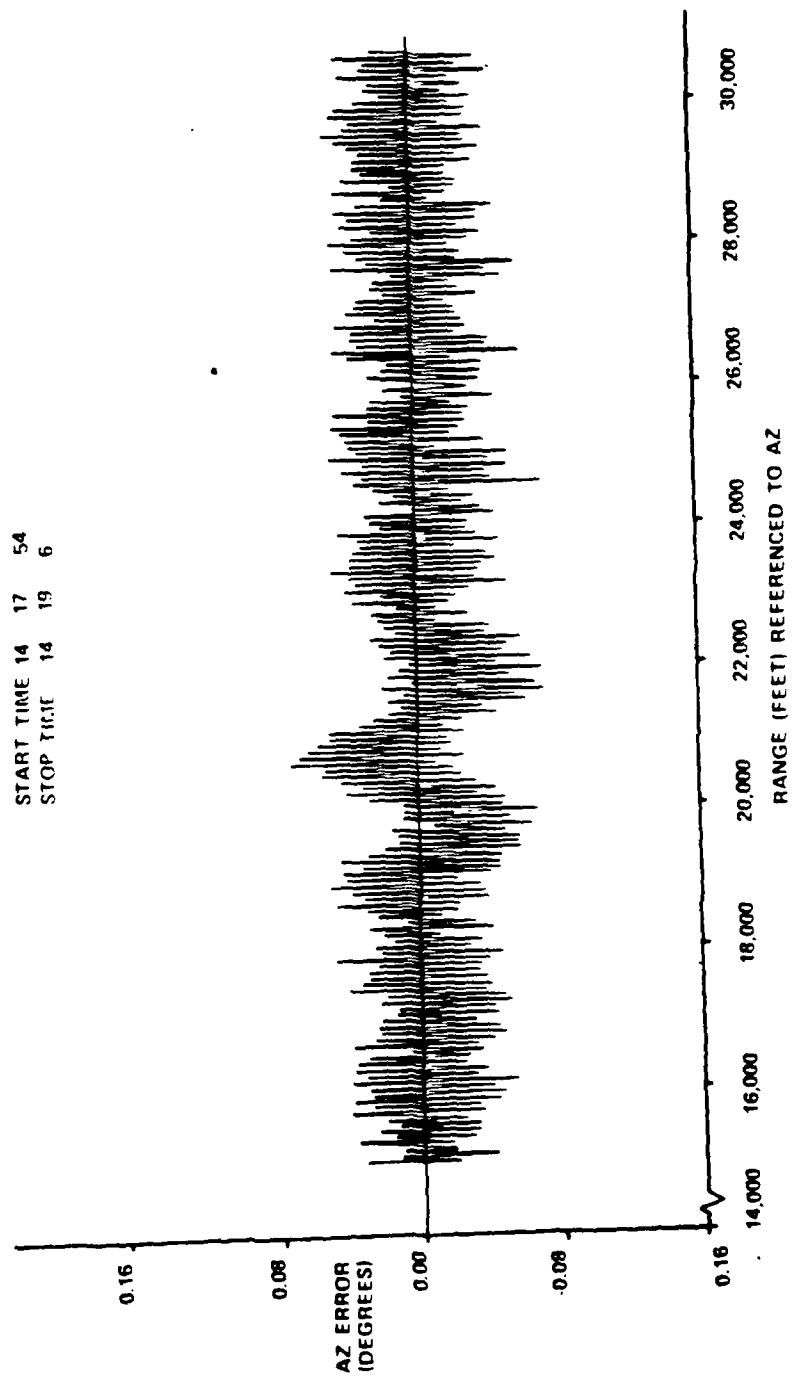


Figure V-7: Azimuth Shadowing.

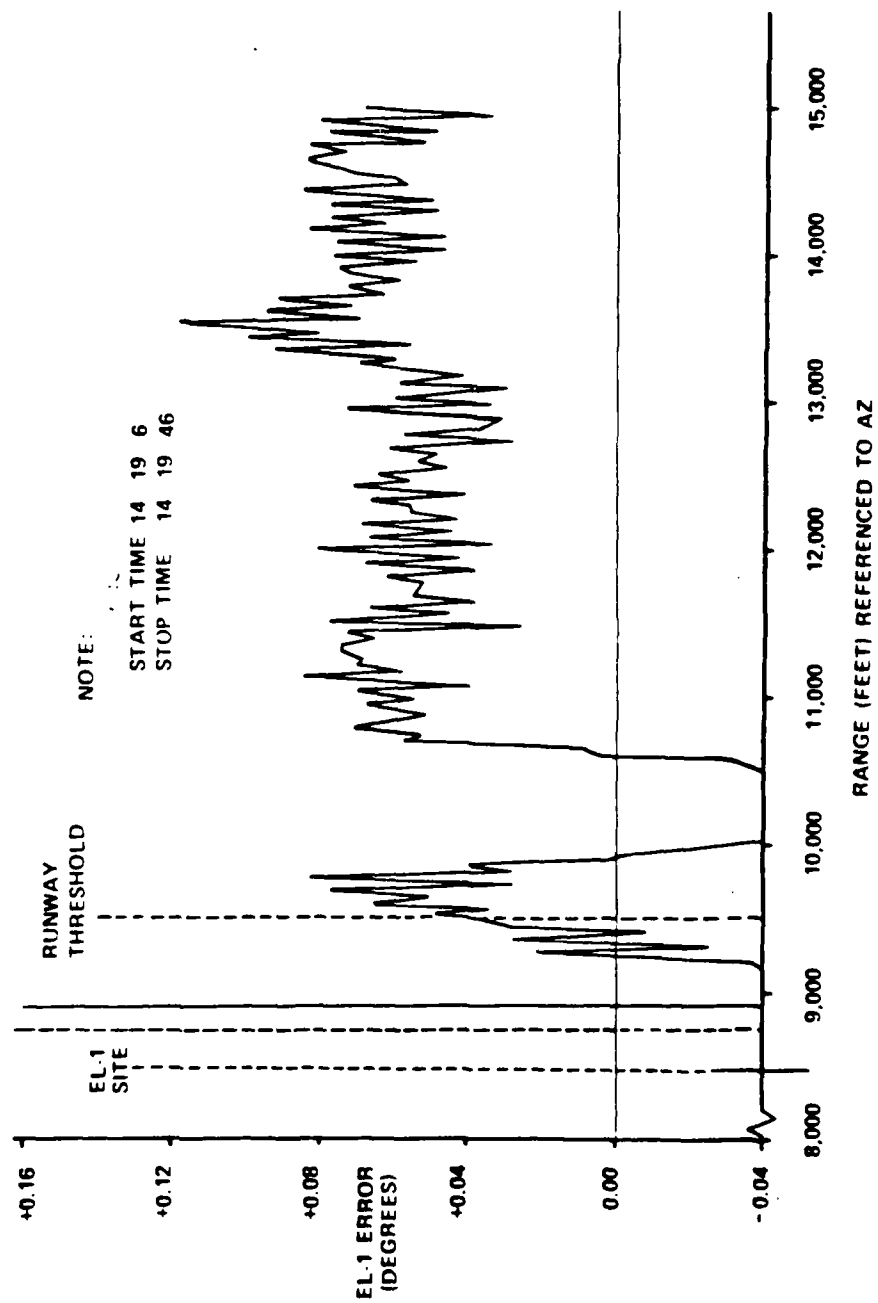


Figure V-3: Elevation Shadowing.

## VI. IMPACT ON MLS TEST RESULTS

### A. General

This section relates the basic tracker errors developed previously to the specific geometries associated with the MLS site installations. The general approach was as follows:

- (1) Translate the  $2\sigma$  tracker errors into  $2\sigma$  spatial position errors for the runway centerline region from EL-2 to (+) 10 nmi.
- (2) Combine the  $2\sigma$  spatial position errors from step (1) with the tracking offsets, i.e., the differences between the MLS antenna locations and the tracker reference point on the aircraft.
- (3) Transform the spatial position errors/tracking offsets from step (2) into the angle and range coordinate systems associated with each "K" system installation.

The transformed angle and range errors represent the  $2\sigma$  uncertainty about the measured error values. For most cases the errors are symmetrical about zero and are most likely normally distributed. For those cases where geometry-dependent errors were present (along with the random errors), the random distribution was plotted about the geometry-dependent error.

It should be stressed that the most probable MLS error is still the measured error for those cases with no significant geometry-dependent errors. For those cases with geometry-dependent tracker errors, the most probable MLS error is the measured error minus the geometry-dependent

tracker error. The region within the  $2\sigma$  upper and lower limits is also the region within which the tracker errors will be contained 95% of the time.

#### B. Wallops Station

##### 1. FPS-16 Radar

The error sources indicated in Table VI-1 have been established for the FPS-16 radar:

TABLE VI-1: FPS-16 RADAR ERROR SOURCES.

Type of Error	Function	Value	Source
System Bias	Angle Range	0.0029° 7 ft.	Section II.A.
System Noise ( $2\sigma$ )	Angle Range	0.0003°* 0.4 ft.*	Sections II.A.
Low Frequency Bias Drift ( $2\sigma$ )	Angle Range	0.012 17 ft.	Section III.A.

\*Value obtained by multiplying the  $2\sigma$  noise value from the Wolfe Study by the variance reduction ratio (0.03) of filter (See Section IV.B.).

Note: RSS Angle Errors = 0.0123° ( $2\sigma$ )  
RSS Range Errors = 18.4 feet ( $2\sigma$ )

In addition to the random errors described above, two error sources have been identified that are dependent on range; (1) the aircraft beacon accuracy as a function of signal strength, and (2) a propagation correction for transmitting through the atmosphere. NASA Wallops Station has

estimated that the decrease in signal strength as a function of range translates into range errors per Table VI-2.

TABLE VI-2: FPS-16 RADAR RANGE ERROR VS. RANGE DUE TO SIGNAL STRENGTH.

Range From FPS-16 Radar (NMI)	Range Error (Feet)
1/4	0
2	4
5	6
20	9

The three transmitter systems at Wallops Station affected significantly by propagation delays through the atmosphere are the the FPS-16 range system, the T.I. DME and the Hazeltine DME. The status of each system during the test period was as indicated in Table VI-3.

TABLE VI-3: TRANSMITTER CORRECTION STATUS FOR ATMOSPHERIC PROPAGATION DELAY.

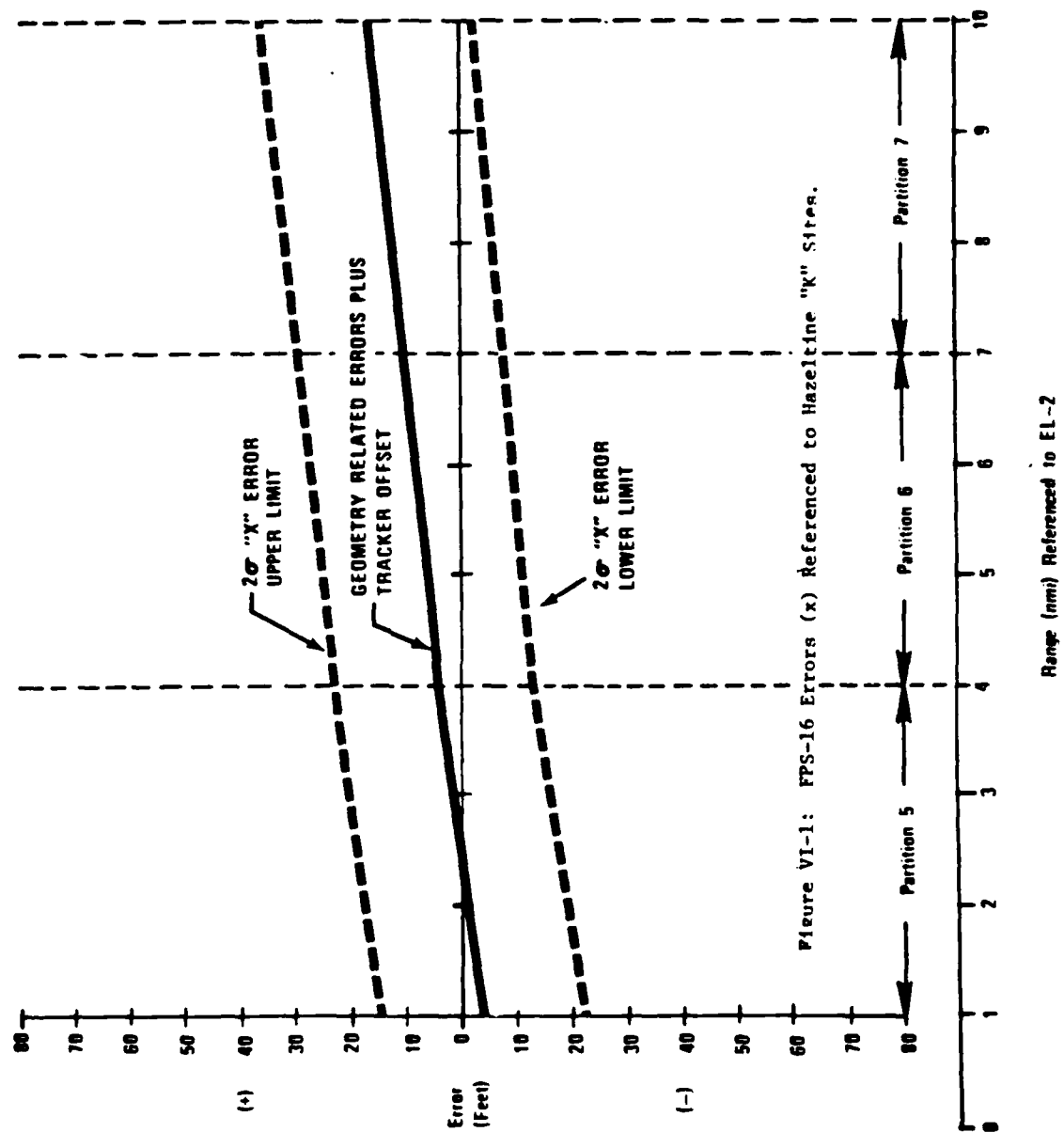
Transmitter System	Status
FPS-16 Radar	Correct at 5.5 nmi (0.5° EL) as a result of a system calibration prior to each flight.
Hazeltine DME	No correction.
T.I. DME	Fixed index of refraction correction equivalent to a constant altitude of 1,375 ft.

The  $2\sigma$  FPS-16 range errors were combined with geometry-dependent range errors (beacon response, propagation delay differences and tracking offsets) and translated to the Hazeltine runway. Figure VI-1 through VI-4 show the  $2\sigma$  FPS-16 "x", "y", and "z" errors translated into MLS range, azimuth and elevation errors referenced to the Hazeltine "K" system transmitters.

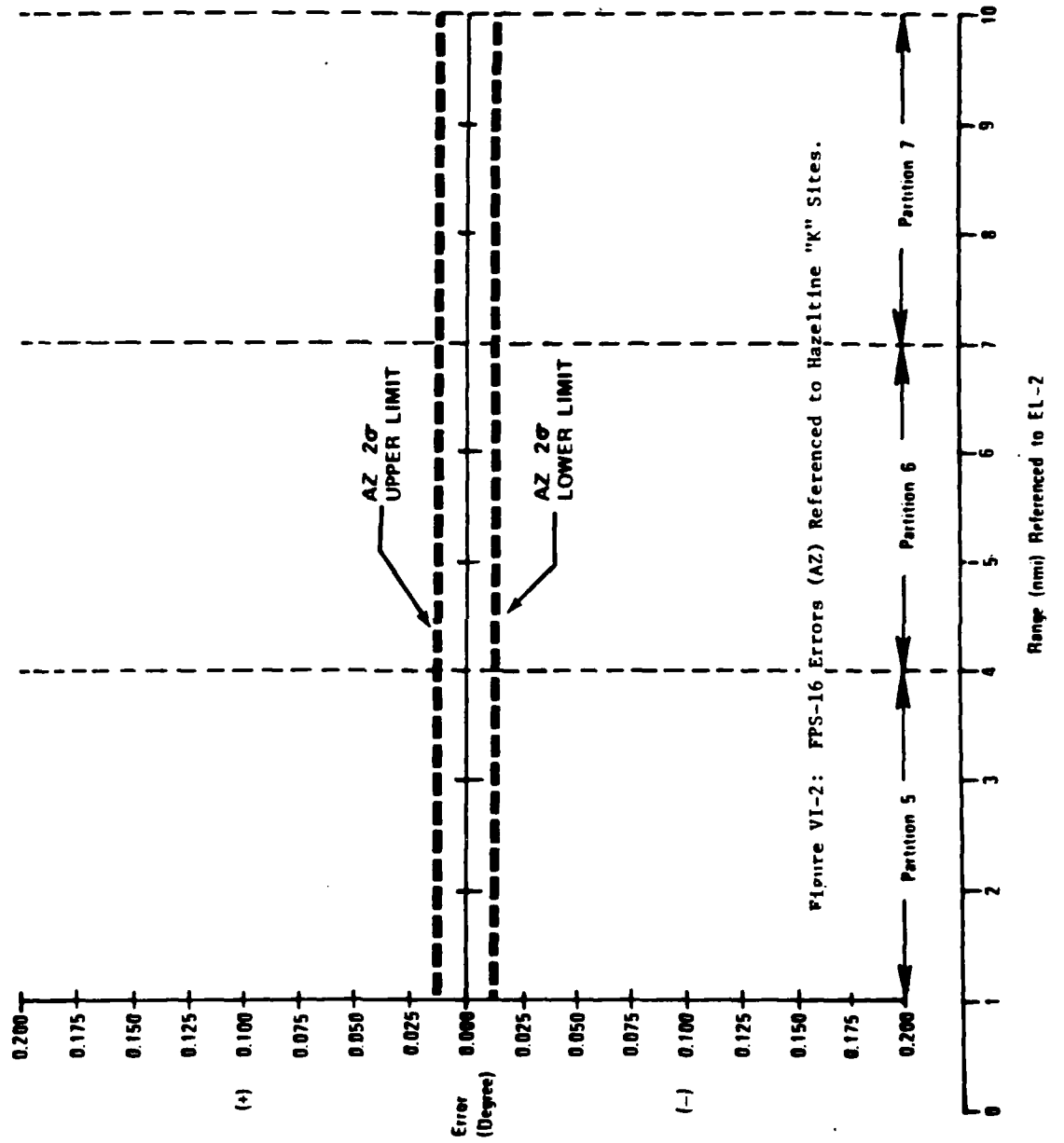
The  $2\sigma$  FPS-16 range errors were combined with geometry-dependent errors (beacon response, propagation delay differences and tracking offsets) and translated to the T.I. runway. Figures VI-5 through VI-8 show the  $2\sigma$  FPS-16 "x", "y" and "z" axes errors translated into MLS range, azimuth and elevation errors referenced to the T.I. "K" system transmitters.

## 2. Photogrammetric System (PMS)

The basic spatial position accuracy of the PMS was established by the error analysis (Section II.A.3.) and corroborated by the on-site static calibration tests. The static test results agreed basically with the error analysis calculation even though the static results contained potential errors not attributable to the PMS. For example, the object photographed was an antenna on a mast attached to a truck that was centered over a surveyed runway test point, and the bias components of the range and azimuth errors probably include truck centering errors. Noise errors not attributable to photogrammetry could have been introduced by the difficulty in reading the image plane coordinates of an unmarked point on the object antenna; and also by the small movements of the antenna mast caused by wind and vibrations. Since the static errors







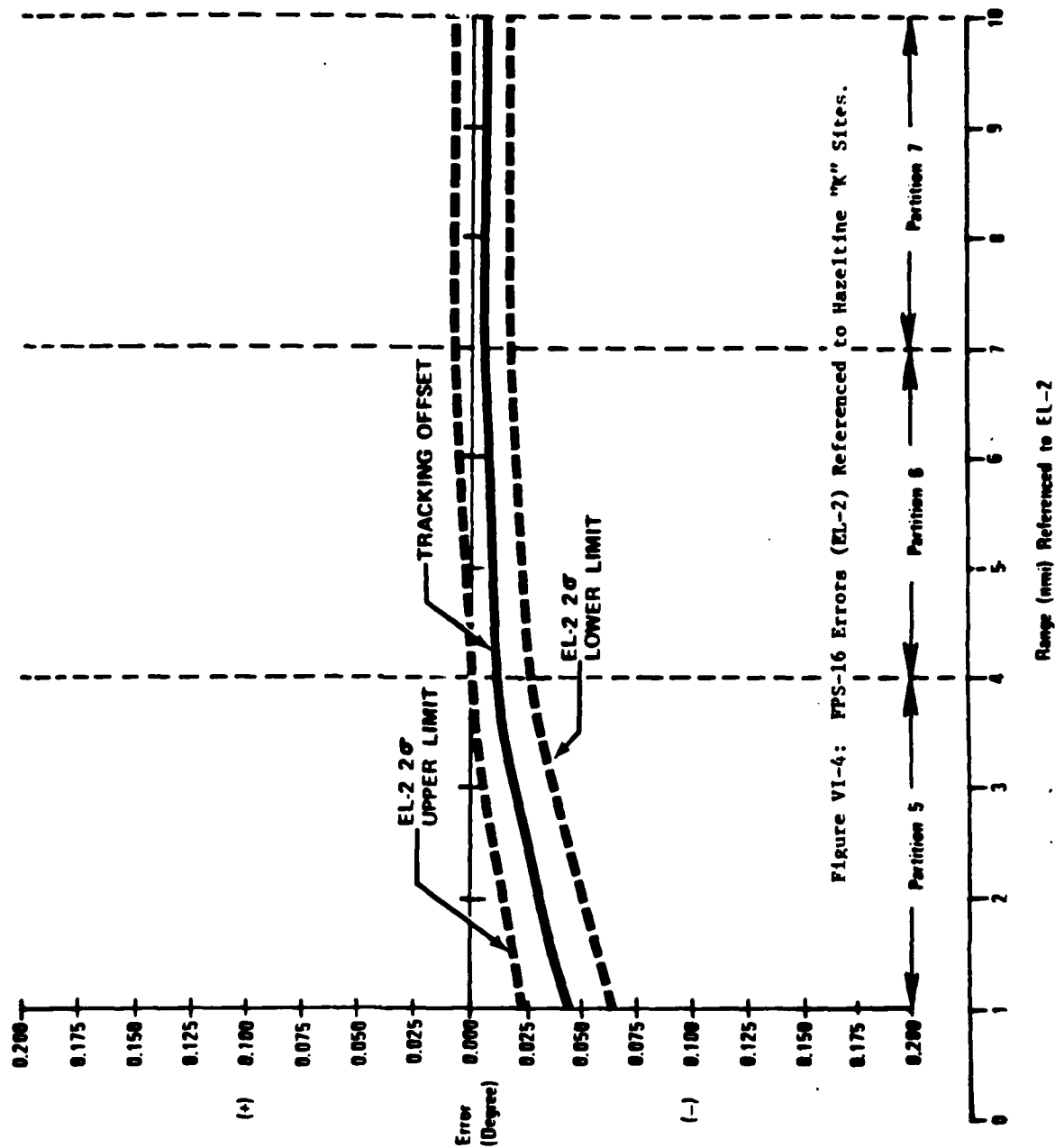


Figure VI-4: FPS-16 Errors (EL-2) Referenced to Hazeltine "K" Sites.

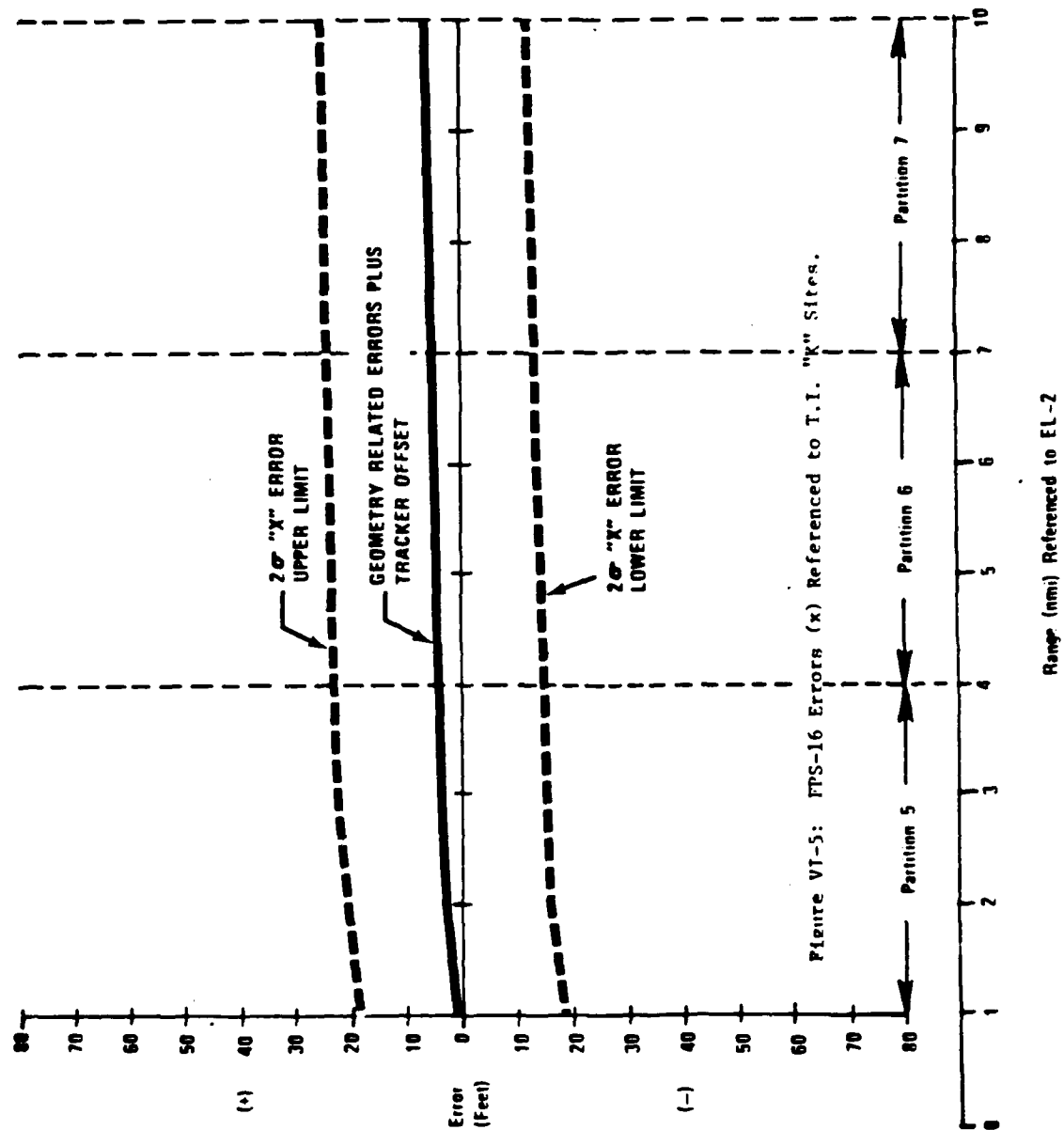


Figure VI-5: FPS-16 Errors (x) Referenced to T.I. "K" Sites.

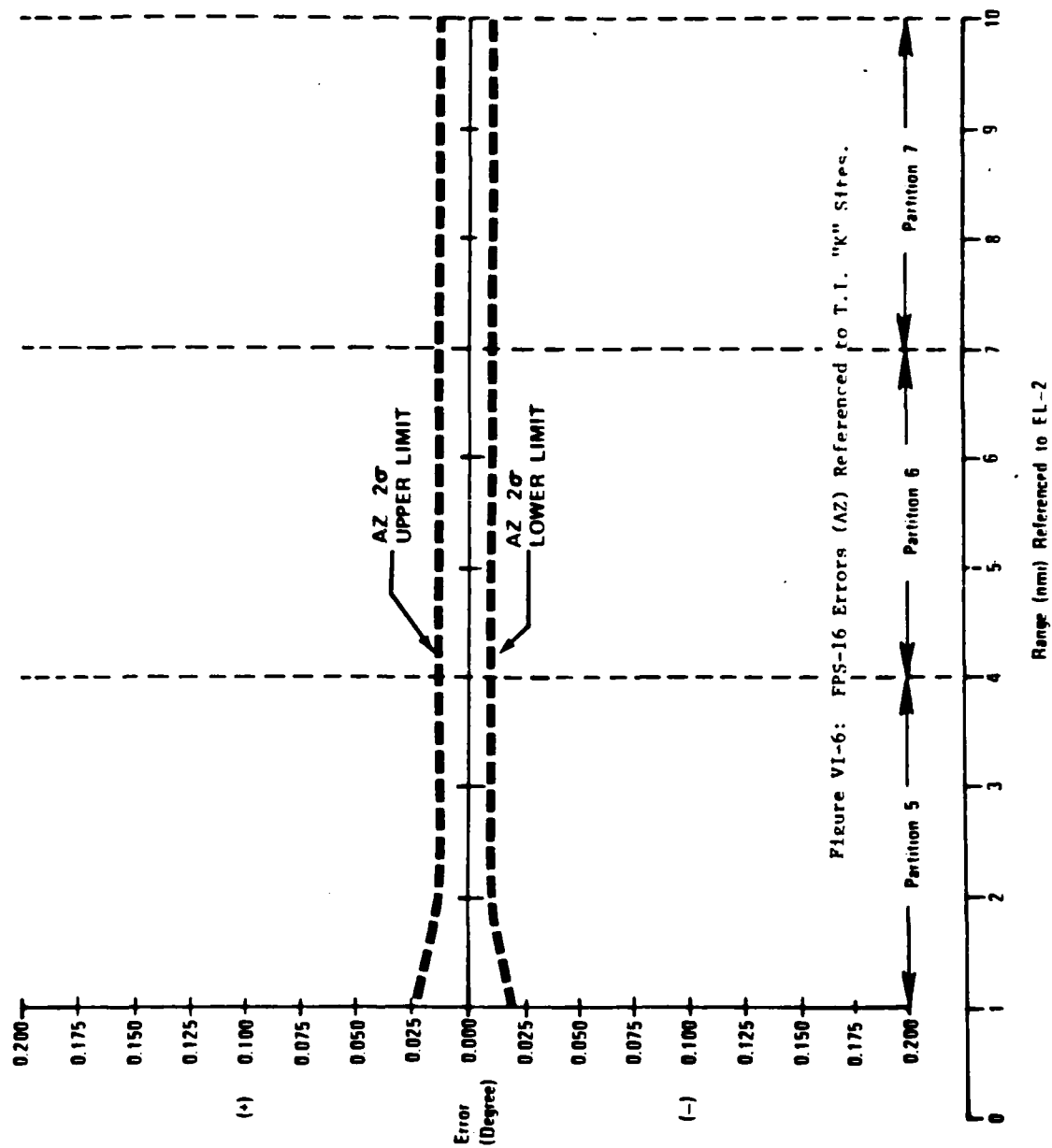


Figure VI-6: FPS-16 Errors (AZ) Referenced to T.L. "K" Sites.

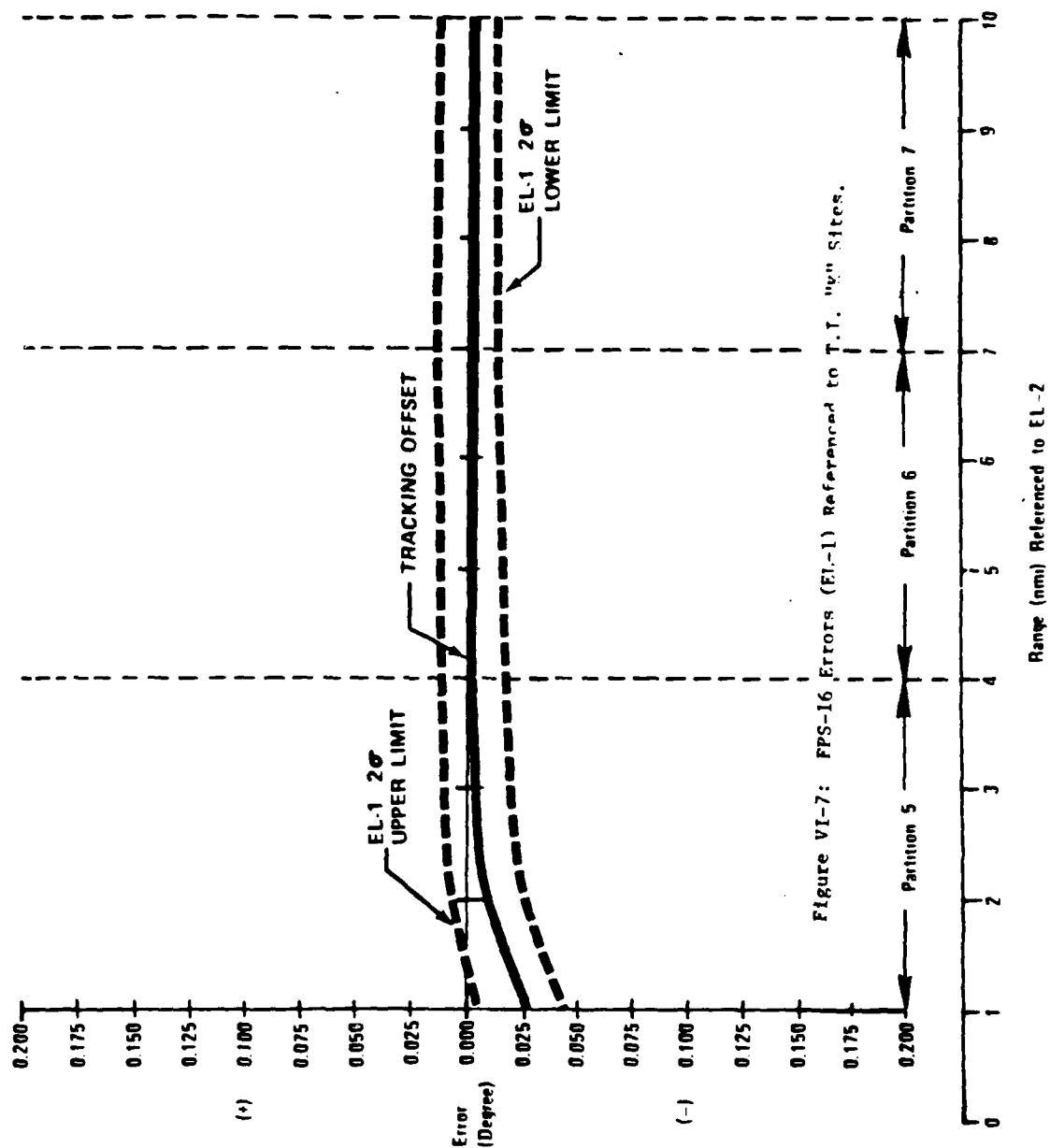


Figure VI-7: FPS-16 Errors (EL-1) Referenced to T.I. "u" Sites.

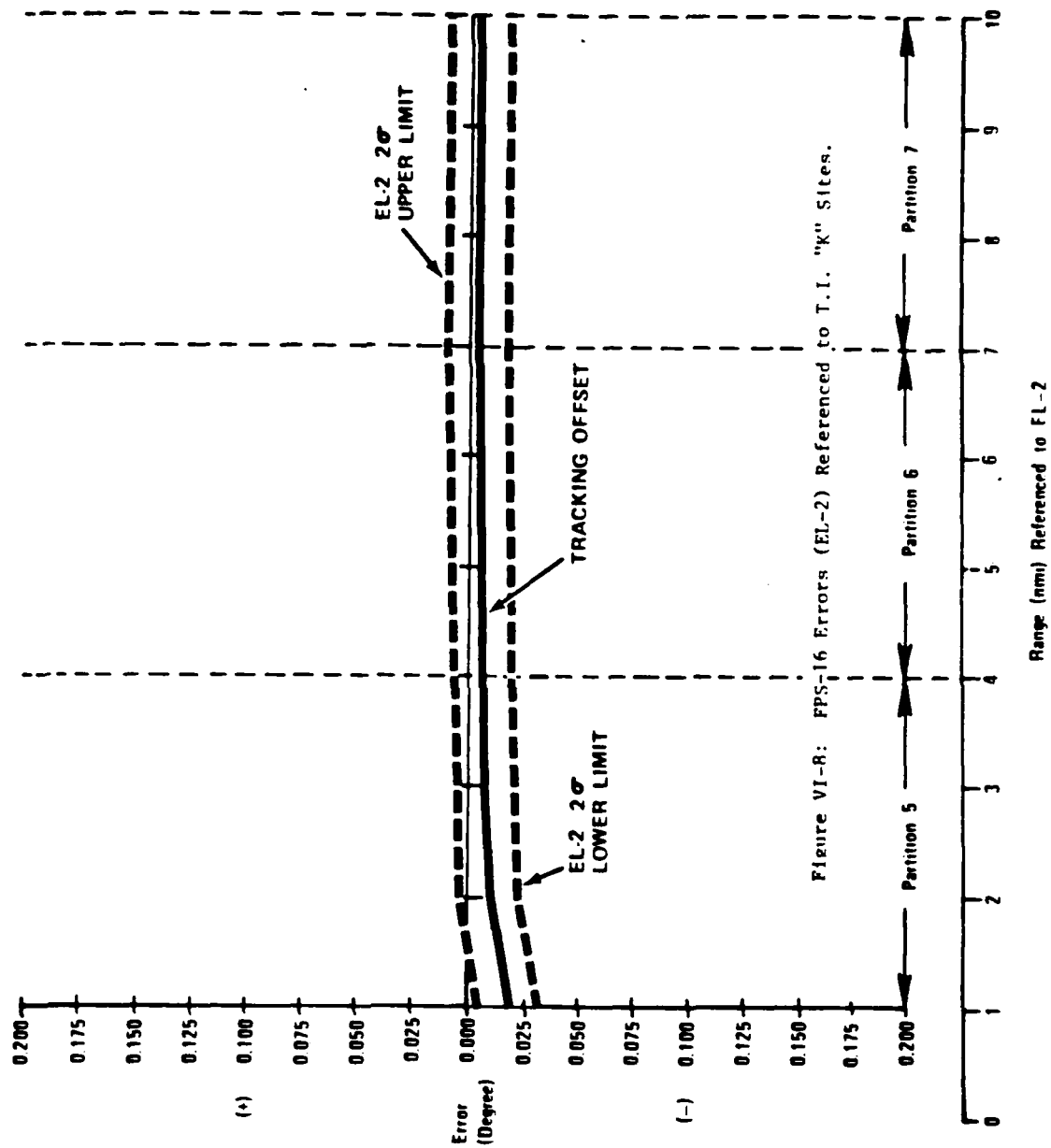


Figure VI-8: FPS-16 Errors (EL-2) Referenced to T.I. "K" Sites.

supported the PMS error analysis, values were translated into the MLS angle system. Figures VI-9 through VI-12 show the  $2\sigma$  errors combined with the tracking offset (C-54) and translated to the Hazeltine EL-2 site. Figures VI-13 through VI-16 show the  $2\sigma$  photogrammetric errors combined with the tracking offsets (C-131) and translated to the T.I. EL-2 site.

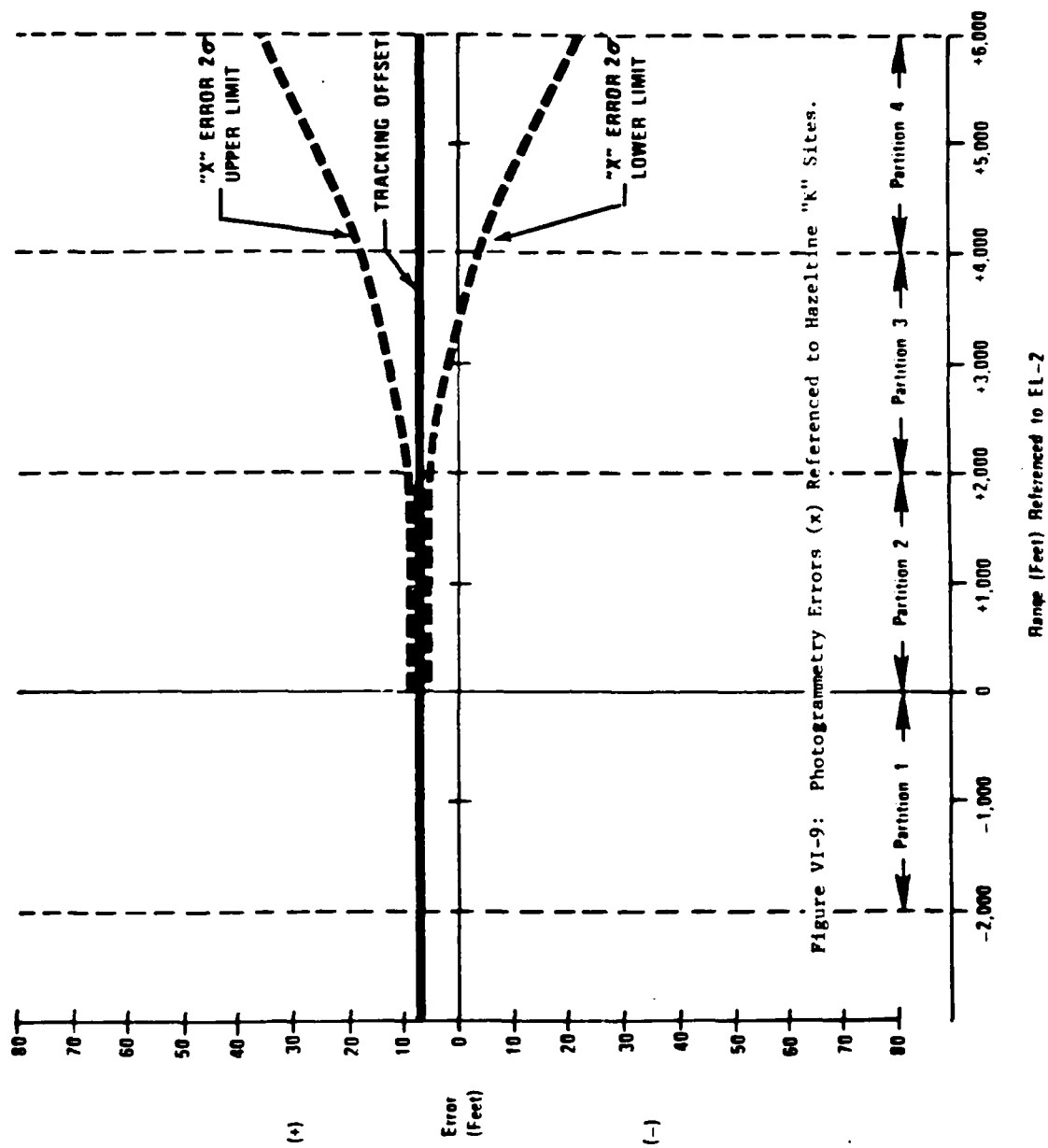
#### C. NAFEC

##### 1. Phototheodolite System

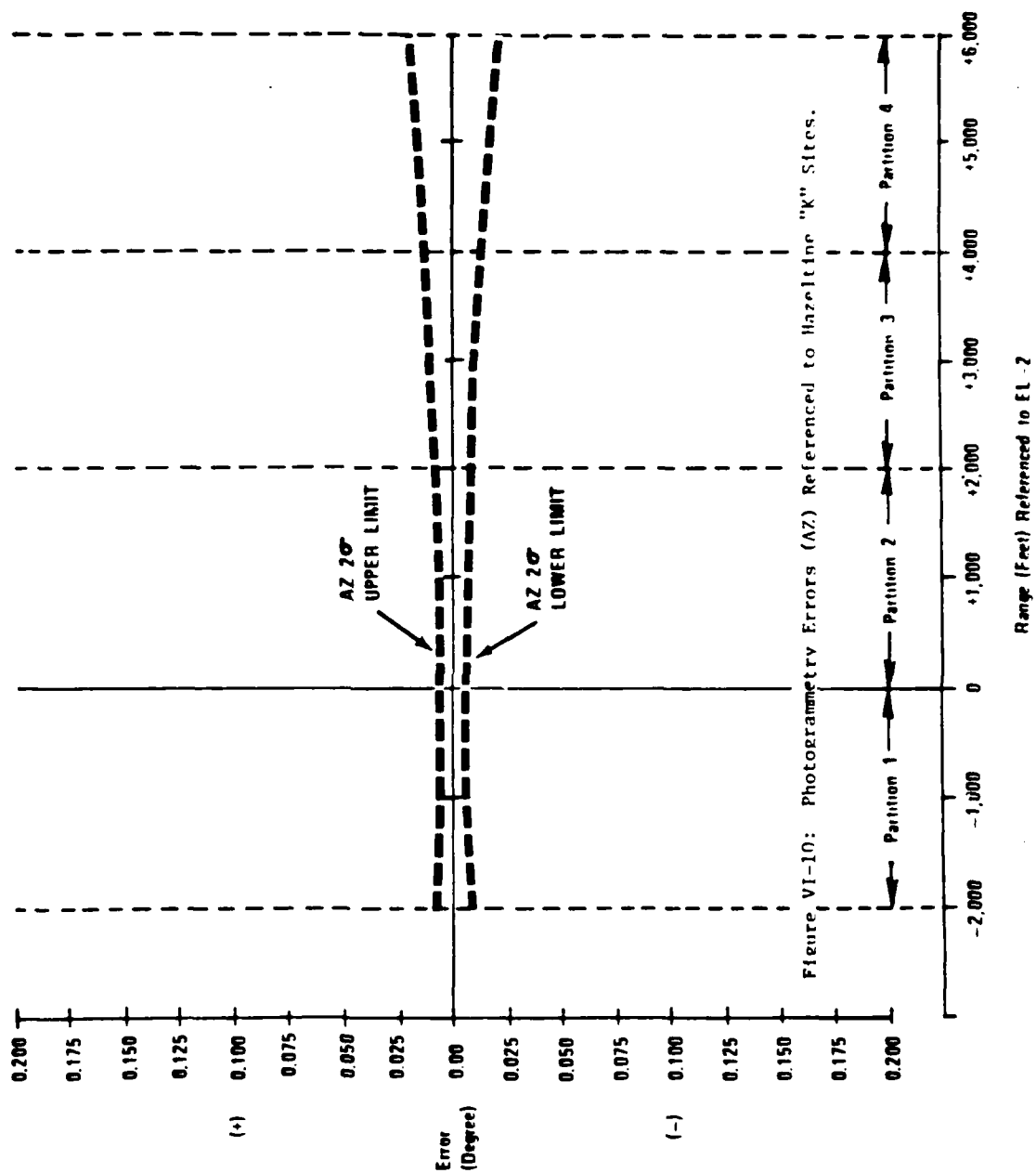
The spatial position accuracy of the phototheodolite system was established by the error analysis (Section II.B.2) and the static calibrations (Section III.B.1). The static calibrations indicated a residual  $2\sigma$  noise level of approximately two feet in all axes. Therefore the theoretical curves from the error analysis were adjusted to coincide with a 2-foot  $2\sigma$  error at both runway thresholds. These  $2\sigma$  adjusted spatial position errors were combined with the tracking offsets (DC-6 for ITT/G and C-118 for Bendix) and then translated into the MLS coordinate system. Figures VI-17 through VI-24 show the  $2\sigma$  range, azimuth, EL-1 and EL-2 errors referenced to the Bendix EL-2 site. Figures VI-25 through VI-32 show the  $2\sigma$  EL-1, EL-2, azimuth and range errors referenced to the ITT/G EL-2 site.

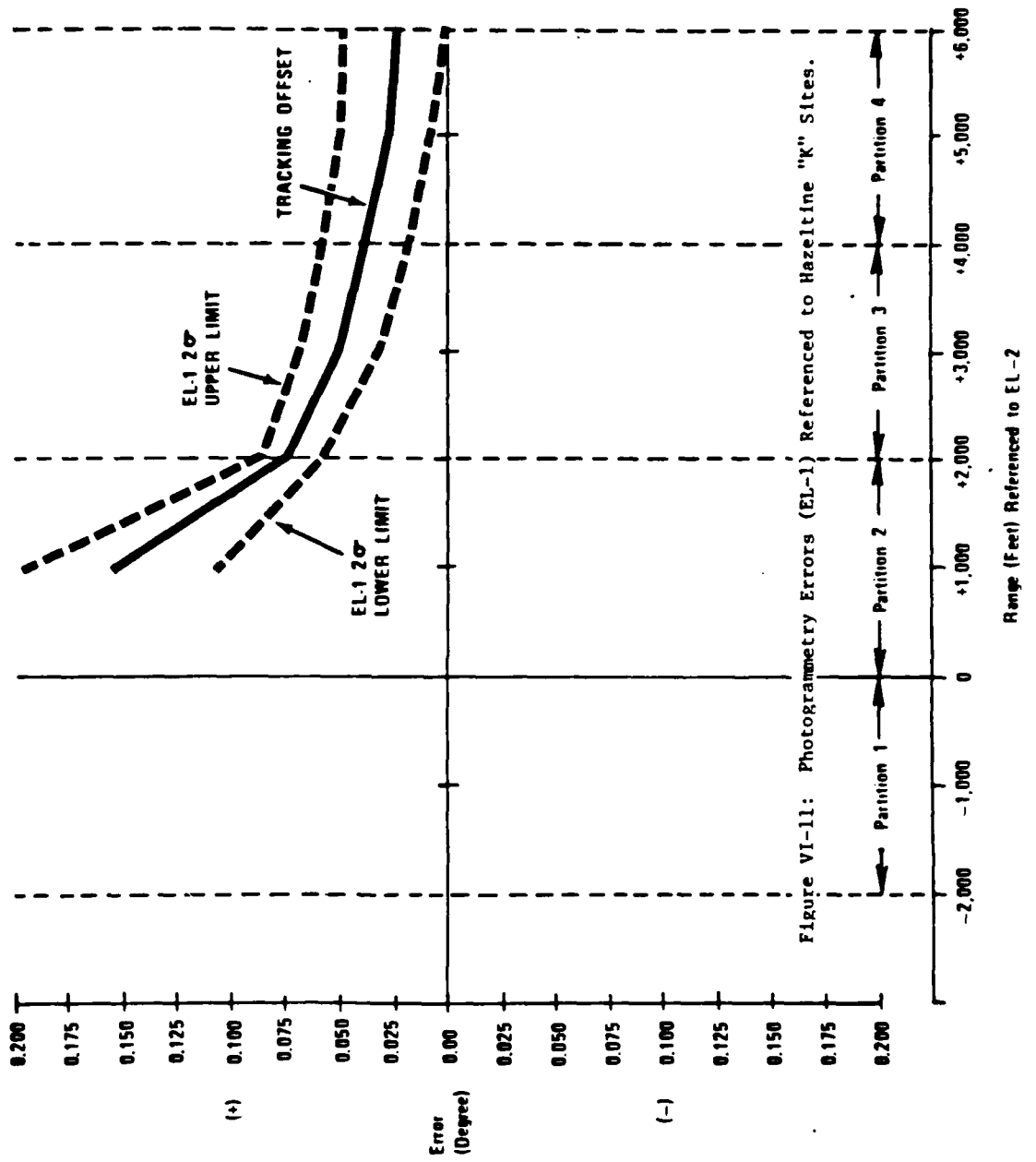
##### 2. EAIR

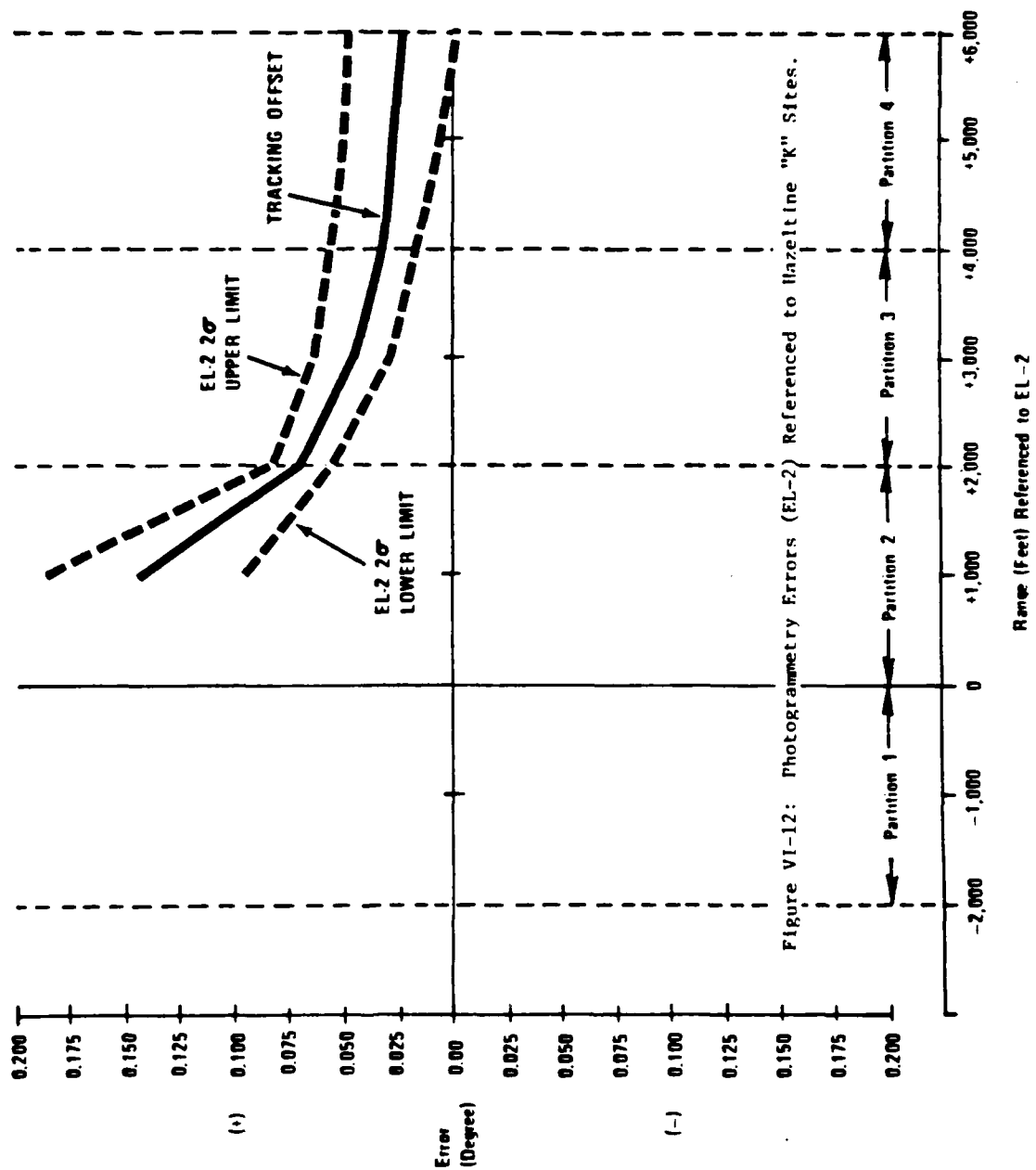
The accuracy of the EAIR system was established by the phototheodolite/EAIR comparison study performed by NAFEC (see Section V). This study established the errors for the EAIR system shown in Table VI-4.











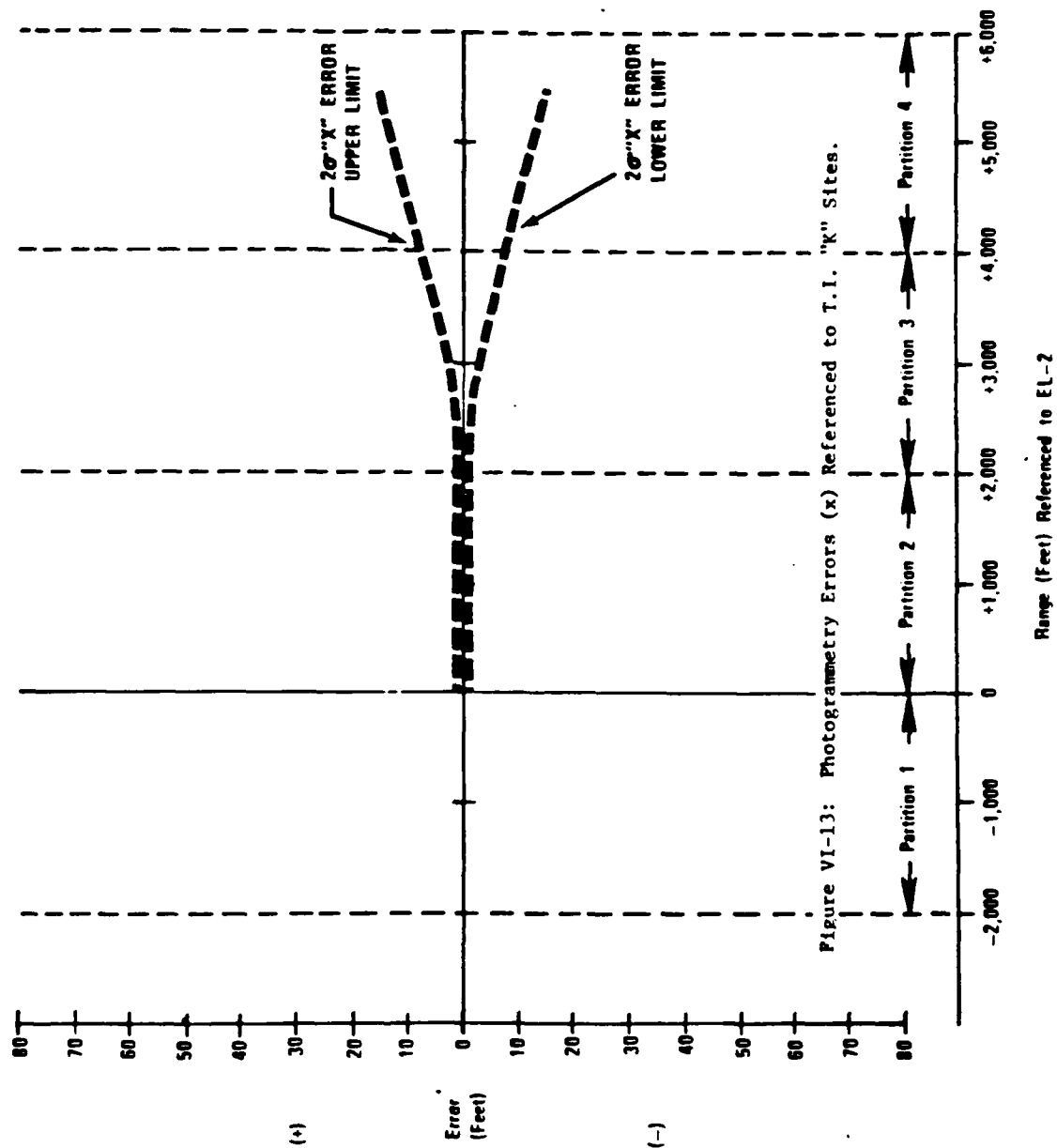


Figure VI-13: Photogrammetry Errors (x) Referenced to T.I. "K" Sites.

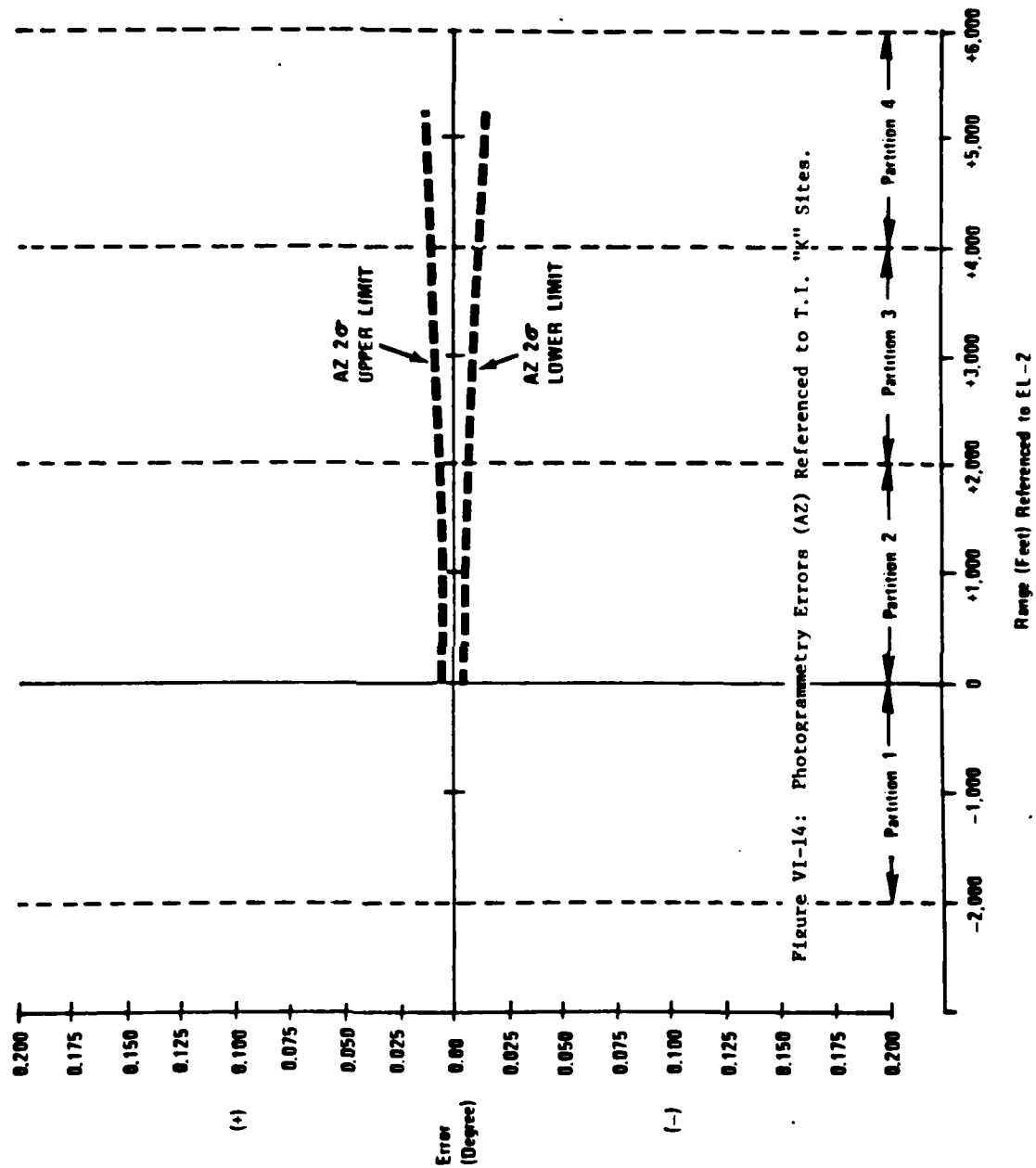


Figure VI-14: Photogrammetry Errors (AZ) Referenced to T.I. "K" Sites.

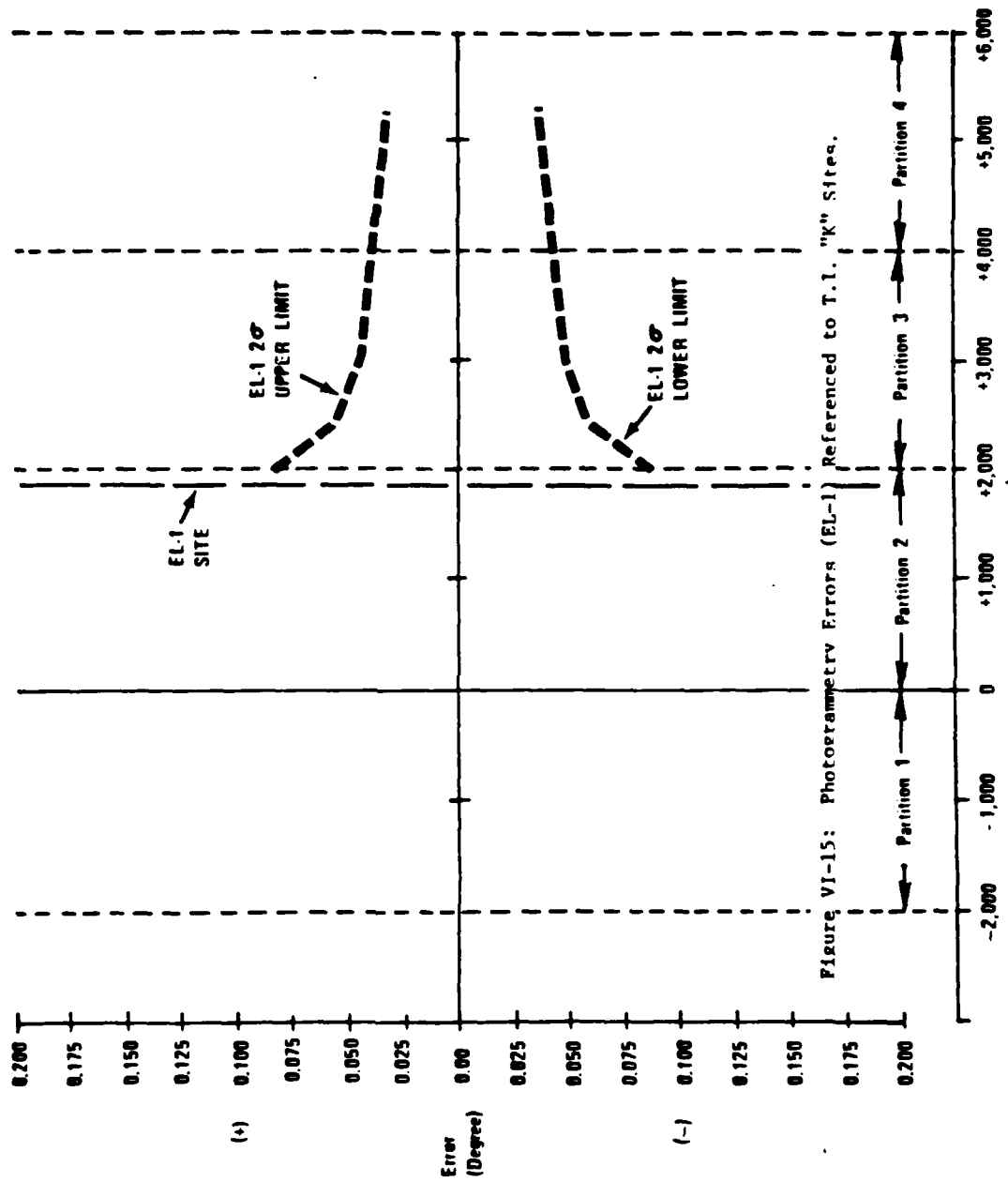
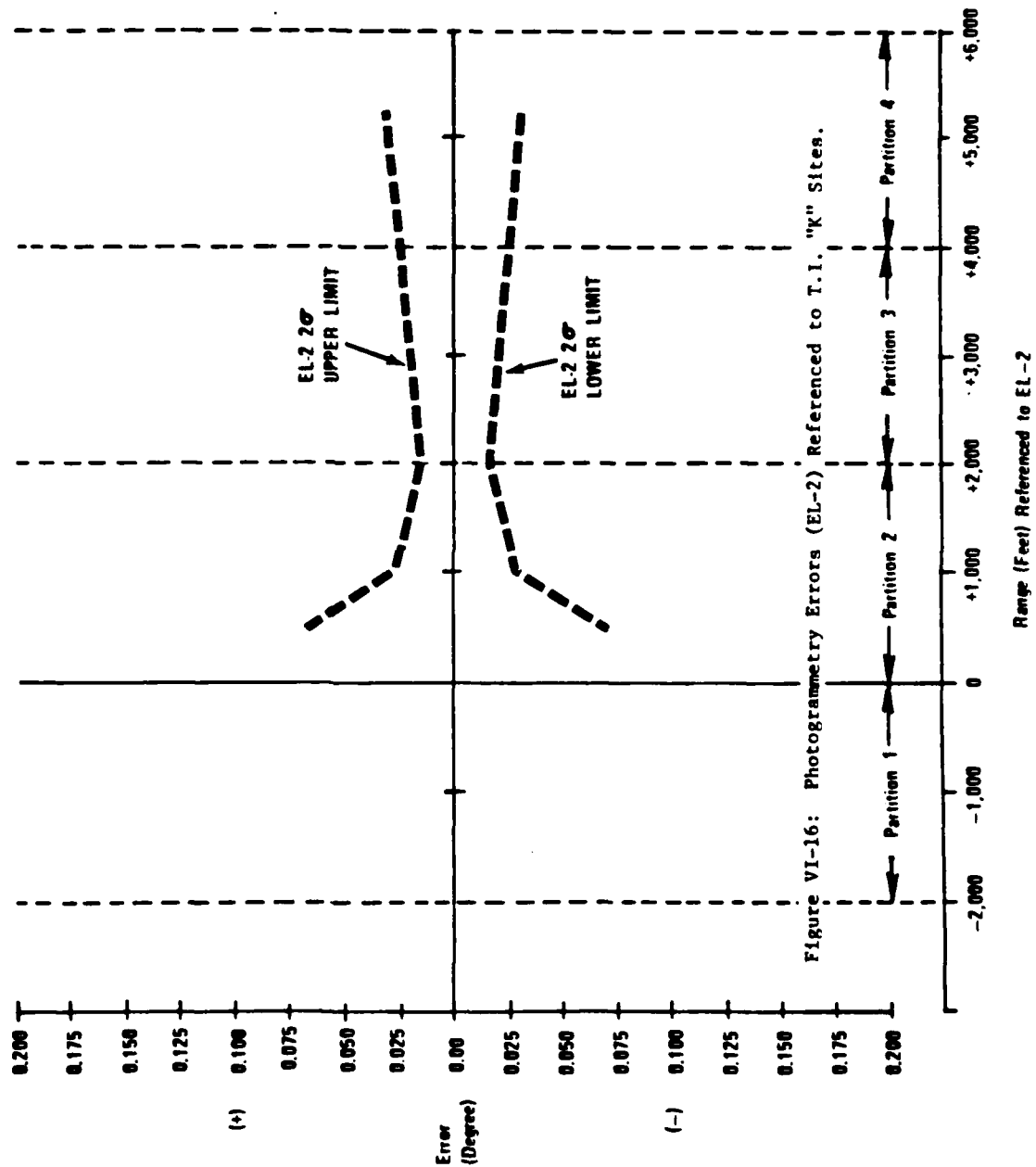


Figure VI-15: Photogrammetry Errors (EL-1) Referenced to T.L. "K" Sites.



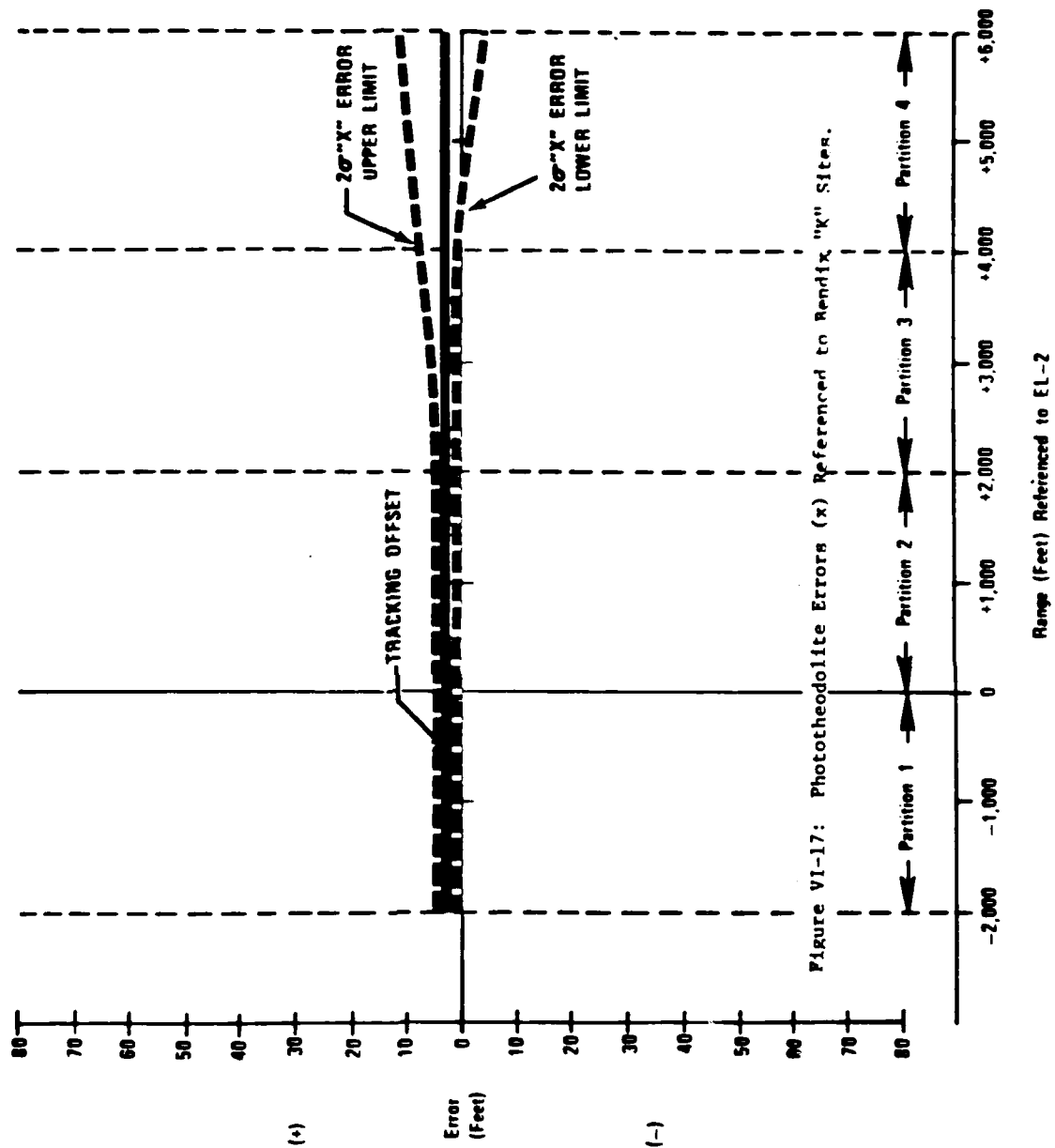


Figure VI-17: Phototheodolite Errors (x) Referenced to Bench "K" Sides.



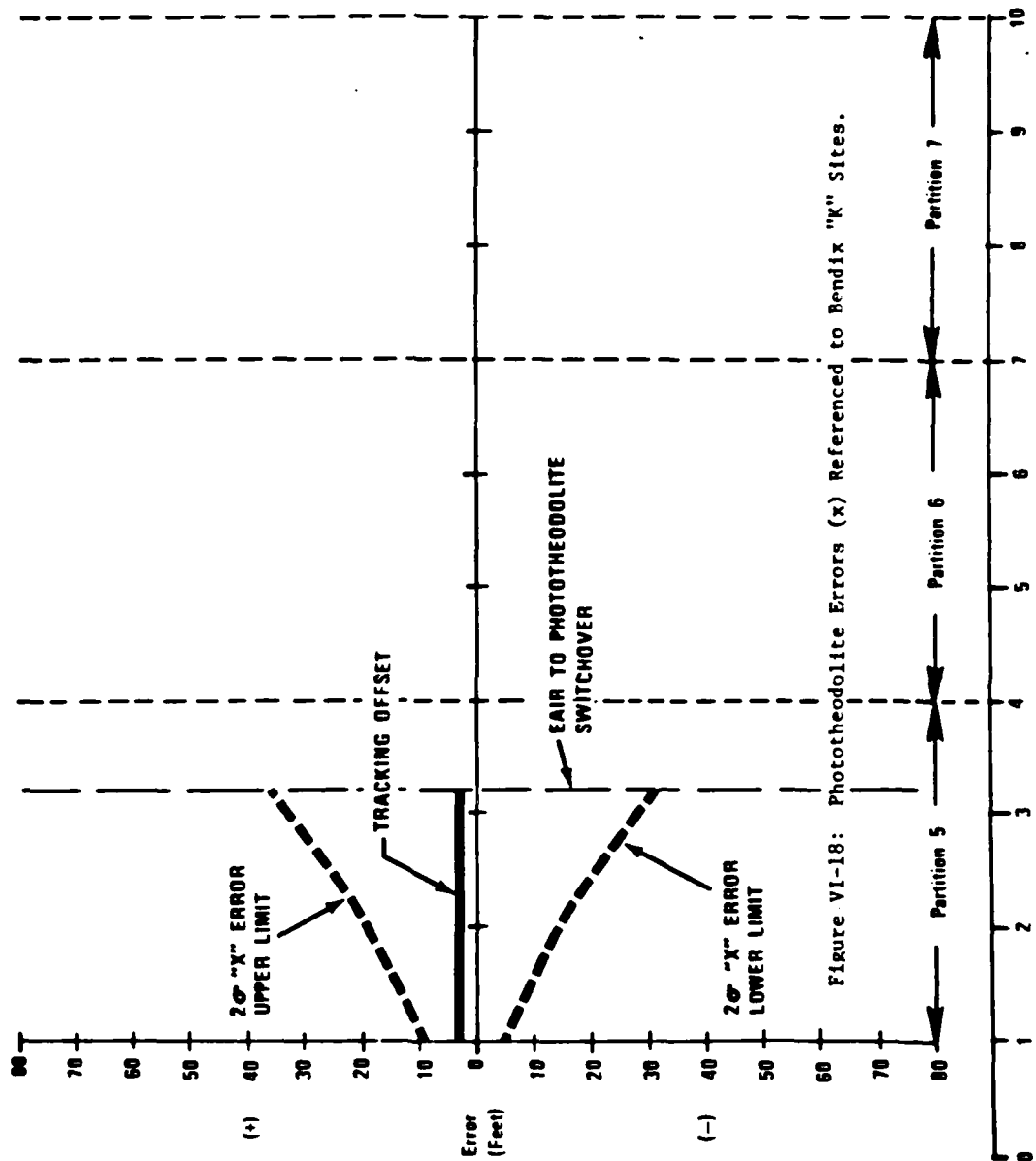
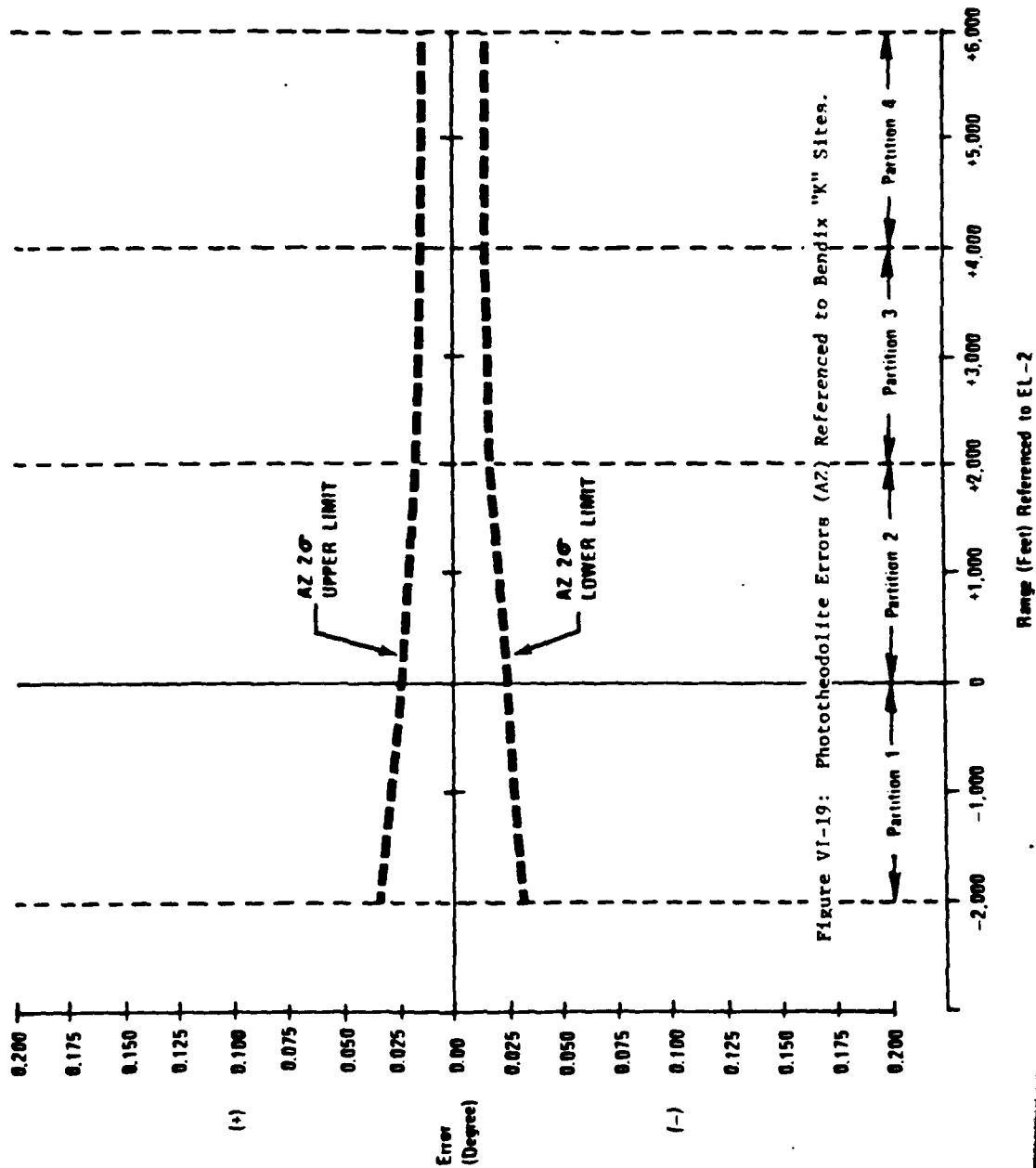


Figure VI-18: Phototheodolite Errors (x) Referenced to Bendix "K" Sites.

Range (nmi) Referenced to EL-2



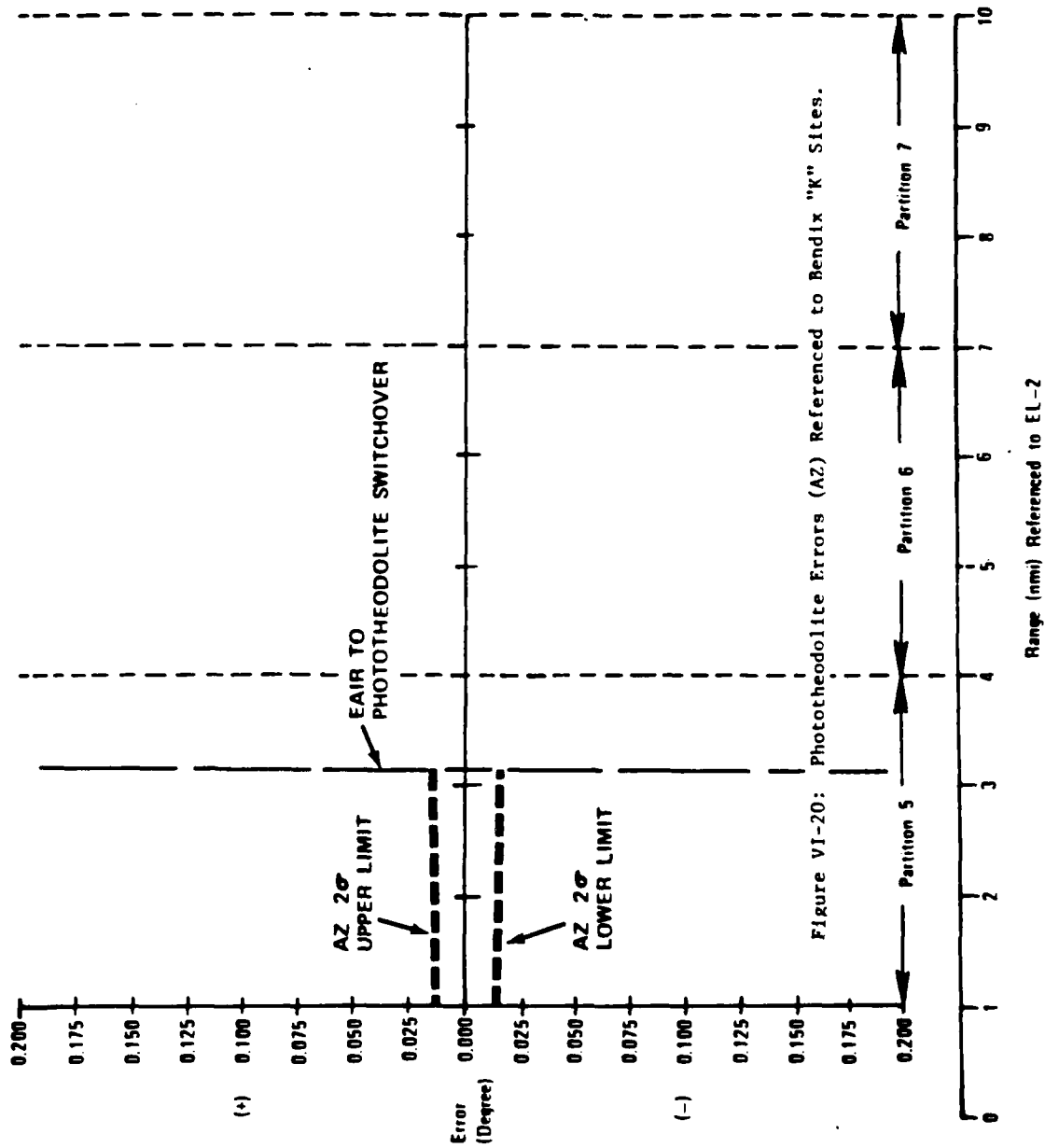


Figure VI-20: Phototheodolite Errors (AZ) Referenced to Bendix "K" Sites.

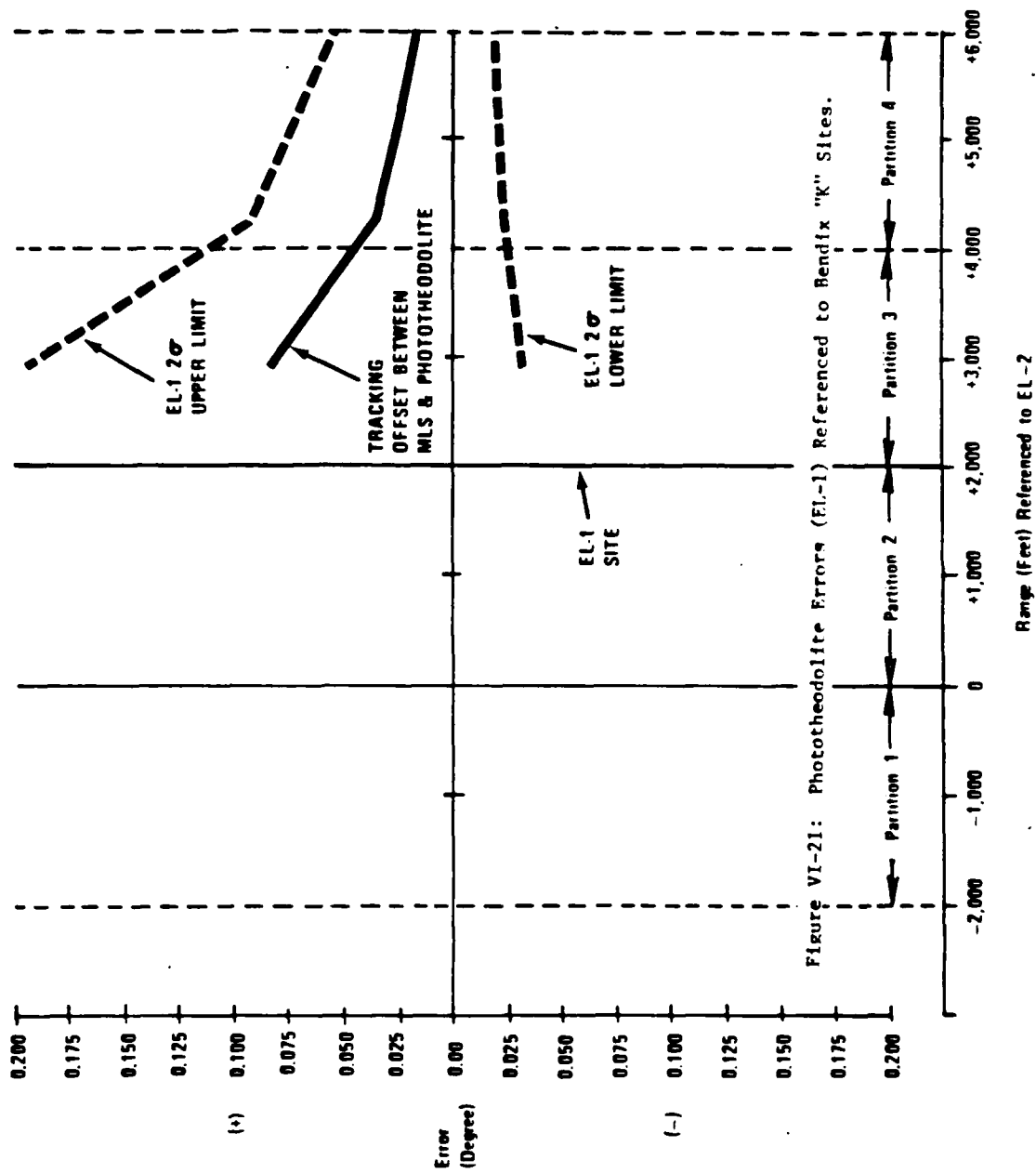


Figure VI-21: Phototheodolite Errors (EL-1) Referenced to Bendix "K" Sites.

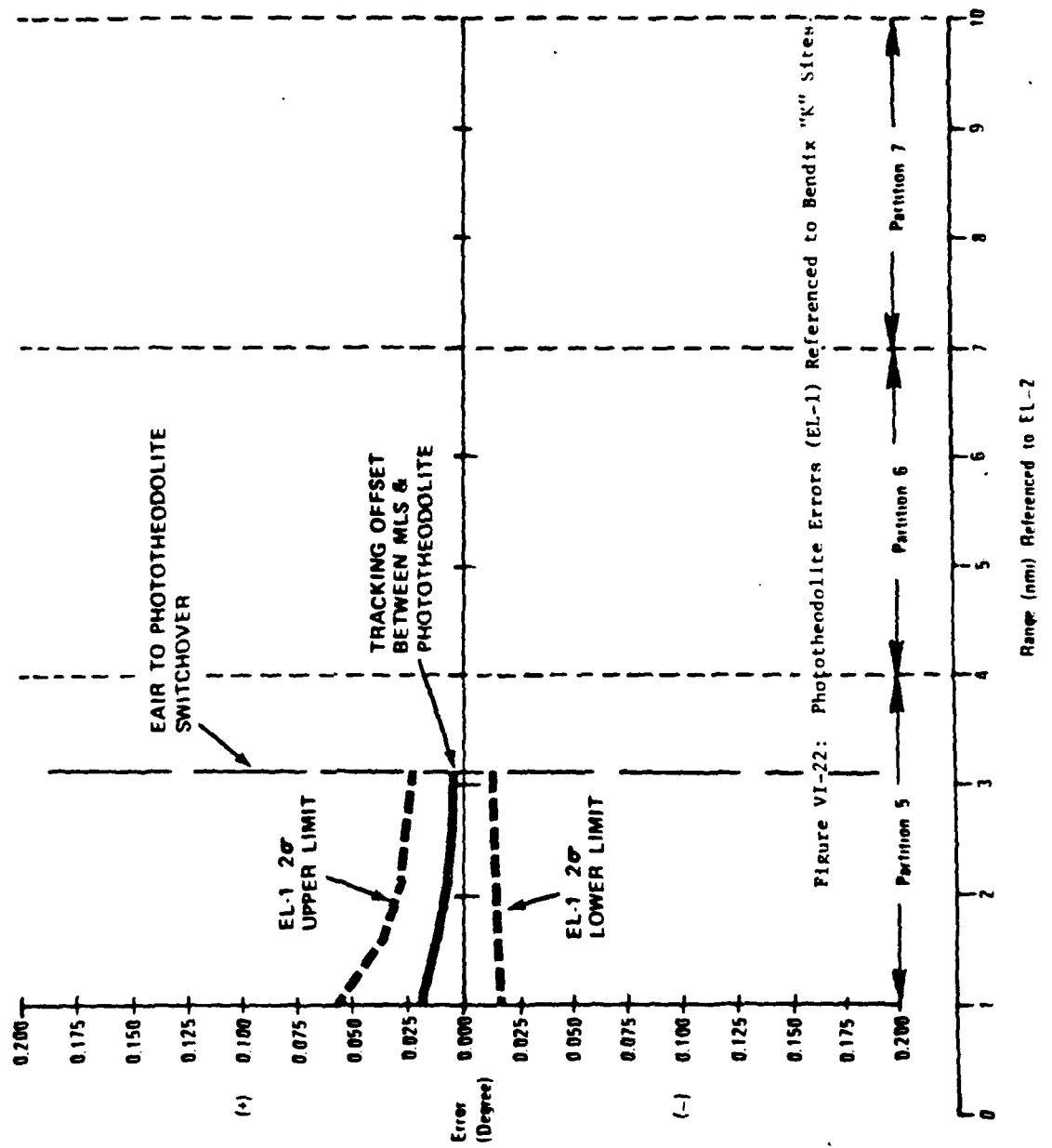


Figure VI-22: Phototheodolite Errors (EL-1) Referenced to Bendix "K" Sites

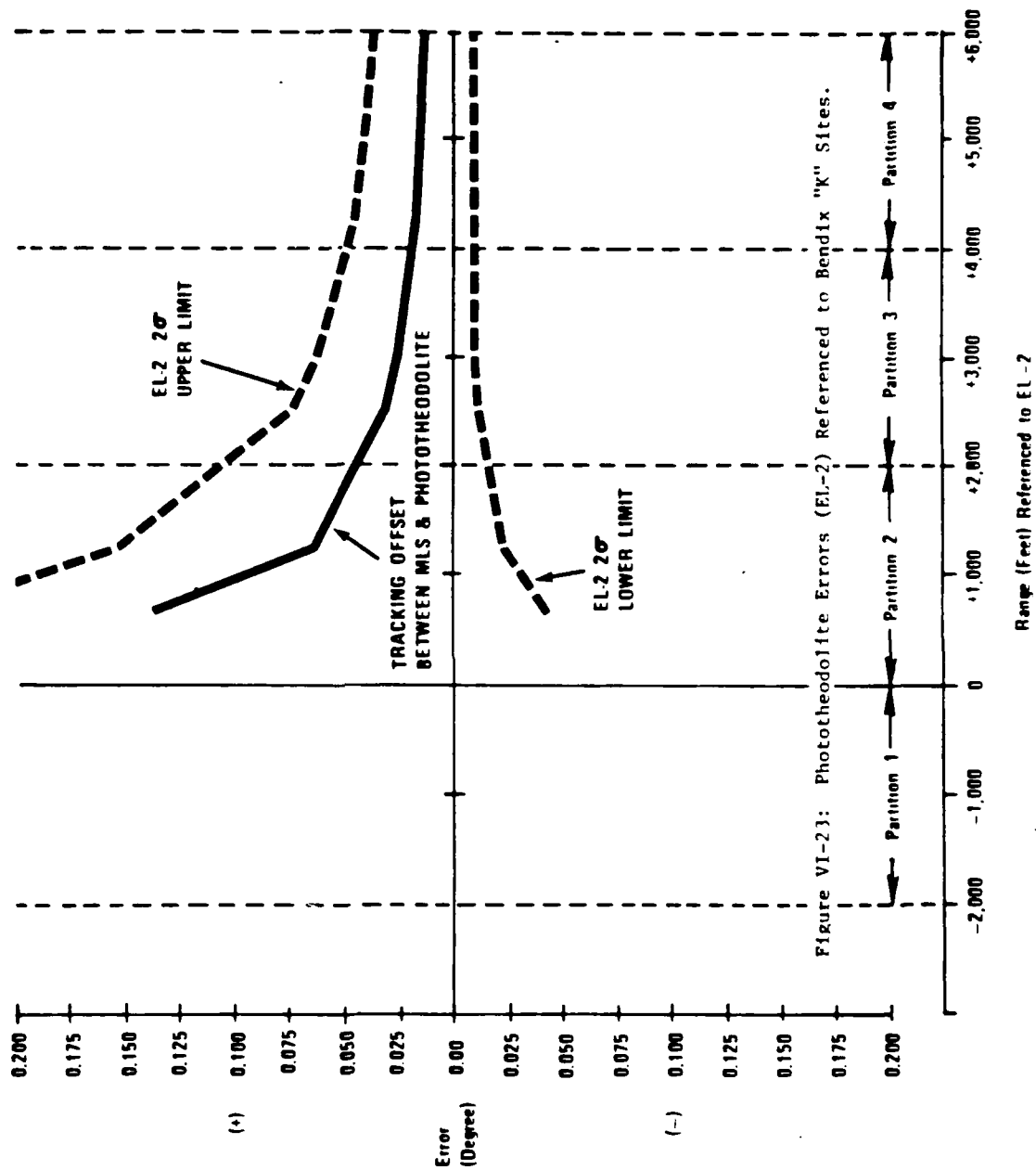
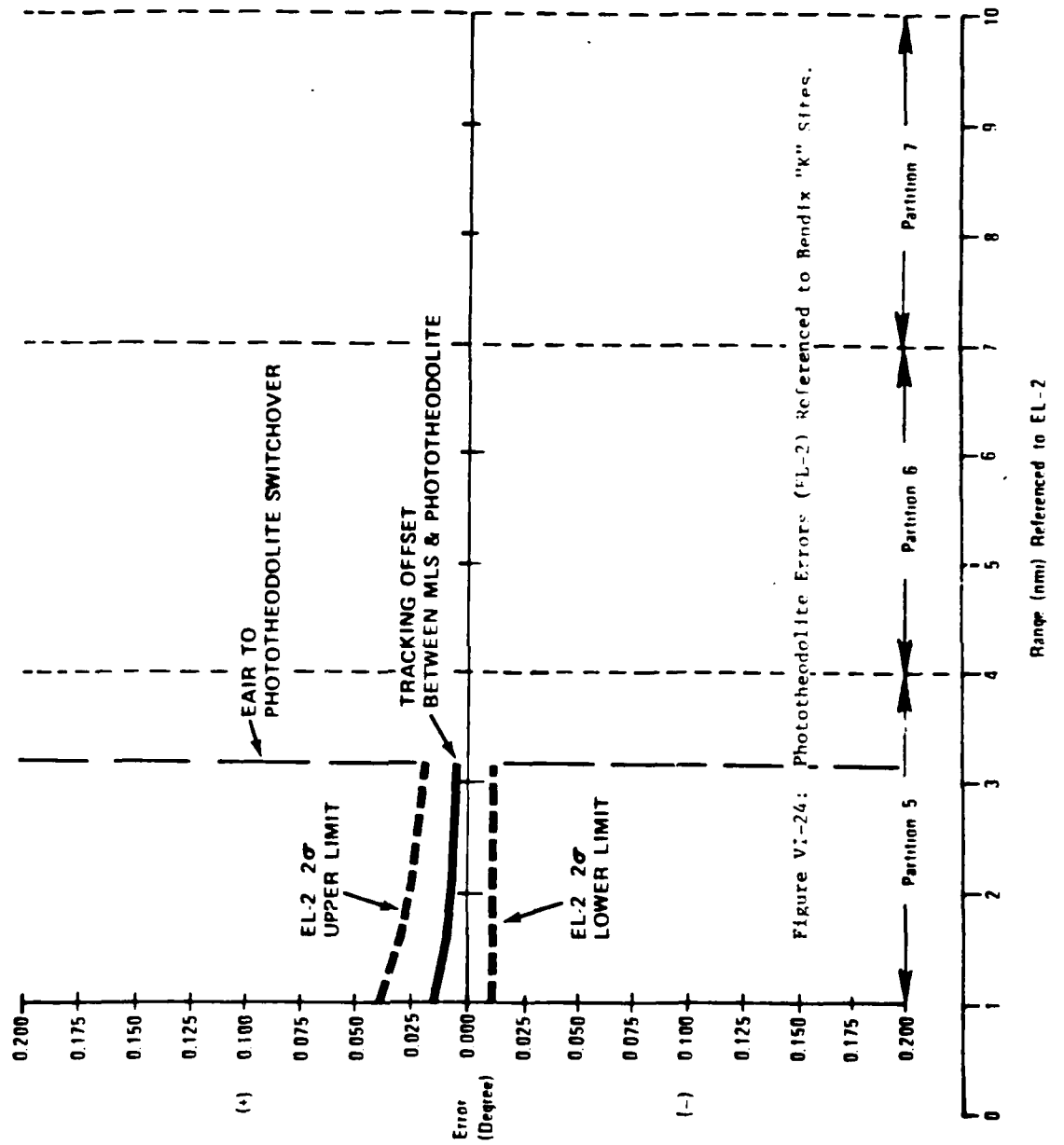


Figure VI-23: Phototheodolite Errors (EL-2) Referenced to Bendix "K" Sites.



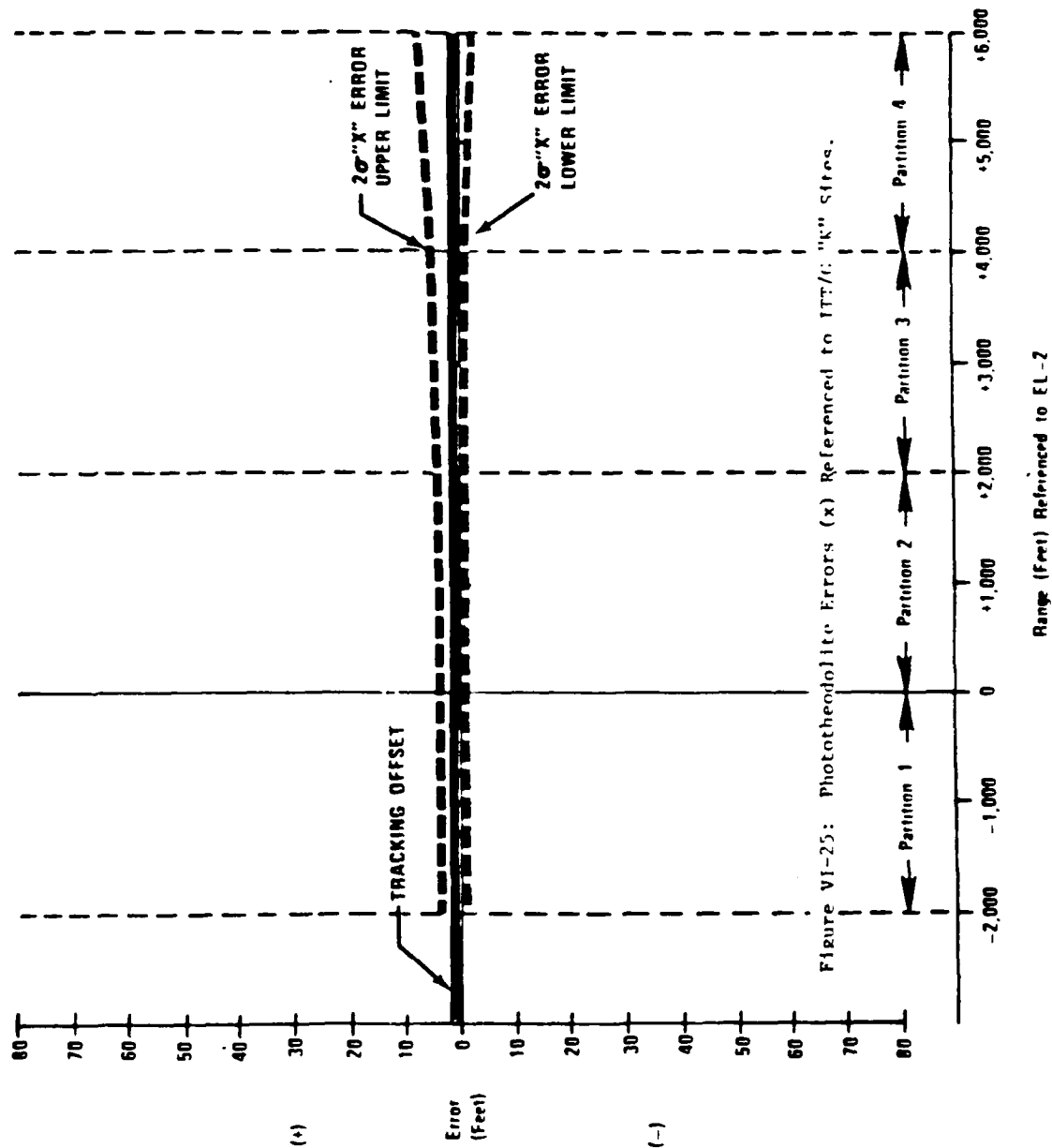
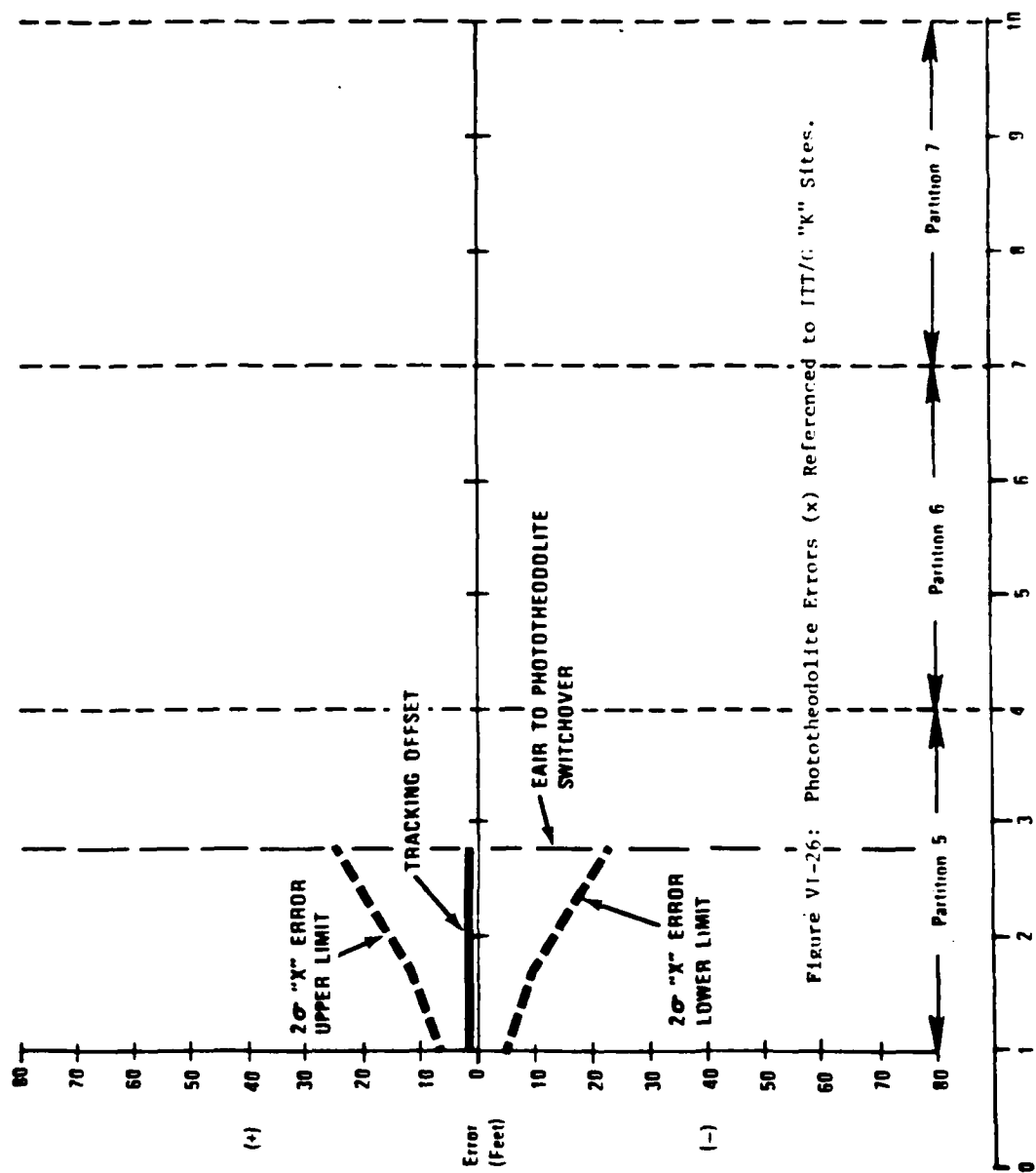


Figure VI-25: Phototheodolite Errors (x) Referenced to ITT/C: "K" Sites.





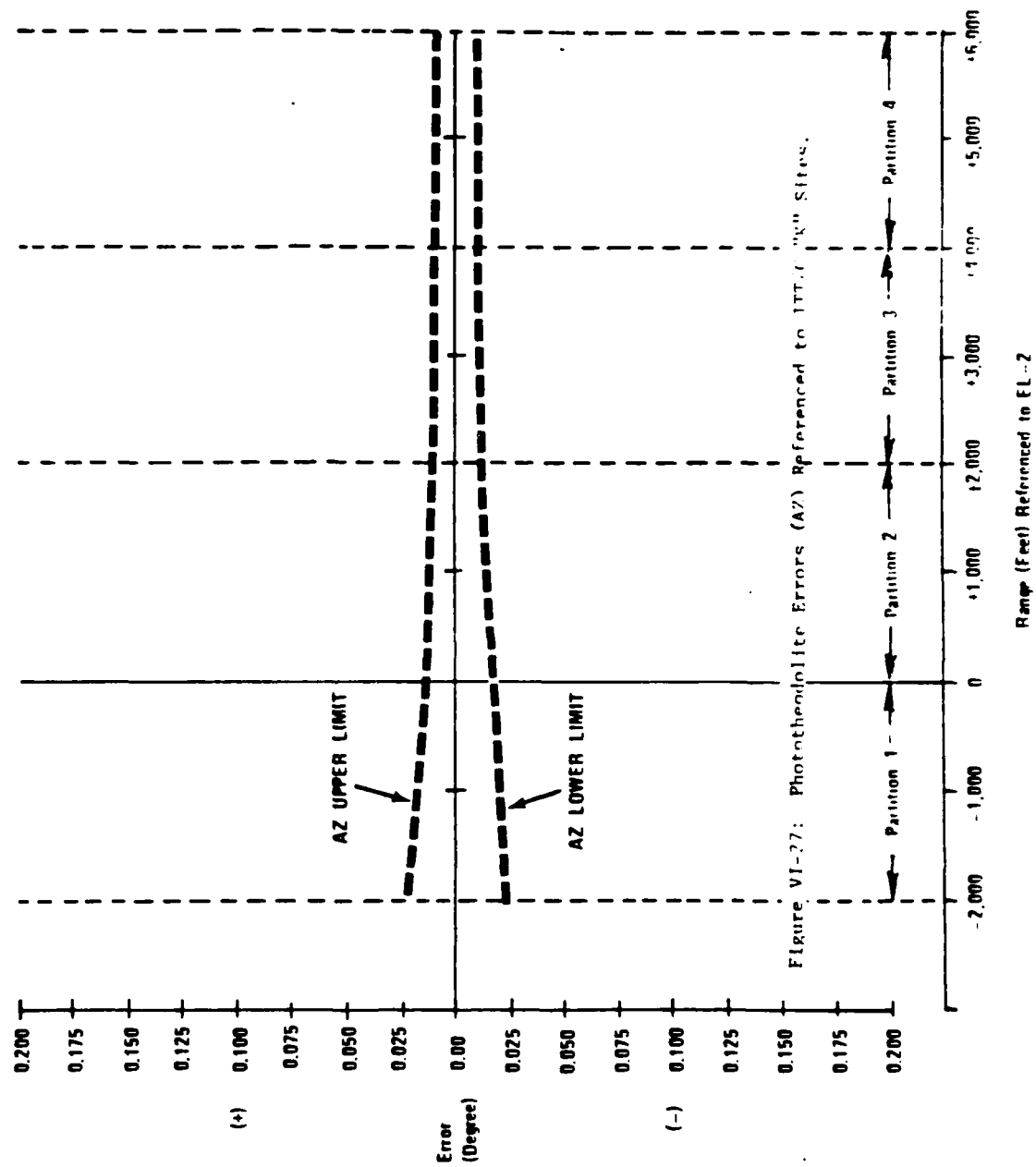


Figure VI-27: Phototheodolite Errors (AZ) Referenced to I.T.T. "X" Sites.

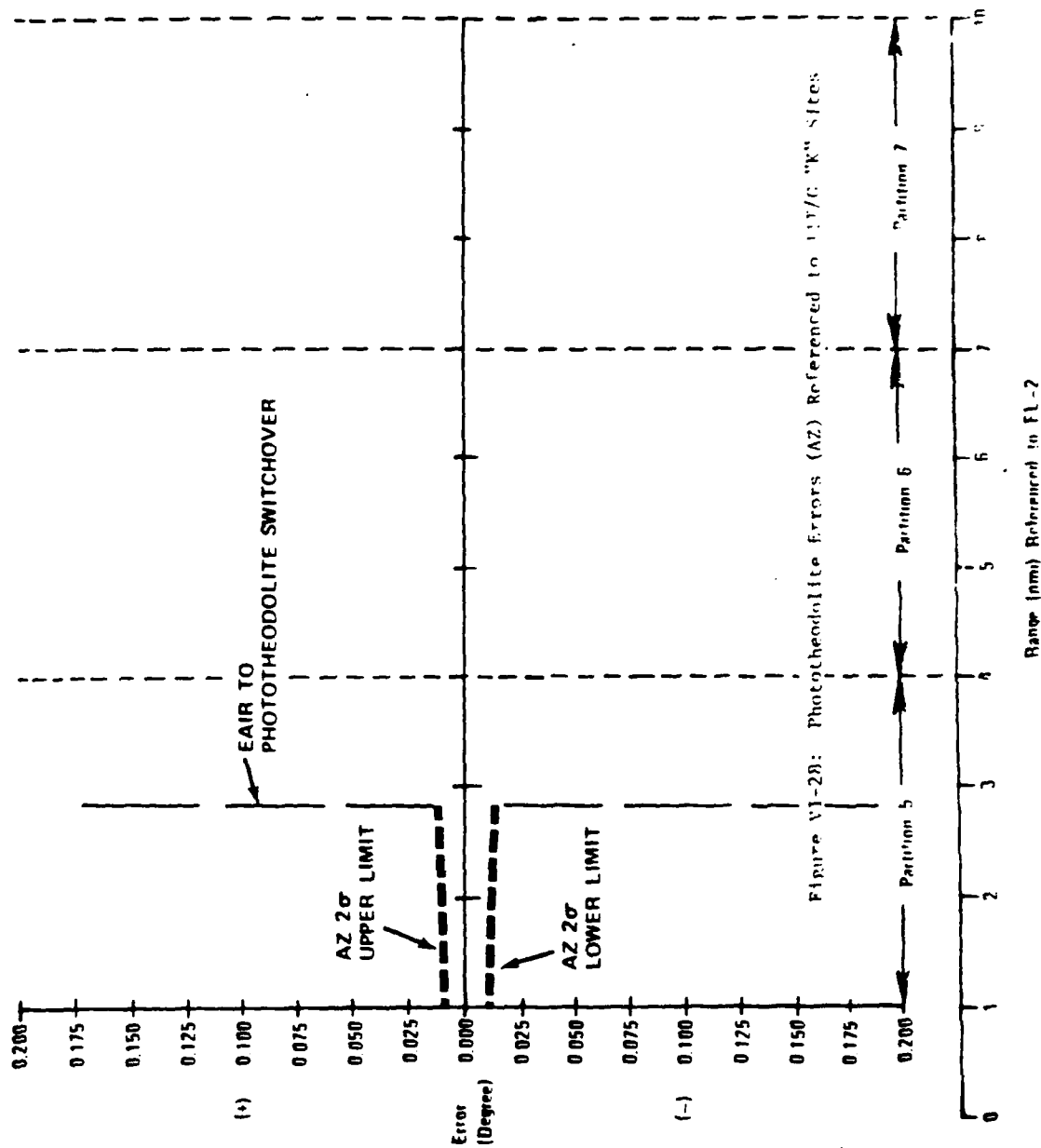


Figure VI-28: Photoconductive Errors (AZ) Referenced to 117°C "K" Sites

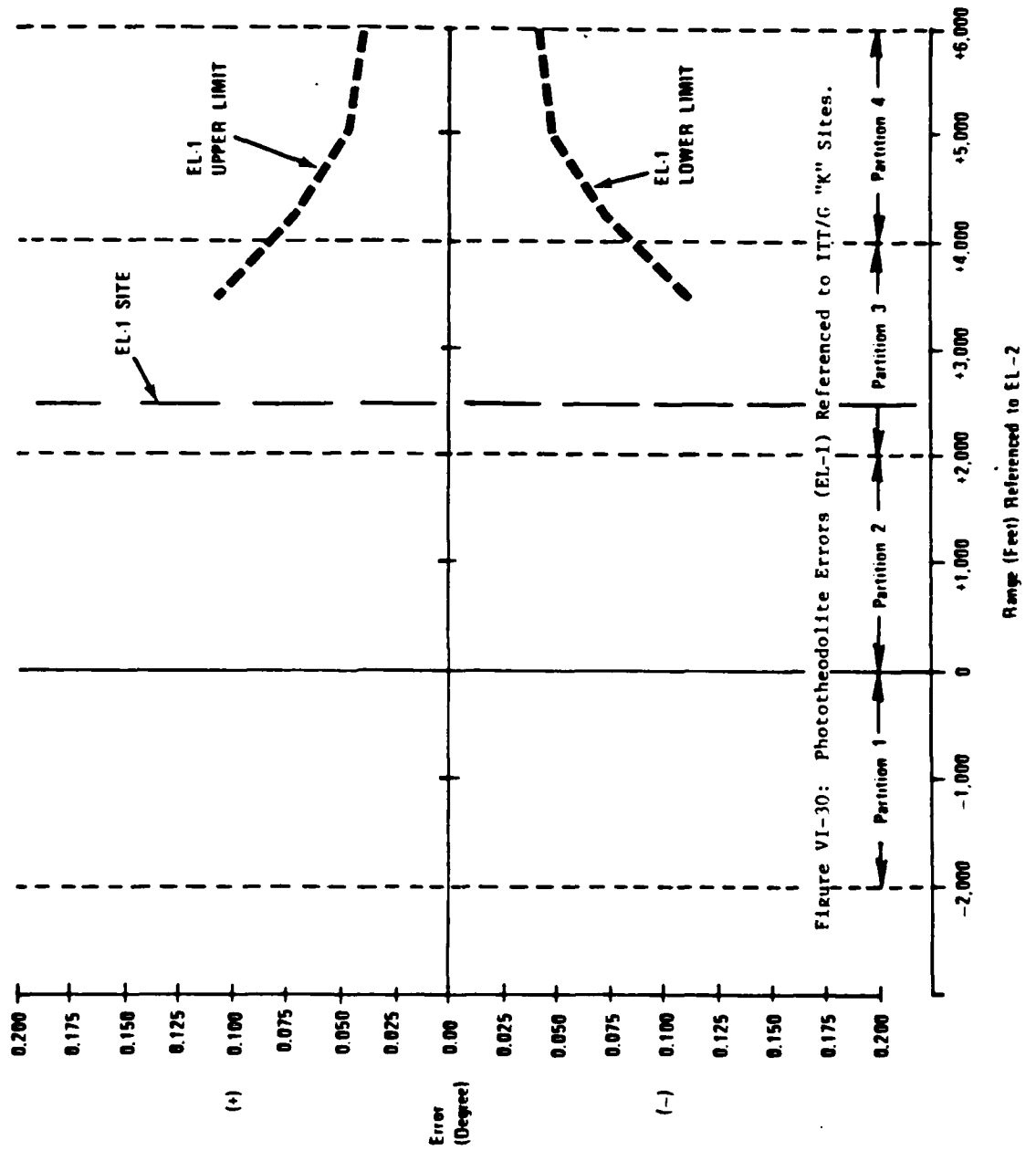
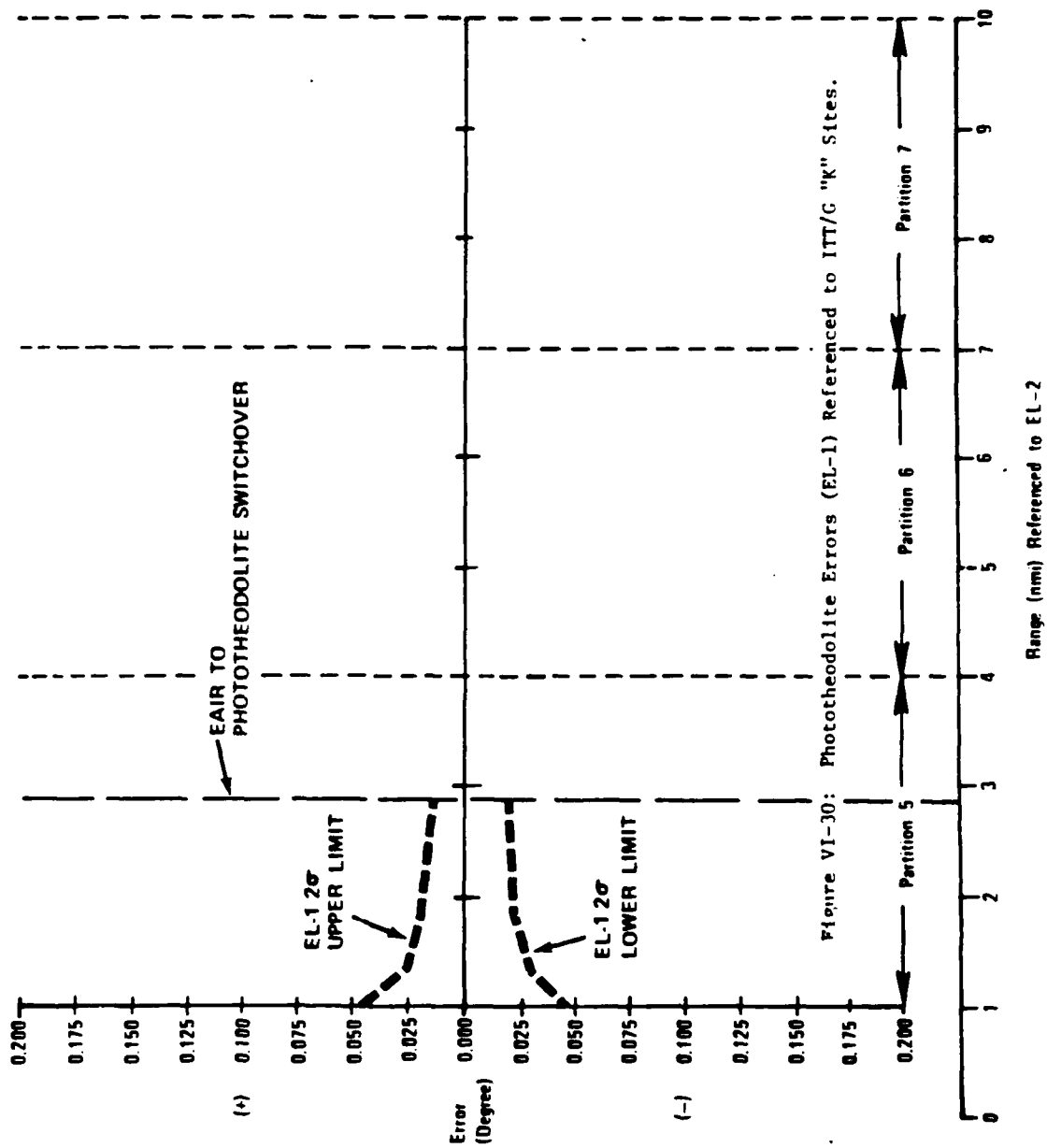
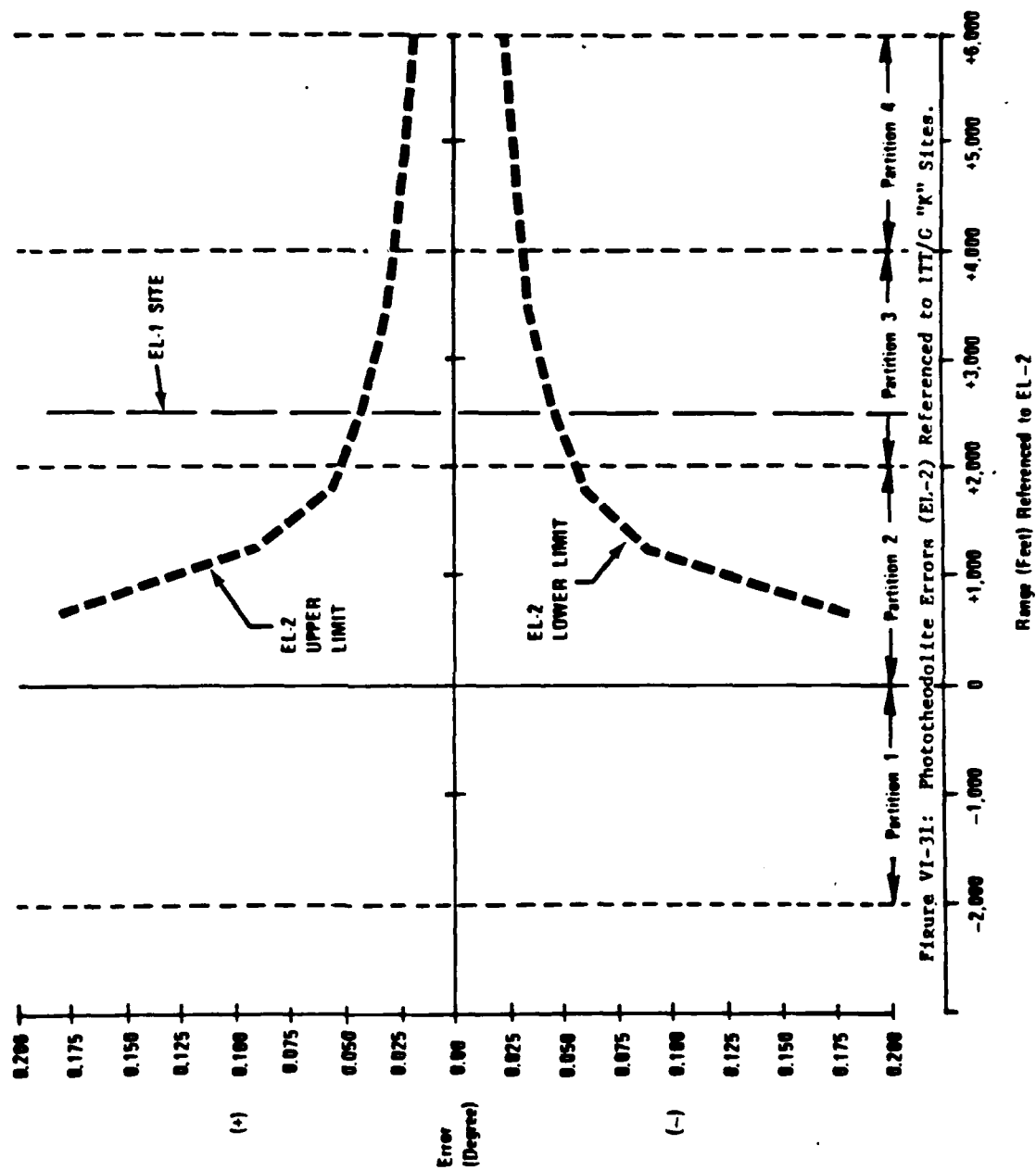


Figure VI-30: Phototheodolite Errors (EL-1) Referenced to IIT/G "K" Sites.





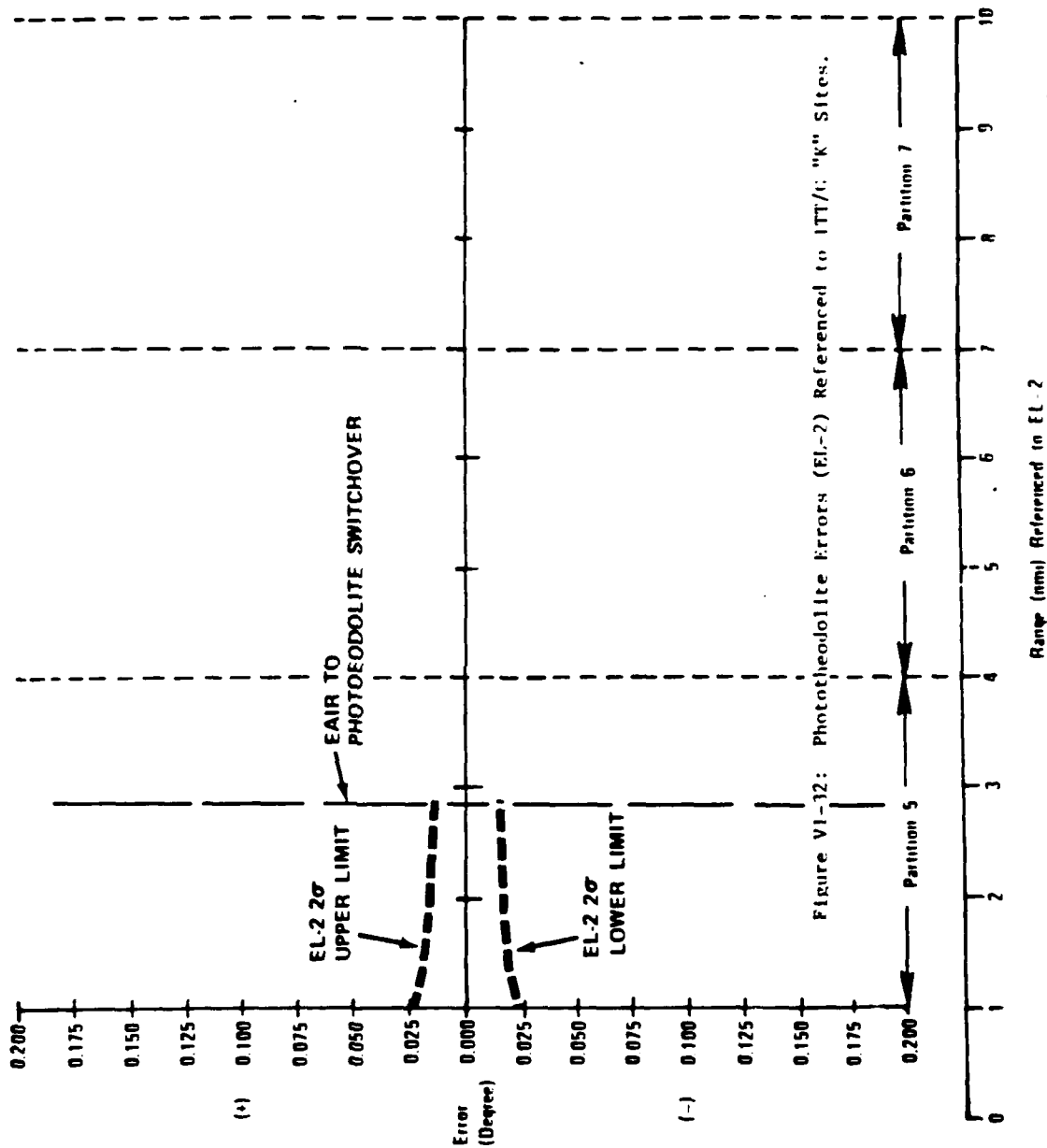


Figure VI-32: Photoconductor Errors (EL-2) Referenced to ITT/K Sites.

TABLE VI-4: EAIR ERRORS

Function	2 $\sigma$ Error
Range	42.4 ft.
Azimuth	0.055°
Elevation	0.034°/about (-) 0.043°

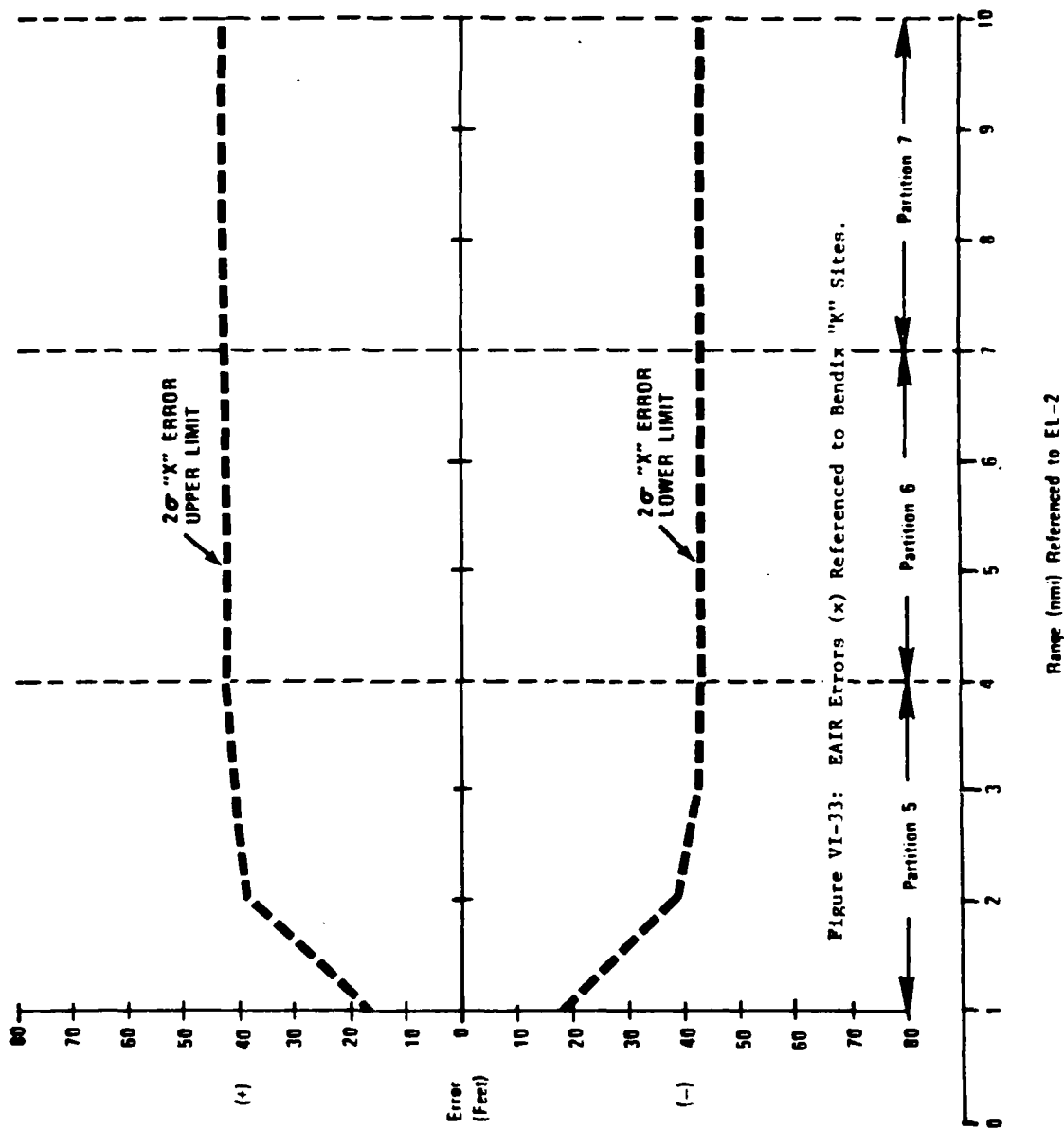
It should be noted that the above errors are in the MLS coordinate system, not the radar mount coordinate system. Thus the above errors may be applied directly to the measured MLS values only in the region of phototheodolite switchover (19,000 to 25,000 feet from azimuth). These MLS errors equate to radar angular mount errors per Table VI-5:

TABLE VI-5: EAIR ERROR AT PHOTOTHEODOLITE SWITCHOVER REGION

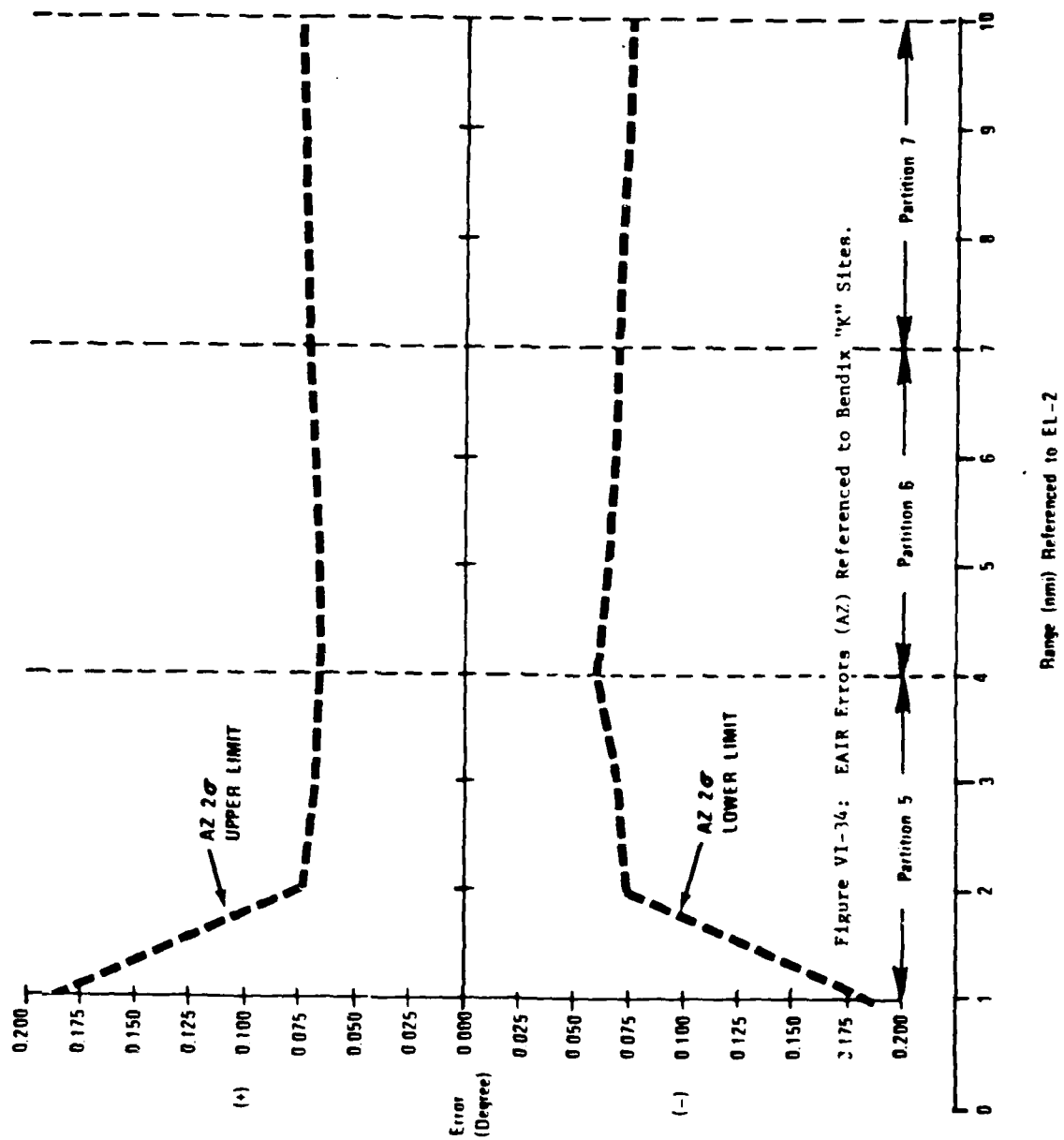
Function	2 $\sigma$
Azimuth	0.088°
Elevation	0.040°/about (-) 0.050°

Figures VI-33 through VI-36 show the EAIR 2 $\sigma$  error values combined with the tracking offsets (C-118) and transformed to the MLS coordinate system for the Bendix runway. Figures VI-37 through VI-40 show the EAIR errors combined with the tracking offsets (DC-6) and transformed to the MLS coordinate system ITT/G runway.

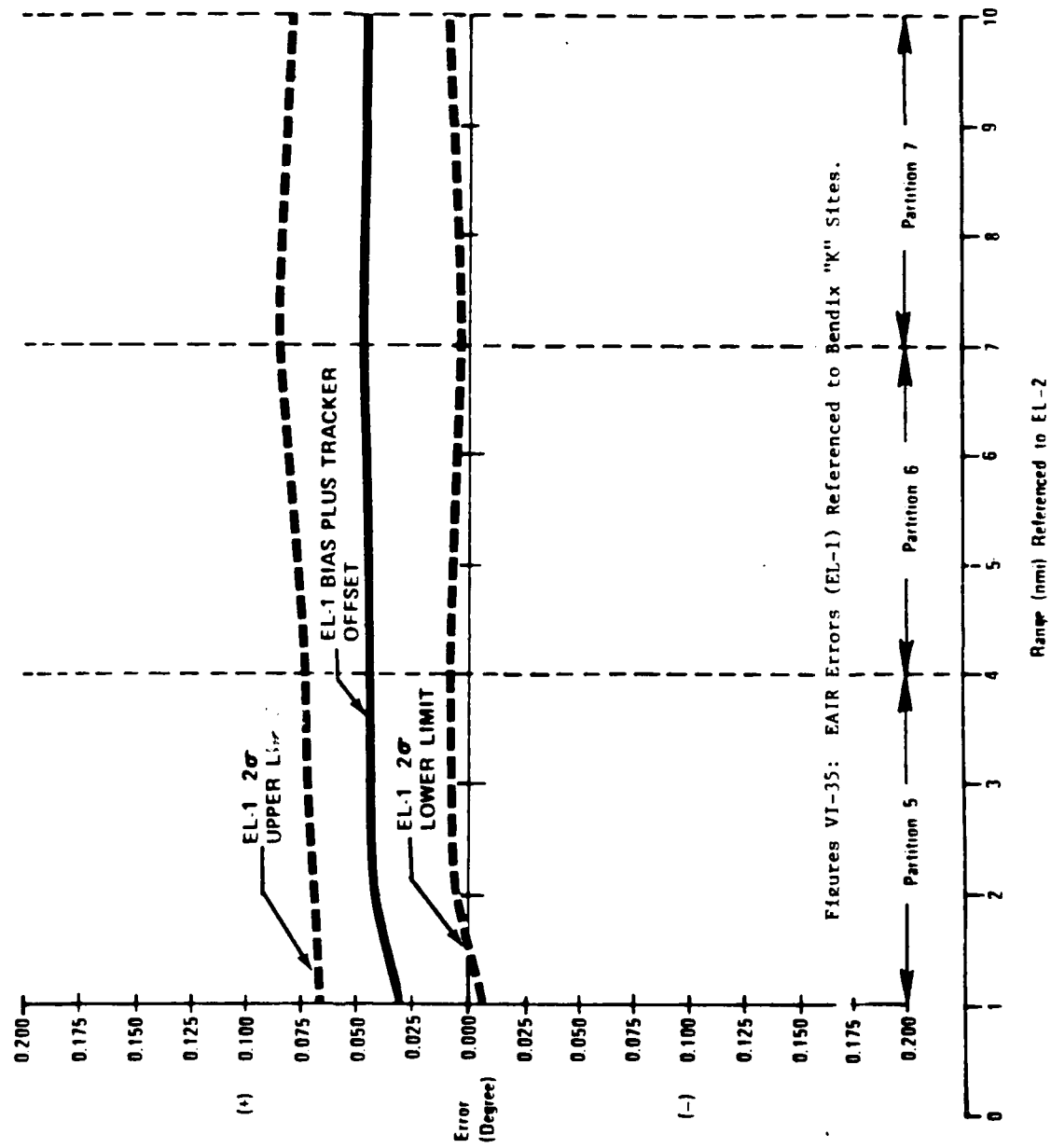




Changed  
18Dec74



VI-40



Figures VI-35: EAIR Errors (EL-1) Referenced to Bendix "K" Sites.

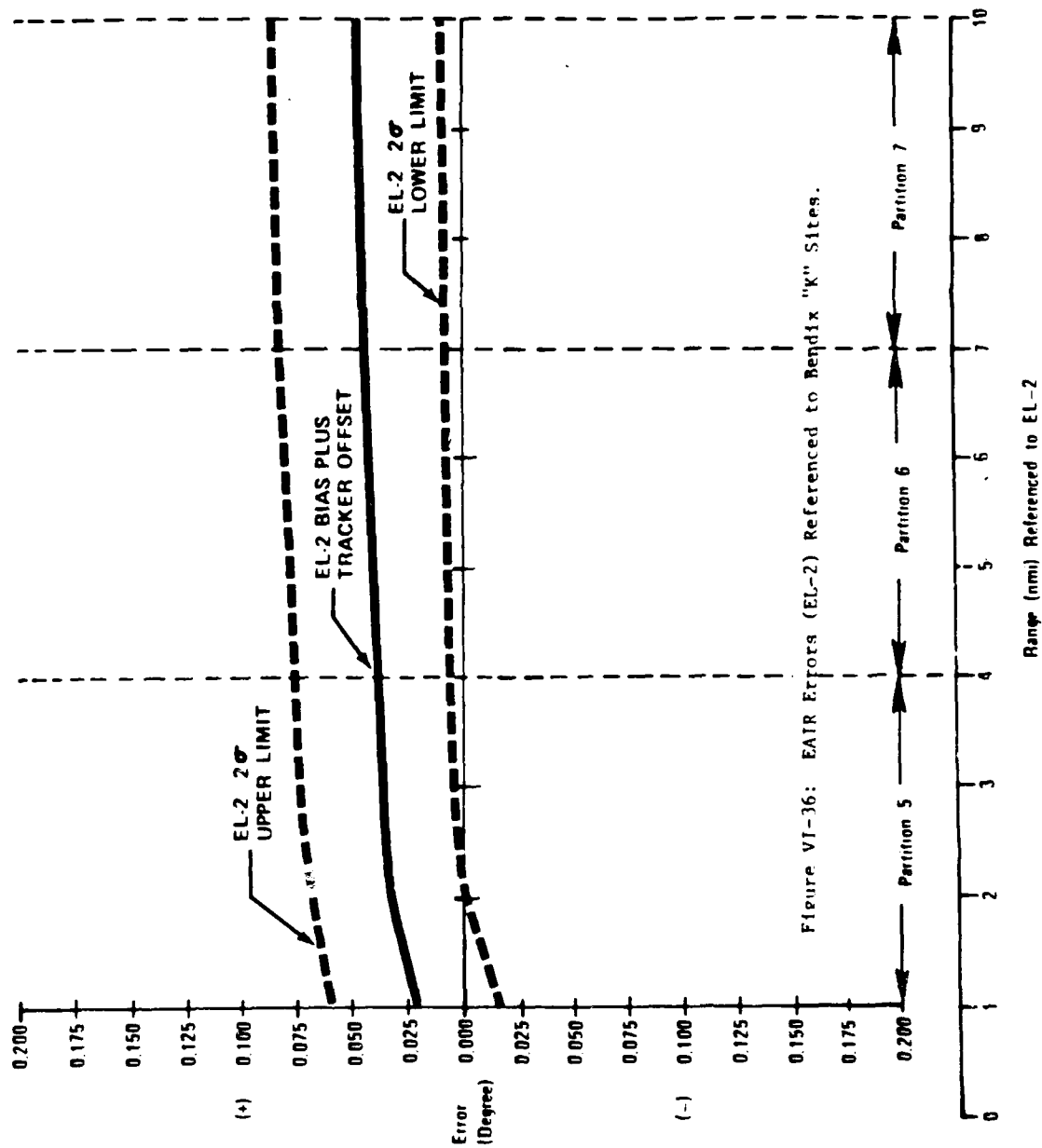


Figure VI-36: EL-2 Errors (EL-2) Referenced to Bendix "K" Sites.

AD-A131 738

MICROWAVE LANDING SYSTEM PHASE II TRACKER ERROR STUDY  
(U) FEDERAL AVIATION ADMINISTRATION WASHINGTON DC

3/3

SYSTEMS RESEARCH AND DEVELOPMENT SERVICE DEC 74

UNCLASSIFIED

FAA/RD-74-207

F/G 17/7

NL

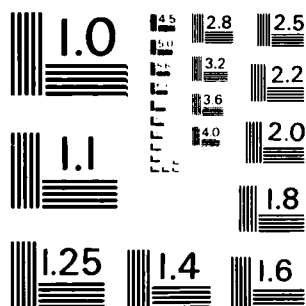


END

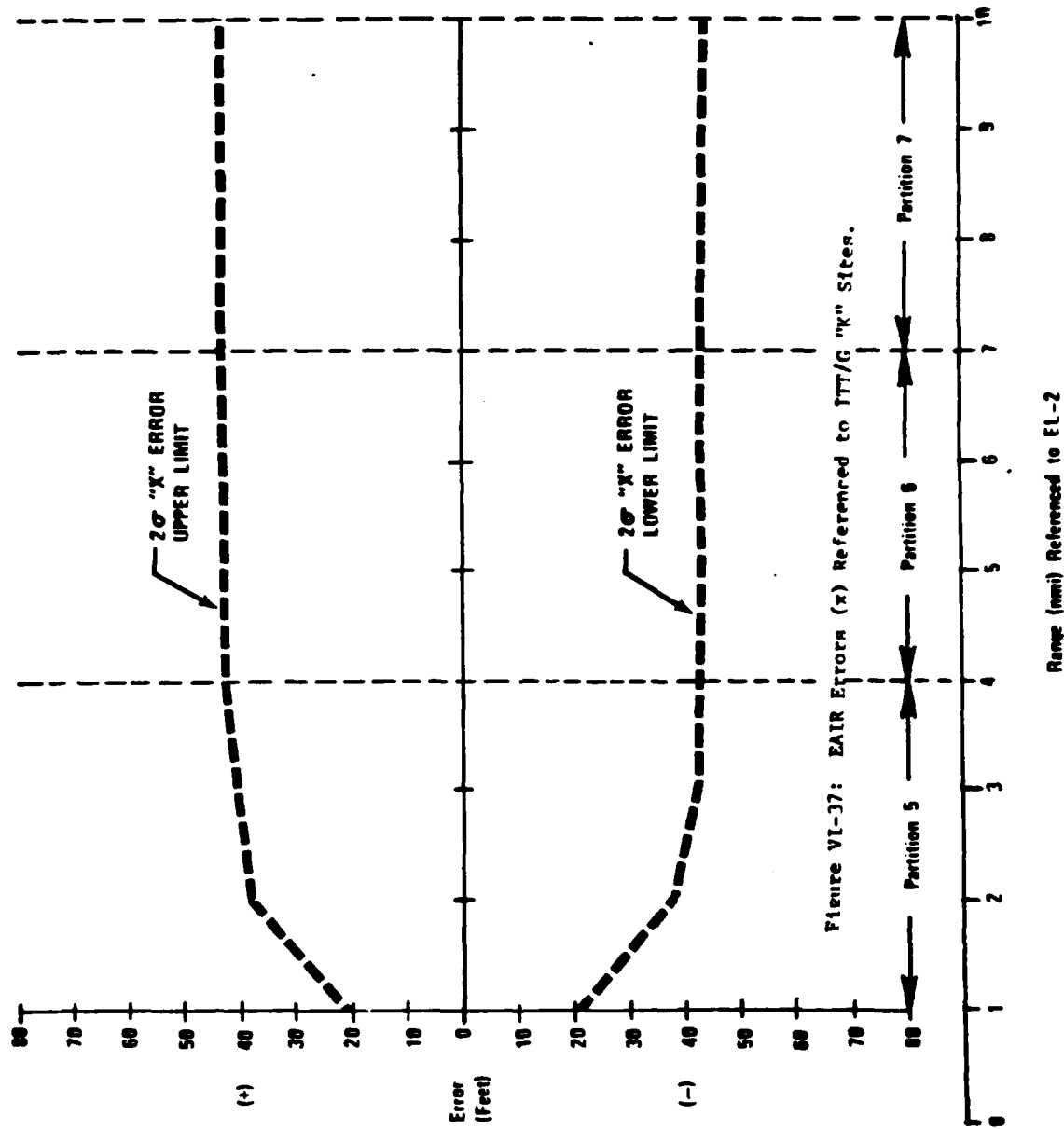
DATE

FILMED

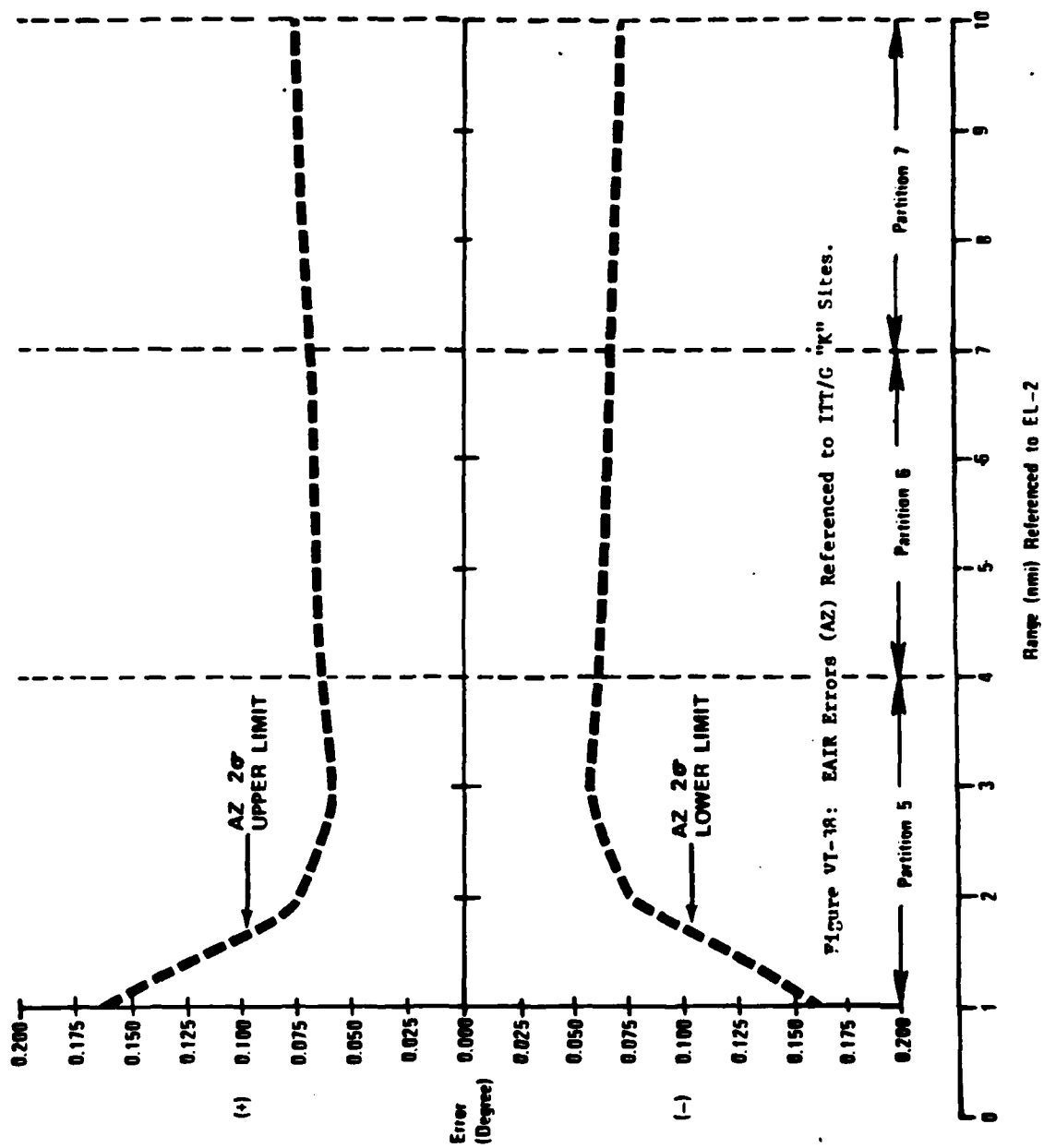
DTIC



MICROCOPY RESOLUTION TEST CHART  
NATIONAL BUREAU OF STANDARDS - 1963 - A



VI-43





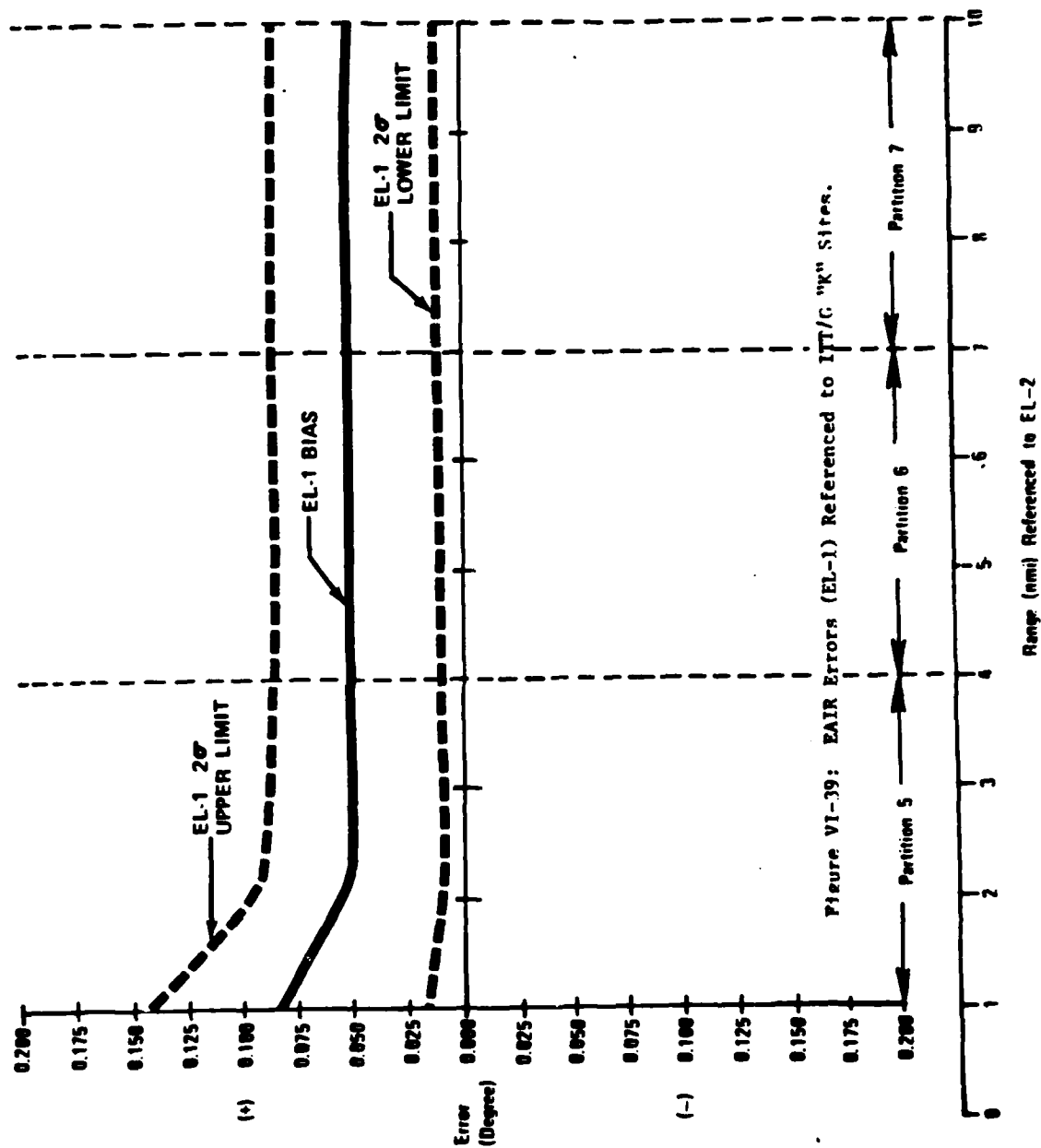
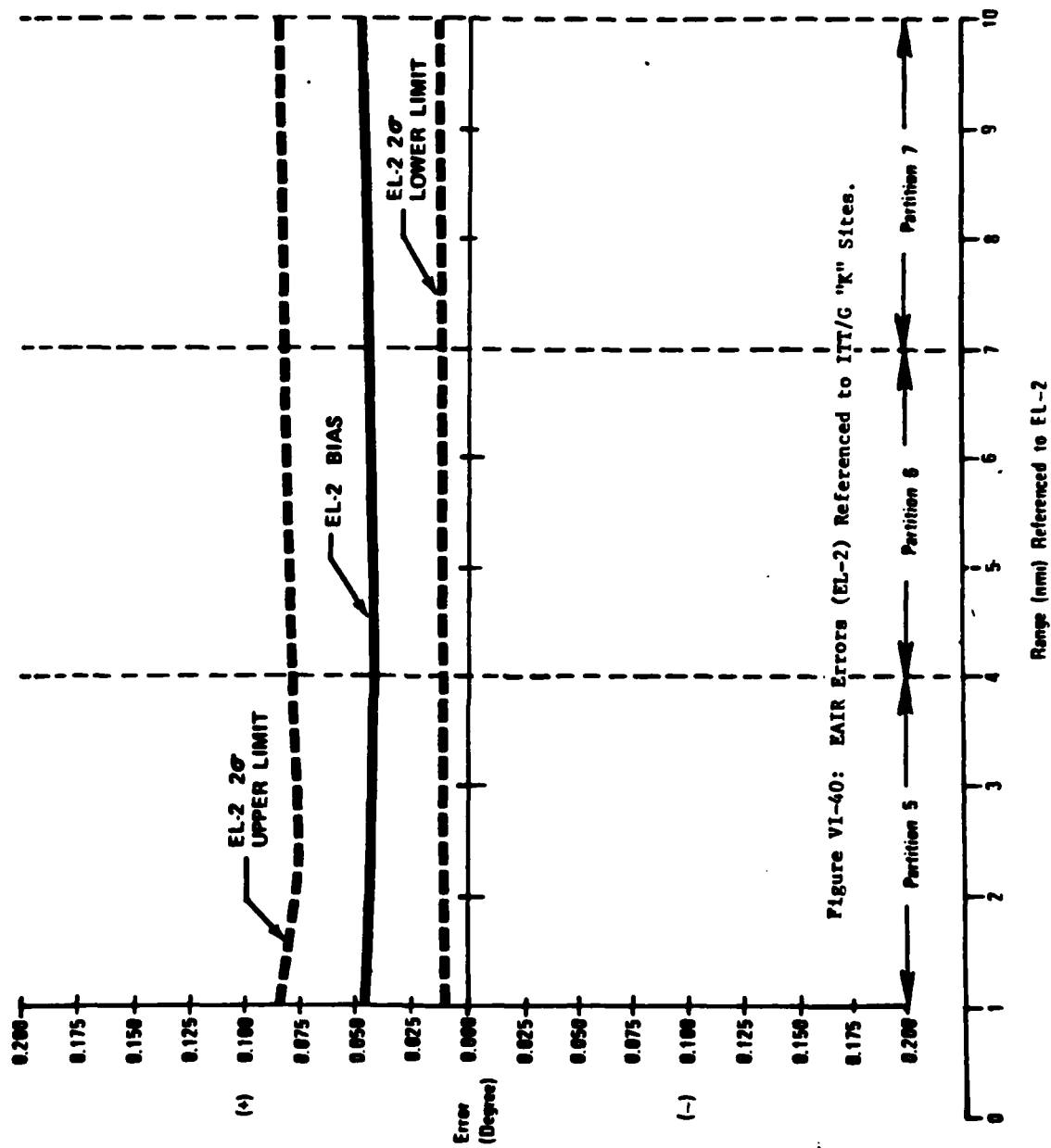


Figure VI-39: BAIR Errors (EL-1) Referenced to ITT/C "K" Sites.



END

DATE  
FILMED

9 — 83

DTIC